THE UNIVERSITY *of* EDINBURGH

Evaluating the Structure-Property Relationships of Pressure-Responsive Materials

Jonathan Gordon Richardson

A thesis submitted in fulfilment of the requirements for the degree of

Doctor of Philosophy to the School of Chemistry,

University of Edinburgh

2021

Declaration

I declare that this thesis has been written by me and that the work carried out is my own, or I have made a substantial contribution towards it except where specific reference is made to another. This work has not been submitted for another degree or professional qualification.

Jonathan Richardson

4th January 2021

Abstract

The field of material science is continuously working on identifying and designing materials for highly-desired applications, such as for gas separation, energy storage, or as part of electronic or sensory devices. This includes a sub-class of materials whose functionality is pressure-responsive, opening up a new plethora of new design possibilities. The capabilities of candidate materials are, however, often evaluated without a thorough understanding of the material structure and how it enables certain properties to be exhibited. The structure-property relationship is central to fully appreciate the behaviour of these materials and facilitate more targeted material development. The overarching theme of this thesis is to provide greater understanding of the structure-property relationships of a selection of pressure-responsive materials, *via* the use of high-pressure X-ray diffraction and various complementary computational techniques. Prior to the experimental chapters, Chapter One provides an overview of the importance of the structure-property relationship in materials alongside two exemplary investigations from the literature and Chapter Two focuses on the theory and defining characteristics of the investigative techniques used in this thesis to outline their suitability and complementary nature to explore the structural and property responses of materials.

Chapter Three focuses on the extensive investigation of four square-planar Pt(II) complexes, specifically two 1,2-dionedioximato complexes and two Magnus salts, which form one-dimensional stacks of metal centres in the solid state and have been identified for their piezoresistivity capabilities through the contraction of the short Pt···Pt separation distances. The full structural response of these four compounds to pressure have been evaluated experimentally for the first time, with platinum bis(1,2-benzoquinonedioximato) demonstrating by far the strongest anisotropic pressure-volume response. Solid-state hybrid density functional theory calculations revealed this response was enabled by strong Pt···Pt interaction in the valence band

and a combination of Pt···Pt and inter-ligand interactions in the conduction band, the latter of which had not been identified in previous studies. These interactions thus result in a small ambient-pressure electronic band gap (0.5 eV), which contracted quickly to form the metallic state by 1 GPa. The other Pt complexes did not exhibit such strong responses due to a lack of the desired strong interlayer interactions in one or both of the frontier bands. The results discussed herein have provided a more detailed set of design criteria for future piezoresistive material development.

Chapter Four continues in a similar manner to Chapter Three, in terms of the touted application of the material under investigation and the techniques utilised, but instead focuses on two polymorphs of an Au(I) dithiolene Mott insulator. In this material, the unpaired electron site is delocalised across the dithiolene components of the ligand and thus communication between neighbouring sites stems mainly from S···S interactions, rather than Au···Au interactions. Both polymorphs were determined to have similar ambient pressure band gaps (*ca.* 0.50 eV) thereby slightly overestimating the literature-stated experimental band gap (0.22 eV). The $P2_1/c$ polymorph showed a stronger pressure-volume response and faster band gap compression, the latter due to greater delocalisation of the Hubbard sub-bands originating from short S···S interactions (< 4 Å) in two directions of the crystal structure. On the other hand, the newly-discovered $P2_1$ polymorph displayed a poor band gap response due to only possessing uni-directional S···S interactions, although the results obtained were hindered by poor crystal quality. These results however further highlight the relationship between crystal packing and the material properties, providing a word of caution to future research in this field that the possibility of polymorphism must be considered carefully.

Chapter Five builds upon the current understanding of the small heterocyclic radical molecule 1,3,5-triathia-2,4-6-triazapentalenyl (TTTA) which is known to exhibit magnetic bistability *via* a strongly hysteretic paramagnetic-diamagnetic switch with an associated structural phase transition between $P2_1/c$ and $P\bar{1}$ polymorphs. Both

polymorphs are dominated visually by π-stacking columns, with these columns linked by short lateral N···S interactions. This new study has revealed the full structural response of the $P2_1/c$ polymorph under pressure, and suggests that the literature-reported gradual suppression of paramagnetism in this material as a response to pressure is due to the decreasing intermolecular separation in the regular π-stacking chains instead of a full structural phase transition as seen under variable temperature. Furthermore, semi-empirical calculations were utilised to calculate the strength of the myriad of intermolecular interactions in both polymorphs, which revealed that the strongest inter-column interactions are comparable to the slipped π-stacking interactions (*ca.* 30 kJ mol^{-1}), verifying their importance in the construction of the two polymorphs and as the source of the wide magnetic hysteresis.

Chapter Six switches focus to a small-pore Sc-based metal-organic framework which has been identified from various crystallographic studies to undergo a $Fddd \rightarrow C2/c$ structural phase transition upon sufficient adsorption of CO_2, as a pure gas or as part of a gas mixture, and shows strong selective uptake for CO_2 over CH_4 which is a highly desirable trait. To provide clarity to the results obtained from X-ray diffraction experiments, classical grand canonical Monte-Carlo simulations have been employed on various fixed structures of the framework obtained under a range of experimental conditions to investigate the adsorption site hierarchies of both CO_2 and CH_4 and quantify the strength of the guest-framework interactions. This study has shown that the selectivity for CO_2 uptake in this material stems from stronger CO_2-framework interactions (between -40 and -20 kJ mol^{-1}) compared to those calculated between CH_4 and framework (no stronger than -20 kJ mol^{-1}). Furthermore, a shift to stronger CO_2 adsorption site energies was observed during the phase transition, whereas no such change in energy was seen in the simulations involving CH_4 adsorption, thus clarifying the different structural responses observed experimentally. This study has highlighted the strengths of utilising classical-based simulations for analysing these type of systems as well how changes in adsorption site environment are highly correlated with subtle changes in the framework structure.

Lay Summary

There is continuous development of new materials to overcome some of the largest technological challenges of modern times, including devising innovations to combat climate change and our dependency on non-renewable resources, designing the next generation of computer components, and discovering a plethora of possibilities for new electronic or sensory devices. The development of such materials, under the umbrella term of material science, is an interdisciplinary process, with expertise required from all realms of chemistry, physics and engineering to complete the journey of synthesising candidate materials, analysing their performance, and ultimately releasing the material commercially as part of a completed product. This entire process can be resource-intensive, in terms of chemicals, time and money, and therefore any procedures which can optimise the process are highly sought after.

One procedure to accelerate the process, and avoid wasting considerable resources, is to identify suitable candidate materials prior to the synthetic stage. This therefore raises the question of what makes a good candidate material. The properties of a material, which can be exploited for specific applications, are strongly linked to its structure. The structure of materials has two levels; firstly, there is the structure of the individual molecules and, secondly, in the case of solid-state materials which are the focus of this thesis, the well-ordered arrangement of the molecules (imagine a repeating 3-D wallpaper pattern) and the nature of the interactions between them. However, the importance of the relationship between the structure and properties of the material is often overlooked, restricting progress towards identifying and designing more efficient materials.

This thesis aims to demonstrate the importance in evaluating the relationship between the structure and properties of a variety of materials, specifically those which are responsive to the application of pressure. The structure-property relationships have been deduced by a combined effort of utilising X-ray crystallography, to study

the full structural response of the material under pressure, and computational calculations, which can be used to verify the structural response of the material and link it to the specific property response. This two-stage methodology allows us to gain greater insight into currently-available materials, which can lead to more-detailed design criteria for new materials and to plug gaps in the current understanding of these materials in the literature.

Dedication

Para Astrid, mi amor. Gracias por todo tu apoyo.

Te quiero, siempre, con todo mi corazón.

"Find your strength when there is none…

Can't you see how far you've come?"

Myles Kennedy

Alter Bridge, *Losing Patience* (Napalm Records, 2016)

"You're not going to be defined by your failures…

You'll be defined by the fact that you refused to give up."

Brent Smith

Promotional interviews for *Attention Attention* (Atlantic Records, 2018)

Acknowledgements

There have been so many people who have provided invaluable help and support through the last few years; hopefully I haven't forgotten to thank anyone, and apologies in advance if I have!

Firstly, Carole, thank you for adopting me for the final two years, for being the perfect balance of firm and friendly, and for not judging me (externally at least!) for any of my foolish questions, DFT-related or otherwise, and for your incredible patience with me during the writing process! To Stephen, your enthusiasm convinced me to work with you within five seconds of meeting you. I'm sorry we didn't get to work together even more, but you had an amazing opportunity which couldn't be passed up. Thanks for all your patience with all my crystallographic needs! To Tina, Claire and Gaël, the GCMC terrific trio, for their amazing crash-courses on the ins and outs of classic simulations! And to Simon, thanks for all the time spent on your crystallographic symmetry lessons, it was greatly appreciated.

A special thanks must go to the graduate school committee at the School of Chemistry for the award of the Principal's Career Development Scholarship, for giving me the incredible opportunity to go on this research journey. I also gratefully acknowledge all the technical support and expertise during my PhD, at the Diamond Light Source I19 Beamline and at the University of Edinburgh. Furthermore, access to the Edinburgh Compute and Data Facility, the UK Tier 2 High Performance Computing Hub (Thomas at UCL) and all the crystallographic equipment I have used during the course of the PhD has been extremely appreciated.

To all the friendly faces I have had the pleasure of working with over the last few years: Matt, Helen D, Jacob, Gary, Ed, Charlie, Giulia, Nico, Scott, Alif, Gemma, Rebecca, Xiaojiao, Sumit, all the folks in Room 234 and from computational cake, my

wonderful collaborators (Neil, Asato, Helen B, Lisette), Ross Forgan, Mark Warren, and all the Chem 2 Inorganic and Materials Chemistry demonstrating teams!

To Wally, Bec, James, Neil, Brian, Luke, Stewart, Cameron, Eleanor, Debs, Liam, Innis and Stanley: thank you for all the fun times, mostly spent distrusting each other over board games or video games, having general catch-ups, and for cheering me up after long hours in the office. You've helped me more than you can imagine. You're all amazing! And to the best friend anyone could ask for, Jake: thanks for looking after me, bud!

To my Spanish family: Paco, for all of your music suggestions and late-night conversations which proved to be hugely welcome distractions; Inma, your hospitability and fantastic cooking was so appreciated during the thesis writing process; and to the rest of the Cañizares and Rosell families, you have made me feel incredibly welcome and I can't thank you enough for that.

To Alan, thanks for all the support and for always knowing how to ask just one more question!

To Mum, thank you for always trusting me and letting me follow my gut instinct to go on these university adventures over the last few years. I know it must seem like I'm in a different world to what you're used to, but I wouldn't have been close to achieving what I have without your love and support throughout.

And lastly, Astrid, to whom this thesis is dedicated. Thank you for being right by my side throughout my highs and lows. This thesis is just as much yours as it is mine. I'm so incredibly lucky to have you in my life.

List of Abbreviations

AFM	Antiferromagnetic
B	Bulk Modulus
BDC	1,4-benzenedicarboxylate
BFGS	Broydon-Fletcher-Goldfarb-Shanno
BLYP	Becke-Lee-Yang-Parr
BQD	bis(1,2-benzoquinonedioximato)
BZ	Brillouin Zone
CASTEP	Cambridge Serial Total Energy Package
CCD	Charged Couple Device
CO	Crystalline Orbital
COHP	Crystal Orbital Hamilton Population
CPO	Coordination Polymer of Oslo
CSD	Cambridge Structural Database
DAC	Diamond Anvil Cell
DFT	Density Functional Theory
DLS	Diamond Light Source
DTA	1,3,2-dithiazolyl
EH2	Experimental Hutch 2
EoS	Equation of State
FM	Ferromagnetic
GCMC	Grand Canonical Monte-Carlo
GGA	Generalised Gradient Approximation
HF	Hartree-Fock
HOCO	Highest Occupied Crystalline Orbital
HOMO	Highest Occupied Molecular Orbital
HSE	Heyd-Scuseria-Ernzerhof

HT	High Temperature
LDA	Local Density Approximation
LJ	Lennard-Jones
LT	Low Temperature
LUCO	Lowest Occupied Crystalline Orbital
LUMO	Highest Occupied Molecular Orbital
MGS	Magnus Green Salt
MIL	Matériaux de l'Institut Lavoisier
MO	Molecular Orbitals
MOF	Metal-Organic Framework
MP2	Second Order Møller-Plesset Perturbation Theory
PBE	Perdew-Burke-Ernzerhof
PDOS	Projected Density of States
PE	Piezoelectric
PET	Piezoelectric Transistor
PR	Piezoresistive
PTM	Pressure-Transmitting Medium
RMS	Root-Mean-Square
RT	Room Temperature
SCDS	Semi-Classical Density Sums
SCF	Self-Consistent Field
SOMO	Semi-Occupied Molecular Orbital
TS	Tkatchenko-Scheffler
TTTA	1,3,5-triathia-2,4,6-triazapentalenyl
ZIF	Zeolitic Imidazolate Framework

atm[a]	bar	kbar	Pa[b]	kPa	MPa	GPa	psi[c]	Torr[d]
0.96852	1	0.001	100000	100	0.1	0.0001	14.5038	750.062
1	1.01325	0.00101	101325	101.325	0.1013	0.000101	14.6959	760.000
1.97385	2	0.002	200000	200	0.2	0.0002	29.0075	1500.12
2.96077	3	0.003	300000	300	0.3	0.0003	43.5113	2250.19
3.94769	4	0.004	400000	400	0.4	0.0004	58.0151	3000.25
4.93462	5	0.005	500000	500	0.5	0.0005	72.5189	3750.31
9.86923	10	0.010	1×10^{6}	1000	1	0.001	145.038	7500.62
98.7	100	0.100	1×10^{7}	10000	10	0.01	1450.38	75006.2
197	200	0.200	2×10^{7}	20000	20	0.02	2900.75	1.5×10^{5}
296	300	0.300	3×10^{7}	30000	30	0.03	4351.13	2.25×10^{5}
395	400	0.400	4×10^{7}	40000	40	0.04	5801.51	3.0×10^{5}
592	600	0.600	6×10^{7}	60000	60	0.06	8702.26	4.5×10^{5}
790	800	0.800	8×10^{7}	80000	80	0.08	11603	6.0×10^{5}
987	1000	1	1×10^{8}	1×10^{5}	100	0.1	14504	7.5×10^{5}
4935	5000	5	5×10^{8}	5×10^{5}	500	0.5	72579	3.75×10^{6}
9869	10000	10	1×10^{9}	1×10^{6}	1000	1	145038	7.5×10^{6}
19739	20000	20	2×10^{9}	2×10^{6}	2000	2	217557	1.5×10^{7}
29,608	30000	30	3×10^{9}	3×10^{6}	3000	3	290075	2.25×10^{7}
39,477	40000	40	4×10^{9}	4×10^{6}	4000	4	580151	3.0×10^{7}
49,346	50000	50	5×10^{9}	5×10^{6}	5000	5	725189	3.75×10^{7}

[a] – standard atmosphere [b] – SI unit of pressure
[c] – pounds per square inch [d] – equivalent to mmHg

Hartrees (au)	kJ/mol	eV	cm^{-1}	kcal/mol	K
1	2625.50	27.21	2.19×10^{5}	627.51	3.18×10^{5}
3.81×10^{-4}	1	0.0103	83.59	0.24	120.27
0.037	96.48	1	8065.19	23.06	11604.33

Table of Contents

Chapter 1

Introduction

Materials science, the design and development of materials for highly desired applications, is a strongly interdisciplinary research field with contributions from synthetic, analytical and theoretical chemistry, physics, and engineering.[1] Examples of such materials which have been of significant focus over recent years include the photovoltaic cell for sunlight-driven energy production,[2, 3] porous metal-organic or covalent-organic frameworks for gas storage and separation,[4-7] and molecular materials which possess switchable properties or bistability for use in data storage and electronic or sensory devices.[8-11] The considerable interest in solid-state materials can be highlighted by the number of entries uploaded to the Cambridge Structural Database,[12] a database for crystalline structure solutions obtained from X-ray and neutron diffraction experiments which are principle structural analysis techniques for crystalline solid state materials. The database has seen accelerating year-on-year growth since its inception (Figure 1.1),[13] with interdisciplinary chemistry and material science being cited as significant contributors. [14]

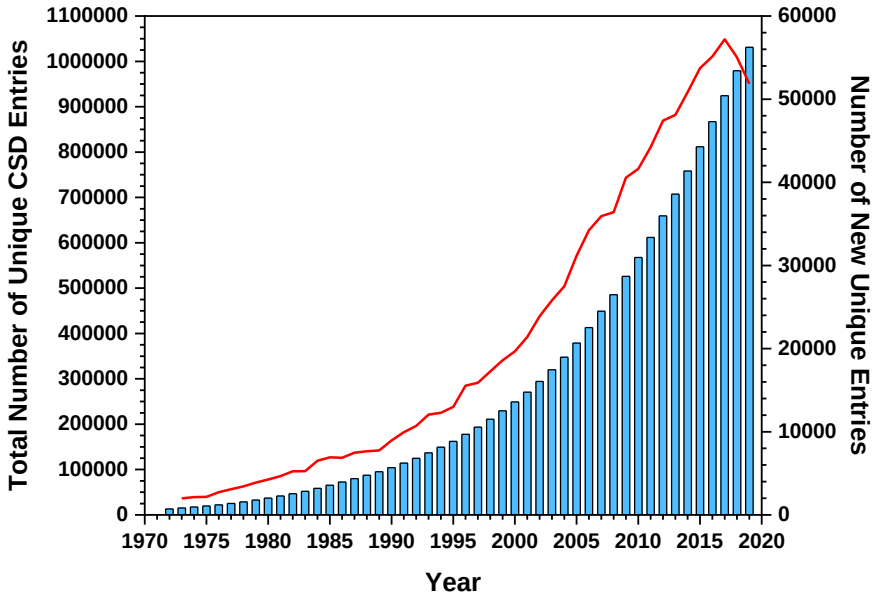

Figure 1.1: Annual end-of-year statistics of the total number of unique entries (blue bars) and new unique entries (red line) submitted to the Cambridge Structural Database, using figures obtained from its official website.[13]

As outlined by the examples provided in the previous paragraph, materials science research is aiming to provide solutions for the largest technological and

environmental challenges of current times. Therefore, there is a need to find materials that fulfil these applications effectively as quickly as possible. However, materials science research carries high time and financial cost, and risks substantial chemical wastage. While the design and development of new materials is always undertaken with certain starting criteria determined by chemical intuition and previous work in the literature, utilising stricter targeted material design and adaptation *via* greater prior understanding of the material properties can only aid the faster identification and implementation of candidate materials.

The properties that a material can exhibit are strongly connected to its structure or specific components of its structure; this strong interplay will hereafter be referred to as the structure-property relationship. From the intramolecular perspective, the structure can be characterised by the atoms present, their connectivity, the molecular conformation and molecular stereoisomerism. However, when considering materials which are present in the crystalline solid state, the intermolecular arrangement of molecules (the relative spatial orientation of individual molecules and the specific nature of intermolecular interactions between molecules) is another vital factor for consideration. Therefore, in order to evaluate the candidacy of materials, it is not sufficient to only study the material properties, but also to provide a full structural characterisation to evaluate how the intramolecular and intermolecular structure hinder or enhance the desired material properties.

A sub-set of material science research is dedicated to the development of pressure-responsive materials. Non-ambient-pressure research, in general, has been of considerable interest over recent years; the range of pressures that are accessible in the laboratory are many orders wider than the range of temperatures accessible, ranging from the ultra-high vacuums ($\approx 10^{-17}$ GPa, 10^{-13} atm) associated with astrophysical research to the extremely high pressures ($\approx 10^{5}$ GPa, 10^{9} atm) associated with geological research.[15-17] With respect to material science, pressure-responsive materials open up a new avenue of possibilities given that certain properties of

materials can be unlocked or switched with the application or release of pressure, which might not otherwise be accessible, and provide an alternative to materials which have high wastage of energy with large heat inputs or outputs. This thesis aims to highlight these possibilities by evaluating the structure-property relationships of a range of pressure-responsive candidate materials.

The current literature understanding on the structure-property relationships of the specific materials discussed in the experimental chapters of this thesis is incomplete and in some cases quite sporadic, thus creating difficulty for researchers to collate information on a particular material class to allow for future targeted material design. This therefore strongly justifies the need for the further investigation of materials already known to the literature, rather than focusing solely on newly-synthesised compounds. Instead of detailing it in this general introduction chapter, an introduction section at the start of each experimental chapter will outline in considerable detail the current understanding of each material discussed therein.

In order to provide a thorough understanding of the structure-property relationships of these materials, a two-stage method is required. Firstly, given that all the materials explored in this thesis are in the solid state and are crystalline, diffraction techniques, such as X-ray crystallography, are ideally suited to evaluate the average structural response. As will be discussed in later chapters, continuous development of X-ray diffraction and high-pressure experimental methods, as well as greater accessibility to synchrotron facilities, over recent decades have resulted in the technique becoming ubiquitous for solid-state research and highly advantageous in being able to provide direct structure solutions,[18-20] compared to those inferred from spectroscopic or spectrometric techniques.

Evaluating the connection between the structural and property responses of the material often relies on delving into the microscopic (molecular and atomic) level, in terms of probing molecular, atomic, and electronic behaviour and energetics.

Therefore, theoretical methods in the form of computational calculations and simulations will act as the second stage of the methodology employed in this thesis, utilising the experimental structure solutions as valuable starting models. There is not one computational technique which can be universally applied to evaluate any property or material type of interest; however, a series of methods and packages are available, each of which has been refined and utilises its strengths for the systems and properties of interest. Throughout the course of this thesis, a variety of computational methods, and the valuable information that can be derived from them, will be illustrated.

Prior to outlining the content of the remainder of the thesis, two case studies will be presented to illustrate the use of the powerful combination of diffraction techniques and computational methods in studying the structure-property relationships of pressure-responsive solid-state materials.

1.1 Case Study 1 – Zeolitic imidazolate frameworks

Zeolitic imidazolate frameworks (ZIFs) are one class of porous metal-organic framework, investigated for various applications including their guest storage capabilities,[21] consisting of functionalised imidazolate linker groups bridging tetrahedral metal centres. ZIF-8, the methyl-functionalised (-CH_3) framework, has been shown, using single crystal high-pressure X-ray diffraction, to undergo a closed-to-open-pore phase transition *via* the rotation of the imidazolate linkers upon adsorption of methanol at 1.47 GPa (Figure 1.2).[22-24]

A more recent investigation, by Hobday *et al.*, aimed to probe the dependency of the high-pressure structural response of ZIFs by varying the functionalisation of the imidazolate linker group.[25] High-pressure X-ray diffraction experiments revealed a similar closed-to-open pore transition in ZIF-90, the formaldehyde-functionalised (-CHO) framework, under methanol adsorption at 0.88 GPa. On the other hand, the

nitro-functionalised (-NO_2) framework, ZIF-65, formed a more closed-pore high-pressure structure above 0.73 GPa (Figure 1.2).

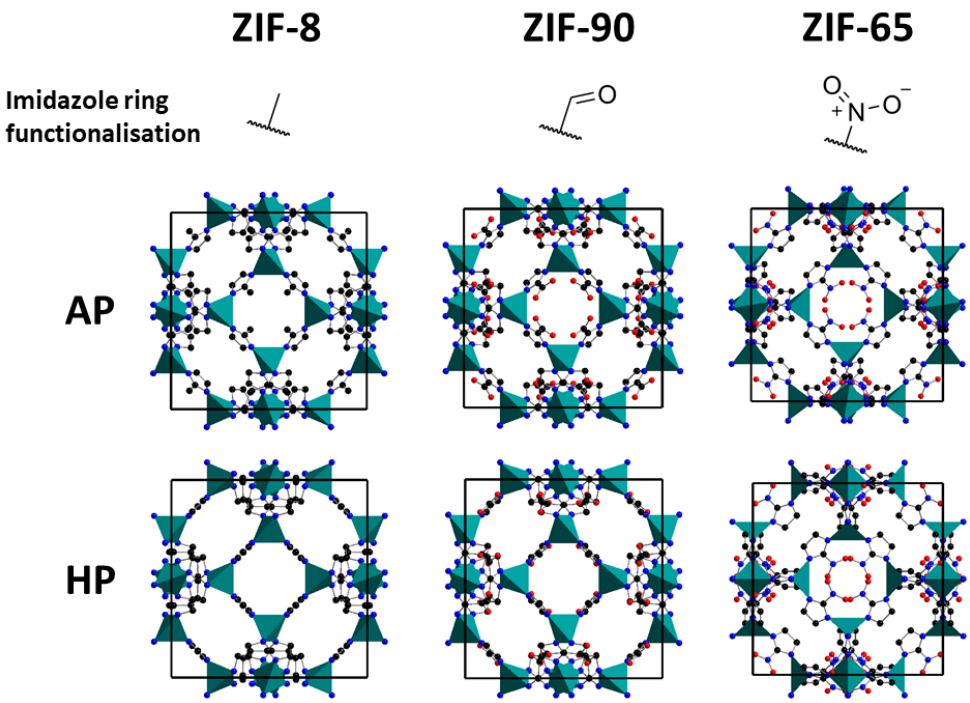

Figure 1.2: Unit cells of three isostructural ZIFs in their ambient pressure (AP) and high-pressure (HP) phases, adapted from the work of Moggach et al. and Hobday et al.[22, 25] Hydrogen atoms have been removed for clarity. C, N and O atoms are coloured black, blue and red respectively, with ZnN_4 units represented by the green tetrahedra. Image created using DIAMOND.[26]

The second stage of the investigation was to utilise computational techniques to rationalise the different directions of linker rotation in these isostructural ZIFs.[25] Through the use of periodic DFT calculations, Hobday *et al.* identified that there was a relatively small energy penalty for the observed linker rotation direction in ZIF-8, whereas a very large energy penalty was observed in the formation of a more closed-pore structure. Similar calculations were undertaken on ZIF-65 and ZIF-90 which revealed smaller energy barriers for the linker rotation in either direction, thus the reasoning for the direction of rotation in these two ZIFs observed experimentally could not be determined solely from this computational method. The final piece of the jigsaw was resolved by use of classical grand-canonical Monte Carlo simulations, used to model the positions of adsorbed methanol molecules in various structures of this group of ZIFs and the resulting interaction energies between the methanol and

the framework. Stronger interaction energies were recorded in the high-pressure phases of all three ZIFs, thus indicating that stronger methanol binding to the framework walls influenced the direction of linker rotation.

This piece of work highlighted the compatibility and complementary nature of not only one but two computational methods with X-ray diffraction experiments, and provided new understanding behind the structural responses of ZIFs. While functionalisation is often undertaken to enhance specific guest uptake or selectivity of a porous material, this study has highlighted that functionalisation can result in differing structural responses.

1.2 Case Study 2 –Pyrazolate-based gold trimers

The second case study concerns the study of pyrazolate-based Au(I) trimers, which have been cited for their potential application in imaging and sensory devices due to their condition-sensitive luminescent properties.[27, 28] The solid-state arrangement of these class of materials is dominated by the presence of inter-trimer Au···Au 'aurophilic' interactions, comparable in strength to hydrogen bonding interactions.[29-32]

Woodall *et al.* investigated the structure-property relationships of four of these pyrazolate-based Au(I) trimers (Figure 1.3),[33] with the changes in structure and luminescence evaluated between 100 K and 300 K and between ambient pressure and 10 GPa. Upon resolving the ambient-pressure structures by X-ray diffraction experiments, the solid-state arrangement of the four compounds was revealed to be heavily influenced by the extent of steric bulk on the R_1-R_3 groups on the pyrazolate linkers. The shortest inter-trimer Au···Au contacts were seen in **1**, with contact distances between 3.0 Å and 3.3 Å in all three dimensions, whereas **2** also contained contact distances of *ca.* 3.3 Å but only in one dimension which resulted in stacking of the individual trimers. With phenyl rings (C_6H_6) incorporated onto the pyrazolate

linker, **3** and **4** exhibited much larger inter-trimer Au···Au contacts, with the shortest measured at *ca.* 3.7 Å and 7.6 Å respectively.

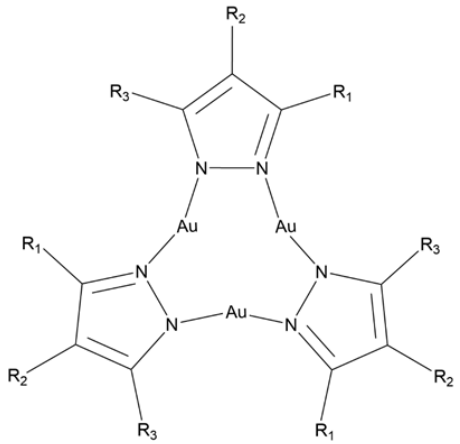

1 R_1: H R_2: H R_3: H

2 R_1: CH_3 R_2: CH_3 R_3: CH_3

3 R_1: C_6H_6 R_2: H R_3: CH_3

4 R_1: C_6H_6 R_2: C_6H_6 R_3: C_6H_6

Figure 1.3: Molecular structures of the pyrazolate-based Au(I) trimers investigated by Woodall et al.,[33] with the varying functionalisation of the pyrazolate bridging ligands.

The shortest inter-trimer Au···Au contacts present in these compounds directly affected the luminescent properties exhibited; at ambient conditions, only **1** and **2** exhibited luminescence, with emission peaks observed at 13000-15000 cm^{-1}. With decreasing temperature or increasing pressure, the resulting contraction in the Au···Au contact distances coincided with a red shift of these luminescence emission peaks (in other words, shifting to higher wavelengths, and thus corresponding to a decrease in the size of the optical band gap) or the emergence of new emission peaks. Decreasing temperature or increasing pressure also resulted in luminescence being exhibited by **3**, whereas **4** continued to show no luminescence under any tested non-ambient conditions.

The experimental work was followed up by solid-state computational calculations, which firstly verified the extent of structural contraction observed for the four compounds at non-ambient conditions. Furthermore, for **1**, the optical band gap was calculated to decrease with decreasing Au···Au contact distances, thus verifying the red shift observed experimentally under low temperatures or high pressures. Lastly, these calculations revealed that the nature of the lowest occupied crystalline orbital

(LUCO) involved significant inter-trimer interactions, indicating the importance in close trimer packing in the solid state for the compound to exhibit luminescence, and thus why they are non-existent in **4**.

This study, through the coupled approach of experimental and computational methods, successfully evaluated the structure-property relationships of the four Au(I) pyrazolate-based trimers under the application of pressure. The importance of the intermolecular arrangement *via* short Au···Au contacts in the solid state and how these are controlled by the extent of steric bulk on the trimer ligands was made readily apparent, which should aid targeted future material design.

1.3 Thesis outline

The complementary nature of X-ray diffraction and computational methods are a constant thread throughout this thesis, the specifics of which will be outlined in the methods chapter. After the methods chapter, four experimental chapters are presented with each comprehensively covering the evaluation of the structure-property relationships of a different class of material with varying desired applications. Specifically, this thesis will investigate Pt and Au complexes which have been identified for their capability of undergoing an insulator-to-metal transition upon the application of pressure, a magnetically-bistable molecular material which is therefore a candidate for application in storage and sensory devices, and a small-pore Sc-based framework material which has shown promising gas selective uptake behaviour for application in gas separation. The full structural response of these materials will be evaluated, with the structural models acting as valuable starting points for computational calculations. The calculations will quantify the underlying features of each material to explain, firstly, their structural response and, secondly, the relationship between the structural and property responses to pressure. This new and extensive understanding of the material can then act as a feedback loop in providing a stronger set of criteria for next generation material design.

1.4 References

1. Encyclopedia_Britannica, https://www.britannica.com/technology/materials-science, (accessed April, 2020).
2. P. K. Nayak, S. Mahesh, H. J. Snaith and D. Cahen, *Nat. Rev. Mater.*, 2019, **4**, 269-285.
3. B. Parida, S. Iniyan and R. Goic, *Renew. Sustain. Energy. Rev.*, 2011, **15**, 1625-1636.
4. H. C. Zhou, J. R. Long and O. M. Yaghi, *Chem. Rev.*, 2012, **112**, 673-674.
5. M. Banerjee and M. Schröder, *Functional metal-organic frameworks gas storage, separation and catalysis*, Springer Berlin Heidelberg, Berlin, 2010.
6. H. Yang and J. R. Li, in *Porous Materials for Carbon Dioxide Capture*, ed A.-H. Lu, L.-N. He, R. D. Rogers, D. Su, P.Tundo, Z. C. Chang and S. Dai, Springer Berlin Heidelberg, Berlin, 2014, ch. 3, pp. 79-113.
7. M. S. Lohse and T. Bein, *Adv. Funct. Mater.*, 2018, **28**, 1705553.
8. O. Sato, *Nat. Chem.*, 2016, **8**, 644-656.
9. D. W. Bruce, D. O'Hare and R. I. Walton, *Molecular materials*, Wiley, Chichester, 2010.
10. V. I. Minkin, *Russ. Chem. Bull.*, 2008, **57**, 687-717.
11. A. Coskun, J. M. Spruell, G. Barin, W. R. Dichtel, A. H. Flood, Y. Y. Botros and J. F. Stoddart, *Chem. Soc. Rev.*, 2012, **41**, 4827-4859.
12. C. R. Groom, I. J. Bruno, M. P. Lightfoot and S. C. Ward, *Acta Crystallogr., Sect. B: Struct. Sci., Cryst. Eng. Mater.*, 2016, **72**, 171-179.
13. Cambridge Crystallographic Data Centre, http://www.ccdc.cam.ac.uk/solutions/csd-system/components/csd/, (accessed April, 2020).
14. Cambridge Crystallographic Data Centre, http://ccdc.cam.ac.uk/posters/csd-in-numbers-2019, (accessed April, 2020).
15. A. G. M. Abdulgalil, A. Rosu-Finsen, D. Marchione, J. D. Thrower, M. P. Collings and M. R. S. McCoustra, *ACS Earth Space Chem.*, 2017, **1**, 209-215.
16. R. Jeanloz, P. M. Celliers, G. W. Collins, J. H. Eggert, K. K. M. Lee, R. S. McWilliams, S. Brygoo and P. Loubeyre, *Proc. Natl. Acad. Sci. U.S.A.* , 2007, **104**, 9172-9177.
17. H. K. Mao, B. Chen, J. H. Chen, K. Li, J. F. Lin, W. E. Yang and H. Y. Zheng, *Matter. Radiat.*, 2016, **1**, 59-75.
18. H. R. Powell, *Crystallogr. Rev.*, 2019, **25**, 264-294.
19. A. Jayaraman, *Rev. Mod. Phys.*, 1983, **55**, 65-108.
20. K. Brister, *Rev. Sci. Instrum.*, 1997, **68**, 1629-1647.
21. B. L. Chen, Z. X. Yang, Y. Q. Zhu and Y. D. Xia, *J. Mater. Chem. A*, 2014, **2**, 16811-16831.

22. S. A. Moggach, T. D. Bennett and A. K. Cheetham, *Angew. Chem., Int. Ed.*, 2009, **48**, 7087-7089.

23. M. R. Ryder, B. Civalleri, T. D. Bennett, S. Henke, S. Rudic, G. Cinque, F. Fernandez-Alonso and J. C. Tan, *Phys. Rev. Lett.*, 2014, **113**, 215502.

24. N. Y. Tan, M. T. Ruggiero, C. Orellana-Tavra, T. Tian, A. D. Bond, T. M. Korter, D. Fairen-Jimenez and J. A. Zeitler, *Chem. Commun.*, 2015, **51**, 16037-16040.

25. C. L. Hobday, T. D. Bennett, D. Fairen-Jimenez, A. J. Graham, C. A. Morrison, D. R. Allan, T. Düren and S. A. Moggach, *J. Am. Chem. Soc*, 2018, **140**, 382-387.

26. Brendenburg K. (1999). DIAMOND. Crystal Impact GbR, Bonn, Germany.

27. C. Yang, M. Messerschmidt, P. Coppens and M. A. Omary, *Inorg. Chem.*, 2006, **45**, 6592-6594.

28. V. W. W. Yam and E. C. C. Cheng, *Chem. Soc. Rev.*, 2008, **37**, 1806-1813.

29. K. Doll, P. Pyykko and H. Stoll, *J. Chem. Phys.*, 1998, **109**, 2339-2345.

30. N. Runeberg, M. Schutz and H. J. Werner, *J. Chem. Phys.*, 1999, **110**, 7210-7215.

31. E. R. T. Tiekink, *Coord. Chem. Rev.*, 2014, **275**, 130-153.

32. H. Schmidbaur, *Gold Bull.*, 2000, **33**, 3-10.

33. C. H. Woodall, S. Fuertes, C. M. Beavers, L. E. Hatcher, A. Parlett, H. J. Shepherd, J. Christensen, S. J. Teat, M. Intissar, A. Rodrigue-Witchel, Y. Suffren, C. Reber, C. H. Hendon, D. Tiana, A. Walsh and P. R. Raithby, *Chem. Eur. J.*, 2014, **20**, 16933-16942.

Chapter 2

Experimental and Computational Methods

2.1 Synopsis

This chapter provides an overview of the complementary experimental and computational methods featured in the investigative work in this thesis, and justification for their use. The experimental methods are considered first, which exclusively focus on X-ray crystallography, using both in-house and synchrotron facilities at ambient-pressure and high-pressure, and how the bulk modulus can be extracted from the results of these measurements. The second part concerns the range of computational methods which have been utilised, covering quantum mechanical, semi-empirical and classical methods.

2.2 Experimental Methods

X-ray crystallography is a technique of structural characterisation which is strongly embedded into everyday chemistry research, due to the rapid development in computational resources and instrumentation over recent decades, providing direct structural solution of crystalline samples on the timescale of minutes and hours, all stemming from the original pioneering work by von Laue, Knipping, Friedrich and Bragg (father and son) in the early 1900s.[1, 2] Assuming a crystalline sample of sufficient quality of the material of interest is obtainable, structure determination from diffraction techniques offers advantages over other analytical techniques, in particular for unambiguously determining connectivity and spatial arrangements of the atoms that compose the crystal. Given that this thesis concerns the investigation of structure-property relationships of pressure-responsive materials, the need for characterising the changes in the intramolecular and, more importantly, intermolecular structure of the materials under investigation necessitates the use of diffraction techniques, and thus X-ray crystallography at ambient and high pressures is the sole experimental technique to feature in this thesis.

2.2.1 In-house X-ray crystallography

The ambient pressure structure of the majority of the materials studied in this thesis are already known in the literature. Nevertheless, ambient-pressure diffraction experiments were undertaken using the in-house laboratory diffractometers in order to check the crystal quality, and to ensure all the materials had a high-quality room-temperature (RT) (283-303 K) structure, prior to committing to high-pressure experiments. The ambient pressure structures reported in this thesis were obtained using a pair of in-house laboratory diffractometers at the School of Chemistry: a three-circle Bruker SMART APEX-II goniometer with a CCD detector using Mo-Kα radiation (λ = 0.71073 Å), using a ω-scan sphere data collection strategy (Table 2.1), or a dual-source Rigaku Oxford Diffraction SUPERNOVA diffractometer with a four-circle goniometer and Atlas S2 CCD detector using Cu-Kα radiation (λ = 1.54184 Å), using an optimised strategy according to the indexed crystal lattice to maximise completeness and redundancy.

Table 2.1: Data collection strategy run list used for the ambient pressure diffraction experiments on the Bruker SMART APEX II in-house diffractometer. The ω step size was 0.5°. The κ angle was fixed to 54.8° for all runs.

Run	2θ (°)	ϕ (°)	ω range (°)
1	-28.0	0.0	331.5 to 152.0
2	-28.0	120.0	331.5 to 152.0
3	-28.0	240.0	331.5 to 152.0
4	28.0	60.0	27.5 to 208.0

2.2.2 Synchrotron-based X-ray crystallography

The development of central facilities has greatly enhanced material research, with the availability of tuneable radiation wavelength and high-intensity radiation permitting the study of weakly diffraction samples or undertaking experiments which cannot be fulfilled by in-house instrumentation. In the case of X-ray diffraction experiments, the use of synchrotron radiation results in much faster collection times *via* shorter exposure times. In addition, they also provide greater completeness *via* the capture of

weaker reflections in the diffraction pattern which are otherwise potentially unobservable using in-house diffractometers. While the use of synchrotron facilities aids the collection of ambient pressure diffraction data, its use is strongly justified when collecting high-pressure data because the construction of the high-pressure cells used for these experiments results in a decrease in number and intensity of reflections collected compared to an ambient pressure experiment; this is discussed in more detail in Section 2.2.3.

All high-pressure experiments in this thesis were undertaken at the Diamond Light Source (DLS) (Rutherford Appleton Laboratory, Harwell, UK) synchrotron facility on the I19 beamline, experimental hutch 2 (EH2),[3] on a Newport four-circle diffractometer goniometer equipped with a DECTRIS PILATUS 300K hybrid-pixel detector using synchrotron radiation with λ=0.49598 Å (25.512 keV). The beamline is specifically dedicated for single-crystal diffraction experiments, with the EH2 setup being able to facilitate experiments at various conditions, including at temperatures ranging from 5 K to 1300 K, under exposure of gas pressure using quartz or sapphire capillary gas cells (up to 200 bar),[4, 5] under moderate liquid pressures utilising a sapphire capillary pressure cell and hand-pump setup (up to 1 kbar),[5] and high-pressure by use of diamond-anvil cells (10^{-1}-10^{1} GPa).

2.2.3 High-pressure X-ray crystallography

High-pressure studies prior to the 1960s involved the study of macroscopic properties, rather than the structural response of the material *via* X-ray diffraction.[6] A large breakthrough for the field of high-pressure structural studies came with the development of a cell in which pressure could be applied to a crystal sample by squeezing it between the flat faces (culets) of two opposing diamonds.[7, 8] The diamond anvil cell (DAC) was first reported in the high-pressure diffraction studies of water ice in 1965.[9, 10] Since then, it has undergone significant development, with the most successful design being that devised by Merrill and Bassett,[11] due to its small size and

the move in the field towards the use of internal pressure calibrants, thus proving it more popular than the piston-operated cell alternatives.[6, 12] Continuous improvements and developments have been applied to the design of the DACs over recent decades, to improve the resulting diffraction quality and to remove the toxic Be components in the original design.[6] The DAC has since become an ubiquitous feature of laboratories and synchrotrons focussing on high-pressure research, with cells now capable of working up to 10^3 GPa.[13]

The DAC design utilised for the high-pressure X-ray crystallography experiments in this thesis is a modified version of a Merrill-Basset cell,[14] with all the component parts shown in Figure 2.1A. The cell consists of two steel plates, each with a conical hole with an opening half-angle of 40° to allow the incident and diffracted X-ray beams to enter and leave the cell, respectively. Within this conical hole sit the tungsten carbide backing discs, which hold the opposing embedded anvils in position. The backing discs include a confocal hole to allow the X-ray beam to pass through, to facilitate optical alignment of the anvils and to provide easy viewing of the sample. A 300 μm-thick tungsten gasket containing a 300 μm diameter drilled circular hole is placed between the culets of the opposing anvils; the cylindrical chamber which accommodates the sample under investigation is formed by the edges of the drilled hole and the anvil culets (Figure 2.1B), and is sealed by pushing the upper plate along the guide pins of the lower plate. The separation distance of the two plates is further decreased by tightening three Allen screws, which results in an increase of pressure inside the sample chamber. Prior to drilling the chamber hole, the gasket is pre-indented by around 100 μm in total; this has the dual purpose of increasing the tensile strength of the gasket material and acts as a visual aid to guide the drilling of the sample chamber hole so that it is positioned in the middle of the culets, reducing the risk of compromise to the chamber seal at high pressures.

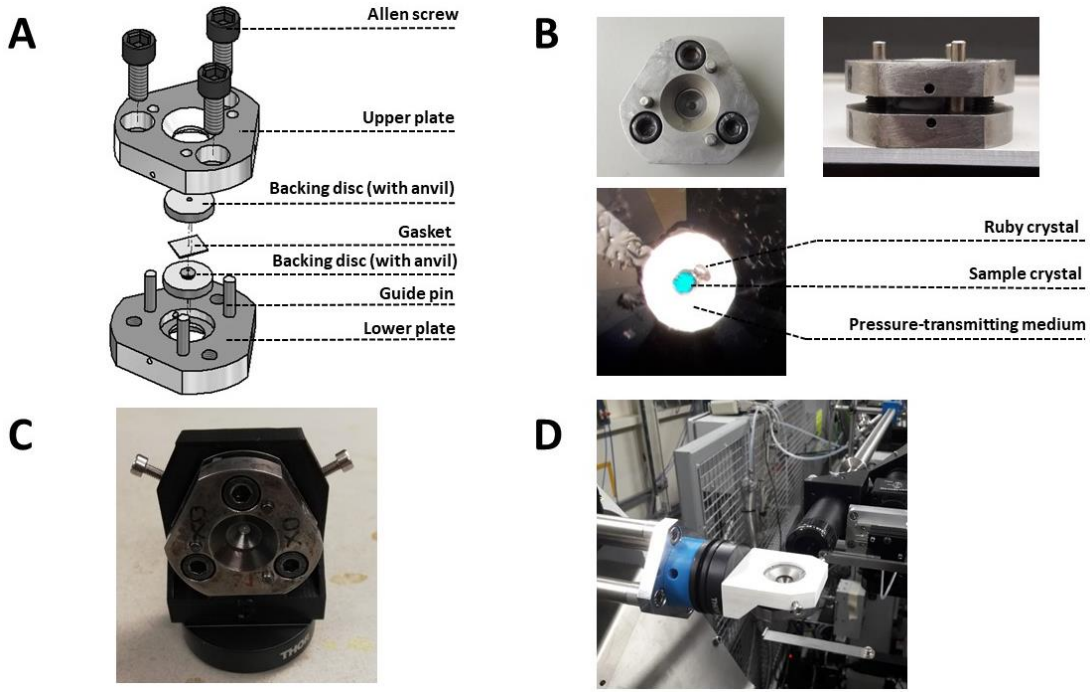

Figure 2.1: A: Exploded view of the Merrill-Basset DAC used for all high-pressure X-ray crystallography experiments in this thesis, with all the component parts named. B: Front (top left) and side (top right) views of closed DAC, with zoomed view of sample chamber and its contents (bottom left). C: 3-D printed DAC mount used on the DLS I19 beamline. D: DAC mounted on the diffractometer on the DLS I19 beamline, orientated perpendicular to the beam direction.

The sample chamber holds the single crystal sample of interest, alongside an internal pressure calibrant (Figure 2.1B). The pressure calibrant used for all the work discussed in this thesis took the form of ruby (Cr^{3+}-doped α-Al_2O_3) crystals. The ruby crystals, upon the application of green light (λ= 520-560 nm), exhibit sharp-line fluorescence with a distinctive doublet peak at λ = *ca.* 693 nm (R_1) and *ca.* 694 nm (R_2), with R_1 shifting with applied pressure at a linear rate of 0.0274(2) GPa nm^{-1}.[15-17] This ruby fluorescence method is a well-established pressure-measuring technique; it can be easily undertaken using standard laboratory spectrometers and has practical advantages over using an internal diffraction standard.

Pressure is applied to the sample crystal by filling the sample chamber with a liquid pressure-transmitting medium (PTM) prior to closing the cell. In all the high-pressure experiments for this thesis, the PTM, consisting of long-chain molecules, such as those comprising Fluorinert and Daphne oils (Table 2.2), causes hydrostatic compression of

the crystal sample. However, in the case of porous materials, such as metal-organic frameworks, the use of a PTM comprised of small molecules can lead to the PTM penetrating the porous structure.[18-20]

Table 2.2: List of commonly used pressure transmitting medium solvents and their maximum hydrostatic pressure, obtained from the literature.

Pressure transmitting medium		Maximum hydrostatic pressure (GPa)	Ref.
Long-chain perfluorinated amines	FC-70	0.5-2.0	5, 19, 21
	1:1 FC84/FC-87	2.3	22, 23
Long chain alkylsilanes	Daphne 7474	3.7	23, 24
Iso-pentane/n-pentane mixtures	1:1 iso-/n-pentane	7.4	23
Methanol/ethanol mixtures	4:1 methanol/ethanol	9.8-10.5	23

Due to the small size and relatively low weight of the DAC, it can be easily attached directly onto the goniometer head of the diffractometer, or in a custom-made holder such as that used on the DLS I19 beamline (Figure 2.1C), and placed onto the diffractometer in a similar manner as the mounts used for ambient pressure single crystal diffraction experiments (Figure 2.1D). However, the nature of the data collection strategy used for high-pressure samples is highly specialised, as specific data collection strategies which minimises the shielding of the detector by the body of the DAC must be employed;[25] those used for all the high-pressure diffraction experiments in this thesis is shown in Table 2.3.

Table 2.3: Data collection strategy run list used for all high-pressure diffraction experiments undertaken at the DLS I19 beamline for the work in this thesis. Images were collected with a ω step size of 0.2°, optimised for radiation wavelength λ=0.49598 Å.

Run	2θ (°)	κ (°)	ϕ (°)	ω range (°)
1	-20.0	70.0	-24.232	-150.0 to -90.0
2	-20.0	70.0	155.768	-150.0 to -94.0
3	20.0	70.0	155.770	-105.0 to -74.0
4	20.0	70.0	-24.230	-105.0 to -74.0
5	20.0	-70.0	24.230	-96.0 to -30.0
6	-20.0	-70.0	-155.770	-106.0 to -66.0
7	-20.0	-70.0	24.230	-106.0 to -66.0
8	20.0	-70.0	-155.770	-96.0 to -30.0

As well as the specialised data collection strategy, the data processing method for high-pressure diffraction data is non-standard. Complications arise from the inclusion of reflections from diffraction of the diamond anvils, which are large and very intense, and thus can overlap with sample reflections. Moreover, reflections originating from diffraction of the tungsten gasket result in powder rings in the diffraction pattern. Therefore, the data processing method is far more intensive than that for ambient pressure data, even if the sample is well-diffracting, since care must be taken to remove all non-sample reflections as well as discounting areas of the detector shaded by the DAC. During the data processing procedure an additional setting within the CrysAlisPro software,[26] used for all high-pressure data processing in this thesis, was applied to only consider reflections within the DAC opening half-angle of 38°, in order to avoid reflections caught on the edge of the DAC opening angle. Despite the number of reflections collected being reduced by at least 60 % compared to ambient pressure collections due to shading by the body of the DAC, 100 % completeness can still be obtained; incomplete data is normally attributed to systems with low symmetry Laue groups or poorly diffracting crystals.

2.2.4 Bulk modulus

One of the mechanical properties that can be extracted from variable-pressure diffraction experiments is that of the bulk modulus (B), which quantifies the resistance of a material to hydrostatic compression; a material with a lower bulk modulus is less resistant to the application of pressure than a material with a higher bulk modulus. The more formal description of the bulk modulus is the change in volume of the substance against the change in pressure at constant temperature and is defined as:

$$B = -V\left(\frac{dP}{dV}\right)_T \qquad \textit{Equation 2.1}$$

where B is the bulk modulus, V is volume, P is pressure, and T is temperature. The bulk modulus is obtained by fitting an ideal equation-of-state (EoS) to the volume-pressure data curve and allows for a simplistic comparison of the volumetric-pressure response of various materials, as demonstrated in Chapter 3.

The specific EoS used in this thesis is the 3rd-order Birch-Murnaghan EoS (Equation 2.2),[27] due to its common use in the literature,[28-32] despite some known limitations.[33]

$$p = \frac{3B_0}{2}\left[\left(\frac{V_0}{V}\right)^{\frac{7}{3}} - \left(\frac{V_0}{V}\right)^{\frac{5}{3}}\right]\left\{1 + \frac{3}{4}(B_0' - 4)\left[\left(\frac{V_0}{V}\right)^{\frac{2}{3}} - 1\right]\right\} \qquad \textit{Equation 2.2}$$

Where p is pressure, B_0 is the bulk modulus, B_0' is the derivative bulk modulus with respect to pressure, V_0 is the unit cell volume at $p = 0$, and V is the volume of the compressed unit cell. This EoS is derived from a Taylor expansion series in which the inclusion of higher order derivative terms allows for finer and more complex details to be taken into account.[27]

2.3 Computational Methods

While X-ray diffraction acts as a highly valuable method for direct solution of the material structural response under various conditions, it cannot provide a quantitative description of the material property response nor of the energetics of the system. Computational methods have thus been used extensively in this thesis to complement the results obtained from X-ray diffraction experiments, utilising the experimentally-obtained crystal structures as starting models. A wide range of computational methods are available, however none of which can be applied to all system types nor can be used to calculate every material property of interest. Therefore, the choice of computational method must be carefully considered depending on the system type and objective at hand.

The computational methods which have been used in this thesis are as follows, with the underlying theory for each outlined in the-sections 2.3.1-2.3.3:

- First-principle (quantum-mechanical) methods, which involve the explicit description of the electrons, with the energy of the system being obtained as a solution of the Schrödinger equation.
- Semi-empirical methods, which incorporate first-principle methods but with additional approximations, with the resulting gaps filled by parameterisation.
- Classical (molecular mechanical) methods, which ignore electrons completely (with atoms being treated as classical objects) and thus utilise highly-parameterised force fields to describe how the system energy is affected by changes in conformation.

2.3.1 Quantum mechanical methods

The background information and theory regarding quantum mechanical methods presented in this chapter stems from the textbooks of Rankin, Mitzel and Morrison,[2] Young,[34] Solomon, Scott and King,[35] Jensen,[36] Parr and Yang,[37] Scholl,[38] and Fujita and Ito.[39]

Quantum mechanical, or first-principle, methods aim to solve the Schrödinger Equation, which describes the energy of the system (E) according to the system wavefunction (Ψ), as follows:

$$\hat{H}\Psi = E\Psi \qquad \textit{Equation 2.3}$$

where $\hat{H}$ is the Hamiltonian, the energy operator which acts upon the wavefunction to extract the potential and kinetic energy terms. First-principle methods involve the electrons being explicitly defined, and the system is determined *ab initio*; the input file only contains information on the atom types and starting positions, and the calculation determines the chemical bonding and electron distribution throughout the system. The energy of the system contains contributions of the kinetic energies of the nuclei and electrons and the potential energies arising from electron-electron, nuclei-electron and nuclei-nuclei interactions. However, the complicated nature of this equation means that exact solutions can only be solved for 1-electron systems, which is extremely restrictive. Therefore, only approximate solutions for N-electron systems can be obtained, with the type and complexity of the approximations applied indicating the specific method or level of theory.

The first approximation applied to systems in first-principle methods is the Born-Oppenheimer Approximation, which states that the electrons in the system move considerably faster than the heavy atomic nuclei.[40] The kinetic energy of the nuclei is thus approximated to be zero and the repulsion between pairs of atomic

nuclei can be determined as a constant. As a result of this approximation, the system is simplified down to an electron-only problem. The electron-electron repulsion contribution to the potential energy of the system is the most problematic to overcome, and its strong contribution means it cannot be outright ignored.

Hartree-Fock (HF) theory aims to overcome the problems with the electron-electron term by firstly ignoring electron correlation, the behaviour of each electron being dependent on the behaviour of all other electrons, by assuming that each electron is experiencing a uniform electric field (Hartree theory).[41, 42] Secondly, an exact solution for electron exchange, the lowering of energy caused by the pairing of two electrons of opposite spins, is provided by the use of asymmetric wavefunction (Fock theory),[43, 44] so that the wavefunction will collapse to zero if two electrons of the same spin try to occupy the same orbital. Higher levels of theory, such as Møller-Plesset perturbation series,[45] build upon HF theory by approximating the correlation energy.

Density functional theory (DFT) provides an alternative methodology for determining the electron-electron term. It is built upon the principle that the energy of the system can be obtained from a three-dimensional variable (x, y, z) functional, referred to as the exchange/correlation functional, of the electron density (ρ).[46, 47] However, the exact functional that provides the correct ground-state energy is not known, and thus a variety of functionals devised from a range of approximations have been reported. All currently-reported functionals provide an approximate solution to both electron exchange and correlation, and are built by a combination of the construction of one-electron holes.[48]

Combining HF and DFT methods results in hybrid DFT functionals, which benefit from being able to provide an exact electron-exchange solution and approximate electron-correlation solution at a relatively low cost. The wide array of hybrid DFT functionals that are available differ in terms of, firstly, the DFT functional they are based upon and, secondly, the weighting between the HF and DFT electron exchange

terms. Surveying the range of hybrid functionals available for use is particularly important when semi-conducting materials are under investigation, which is the case in Chapters 3 and 4 of this thesis, with the construction of the functional greatly influencing the calculated value of the electronic band gap. The next two sub-sections discuss the types and construction of DFT and hybrid DFT functionals, with sub-sections 2.3.1.3-2.3.1.5 focussing on the types of basis set constructions and the inclusion of pseudopotentials.

2.3.1.1 Introduction to functionals

The most commonly-used pure-DFT functionals can be classified by either incorporating the local density approximation (LDA) or the generalised gradient approximation (GGA).[35, 49] LDA utilises an uniform electron gas, such that ρ is constant throughout all space, with the functional describing the change in the exchange-correlation energy with respect to changes in ρ. This information is then extrapolated onto the electron density in discrete regions of the real system. These functionals work well for metallic systems, given the near constant delocalised nature of the electrons in these systems, however they work poorly for molecular systems in which chemical bonding is strongly characterised by greatly varying ρ. Thus, GGA is more-commonly-used for those systems, given the functional contains information on ρ and its gradient. Commonly-used GGA-based functionals include BLYP[50,51] and PBE,[52] both being prominent functionals in the CASTEP code.[53] The addition of contributions from HF theory to the BLYP and PBE GGA-functionals produced the hybrid functionals B3LYP[54] and PBE0 and HSE06 respectively.[55-57]. The construction of each of these three hybrid functionals is shown in section 2.3.1.2. HSE06, in particular, has shown to be highly successful in replicating experimental electronic band gaps,[58-60] even for materials containing heavy elements for which replication of experimental band gaps is usually adversely affected by the presence of spin-orbit coupling,[61] and thus its use features heavily in Chapters 3 and 4.

2.3.1.2 Construction of specific hybrid functionals

PBE0 and HSE06 (or simply HSE) are two related hybrid functionals since they both incorporate the PBE exchange and correlation terms, but differ in terms of how the additional HF exchange correlation term is incorporated.[57,58] The construction of the PBE0 and HSE functionals into component exchange (E_X) and correlation (E_C) energy terms derived from HF and PBE is as follows:

$$E_{XC}^{PBE0} = E_C^{PBE} + aE_X^{HF} + (1-a)E_X^{PBE} \qquad \textit{Equation 2.4}$$

$$E_{XC}^{HSE} = E_C^{PBE} + aE_X^{HF,SR}(w) + (1-a)E_X^{PBE,SR}(w) + E_X^{PBE,LR}(w) \qquad \textit{Equation 2.5}$$

where SR and LR refer to the short range and long range respectively, w is the variable that determines the cut-off between short-range and long-range interactions, and a is the weighting factor for the exchange-energy term between HF and GGA. For both PBE0 and HSE06 functionals, a = 0.25. However, it is apparent that setting a to equal zero would result in both functionals behaving like the PBE functional, with no HF exact exchange involved.

The PBE0 functional, while successful at replicating the band gap values of highly insulating materials, was found to overestimate the band gap for low and moderate band gap semiconductors due to HF exact exchange term being applied across all range of interactions, when it is only necessary for short ranges.[62,63] The development of the HSE functional aimed to tackle this systematic failure of PBE0 by applying the 1:3 split between the HF exact-exchange and PBE approximate-exchange terms only for short-range interactions, whereas long-range interactions are represented solely by the PBE approximate exchange, as shown in Equation 2.5.[57] The definition of short-range and long-range is defined by the variable factor w. If $w \to 0$, the short-range term is applied infinitely and the HSE functional collapses to the PBE0 functional, whereas if $w \to \infty$ the short-range terms trend to zero and therefore the functional generates a result similar to that given by the PBE functional. Although the

HSE functional underestimates the band gap for highly-insulating materials, it performs well for small and moderate band gap semiconductors (below 6 eV).[60,62,63]

A very widely-used hybrid functional, which also features in this thesis in Chapters 3-5, is B3LYP.[49] It is so-called because of it consisting of three different components to describe the electron exchange and electron correlation,[54] specifically the BLYP functional, an LDA-based functional and exact HF exchange as follows:

$$E_{XC}^{B3LYP} = 0.08E_x^{LDA} + 0.72E_x^{BLYP} + 0.20E_x^{HF} + 0.81E_C^{BLYP} + 0.19E_C^{LDA} \qquad \textit{Equation 2.6}$$

based upon a similar construction devised for the B3PW91 functional.[64] The LDA contribution to the B3LYP functional is low, attributing only 8% of the exchange component and 19 % of the correlation component. Therefore, similar to the HSE and PBE0 functionals, the majority of the B3LYP functional stems from contributions by the GGA and HF components. B3LYP has been shown in the literature and in this thesis (in Chapter 3, specifically) to demonstrate a similar performance of calculating band gaps of semi-conductors to the HSE functional due to its construction.[62] However, since it is a global hybrid like PBE0 in that the HF component is applied across all ranges of interactions, calculations utilising the B3LYP functional suffer from higher compute times compared to the screened HSE functional. Therefore, in general, due to the good performance and lower compute times associated with the HSE functional, it is the main functional of choice for a majority of the discussion of results in Chapters 3 and 4.

2.3.1.3 Localised basis sets

Alongside the various options of levels of theory which can be employed, an additional consideration is the type and quantity of basis sets to be used in the calculation. The system wavefunction, and thus electron density of the system, is described by basis sets, which are in turn simply combinations of basis functions. A

greater number of basis functions per basis set and greater number of basis sets overall should lead to a more accurate description of the system wavefunction, but also leads to a more resource-intensive calculation.

One type of basis set approach is to think of electrons as being assigned to localised atomic orbitals on specific atoms in the system of interest, fitting in with the traditional chemist's view of how electrons behave inside molecules, with these atomic orbitals then able to combine to form molecular orbitals to form the system wavefunction. The basis functions which contribute to the formation of the basis set describe the size and shape of the various atomic orbital required to describe the system. This approach is intuitively known as using localised basis sets, and can be readily applied for use on isolated molecules (as is the case for the GAUSSIAN package).[65] It can also be applied for use on crystalline systems (as in the CRYSTAL package, used in Chapters 3 and 4),[66] as long as the symmetry of the system, which describes the relationship between neighbouring molecules, is provided to allow the basis sets to be replicated throughout the crystal structure.

The system wavefunction (ψ) is determined by the sum of all the basis sets describing the system of interest, which in turn consist of the combination of basis functions (ϕ_i) with their contributions weighted according to coefficients (c_i), as follow:

$$\psi = \sum_i c_i \, \phi_i \qquad \textit{Equation 2.7}$$

Optimisation of the system wavefunction for a certain system geometry is obtained by adjusting the weighting coefficient values until the system energy minimum is found. Extra functions can be added to basis sets to take into account strongly diffuse or polarised atomic orbitals, in necessary for the specific system under investigation.

2.3.1.4 Delocalised basis sets

An alternative approach to basis set construction is to consider the electrons as being delocalised through the whole system with their behaviour being dictated by the construction of the ionic lattice, rather than being associated or localised to a specific atomic orbital. This type of basis set is thus known as a delocalised basis set, and can be applied to solid-state systems in which the construction of the ionic lattice is continuous in all directions. With this approach, the electrons are thought of as waves propagating through the solid-state system, and thus the basis sets used to describe the system wavefunction are combinations of weighted sinusoidal waves with varying wavelengths, to illustrate the various energies of the electrons in the system, in proportion with the dimensions of the unit cell. The wavefunction $\psi(r)$ is thus defined as follows:

$$\psi(r) = \sum_G C_G exp(iG, r) \qquad \textit{Equation 2.8}$$

where $\psi(r)$ is the wavefunction at position r, C_G is the weighting coefficient and $exp(iG, r)$ is the representation of a plane wave with respect to the reciprocal lattice vectors G. In a similar manner to the localised basis sets, the wavefunction of the system is found by optimising the values of the weighting coefficients (C_G). The CASTEP package, used for the investigations in Chapters 3 and 6, makes use of these delocalised plane wave basis sets.[53] The quality of the basis set is controlled by indicating an energy cut-off, marking the maximum energy value of plane waves which can be utilised; in a similar manner to adding more basis functions to localised basis sets, defining a higher energy cut-off should lead to a more accurate description of the system but increases the computing time required.

Earlier in this section, the term *unit cell* was introduced to mark the wavelengths of plane waves required to describe the system of interest. The unit cell is crystallographic terminology for a certain portion of the solid-state system which

contains all the symmetry operations required to describe the relative spatial arrangement of the molecules in the system. The unit cell, as an individual building block, can then be replicated by translation in all three directions to form a 3-D infinite array. Rather than having to model all the molecules in these infinite system, many of which are replicas of each other, calculations undertaken on these solid-state systems only need to focus on the contents of the unit cell by applying periodic boundary conditions. These boundary conditions are soft, therefore allowing electron density or ions (when the BO Approximation is lifted) to leave through one face of the unit cell and re-emerge through the opposite face.

The concept and use of periodic boundary conditions stems from Bloch's theorem, which describes the wavefunction $\psi(\boldsymbol{r})$ in a lattice-periodic potential, such that

$$V(\boldsymbol{r} + \boldsymbol{R}) = V(\boldsymbol{r}) \qquad \textit{Equation 2.9}$$

where V is the potential along a certain vector in the three directions (x, y, z) of the crystal lattice and $\boldsymbol{R}$ is the Bravais lattice vector such that

$$\boldsymbol{R} = n_1\boldsymbol{a_1} + n_2\boldsymbol{a_2} + n_3\boldsymbol{a_3} \qquad \textit{Equation 2.10}$$

where n_j are integers and $\boldsymbol{a_j}$ are primitive vectors of the crystal lattice. This wavefunction takes the form of a plane wave, modulated by a periodic function $u(\boldsymbol{r})$ as follows:

$$\psi(\boldsymbol{r}) = u(\boldsymbol{r}) \exp(i\boldsymbol{k}\boldsymbol{r}) \qquad \textit{Equation 2.11}$$

where $\psi(r)$ is the wavefunction at vector $\boldsymbol{r}$, $exp(i\boldsymbol{k}\boldsymbol{r})$ is the representation of a plane wave, k is the wave vector and $u(\boldsymbol{r})$ is the periodic function such that

$$u(\boldsymbol{r} + \boldsymbol{R}) = u(\boldsymbol{r}) \qquad \textit{Equation 2.12}$$

Therefore, the definition for the wavefunction in Equation 2.11 takes a similar to that shown in Equation 2.8. Furthermore, since the wavefunction associated with **r**, $\psi(\boldsymbol{r})$, is periodic and equal to the wavefunction associated with $(\boldsymbol{r}+\boldsymbol{R})$, $\psi(\boldsymbol{r}+\boldsymbol{R})$, the probability distribution function $P(\boldsymbol{r}) = |(\psi(\boldsymbol{r})|^2$ is also lattice periodic.

2.3.1.5 Pseudopotentials

The description of basis sets described in Sections 2.3.1.3 and 2.3.1.4 lead to the consequence that the same amount of effort and consideration is given to the description of both core and valence electrons. This however comes at a high computational cost which is not ideal, especially since the core electrons do not contribute to molecular properties and chemical bonding. Furthermore, especially for delocalised plane-wave basis sets, the interaction between valence and core electrons and the relativistic effects acting on the core electrons in heavy elements result in an even greater number of plane waves being required, further adding to the computational cost. In order to decrease computational demand, the functions for the core electrons can be replaced by a pseudopotential, also referred to as an effective core potential, thus only the valence electrons are described explicitly. In the CRYSTAL code pseudopotentials for heavy atoms are incorporated into their pre-determined localised basis set descriptions whereas the CASTEP code utilises 'on-the-fly' pseudopotentials.

2.3.2 The PIXEL method

The semi-classical density sums (SCDS) method, more commonly known as the PIXEL method, is a computational technique capable of calculating full crystal lattice energies and intermolecular energies of individual intermolecular dimers in the crystal lattice, alongside a breakdown of the energies into Coulombic, polarisation, dispersion and repulsion terms.[67] Therefore, a hierarchy of the most directing interactions in the crystal structure can be obtained and interactions of similar

energies can be distinguished by the contribution of each of component energy terms, both of which can be linked to aspects of the crystal structure such as the relative orientations of the molecules and close atom···atom contacts. While DFT and other first-principle methods can be utilised to determine interaction and lattice energies,[68] the high computational demands result in the methods being constrained to use on small systems; the PIXEL method is a semi-empirical method and thus does not suffer from these constraints, with the calculations regularly undertaken on a desktop computer.

The various steps of the PIXEL method are outlined in Figure 2.2. It can be applied to the geometry of experimental structure solutions or optimised structures; in the case of the former, the X-H bond distances require extension to the standard bond lengths acquired from neutron diffraction experiments. Firstly, a non-optimising quantum mechanical calculation, normally of MP2/6-31G**, is undertaken which calculates the electron density around the molecule(s) of the asymmetric unit (**1**), hereafter referred to as the central molecule(s). This electron density cloud is then split into small cubes (pixels), with dimensions of < 0.1 Å (**2**) and each pixel is assigned to the closest proximity atom within the molecule. Any pixels with a charge of less than 10^{-6} electrons are removed and the remaining electron density is renormalised so that the neutral charge across the molecule is maintained. To speed up later sets of calculations, pixels are condensed into superpixels, each consisting of $n \times n \times n$ pixels (**3**), with a condensation level (n) of 3 or 4. The next stage is to undertake a lattice calculation, which uses the symmetry operations associated with the assigned space group of the crystal lattice to create a sphere of molecules around the central molecule with a radius ≥ 15 Å. The interaction energies between the central molecule and all other molecules in the spherical cluster are then calculated in turn, by determining the different energy contributions to the overall interaction energy (**4**). The methods for calculating these component energy terms are shown in Equations 2.6 to 2.18, as described in the published description of the PIXEL method by Gavezzotti.[67, 69-71]

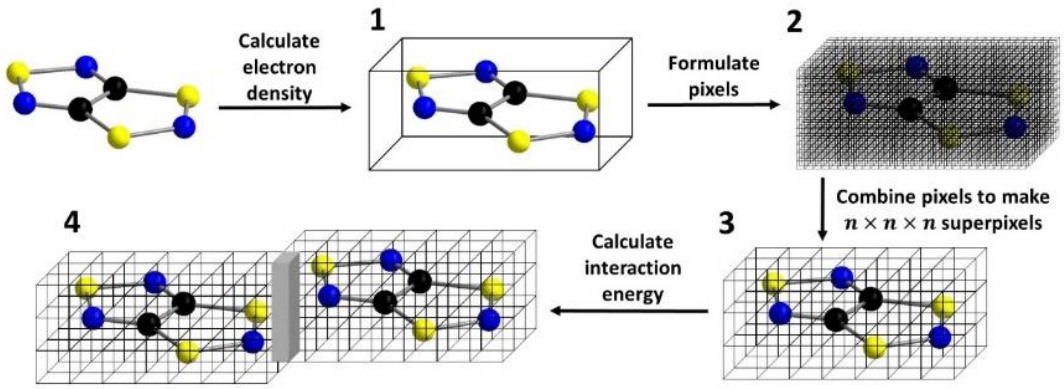

Figure 2.2: Basic schematic outlining the various stages of the PIXEL method calculations. The molecule shown is TTTA, which is discussed in Chapter 5. The grey area in 4 indicates electron density overlap between neighbouring molecules.

On the central molecule, ρ_k defines the electron density in the pixel of volume V_k centred around the point $k = [x_k, y_k, z_k]$, and each pixel thus has the charge $q_k = \rho_k V_k$, while each atom nucleus at point j has the charge Z_j. The second molecule, for which the interaction energy with the central molecule is being calculated, thus has equivalent ρ_i, q_i and Z_m values. The Coulombic energy (E_{COUL}) between the two molecules is the summation of all pixel-pixel, pixel-nucleus and nucleus-nucleus electrostatic interactions at distance R, determined by summing the electrostatic potentials generated by the central molecule on all pixels (ϕ_i) and on all nuclei (ϕ_m) of the second molecule using Coulomb law-type equations as follows:

$$E_{COUL} = \sum_i q_i \varphi_i + \sum_m q_m \varphi_m \qquad \textit{Equation 2.13}$$

$$\phi_m = \frac{1}{4\pi\varepsilon_0}\left[\sum_k {q_k}/{R_{ik}} + \sum_j {Z_j}/{R_{ij}}\right] \qquad \textit{Equation 2.14}$$

$$\phi_m = \frac{1}{4\pi\varepsilon_0}\left[\sum_k {q_k}/{R_{km}} + \sum_m {Z_j}/{R_{km}}\right] \qquad \textit{Equation 2.15}$$

The polarisation energy term refers to the strength of electric field applied to the electron cloud of the central molecule by neighbouring molecules. The total polarisation energy ($E_{POL,TOT}$) is calculated by the summation of the polarisation

energy at each pixel ($E_{POL,i}$), which in turn are calculated by the electric field exerted by surrounding molecules at point i (ε_i) and the polarisability at point i (α_i).

$$E_{POL,TOT} = \sum_i E_{POL,i} = \sum_i -\frac{\alpha_i[\varepsilon_i d_i]^2}{2} \qquad \textit{Equation 2.16}$$

$$\alpha_i = q_i \alpha_{atom} / Z_{atom} \qquad \textit{Equation 2.17}$$

where $\alpha_{atom}$and Z_{atom} are the polarisability and charge of the assigned atom for pixel i. The polarisation energy term includes a dampening factor d_i which sets $E_{POL,i}$ to zero if the electric field exceeds the ε_{max} value (set by default to 150×10^{10} V m^{-1}) when very short intermolecular separations arise, and is defined as follows:

$$d_i = exp\left[-\left(\varepsilon_i/(\varepsilon_{max} - \varepsilon_i)\right)\right] \qquad \textit{Equation 2.18}$$

where ε_{max} is the adjustable maximum electric field value.

The dispersion energy (E_{DISP}), between two molecules A and B, is calculated by the summation of intermolecular pixel-pixel terms in a London-type expression:

$$E_{DISP,AB} = \frac{-3}{4}\sum_{i,A}\sum_{j,B} E_{OS} f(R) \alpha_i \alpha_j / \left[(4\pi\varepsilon^0)^2 \left(R_{ij}\right)^6\right] \qquad \textit{Equation 2.19}$$

This calculation includes a dampening function $f(R)$, which kicks in only when $R_{ij} < D$, where D is set by default to 3.5 Å.

$$f(R) = exp\left[-\left(D/R_{ij} - 1\right)^2\right] \qquad \textit{Equation 2.20}$$

E_{OS} in Equation 2.19 refers to the 'oscillator strength', which considers that each individual pixel is a separate oscillator with its own ionisation potential (I_i), which in turn is related to the ionisation potential of the atom the pixel belongs to (I^0) and the

distance between the pixel and its assigned atom (R_i). β is an empirical, atom-dependent parameter.

$$E_{OS} = \left(I_i I_j\right)^{1/2} \quad \textit{Equation 2.21}$$

$$I_i = I^0 \exp(-\beta R_i) \quad \textit{Equation 2.22}$$

The repulsion energy is proportional to the extent of overlap between non-condensed intermolecular pixel pairs, summed to give a total overlap integral (S_{AB}) between the two molecules A and B, as follows:

$$S_{AB} = \sum_{i,A} \sum_{j,B} [\rho_i(A)\rho_i(B)]V \quad \textit{Equation 2.23}$$

This overlap integral is sub-divided into the contribution from each atom pair, thus giving S_{mn}. The repulsion energy for each atom pair ($E_{REP,mn}$) is calculated by scaling this atom-pair pixel overlap integral by two adjustable positive parameters (K_1 and K_2) and the Pauling electronegativity difference between the two atoms ($\Delta\chi_{mn}$) to account for the distortions in the electron clouds caused by different atom types.

$$E_{REP,mn} = (K_1 - K_2\Delta\chi_{mn})S_{mn} \quad \textit{Equation 2.24}$$

Summing over all atom pairs results in the total repulsion energy (E_{REP}):

$$E_{REP} = \sum_{m,n} E_{REP,mn} \quad \textit{Equation 2.25}$$

The total interaction energy (E_{TOTAL}) between a molecular pair is the summation of the four component energy terms, and the total lattice energy is then determined by the summation over all interaction energies for the central molecule with every molecule in the cluster:

$$E_{TOTAL} = E_{COUL} + E_{POL} + E_{DISP} + E_{REP} \quad \textit{Equation 2.26}$$

As previously stated, the display of both the component and total energies in the output files greatly aids the distinction between the wide array of intermolecular interactions identified within the crystal structure, especially between interactions which have very different intermolecular arrangements but coincidentally have the same total energy. Furthermore, since the PIXEL method considers interactions as between whole molecules,[72] it should not be biased towards always identifying the most influential interactions in the crystal structure as those with short atom···atom contacts, which could be the case if it was hypothesised by viewing the crystal structure by eye. Any short atom···atom contacts of importance can be identified by the researcher once the interaction energy hierarchy has been obtained.

While the PIXEL method benefits from being a semi-empirical method with its relatively fast calculation speed, this also brings a downside with its reliance on the five adjustable parameters for calculating the various energy terms as shown in Equations 2.13-2.26. Deficiencies in the theory applied to calculate the individual energy terms and the values used for each of the parameters are thus important points of consideration; changes in the parameters were reported in early publications utilising the PIXEL method.[71, 73] It has also stated that the PIXEL method might have intrinsic difficulties in its description of hydrogen bonding interactions, which are known to be more energetic and thus more structure-directing than other classes of interaction, due to an underestimation of the covalent component of the interaction which would lead to a calculated interaction energy weaker than expected.[67] Furthermore, the partitioned lattice energies have been found in some cases to be sensitive to relatively small structure variations.[74] That being said, the PIXEL method has since been successful applied in characterising the interaction energy hierarchy for crystal lattices for a variety of systems,[69, 75-78] including those with prominent hydrogen-bonding interactions,[79-81] with the calculated interaction energies being in good agreement with those calculated using perturbation theory methods.

2.3.3 Classical simulations

Chapter 6 concerns the adsorption of gas molecules in a porous framework material, with the aim of evaluating the extent of gas loading at various pressures and the strength of guest-framework interaction energies. As highlighted in the introduction of Chapter 6, first-principles methods are not appropriate to handle these type of many-body systems, since they cannot replicate the partial occupancy observed experimentally in the bulk framework material and are limited in replicating only one 'snapshot' of the gas molecule locations. Classical simulation methods, specifically the grand canonical Monte Carlo (GCMC) method, on the other hand, have been very successful in evaluating these types of systems.[82-86] An overview of the underlying theory of statistical mechanics, ensembles, the Monte Carlo method and fugacity is described across the next four sub-sections; the underlying theory presented therein stems from the textbooks of Hill,[87] Frenkel and Smit,[88]Anderson,[89] and DeVoe.[90]

2.3.3.1 Statistical mechanics

Statistical mechanics is the utilisation of mathematical relationships to connect the information recorded on the molecular level to the macroscopic properties of interest, and thus facilitates the study of many-body systems. When considering the adsorption of gas molecules inside a porous adsorbent material, the microscopic properties are the instantaneous location and momentum of each adsorbed molecule, with each such configuration of molecules classed as a microstate. The same system at equilibrium on the macroscopic level can also be described by thermodynamic properties such as pressure, volume and temperature.

One of the main underlying principles of statistical mechanics is that at equilibrium the system will go through all possible microstates given infinite time. An ensemble, a large collection of possible microstates, portrays the same average properties in phase space as it does over time; this is the ergodic hypothesis. Furthermore, the first

postulate of statistical mechanics is that, for an ergodic system, the macroscopic property of the system (M) can be determined by sampling a sufficient number of the instantaneous microstates with the macroscopic property of interest having no dependency on the starting configuration of the system, as follows:

$$M_{observed} = \langle M \rangle_{ensemble} = \sum_k M_k P_k \qquad \textit{Equation 2.27}$$

where $M_{observed}$ is the average macroscopic property over time, equivalent to the ensemble average, $\langle M \rangle_{ensemble}$, which is equal to the sum over all microstates k multiplied by the probability of observing each microstate P_k.

Microstates that belong to the same ensemble must share three constant properties; common examples include the canonical (N, V, E), micro canonical (N, V, T), isobaric isothermal (N, P, T) and grand canonical (μ, V, T) ensembles. Given that the number of molecules in the system, *N*, is allowed to fluctuate with the grand canonical ensemble, it is ideally suited for the study of adsorption and behaviour of gas molecules in porous materials. The ensemble facilitates movement of the gas molecules between the adsorbent phase and an external gas phase reservoir in order to reach equilibrium, for each desired pressure level, at which the chemical potential, μ, between the two phases is at equilibrium. This replicates the experimental conditions in which a single crystal of the adsorbent material is surrounded by the bulk gas in a capillary gas cell. By probing the amount of gas adsorbed at various pressures, simulated adsorption isotherms can be obtained.

The probability (P_k) of obtaining a specific microstate k in the grand canonical ensemble containing N molecules with a total system energy of E_k is described as follows:

$$P_k = \frac{[exp(-\beta E_k)][exp(\beta \mu N)]}{Q(\mu, V, T)} \qquad \textit{Equation 2.28}$$

The denominator of Equation 2.28 is the grand-canonical partition function, Q, which is the sum of the probabilities of all possible microstates, described as follows:

$$Q(\mu, V, T) = \sum_{k} \sum_{N} [exp(\beta\mu N)][exp(-\beta E_k)] \qquad \textit{Equation 2.29}$$

where $\beta = {}^{1}/_{k_B T}$, where k_B is Boltzmann constant and T is temperature. Equation 2.27 can thus be adapted to specifically be used for the grand canonical ensemble, as shown:

$$\langle M \rangle_{\mu VT} = \frac{1}{Q(\mu, V, T)} \sum_{k} \sum_{N} M_k \, [exp(\beta\mu N)][exp(-\beta E_k)] \qquad \textit{Equation 2.30}$$

Equation 2.30 is very difficult to calculate using quantum mechanical methods, due to the large size of the ensemble required. Therefore, it is necessary to switch to a classical expression, in which the individual microstates are described by the individual molecule positions ($\boldsymbol{s}$) and momenta ($\boldsymbol{q}$), referred to collectively as phase space; the integration of all configurations (M) in phase space and their respective probabilities (p) yields the macroscopic property of the ensemble, as follows:

$$M = \int M(\boldsymbol{q}, \boldsymbol{s}) \, p(\boldsymbol{q}, \boldsymbol{s}) d\boldsymbol{q} \, d\boldsymbol{s} \qquad \textit{Equation 2.31}$$

The energy of the system, denoted by E_k in Equation 2.30, can be simplified by splitting into its two component parts. The potential energy, denoted hereafter as $U(\boldsymbol{s}^N)$, is determined by the intermolecular interactions and thus is dependent on the positions of the guest molecules. The kinetic energy is only dependent on the momenta of the molecules, and can be determined by the expression for the kinetic energy of a monoatomic particle:

$$E_k = {}^{V}/_{\Lambda^3} \qquad \textit{Equation 2.32}$$

where Λ is the thermal de Broglie wavelength, such that

$$\Lambda = h\sqrt{\beta/2\pi m} \qquad \textit{Equation 2.33}$$

where h is Planck's constant and m is the mass of the particle.

Equations 2.28 and 2.30 can be re-written to take into account the classical description of the system, to describe the probability of obtaining a specific microstate of N molecules at positions $\boldsymbol{s}$ and how the macroscopic property of the ensemble can be determined by integrating across the entirety of the phase space.

$$P(\boldsymbol{s}^N) = \frac{1}{Q(\mu,V,T)}\frac{V^N}{\Lambda^{3N}N!}[exp(-\beta U(\boldsymbol{s}^N))][exp(\beta\mu N)] \qquad \textit{Equation 2.34}$$

$$\langle M\rangle_{\mu VT} = \frac{1}{Q(\mu,V,T)}\sum_N \frac{V^N}{\Lambda^{3N}N!}\int M(\boldsymbol{s}^N)[exp(\beta\mu N)][exp(-\beta U(\boldsymbol{s}^N))]\ d\boldsymbol{s}^N \qquad \textit{Equation 2.35}$$

2.3.3.2 Grand canonical Monte Carlo simulation method

The grand canonical Monte Carlo (GCMC) simulation method involves integrating Equation 2.35 over a series of randomly generated points in phase space, from which the macroscopic property $\langle M\rangle$ can be determined. In the case of the study of gas adsorption into porous materials, the property of interest is the number of adsorbed gas molecules in the porous channels of the material; the reported guest loadings are the average number of gas molecules observed throughout the production run once the system has equilibrated.

In order to achieve the configurations of gas molecules inside the porous channels a variety of move types are randomly undertaken, as follows:

- Insertion: a molecule is inserted from the external reservoir into the simulation cell containing the lattice of the porous material.

- Deletion: a random molecule is removed from the simulation cell and returned to the external reservoir.
- Displacement: A random molecule inside the simulation cell is moved, by a random displacement, to another position inside the simulation cell. In the case of molecules consisting of more than one atom, this includes orientational and conformational moves as well as translational moves.

Through the combination of these moves, the molecules undertake a random walk through the porous channels to sample all the possible points of phase space. In its simplest form, each point contributes equal weighting to the overall integral. However, the probability of sampling each point ($\boldsymbol{r}^n$) is proportional to the Boltzmann factor $\left(exp\left[-\frac{U(\boldsymbol{r}^n)}{k_BT}\right]\right)$ of that point. The algorithm of moves ultimately generates a Markov chain of configurations, in that the transformation to any new configuration (n) is only dependent on the current configuration (o) and not on the previous configurations, and thus the sequence is memory-less.

While the trialling of moves to generate the new configuration from the current configuration is entirely random, thus conserving detailed balance, each move has an acceptance criterion which ultimately determines if the move is accepted or if the old configuration is maintained until the next trial move.[88] The acceptance criterion for the displacement move is defined by:

$$acc\ (o \rightarrow n) = \min(1, exp[-\beta(U(n) - U(o))] \qquad \textit{Equation 2.36}$$

where $\beta = {}^{1}/_{k_BT}$, where k_B is Boltzmann constant and T is temperature, and states that the move will always be accepted if the energy of the system decreases. If the energy of the new configuration is higher, instead of instantly rejecting the move, the difference in the potential energies of the two configurations are compared to a randomly generated number, with the possibility of the move still being accepted, to ensure that the system does not become trapped in local energy minima. Similar

acceptance criteria are defined as follows for insertion and deletion moves respectively for system containing N molecules:

$$acc\ (o \rightarrow n) = \min\left(1, \frac{V}{\Lambda^3(N+1)} exp[\beta\{\mu - U(n) + U(o)\}]\right) \qquad \textit{Equation 2.37}$$

$$acc\ (o \rightarrow n) = \min\left(1, \frac{\Lambda^3 N}{V} \exp[-\beta\{\mu + U(n) - U(o)\}]\right) \qquad \textit{Equation 2.38}$$

The chemical potential, μ, can be expressed as a function of fugacity (f):

$$\mu = \frac{\ln(\beta f \Lambda^3)}{\beta} \qquad \textit{Equation 2.39}$$

and therefore, by using an EoS (such as the Peng Robinson EoS used in this thesis[87]), the pressure inside the reservoir can be determined. An explanation of fugacity, and thus its relation with pressure, is presented in the next sub-section.

2.3.3.3 Fugacity

At the end of the previous sub-section, the term *fugacity* was introduced and was stated as being related to pressure by equation of states, but otherwise was not described further; this will be addressed in this sub-section. Prior to a description of fugacity, a description of pressure must be provided. The pressure of a gas (P) is related to the volume of the gas (V) by the ideal gas law, as follows:

$$P = \frac{RT}{V} \qquad \textit{Equation 2.40}$$

where R is the gas constant and T is the temperature of the system. As suggested by its name, this law is only applicable to an ideal gas, in other words a hypothetical gas which consists of particles which do not experience any intermolecular interactions. On the other hand, real gases do experience intermolecular interactions, which in turn will cause a measureable difference in the volume of the real gas to the volume of the

hypothetical ideal gas at the same pressure and temperature. At low pressures or high temperatures, real gases behave vey similarly to ideal gases, since the gas particles are sufficiently separated that intermolecular interactions are negligible; the effect of intermolecular interactions grows stronger with increasing pressure or decreasing temperature.

The differential in Gibbs energy (dG) of an ideal pure gas of a fixed amount, with temperature (T) and pressure (P) as independent variables, is as follows:

$$dG = -S\,dT + V\,dP \qquad \textit{Equation 2.41}$$

where S is the entropy of the system. Equation 2.41 can be divided by the number of moles of substance (n) to give the differential of the chemical potential of the ideal pure gas as a function of molar entropy (S_m) and molar volume (V_m):

$$d\mu = -S_m\,dT + V_m\,dP \qquad \textit{Equation 2.42}$$

$$\text{since } \mu = G_m = \frac{G}{n} \qquad \textit{Equation 2.43}$$

Partial derivatives can be formed for the molar entropy and molar volume coefficients on the right hand side of Equation 2.43, such that:

$$\left(\frac{d\mu}{dT}\right)_P = -S_m \qquad \textit{Equation 2.44}$$

$$\left(\frac{d\mu}{dP}\right)_T = V_m \qquad \textit{Equation 2.45}$$

Equation 2.45 can be re-written to show how $d\mu$ can be calculated for a pure ideal gas at two different pressure points (P_1 and P_2) at fixed temperature T, as follows:

$$d\mu = \int_{P_1}^{P_2} V_m\,dP \qquad \textit{Equation 2.46}$$

Equation 2.33 can be substituted into Equation 2.39, as follows:

$$d\mu = \int_{P_1}^{P_2} \frac{RT}{P}\, dP \qquad \textit{Equation 2.47}$$

$$d\mu = \mu_{P_2} - \mu_{P_1} = RT \ln \frac{P_2}{P_1} \qquad \textit{Equation 2.48}$$

To simplify Equation 2.48, pressure value P_1 can be set to standard pressure P° (1 bar, 10^5 kPa), which equates to the standard gas state at which the gas behaves like an ideal gas. The chemical potential μ_{P_1} can thus be set to μ°, the standard chemical potential, and μ_{P_2} and P_2 can be simplified to μ and P respectively, as follows:

$$d\mu = \mu - \mu^\circ = RT \ln \frac{P}{P^\circ} \qquad \textit{Equation 2.49}$$

$$\mu = \mu^\circ + RT \ln P \qquad \textit{Equation 2.50}$$

As discussed previously in this section, most gases do not behave like ideal gases, especially at higher pressures or lower temperatures at which the volume of decreases and the higher density of gas causes intermolecular interactions to be non-negligible in strength. Equations 2.47-2.49 can be modified slightly to define fugacity, f, the function of the equation for real gases:

$$d\mu = \int_{P_1}^{P_2} \frac{RT}{f}\, dP \qquad \textit{Equation 2.51}$$

$$d\mu = \mu_{P_2} - \mu_{P_1} = RT \ln \frac{f_{P_2}}{f_{P_1}} \qquad \textit{Equation 2.52}$$

Therefore, the difference in chemical potential of a real gas at pressures P_1 and P_2 is defined by a ratio of the fugacity values at each of these pressure points, $RT \ln \frac{f_{P_2}}{f_{P_1}}$. Fugacity and its relationship to pressure cannot be defined using this ratio, however. If P_1 is a sufficiently low pressure such that the real gas behaves similarly to an ideal gas, thus obeying the limit $\lim_{P \to 0} \left(\frac{f}{P}\right) = 1$, f_{P_1} can be simply defined as P°, and the

integral can then be used for any value of P at the same temperature as that for P° to calculate f.

$$d\mu = \mu - \mu^\circ = RT \ln \frac{f}{P^\circ} \qquad \textit{Equation 2.53}$$

Fugacity, f, therefore has the same units pressure and is described as *effective pressure*,[89] since it is the pressure required of a hypothetical ideal gas to possess the same chemical potential as the equivalent real gas at the same temperature, as defined by rearranging Equation 2.53:

$$f = P^\circ \exp\left[\frac{\mu - \mu^\circ}{RT}\right] \qquad \textit{Equation 2.54}$$

The ratio between f and P is defined by the fugacity coefficient, φ, which is unique to each fugacity value and never exceeds the value of 1, such that:

$$f_i = \varphi_{f_i} P \qquad \textit{Equation 2.55}$$

where φ_{f_i} is the fugacity coefficient at fugacity value f_i. Figure 2.3 shows the fugacity-pressure curves for CO_2 and CH_4 up to pressures of 100 bar, calculated using the Peng-Robinson EoS.[91] At low pressures (below 10 bar), fugacity and pressure are almost equivalent, whereas noticeable deviation between fugacity and pressure can be seen above 10 bar, with the individual curves for CO_2 and CH_4 deviating from the curve for $\varphi_{f_i} = 1$ at different extents due to the varying nature and strength of intermolecular interactions of the two gases.

The Multipurpose Simulation Code (MuSiC v3),[92] used for the GCMC simulations discussed in Chapter 6, utilises fugacity as an input value, rather than pressure, due to it aiming to replicate experimental conditions in which the gases will not be necessarily behaving similarly to ideal gases. Therefore, the discussion around the

results of these simulations uses the term *fugacity*, rather than *pressure*, and the calculation of the fractional fugacities of the simulated CO_2/CH_4 gas mixture (1:1 in terms of experimental pressure) was undertaken using the Peng-Robinson EoS.[91]

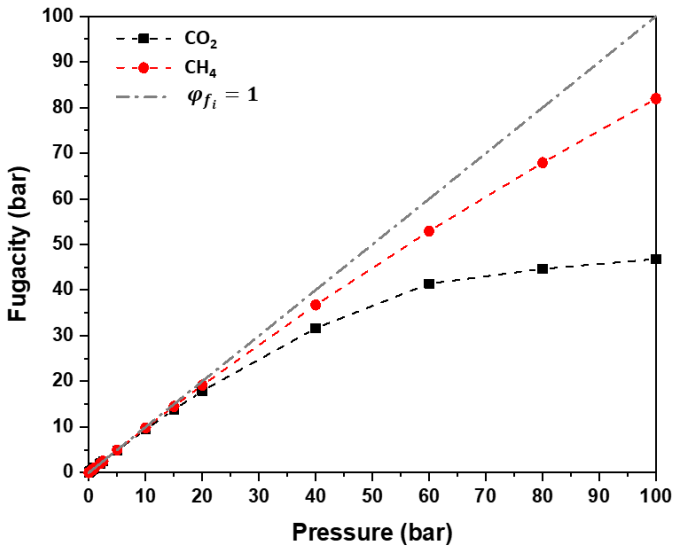

Figure 2.3: Fugacity-pressure curves for CO_2 (black squares) and CH_4 (red circles), calculated using the Peng-Robinson EoS,[91] up to 100 bar. The grey dash-and-dot line indicates the curve for which at every pressure value the fugacity coefficient φ_{f_i} is equal to 1.

2.3.3.4 Potentials

The Monte Carlo simulations utilise force fields, to model both guest-adsorbent and guest-guest interactions, and to determine the resulting potential energies of each guest molecule in each configuration. The potential energy contains contributions from bonded and non-bonded interactions; however, given the GCMC simulations in this thesis consider the interaction between the fixed coordinate framework and small, rigid guest molecules, only the non-bonded component needs to be considered. This is split into Coulombic (electrostatic) and van der Waal (dispersion) components, with the former only applying to polar and quadrupolar guest molecules such as CO_2.

The total electrostatic component of the potential energy (U_{COUL}) is calculated by the summation of every charge pair in the system using the Ewald summation method,

utilising the partial charges which are assigned to each individual atom of the adsorbent material and guest molecules, as follows:

$$U_{COUL} = \sum_{i}^{N} \sum_{j=i+1}^{N} \frac{q_i q_j}{4\pi\varepsilon_0 r_{ij}} \qquad \textit{Equation 2.56}$$

where q_i and q_j are the charges on the pair of atoms, r_{ij} is the distance between the two atoms and ε_0 is the permittivity in a vacuum.

The dispersion potential energy (V_{ij}) is determined using the Lennard-Jones (LJ) 12-6 potential, defined as:

$$V_{ij} = 4\varepsilon_{ij}\left[\left(\frac{\sigma_{ij}}{r_{ij}}\right)^{12} - \left(\frac{\sigma_{ij}}{r_{ij}}\right)^{6}\right] \qquad \textit{Equation 2.57}$$

where V_{ij} is the dispersion potential energy between two atoms i and j separated by distance r_{ij}, ε_{ij} is the depth of the combined energy well of the two atoms and σ_{ij} is the combined LJ sphere diameter. In order to determine the values of σ_{ij} and ε_{ij}, mixing rules are applied to the σ and ε values of the individual atoms or molecules. The most commonly-used, which are utilised for the work in this thesis, are the Lorentz-Berthelot rules, defined as follows:

$$\sigma_{ij} = \frac{\sigma_{ii} + \sigma_{ij}}{2} \qquad \textit{Equation 2.58}$$

$$\varepsilon_{ij} = \sqrt{\varepsilon_{ii}\varepsilon_{jj}} \qquad \textit{Equation 2.59}$$

Through the use of the LJ 12-6 potential, it is apparent that the strength of the calculated dispersion energy between two molecules rapidly decreases with an increase in r_{ij}; in GCMC simulations a cut-off radius (of at least 15 Å) is often defined beyond which all guest-guest and guest-adsorbent interactions are assumed to be negligible and thus are not accounted for.

During the classical simulation production run, periodic boundary conditions are applied onto the simulation cell to duplicate the simulation cell and its contents in all directions, as shown by the two-dimensional example in Figure 2.4. This is necessary to replicate the bulk phase of the adsorbent material and thus remove the surface effects which would be prevalent for small simulation boxes without periodic boundary conditions. The primary simulation box length needs to be at least twice the value of the interaction cut-off radius, so that each atom in the primary simulation cell can only interact with the closest representation of every other atom in the system, thus avoiding double-counting of interactions or self-interaction.

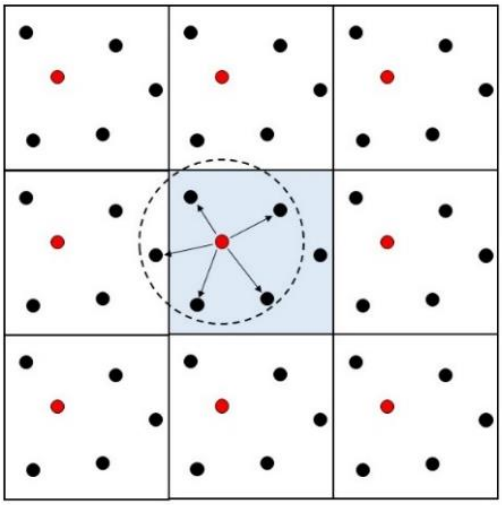

Figure 2.4: 2-D Visualisation of periodic boundary conditions (PBCs). The blue shading indicates the primary simulation cell. Red spheres indicate the duplication of atoms by the PBCs in neighbouring simulation cells. The dashed line indicates the cut-off radius, beyond which interactions are ignored.

2.4 References

1. H. R. Powell, *Crystallogr. Rev.*, 2019, **25**, 264-294.
2. D. W. H. Rankin, *Structural methods in molecular inorganic chemistry.*, John Wiley & Sons, Chichester, UK, 2013.
3. H. Nowell, S. A. Barnett, K. E. Christensen, S. J. Teat and D. R. Allan, *J. Synchrotron Radiat.*, 2012, **19**, 435-441.
4. J. Sotelo, PhD thesis, University of Edinburgh, 2015.
5. C. J. McMonagle, PhD thesis, University of Edinburgh, 2018.
6. A. Katrusiak, *Acta Crystallogr A*, 2008, **64**, 135-148.
7. J. C. Jamieson, A. W. Lawson and N. D. Nachtrieb, *Rev. Sci. Instrum.*, 1959, **30**, 1016-1019.
8. C. E. Weir, E. R. Lippincott, A. Vanvalkenburg and E. N. Bunting, *J. Res. Nat. Stand. Sec. A*, 1959, **63**, 55-62.
9. C. Weir, S. Block and G. J. Piermarini, *J. Res. Nat. Stand. Sec. C*, 1965, **C 69**, 275-281.
10. S. Block, C. W. Weir and G. J. Piermarini, *Science*, 1965, **148**, 947-948.
11. L. Merrill and W. A. Bassett, *Rev. Sci. Instrum.*, 1974, **45**, 290-294.
12. A. Jayaraman, *Rev. Mod. Phys.*, 1983, **55**, 65-108.
13. L. Dubrovinsky, N. Dubrovinskaia, V. B. Prakapenka and A. M. Abakumov, *Nat. Commun.*, 2012, **3**, 1163.
14. S. A. Moggach, D. R. Allan, S. Parsons and J. E. Warren, *J. Appl. Crystallogr*, 2008, **41**, 249-251.
15. G. J. Piermarini, S. Block, J. D. Barnett and R. A. Forman, *J. Appl. Phys.*, 1975, **46**, 2774-2780.
16. R. A. Forman, S. Block, J. D. Barnett and G. J. Piermarini, *Science*, 1972, **176**, 284-285.
17. R. A. Forman, S. Block, J. D. Barnett and G. J. Piermari, *Bull. Am. Phys. Soc*, 1972, **17**, 351.
18. A. J. Graham, D. R. Allan, A. Muszkiewicz, C. A. Morrison and S. A. Moggach, *Angew. Chem., Int. Ed.*, 2011, **50**, 11138-11141.
19. C. L. Hobday, R. J. Marshall, C. F. Murphie, J. Sotelo, T. Richards, D. R. Allan, T. Düren, F. X. Coudert, R. S. Forgan, C. A. Morrison, S. A. Moggach and T. D. Bennett, *Angew. Chem., Int. Ed.*, 2016, **55**, 2401-2405.
20. S. A. Moggach, T. D. Bennett and A. K. Cheetham, *Angew. Chem., Int. Ed.*, 2009, **48**, 7087-7089.
21. T. Varga, A. P. Wilkinson and R. J. Angel, *Rev. Sci. Instrum.*, 2003, **74**, 4564-4566.

22. V. A. Sidorov and R. A. Sadykov, *J. Phys.: Condens. Matter*, 2005, **17**, S3005-S3008.
23. S. Klotz, J. C. Chervin, P. Munsch and G. Le Marchand, *J. Phys. D: Appl. Phys.*, 2009, **42,** 075413.
24. K. Murata, K. Yokogawa, H. Yoshino, S. Klotz, P. Munsch, A. Irizawa, M. Nishiyama, K. Iizuka, T. Nanba, T. Okada, Y. Shiraga and S. Aoyama, *Rev. Sci. Instrum.*, 2008, **79**, 085101.
25. A. Dawson, D. R. Allan, S. Parsons and M. Ruf, *J. Appl. Crystallogr*, 2004, **37**, 410-416.
26. CrysAlisPro, Oxford Diffraction/Aligent Technologies UK Ltd, Yarnton, UK
27. F. Birch, *Phys. Rev.*, 1947, **71**, 809-824.
28. G. A. Craig, C. H. Woodall, S. C. McKellar, M. R. Probert, K. V. Kamenev, S. A. Moggach, E. K. Brechin, S. Parsons and M. Murrie, *Dalton Trans.*, 2015, **44**, 18324-18328.
29. J. L. Zhu, S. M. Feng, L. J. Wang, C. Q. Jin, X. H. Wang, L. T. Li, Y. C. Li, X. D. Li and J. Liu, *High Pressure Res.*, 2010, **30**, 265-272.
30. J. Zhao, N. L. Ross, R. J. Angel, M. A. Carpenter, C. J. Howard, D. A. Pawlak and T. Lukasiewicz, *J. Phys.: Condens. Matter*, 2009, **21**, 235403.
31. I. Shirotani, J. Hayashi and K. Takeda, *Mol. Cryst. Liq. Cryst.*, 2005, **442**, 157-166.
32. J. A. Dolyniuk and K. Kovnir, *Materials*, 2016, **9**, 692.
33. T. B. Ballaran, in *High-Pressure Crystallography: from Fundamental Phenomena to Technological Applications*, ed E. Boldyrena and P. Dera, Springer, Dordrecht, 2010, ch. 12, 135-145.
34. D. C. Young, *Computational chemistry: a practical guide for applying techniques to real world problems*, Wiley, New York, N.Y., 2001.
35. E. I Solomon, R. A. Scott, R. B. King, *Computational Inorganic and Bioinorganic Chemistry*, John Wiley & Sons, Chichester, N.J., 2009.
36. F. Jensen, *Introduction to Computational Chemistry* (3rd edition), John Wiley & Sons, New York, N.Y., 2016.
37. R. G. Parr, *Density-Functional Theory of Atoms and Molecules*, Oxford University Press, Oxford, UK, 1989.
38. D. S. Sholl and J. A. Steckel, *Density Functional Theory: A Practical Introduction*, Wiley, Hoboken, N.J., 2009.
39. S. Fujita and K. Ito, *Quantum Theory of Conducting Matter*, Springer, New York, N.Y., 2007
40. M. Born and R. Oppenheimer, *Ann. Phys-Berlin*, 1927, **84**, 0457-0484.
41. D. R. Hartree, *Proc. Camb. Phil. Soc.*, 1928, **24**, 89-110.
42. D. R. Hartree, *Proc. Camb. Phil. Soc.*, 1928, **24**, 111-132.
43. V. Fock, *Z. Phys.*, 1930, **62**, 795-805.

44. D. R. Hartree, F. R. S. Hartree and W. Hartree, *Proc. R. Soc. A.*, 1935, **150**, 0009-0033.
45. C. Moller and M. S. Plesset, *Phys. Rev.*, 1934, **46**, 0618-0622.
46. W. Kohn and L. J. Sham, *Phys. Rev.*, 1965, **140**, 1133-1138.
47. P. Hohenberg and W. Kohn, *Phys. Rev. B*, 1964, **136**, B864-871.
48. A. D. Becke, *J. Chem. Phys.*, 2014, **140**, 18A301.
49. K. Burke, *J. Chem. Phys.*, 2012, **136**, 150901.
50. A. D. Becke, *Phys. Rev. A*, 1988, **38**, 3098-3100.
51. C. T. Lee, W. T. Yang and R. G. Parr, *Phys. Rev. B*, 1988, **37**, 785-789.
52. J. P. Perdew, K. Burke and M. Ernzerhof, *Phys. Rev. Lett.*, 1996, **77**, 3865-3868.
53. S. J. Clark, M. D. Segall, C. J. Pickard, P. J. Hasnip, M. J. Probert, K. Refson and M. C. Payne, *Z. Kristallogr. Cryst. Mater.*, 2005, **220**, 567-570.
54. P. J. Stephens, F. J. Devlin, C. F. Chabalowski and M. J. Frisch, *J. Phys. Chem.*, 1994, **98**, 11623.
55. J. P. Perdew and M. Ernzerhof, *J. Chem. Phys.*, 1996, **105**, 9982.
56. C. Adamo and V. Barone, *J. Chem. Phys.*, 1999, **110**, 6158-6170.
57. J. Heyd, G. E. Scuseria and M. Ernzerhof, *J. Chem. Phys.*, 2003, **118**, 8207-8215.
58. J. Heyd and G. E. Scuseria, *J. Chem. Phys.*, 2004, **121**, 1187-1192.
59. J. Heyd, J. E. Peralta, G. E. Scuseria and R. L. Martin, *J. Chem. Phys.*, 2005, **123**, 174101.
60. A. V. Krukau, O. A. Vydrov, A. F. Izmaylov and G. E. Scuseria, *J. Chem. Phys.*, 2006, **125**, 224106.
61. J. E. Peralta, J. Heyd, G. E. Scuseria and R. L. Martin, *Phys. Rev. B*, 2006, **74**, 073101.
62. A. J. Garza and G. E. Scuseria, *J. Phys. Chem. Lett.*, 2016, 7, 4165-4170.
63. P. Borlido, J. Schmidt, A. W. Huran, F. Tran, M. A. L. Marques and S. Botti, *Npj Comput. Mater.*, 2020, **6**, 96.
64. A. D. Becke, *J. Chem. Phys.*, 1993, 98, 5648.
65. M. J. Frisch, G. W. Trucks, H. B. Schlegel, G. E. Scuseria, M. A. Robb, J. R. Cheeseman, G. Scalmani, V. Barone, B. Mennucci, G. A. Petersson, H. Nakatsuji, M. Caricato, H. X. Li, P. Hratchian, A. F. Izmaylov, J. Bloino, G. Zheng, J. L. Sonnenberg, M. Hada, M. Ehara, K. Toyota, R. Fukuda, J. Hasegawa, M. Ishida, T. Nakajima, Y. Honda, O. Kitao, H. Nakai, T. Vreven, J. A. Montgomery, Jr., J. E. Peralta, F. Ogliaro, M. Bearpark, J. J. Heyd, E. Brothers, K. N. Kudin, V. N. Staroverov, R. Kobayashi, J. Normand, K. Raghavachari, A. Rendell, J. C. Burant, S. S. Iyengar, J. Tomasi, M. Cossi, N. Rega, J. M. Millam, M. Klene, J. E. Knox, J. B. Cross, V. Bakken, C. Adamo, J. Jaramillo, R. Gomperts, R. E. Stratmann, O. Yazyev, A. J. Austin, R. Cammi, C. Pomelli, J. W. Ochterski, R. L. Martin, K. Morokuma, V. G. Zakrzewski, G. A. Voth, P. Salvador, J. J. Dannenberg, S. Dapprich, A. D. Daniels, Ö. Farkas, J. B. Foresman, J. V. Ortiz, J. Cioslowski and D. J. Fox, GAUSSIAN09, Gaussian Inc., Wallingford, C.T., 2009.

66. R. Dovesi, A. Erba, R. Orlando, C. M. Zicovich-Wilson, B. Civalleri, L. Maschio, M. Rerat, S. Casassa, J. Baima, S. Salustro and B. Kirtman, *Wiley Interdiscip. Rev. Comput. Mol. Sci.* 2018, **8**: e1360.

67. A. Gavezzotti, *Molecular aggregation: structure analysis and molecular simulation of crystals and liquids*, Oxford University Press, Oxford, 2013.

68. S. P. Thomas, P. R. Spackman, D. Jayatilaka and M. A. Spackman, *J. Chem. Theory Comput.*, 2018, **14**, 1614-1623.

69. A. Gavezzotti, *Mol. Phys.*, 2008, **106**, 1473-1485.

70. A. Gavezzotti, *J. Phys. Chem. B*, 2002, **106**, 4145-4154.

71. A. Gavezzotti, *J. Phys. Chem. B*, 2003, **107**, 2344-2353.

72. J. D. Dunitz and A. Gavezzotti, *Angew. Chem., Int. Ed.*, 2005, **44**, 1766-1787.

73. A. Gavezzotti, *CrystEngComm*, 2003, **5**, 429-438.

74. A. Gavezzotti, *CrystEngComm*, 2003, **5**, 439-446.

75. J. D. Dunitz, *Chembiochem*, 2004, **5**, 614-621.

76. J. D. Dunitz and A. Gavezzotti, *Chem. Soc. Rev.*, 2009, **38**, 2622-2633.

77. A. G. P. Maloney, P. A. Wood and S. Parsons, *CrystEngComm*, 2015, **17**, 9300-9310.

78. A. G. P. Maloney, P. A. Wood and S. Parsons, *CrystEngComm*, 2016, **18**, 3273-3281.

79. P. A. Wood, R. S. Forgan, D. Henderson, S. Parsons, E. Pidcock, P. A. Tasker and J. E. Warren, *Acta Crystallogr. B*, 2006, **62**, 1099-1111.

80. P. A. Wood, D. Francis, W. G. Marshall, S. A. Moggach, S. Parsons, E. Pidcock and A. L. Rohl, *CrystEngComm*, 2008, **10**, 1154-1166.

81. A. G. P. Maloney, P. A. Wood and S. Parsons, *CrystEngComm*, 2014, **16**, 3867-3882.

82. J. P. S. Mowat, S. R. Miler, J. M. Griffin, V. R. Seymour, S. E. Ashbrook, S. P. Thompson, D. Fairen-Jimenez, A. M. Banu, T. Düren and P. A. Wright, *Inorg. Chem.*, 2011, **50**, 10844-10858.

83. C. L. Hobday, T. D. Bennett, D. Fairen-Jimenez, A. J. Graham, C. A. Morrison, D. R. Allan, T. Düren and S. A. Moggach, *J. Am. Chem. Soc*, 2018, **140**, 382-387.

84. C. L. Hobday, C. H. Woodall, M. J. Lennox, M. Frost, K. Kamenev, T. Düren, C. A. Morrison and S. A. Moggach, *Nat. Commun.*, 2018, **9**. 1429.

85. A. Gupta, L. A. Clark and R. Q. Snurr, *Langmuir*, 2000, **16**, 3910-3919.

86. Y. S. Bae, K. L. Mulfort, H. Frost, P. Ryan, S. Punnathanam, L. J. Broadbelt, J. T. Hupp and R. Q. Snurr, *Langmuir*, 2008, **24**, 8592-8598.

87. T. L. Hill, *An introduction to statistical thermodynamics*, Dover Publications, New York, N.Y., 1986.

88. D. Frenkel and B. Smit, *Understanding Molecular Simulation*, Academic Press, San Diego, 2nd edn., 2002.

89. G. M. Anderson, in *Thermodynamics of Natural Systems*, Cambridge University Press, Cambridge, UK, 2nd edn, 2005, ch. 8, pp. 198-233.

90. H. DeVoe, in Thermodynamics and Chemistry, University of Maryland, College Park, M.D., 2nd edn, ch. 7, pp. 166-194

91. D. Peng and D. B. Robinson, *Ind. Eng. Chem. Fundam.*, 1976, **15**, 59-64.

92. A. Gupta, S. Chempath, M. J. Sanborn, L. A. Clark and R. Q. Snurr, *Mol. Simul.*, 2003, **29**, 29-46.

Chapter 3

Probing the High Pressure Structural and Electronic Response of Pt-containing Piezoresistive Candidate Materials

3.1: Synopsis

This chapter covers an in-depth investigation into the structural and electronic response to pressure of four planar Pt(II) d^8 complexes, to better understand their different piezoresistivity behaviour. High pressure X-ray diffraction experiments and solid-state calculations have revealed the extent of anisotropy in the volumetric compression and degree of delocalisation in the frontier orbitals in each of the materials. These are crucial factors, alongside the solid-state packing and contact distances between neighbouring metal centres, to explain the broad variation in piezoresistive response in these structurally-related materials.

3.2: Disclaimer

The synthesis of all the complexes presented in this chapter and a majority of the solid-state calculations on $Pt(bqd)_2$ were undertaken by Dr Helen Benjamin (formerly of Robertson group, University of Edinburgh). The in-house ambient and high-pressure X-ray diffraction data on $Pt(bqd)_2$ and $Pt(bqd\text{-}dibutyl)_2$ mentioned in this chapter were initially reported in the MChem final year project report of Edward Broadhurst (University of Edinburgh, 2018);[1] the diffraction experiments and data analysis for that report were undertaken under the dual supervision of myself and Dr Stephen Moggach (now based at the University of Western Australia).

3.3: Introduction

Over recent decades, there has been continual improvement in computer processing performance, driven by an increase in transistor density on processor chips (Moore's Law),[2] and an increase in clock speed (*i.e.* the switching time between the on and off states of each transistor). While the former is continuing unabated, the latter has

stalled as transistors have decreased in size. This is the so-called Dennard scaling breakdown,[3] which limits the minimum operating voltage required to switch the transistor on/off status. This arises due to current metal oxide semiconductors used inside transistors having a minimum voltage threshold (*ca.* 1V); operating at voltages below this level can result in undesirable current leakages in the off-state, which leads to heat production, or slow currents while in the on-state, resulting in inefficient processing.[4, 5] To facilitate progress towards the next generation of computer processors, new forms of transistors are now being sought to overcome the current limitations on operating voltage and high speed state switching.

IBM recently submitted a patent for the piezoelectric transistor (PET).[6] A schematic of a PET is shown in Figure 3.1, with the expectation that the device can operate with minimal input voltages (*ca.* 0.1 V).[7-11] The design incorporates both a piezoelectric (PE) and piezoresistive (PR) component in a sandwich-like arrangement between three metal contacts, labelled as the gate, common and sense. The entire transistor is capped at either end by a high yield material forming a rigid exterior structure.

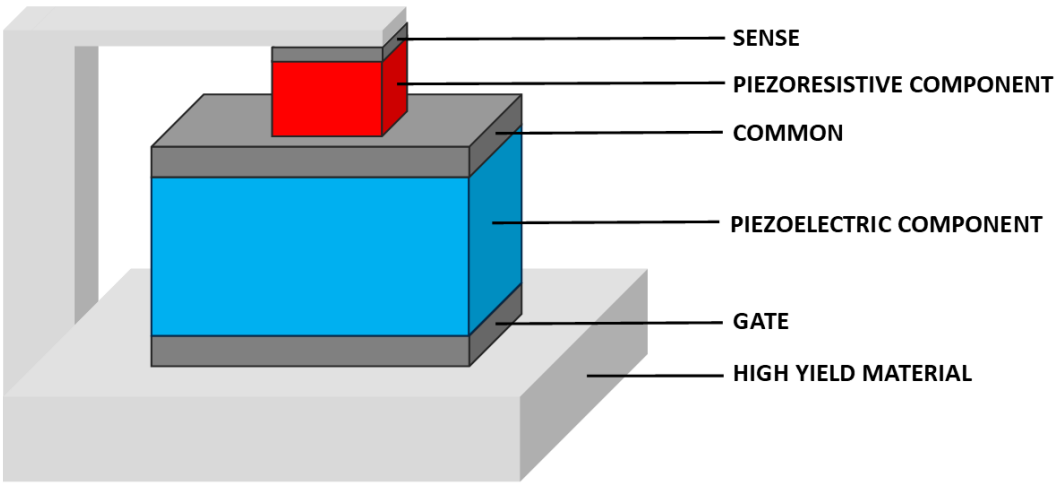

Figure 3.1: A schematic of the design of the piezoelectric transistor, adapted from the designs outlined in US Patent 7 848 135 B2 and in publications by Newns and co-workers (2012). [6, 7, 10, 11, 12]

The transistor switches from the off to on state by the following sequence of processes:[12]

a) an input voltage is applied to the gate.

b) a build-up of charge in the PE component, which is comprised of a material such as lead zirconate titanate,[13] leads to a structural response. This in turn induces a swelling of the PE component, which causes pressure to be applied to the PR component.

c) the PR component undergoes anisotropic compression, facilitating an insulator-to-metal transition. The decrease in resistivity results in charge flow towards the sense, which forms the output signal from the transistor.

Publications concerning the design of PET devices have discussed purely inorganic compounds for the PR component, such as the samarium monochalcogenides (SmX, where X = S, Se, Te), due to their strong piezoresistive behaviour.[14-16] However there are concerns surrounding these materials. SmS, for example, undergoes the desired insulator-metal transition at below 1 GPa but in its thin film form the transition is irreversible, which for application is highly undesirable.[17-19] SmSe and SmTe on the other hand show reversible transitions, but require much higher pressure inputs of at least 2.5 GPa to achieve them,[16, 20] which thus would require higher than desirable gate voltages to operate within the device. Therefore, there is an active search for alternative materials which can undergo reversible transitions at lower pressures.

A number of planar transition metal complexes have been reported to have piezoresistive behaviour, notably $Ir(CO)_2(acac)_2$,[21, 22] the Magnus green salt (MGS) compounds, $[Pt(NH_2R)_3][PtCl_4]$,[21, 22] and the bis(1,2-dionedioximato) family of Pt(II) complexes.[23-25] All contain a 1-D conductive pathway facilitated by electronic communication between stacked metal centres, with conductivity only permitted upon significant contraction of the metal···metal stacking distance. Herein a selection of these known literature compounds, alongside newly-devised derivative

compounds, form the basis for a comprehensive investigative study aimed at fully understanding the structural and electronic response of these compounds; this new-found knowledge can be used to gain further understanding of the piezoresistive response in these materials as well as allow suggestions to be made for future structural modifications to fine-tune their performance.

3.3.1 Pt(bqd)$_2$ and Pt(bqd-dibutyl)$_2$

Pt(bqd)$_2$, where bqd = bis(1,2-benzoquinonedioximato), (CSD refcode: BQDXPT)[26] is one of the standout candidates for piezoresistive application from the bis(1,2-dionedioximato) family of Pt(II) complexes. The molecular structure of Pt(bqd)$_2$ consists of a four-coordinate Pt coordination centre, with cis ∠N-Pt-N angles of *ca.* 80° and 100°, surrounded by two bidentate delocalised ligand systems (Figure 3.2).[26] In the solid state, the compound crystallises in the *Ibam* space group, with 1-D stacking columns of the Pt centres along the crystallographic *c*-axis (Figure 3.3A), resulting in an intra-column Pt···Pt distance of 3.17 Å.[26] Neighbouring molecules in these stacks are not eclipsed, but rather are related by *ca.* 94° and 86° rotations. Due to the *I*-centred symmetry, there is an alternation of the fragments along the [110] direction, allowing the molecules to slot together within each sheet of the material (Figure 3.3B).

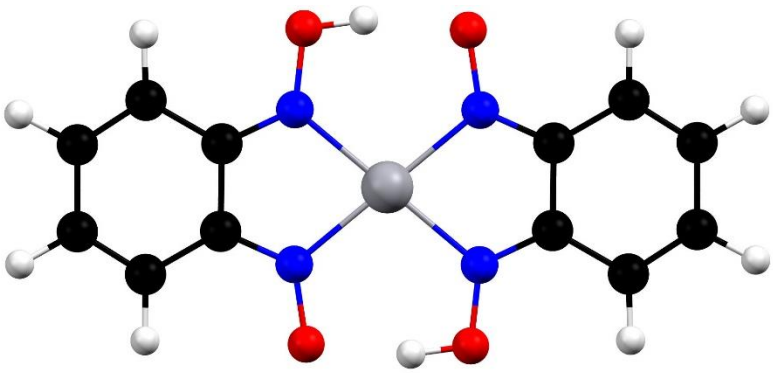

Figure 3.2: Molecular structure of Pt(bqd)$_2$. Atoms are coloured: Pt, dark grey; O, red; N, blue; H, light grey. Image created using Mercury.[27]

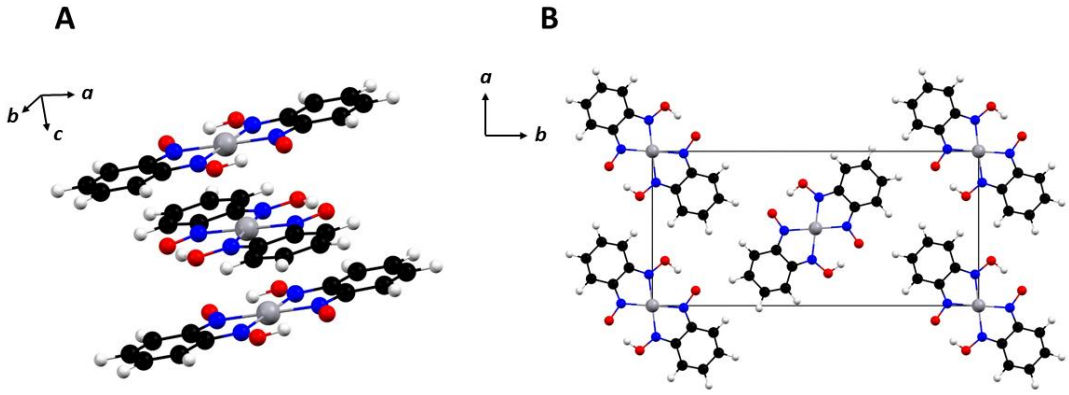

Figure 3.3: Packing of isolated chain along the c axis (A) and in one sheet in the ab plane (B) of $Pt(bqd)_2$. Atoms are coloured: Pt, dark grey; O, red; N, blue; H, light grey. Unit cell edges in Figure 2B are represented by the black lines. Images created using Mercury.[27]

While a variety of band gaps have been quoted for $Pt(bqd)_2$, multiple studies have shown that the material is a semiconductor at ambient pressures, prior to forming a metallic state at around 0.8-1.0 GPa,[23, 28-31] with a four-fold order of magnitude change in resistivity across the 0.0-1.0 GPa pressure range.[29] The formation of the metallic state has been attributed to the mixing of electron density between the $5d_{z^2}$ and $6p_z$ frontier orbitals,[28, 30] as well as a decrease in the Pt···Pt stacking distance, determined from the compression of the unit cell parameters.[29, 31] Moreover, despite the Pt···Pt distance continuing to decrease, resistivity increases above 1 GPa were observed.[29] To date, no high-pressure structures of $Pt(bqd)_2$ have been reported, nor have there been any theoretical studies on this material, and hence there is a lack of explicit understanding on the structural changes, interlayer interactions and frontier orbital nature which could explain the piezoresistive response exhibited by this material between ambient conditions and 2 GPa.

Despite its promising electronic properties, $Pt(bqd)_2$ suffers from a lack of solubility and, thus, processability into the thin spin-coated films required as part of the PET device. To overcome this, modifications to the BQD ligand backbone to incorporate aliphatic chains were proposed. The synthesis of a previously unreported compound $Pt(bqd\text{-}dibutyl)_2$, shown in Figure 3.4, in which *n*-butyl groups have replaced the

hydrogen atoms on the 4 and 5 positions on the phenyl rings, was undertaken to provide valuable insight into how relatively large modifications such as this would impact processability, structure and electronic properties of the material.

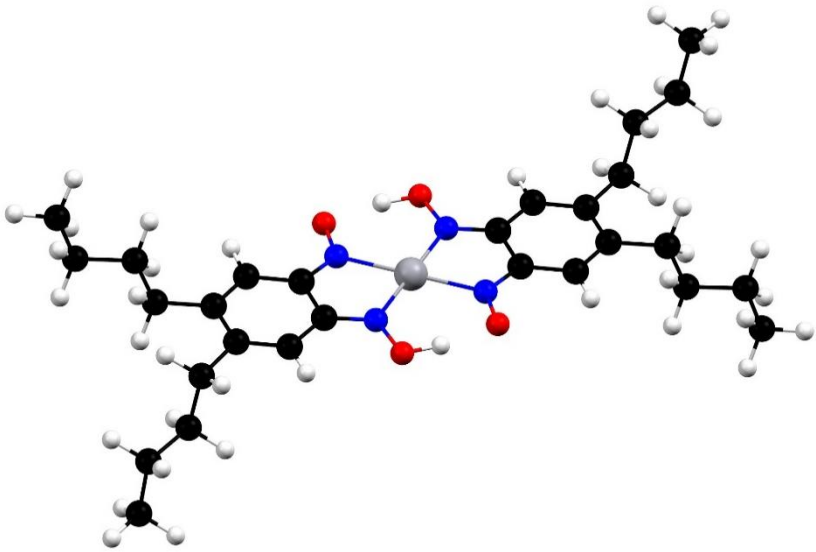

Figure 3.4: Proposed molecular structure of Pt(bqd-dibutyl)$_2$, with atoms coloured: Pt, dark grey; O, red; N, blue; C, black; H, light grey. Image created using Mercury.[27]

3.3.2 Magnus green salts

The Magnus green salt $[Pt(NH_3)_4][PtCl_4]$, hereafter referred as MagNH$_3$, crystallises in the *P*4/*mnc* space group (Figure 3.5), with the solid-state structure consisting of 1-D chains of alternating $[Pt(NH_3)_4]^{2+}$ and $[PtCl_4]^{2-}$ units along the *c* axis direction with a Pt···Pt intra-chain stacking distance of 3.25(1) Å, equating to exactly half of the *c* axis lattice parameter.[32] Neighbouring units along the *c* axis direction are partially staggered so that NH_3 and Cl groups on neighbouring units are not eclipsed, with a Cl-Pt···Pt-N torsion angle of *ca.* -29°. Neighbouring chains along the *ab* plane diagonal are related by a half unit cell translation in the *c* axis direction, prohibiting the close contact of NH_3 groups. These two structural characterisations result in short intra-chain and inter-chain N-H···Cl contacts, ranging between 2.5 Å and 3.0 Å, which have been used to provide an explanation for the rigidity for the structure.[33]

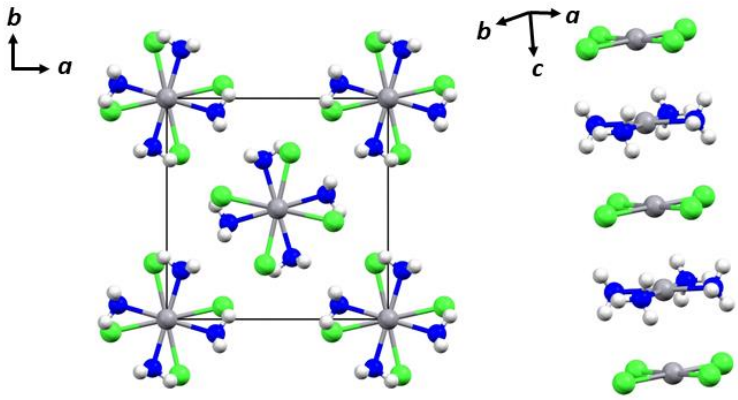

Figure 3.5: Packed unit cell (left) and isolated chain (right) of $MagNH_3$. Atoms are coloured: Pt, dark grey; Cl, green; N, blue; H, light grey. Images created using Mercury.[27]

Some understanding of the structure and property variations of $MagNH_3$ upon the application of pressure have been gained from previous literature studies. Variable pressure conductivity measurements on powder samples of $MagNH_3$ showed that maximum conductivity occurs at around 10 GPa, with two orders of magnitude change in conductivity observed over the 0-10 GPa pressure range.[21] At even higher pressures, the conductivity decreased, thus corresponding to an increase in resistivity.[21] A high-pressure powder X-ray diffraction study, which examined the rate of *c* axis and volumetric compression of $MagNH_3$ up to *ca.* 13 GPa, observed that the Pt···Pt contact distance decreased by around 0.12 Å and 0.27 Å by 2 GPa and 10 GPa respectively, equating to a 3.7% and 8.4 % decrease compared to the structure collected under ambient conditions.[22] Despite this previous study, no solved structures of $MagNH_3$ have been obtained at pressure, and therefore the full structural response of this compound to compression is not currently known.

The results of partial electronic band structure calculations of $MagNH_3$, based on a compression of a 1-D model of an isolated chain of $[Pt(NH_3)_4]^{2+}$ and $[PtCl_4]^{2-}$ units have previously been reported.[33] Intra-column compression of around 6%,[33] (comparable to the structural response observed at 3.5 GPa for the powder sample), prompted a decrease in the electronic band gap from *ca.* 1.0 eV to *ca.* 0.3 eV.[22] However, as pointed

out by the authors of that study, the use of pure DFT methods (i.e. a non-hybrid method, and therefore lacking in exact exchange) resulted in an underestimation of band gap size,[34] and hence further wavefunction optimisation by use of a diagonalization scheme was undertaken to obtain the quoted band gap values.[35] Moreover, since the study only considered a one-dimensional column model, any inter-column interactions and compression along the other unit cell lattice directions were not considered.

A derivative compound of $MagNH_3$, formed by modification of the ammonia ligand component to methylamine, hereafter referred to as $MagNH_2Me$ (CSD refcode: TMAMPT), has been shown to crystallise in the same *P*4/*mnc* space group with the expected larger *a* and *b* unit cell parameters to accommodate the larger ligand (Figure 3.6).[36] However, this modification caused no significant change in the Pt···Pt contact distance, measured as 3.29(2) Å.[36] Other than a slightly larger Cl-Pt···Pt-N torsional angle, *ca.* 30°, the ligand modification had a minimal effect on the ambient pressure solid-state structure as that seen for $MagNH_3$. $MagNH_2Me$ has not been studied in terms of either its structural or electronic response to the application of pressure, and hence the effect of the modest ligand modification is not currently known.

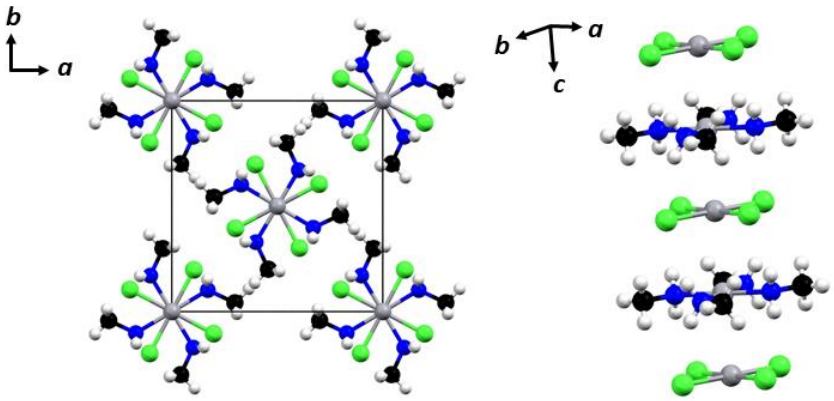

Figure 3.6: Packed unit cell (left) and isolated chain (right) of $MagNH_2Me$. Atoms are coloured: Pt, dark grey; Cl, green; N, blue; C, black; H, light grey. Images created using Mercury.[27]

3.3.3 Aims of research

Existing literature on $Pt(bqd)_2$ and $MagNH_3$ has clearly shown that the two compounds exhibit greatly varying conductivity properties, despite possessing similar metal···metal distances. Therefore, it is apparent that a more detailed description of the structural and electronic responses to pressure are required, to provide greater understanding for molecular design criteria which goes beyond the need for the correct crystal packing to facilitate direct metal orbital overlap with short contact distances. Additionally, the effect of the modifications to both parent compounds on the structural and electronic response must also be examined carefully, to ascertain if the modification has a positive or negative effect on the piezoresistive response; this understanding can be utilised to undertake more targeted modifications in future. Ambient-pressure and high-pressure X-ray diffraction experiments were first undertaken on these four compounds, from which the rate of compression and structural changes throughout the pressure series could be evaluated. The obtained experimental structural models were then used as input models for solid-state calculations to ascertain the change in electronic properties, namely the band gap size and frontier orbital description, throughout their respective pressure series.

3.4: Methods

3.4.1: Ambient-pressure X-ray crystallography

Prior to the high-pressure experiments, ambient pressure and temperature diffraction data were collected on in-house laboratory diffractometers for all four compounds. The diffraction data for $Pt(bqd)_2$ and $Pt(bqd\text{-}dibutyl)_2$ were obtained from a full sphere collection on single crystals, utilising a series of ω scans, on a Bruker SMART APEX II diffractometer with monochromated Mo-Kα X-ray radiation (λ = 0.71073 Å, 17.4 eV).[1] These sets of data were integrated using the program SAINT,[37] with the SADABS absorption correction.[38] The diffraction data for $MagNH_3$ and $MagNH_2Me$ were obtained for single crystals of each material from an optimised collection strategy using monochromated Cu-Kα X-ray radiation (λ = 1.54056 Å, 8 keV) on an Oxford Diffraction SUPERNOVA diffractometer. CrysAlisPro software was utilised for indexing, data integration and the application of empirical absorption corrections.[39] In all cases, structure solutions were carried out using Sir92 within CRYSTALS, with all data refined against F^2.[40, 41] The hydrogen atom positions were added geometrically and allowed to ride throughout the refinement process, except for the oxime atoms in $Pt(bqd)_2$ and $Pt(bqd\text{-}dibutyl)_2$ which were added manually with their positions refined according to the oxime atom positions in the isostructural $Pd(bqd)_2$ complex.[42] All non-hydrogen atoms were refined anisotropically.

3.4.2: High-pressure X-ray crystallography

High-pressure diffraction experiments were undertaken on a single crystal of each of the four compounds in turn, loaded in a modified Merrill-Bassett DAC alongside a ruby crystal (acting as the in-situ pressure calibrant) and the hydrostatic pressure transmitting medium Fluorinert FC-70 (perfluorotri-N-pentylamine).[43, 44]

High-pressure data for all four compounds were obtained at the Diamond Light Source I19 EH2 beamline,[45] utilising a Newport 4-circle κ-geometry diffractometer, installed with a Pilatus 300 K detector, and tuneable monochromatic X-ray radiation set to 0.4859 Å (25.5 keV). Data were collected on a series of ω scans, adapted to avoid shading of the detector from the cell body, with a step size and exposure time of 0.2° and 0.2 s respectively. The data reduction (integration and absorption correction) was undertaken within the CrysAlisPro software.[39] The structure solutions for all high-pressure data was carried out using CRYSTALS.[41] The ambient pressure structure for each respective compound was used as the input model, with the structure allowed to refine against each high-pressure data set and adjust to the updated unit cell parameters. All 1,2 and 1,3 distances were restrained according to the ambient pressure values and planar restraints were applied to the phenyl groups of $Pt(bqd)_2$ and $Pt(bqd\text{-}dibutyl)_2$ (to ensure the aromatic rings were not distorted). Vibrational and thermal similarity restraints were also applied to the ligands. For $Pt(bqd)_2$, $MagNH_3$ and $MagNH_2Me$, data was refined against F^2 with anisotropic atomic displacement refinement for non-hydrogen atoms. For $Pt(bqd\text{-}dibutyl)_2$, data was refined against F, with isotropic atomic displacement refinement for non-hydrogen atoms.

3.4.3: DFT (CASTEP) calculations

To provide clarity to the inconsistent compression trends observed between the in-house[1] and synchrotron pressure series for $Pt(bqd\text{-}dibutyl)_2$, a simulated pressure series was undertaken using DFT calculations. Using the experimental ambient-pressure structure as the input model in all cases, the atomic positions and unit cell parameters was allowed to optimise fully whilst constrained to the $Pna2_1$ space group, at simulated hydrostatic pressures of 0.00, 0.25, 0.50, 0.75, 1.00, 1.25 and 1.50 GPa. All calculations were undertaken using the CASTEP (version 5.11) simulation package, using the Perdew-Burke-Ernzerhof (PBE) exchange-correlation functional, alongside

the Tkatchenko-Scheffler (TS) dispersion correction,[46, 47] with the molecular wavefunction description provided by 'on-the-fly' pseudopotentials and a plane wave basis set operating at 650 eV, which gave convergence of the energy to within 3 meV per atom. The k-point sampling grid was set up so that the k-point separation along each direction of the reciprocal lattice was less than 0.04 $Å^{-1}$. The systems were optimised to the energy minimum on the potential energy surface by means of the Broyden-Fletcher-Goldfarb-Shanno (BFGS) algorithm. Structures were considered to be optimised when the energy per atom, maximum force, maximum stress, and maximum atomic displacement converged to the values of 0.01 meV $atom^{-1}$, 0.03 eV $Å^{-1}$, 0.05 GPa, and 0.005 Å, respectively. The coarser convergence criterion for the atomic displacement was used to reflect the flexibility of the *n*-butyl chains.

3.4.4: Isolated molecule (Gaussian) calculations

Hybrid DFT calculations for $Pt(bqd)_2$, $Pt(bqd\text{-}dibutyl)_2$, $MagNH_3$ and $MagNH_2Me$ were performed using the Gaussian09 package,[48] with analysis of the contribution to molecular orbitals conducted with GaussSum.[49] The calculations were carried out using the B3LYP functional,[50] with the SDD basis set and effective core potentials for Pt and the 6-311G** basis sets for H, C, N, O and Cl atoms.

3.4.5: DFT and hybrid DFT (CRYSTAL17) solid-state calculations

All solid state calculations have been performed using CRYSTAL17,[51, 52] where DFT and hybrid DFT functionals were implemented with crystalline orbitals built from linear combinations of atomic orbitals, developed from Gaussian-type functions for solid-state periodic systems. For $Pt(bqd)_2$ and $Pt(bqd\text{-}dibutyl)_2$, triple zeta valence with polarization quality basis sets for all ligand atoms (O, N, C and H).[54] For the MGS compounds, a triple zeta valence with polarization quality basis set was chosen for Cl atoms,[53] 6-311G(d) basis sets were assigned for N and C atoms,[54] and a 3-1(p)1G

basis set was utilised for H atoms.[55] For all four compounds, the Pt atoms were modelled using the scalar-relativistic pseudopotential as developed by Andrae *et al* (to treat the 60 core electrons);[56] while the remaining [4s4p2d] valence electrons were treated explicitly, as described in the methodology by Doll.[57] The input geometries for optimisation calculations were taken from the experimentally determined X-ray crystal structures.

A range of functionals were tested in calculations for $Pt(bqd)_2$, specifically PBE,[58] B3PW,[59] B3LYP,[50] HSE06,[54, 60, 61] and PBE0.[62] Due to the similarity of results between B3PW and B3LYP, stemming from utilising the same exchange component, this functional was dropped for the calculations undertaken on $Pt(bqd\text{-}dibutyl)_2$ and the MGS compounds. For $MagNH_3$, an additional functional was tested, BLYP,[63, 64] due to its use in the previous pure DFT 1-D study on $MagNH_3$.[33] However, it should be made clear that the previous study made use of a Fock-matrix diagonalisation scheme to counteract the known underestimation of band gaps calculated by pure DFT methods,[33, 35] whereas in this work the functionals used were unmodified.

Taking into account the difference between experimental and calculated unit cell parameters, bond lengths and band gaps from the compounds, it was determined that HSE06 was the most suitable choice of functional, with the choice further justified by literature examples of its performance in calculating band gaps compared to its GGA and global screen counterparts.[65-67] Thus, all the electronic band structures, projected density of states (PDOS) and crystalline orbital Hamilton population (COHP) plots and visualised crystalline orbitals reported in this chapter are from calculations utilising the HSE06 functional.

For $Pt(bqd)_2$ and the MGS compounds, the agreement between the experimental and calculated unit cell parameters was not sufficient, with the D3 dispersion correction causing an over-contraction of at least 3.5 % of the inter-planar separation associated with the *c*-axis parameter. For this reason, all structural optimisations reported herein

have unit cell parameters fixed at experimental values. Atom-only geometry optimisations returned structures that matched well with the experimental structures. Structural optimisations have been performed with Monkhorst-Pack nets[68] of 16 × 16 × 16 for $Pt(bqd)_2$ and 8 × 8× 8 for the MGS compounds, corresponding to a k-point grid spacing of less than 0.02 $Å^{-1}$ and thus 621 and 75 k-points in the irreducible Brillouin Zone (BZ) respectively, such that the total energy difference obtained by using larger Monkhorst-Pack nets was smaller than 10^{-7} Hartree. In order to study the electronic properties and band gap nature of the compounds, full electronic band structures, PDOS plots, crystalline orbital plots and COHP plots have been produced from single point energy calculations on the optimised structure using a greater k-point sampling than stated above. All other optimisation criteria were used as default for CRYSTAL17 (default total energy convergence threshold during optimisation (TOLDEE) of 10^{-7} Hartree, tolerance of the RMS of the gradient (TOLDEG) of $3x10^{-4}$ Hartree and tolerance of the RMS of the atomic displacements (TOLDEE) of $1.2x10^{-3}$ Hartree).[69]

The electronic band structures, PDOS plots, crystalline orbital plots and COHP plots for $Pt(bqd\text{-}dibutyl)_2$ were determined from single-point energy calculations undertaken on the already-optimised structures obtained from the DFT calculations on the CASTEP package, given the better agreement between the experimental and optimised unit cell parameters than that observed from the calculations using CRYSTAL17, using a 12 × 12 × 12 Monkhorst-Pack net, corresponding to a k-point grid spacing of less than 0.02 $Å^{-1}$ and thus 343 k-points in the irreducible BZ, exceeding the minimum k-point sampling for this system.

3.5: Results & Discussion

3.5.1: Ambient-pressure crystallography

The unit cell parameters and solved structures obtained for $Pt(bqd)_2$ and the MGS compounds were in good agreement with the already published structures.[26, 32, 36] Due to the greater precision of the unit cell parameters obtained in this study, the ambient pressure Pt···Pt distances determined in this study for $Pt(bqd)_2$, $MagNH_3$ and $MagNH_2Me$ measured 3.1790(2) Å, 3.2293(3) Å and 3.2489(2) Å respectively.

The newly-synthesised $Pt(bqd\text{-}dibutyl)_2$ was found to crystallise in the non-centrosymmetric $Pna2_1$ space group (a = 20.7074(11) Å, b = 4.9052(2) Å, c = 28.1381(14) Å, Z = 4). The modification of the ligand caused complete disruption of the stacking arrangement previously observed for $Pt(bqd)_2$, with $Pt(bqd\text{-}dibutyl)_2$ adopting a herringbone-type arrangement with no co-planar relationship between neighbouring molecules within each unit cell (Figure 3.7).

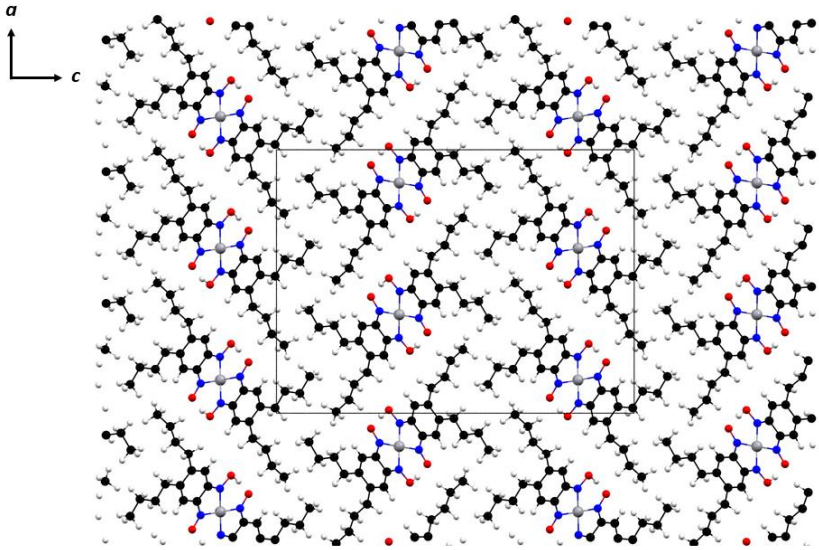

Figure 3.7: Packing diagram of the ambient pressure structure of $Pt(bqd\text{-}dibutyl)_2$, indicating the four Pt centres (dark grey) residing within the unit cell (black lines). The other atoms are coloured: O, red; N, blue; C, black; H, light grey. Images created using Mercury.[27]

As a consequence of the non-planar packing arrangement and addition of the bulky *n*-butyl chains causing greater interlayer separation, the shortest Pt···Pt distance, which occurs between molecules in neighbouring unit cells down the *b* axis direction, measured 4.9052(2) Å, which is *ca.* 1.7 Å longer than that observed in $Pt(bqd)_2$. The stacking of molecules along the *b* axis show a slipped relationship, as shown in Figure 3.8, with no direct overlap between the entirety of the molecule backbone or metal centres. Due to the lack of co-planar solid-state packing in $Pt(bqd\text{-}dibutyl)_2$, its structural response to pressure will be discussed separately to the comparative discussion on the other three compounds.

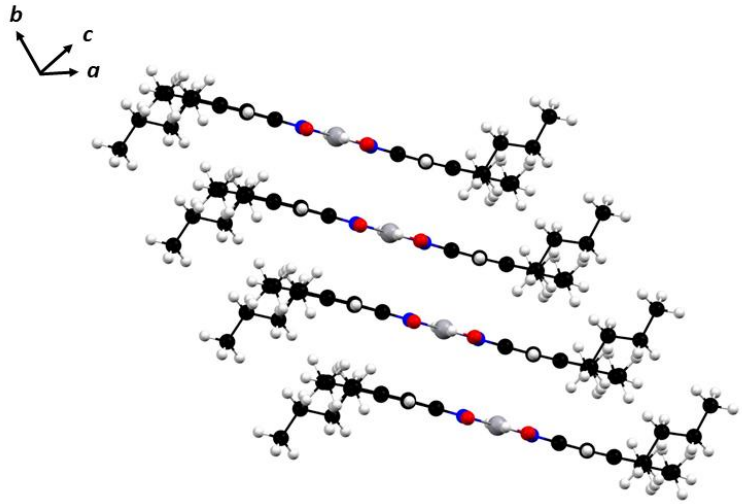

Figure 3.8: Inclined stacking of $Pt(bqd\text{-}dibutyl)_2$ molecules along the b axis direction, with atoms coloured: Pt, dark grey; O, red; N, blue; C, black; H, light grey. Images created using Mercury.[27]

3.5.2: High-pressure crystallography

Good agreement in the compression of the $Pt(bqd)_2$ was observed between the pressure series using the in-house[1] and synchrotron diffraction data; therefore, only the results derived from the higher quality diffraction data obtained from the synchrotron experiments are hereafter discussed. Figure 3.9 shows the extent of volumetric and unit cell compression for $Pt(bqd)_2$ and the two MGS compounds for their respective pressure series.

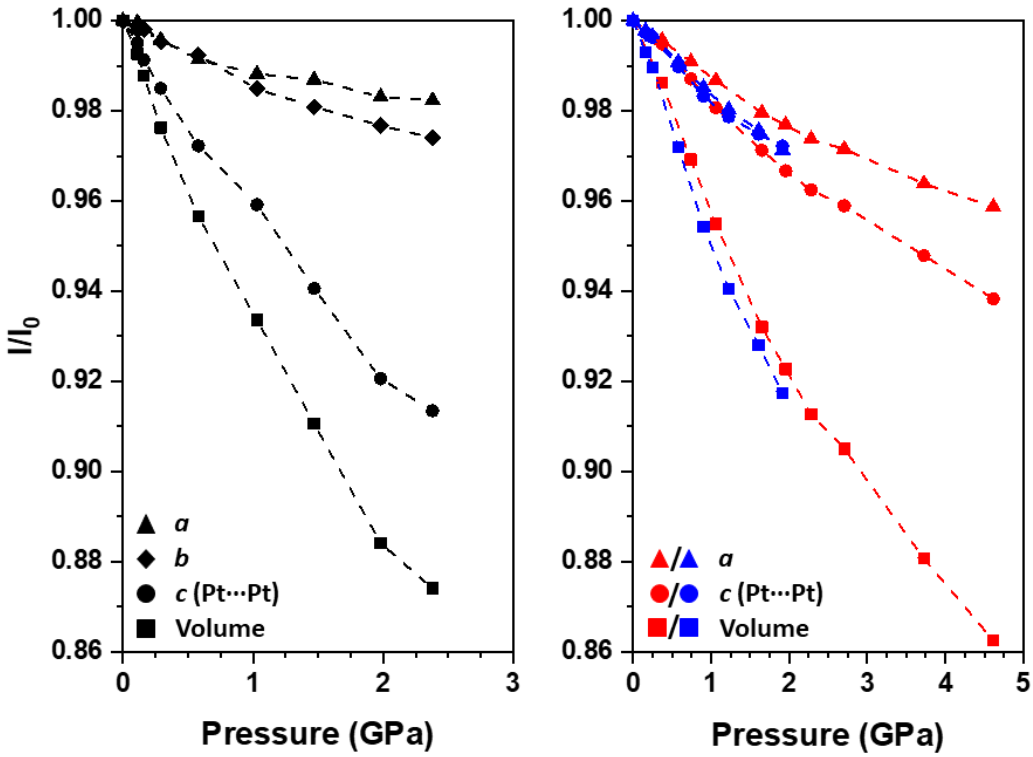

Figure 3.9: Compression of the unit cell parameters, as a fraction of the ambient pressure unit cell parameters, for $Pt(bqd)_2$ (black), $MagNH_3$ (red) and $MagNH_2Me$ (blue). Standard deviations in the unit cell parameters are smaller than the symbols used.

$Pt(bqd)_2$ and $MagNH_3$ both remained in their ambient pressure space groups throughout the entirety of their pressure series, up to 2.38 GPa and 4.62 GPa respectively, but varied greatly in terms of rate of compression observed. The unit cell volume of $Pt(bqd)_2$ decreased by around 7 % by 1 GPa, whereas only 5 % volumetric compression was observed at 1 GPa for $MagNH_3$, both of which were in good agreement with the already-published compression data.[22, 31] The slower rate of volumetric compression for $MagNH_3$ was even more apparent at higher pressures; 13% compression of the ambient unit cell volume was observed by 4 GPa, whereas $Pt(bqd)_2$ reached this extent of compression by 2.38 GPa. By fitting the volumetric compression data to a 3rd order Birch-Murnaghan equation of state (Figure 3.10),[70] bulk modulus values were obtained for $Pt(bqd)_2$ (12.1(7) GPa) and $MagNH_3$ (18.9(7) GPa), with the significant difference (to 3σ) between these values highlighting the more compressible nature of $Pt(bqd)_2$.

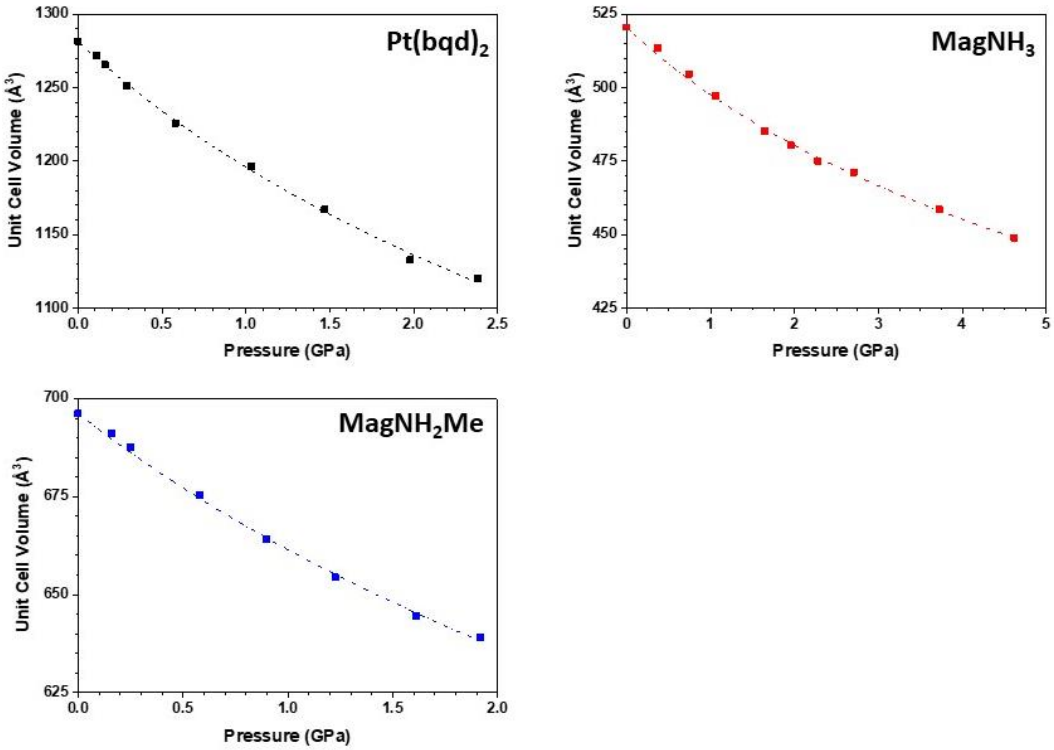

Figure 3.10: Volumetric compression and 3rd-order Birch-Murnaghan fits of $Pt(bqd)_2$, $MagNH_3$ and $MagNH_2Me$. Standard deviations in the unit cell volume are smaller than the symbols used.

In $Pt(bqd)_2$ a significant amount of anisotropy in the compression was observed, with the majority of the compression (between 60% and 70%) stemming from the contraction of the *c* axis direction. The volumetric compression for $MagNH_3$ was also anisotropic, but to a much lesser extent than that observed for $Pt(bqd)_2$ with around 40% of the compression attributed to along the c-axis direction. The higher contribution from the compression of the *c* axis for $Pt(bqd)_2$ compared to $MagNH_3$ is made clearer by Figure 3.11, which shows the change in the Pt···Pt stacking distances across the pressure series. The Pt···Pt stacking distance in $Pt(bqd)_2$ decreased from 3.18 Å to 3.05 Å between 0 and 1 GPa, decreasing further to 2.90 Å by 2.38 GPa, whereas in $MagNH_3$, the Pt···Pt stacking distance decreased from 3.22 Å to only 3.03 Å between ambient conditions and 4.62 GPa.

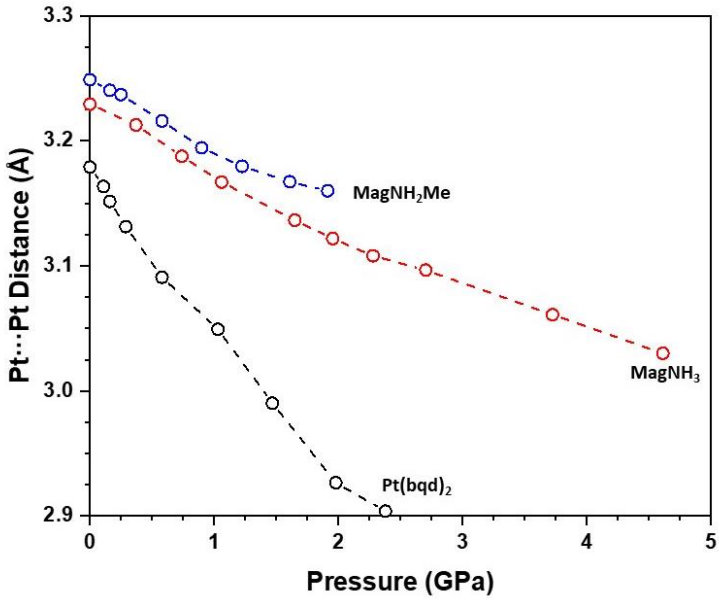

Figure 3.11: Intra-chain Pt···Pt stacking distances in $Pt(bqd)_2$, $MagNH_3$ and $MagNH_2Me$ across their respective pressure series. Error bars are smaller than symbols used.

Throughout the pressure series of both $Pt(bqd)_2$ and $MagNH_3$, no significant structural changes were observed, in terms of the Pt-ligand bond lengths, ∠ligand-Pt-ligand bond angles or the torsional angle between neighbouring molecules stacked down the *c* axis direction. Therefore, the compression of these two compounds can be exclusively described by contraction of the unit cell lattice parameters.

$MagNH_2Me$ remained in the *P*4/*mnc* space group throughout the pressure series up to 1.92 GPa. The rate of volumetric compression was similar to that observed for $MagNH_3$ (Figure 3.9), hence exhibiting a similar bulk modulus value (to 3σ) of 16.5(9) GPa (Figure 3.10). However, the similar bulk modulus value hides the isotropic nature of the compression (Figure 3.9), with no preference in contraction in the *c* axis direction over the *a*/*b* axes. The Pt···Pt stacking distance initially decreased at a similar rate to that observed for $MagNH_3$, before the rate of compression slowed above 1 GPa (Figure 3.11).

Up to 1.92 GPa, no significant intramolecular structural changes in $MagNH_2Me$ were observed in terms of the Pt-ligand bond lengths and the ∠Pt-N-C bond angle, while the ∠N-Pt-N and ∠Cl-Pt-Cl angles were constrained by the assigned space group symmetry. However, a small but significant (to 3σ) decrease in the Cl-Pt···Pt-N torsion angle was observed, increasing from 31.3(2)° to 33.4(4)° between ambient conditions and 1.92 GPa. This suggests that the alkyl substitution of the ammonia ligand had reduced the rigidity of the solid-state structure, hence resulting in more compression in the [110] direction and reducing the necessity for compression along the *c* axis direction.

Between 1.61 and 1.92 GPa, the rate of compression in $MagNH_2Me$ along the *c* axis, and thus contraction of the Pt···Pt stacking distance, had almost plateaued (Figure 3.11). Diffraction data were collected at one further pressure point, at 2.34 GPa, at which point the diffraction quality had diminished, and the data could no longer be indexed in the *P*4/*mnc* space group. It was instead determined that a phase transition to the lower symmetry *C*2/*c* space group had occurred *via* an unidentified orthorhombic phase. While the *C*2/*c* structure has not yet been solved, the unit cell parameters alone show that the *c* axis lattice parameter decreased sharply from 6.32 Å to 6.27 Å between 1.96 and 2.34 GPa. Therefore, it appears that the phase transition is a result of forcing the structure beyond the impasse along the *c* axis. Without the structure solution it is unknown what effect the phase transition has had on the Pt···Pt stacking arrangement, however it is predicted, based upon the determined space group, that the Pt···Pt stacking chains are now slightly slanted, which would have an adverse effect on orbital overlap along that direction.

Similar to $Pt(bqd)_2$, $Pt(bqd\text{-}dibutyl)_2$ was studied using high-pressure X-ray diffraction experiments using in-house laboratory[1] and synchrotron diffractometers. However, discrepancies were observed between the two pressure series obtained for $Pt(bqd\text{-}dibutyl)_2$, mostly likely due to poor crystal quality of the sample of

Pt(bqd-dibutyl)$_2$ used for the experiments at the synchrotron. Figure 3.12 shows the compression along all the unit cell parameters across the two pressure series.

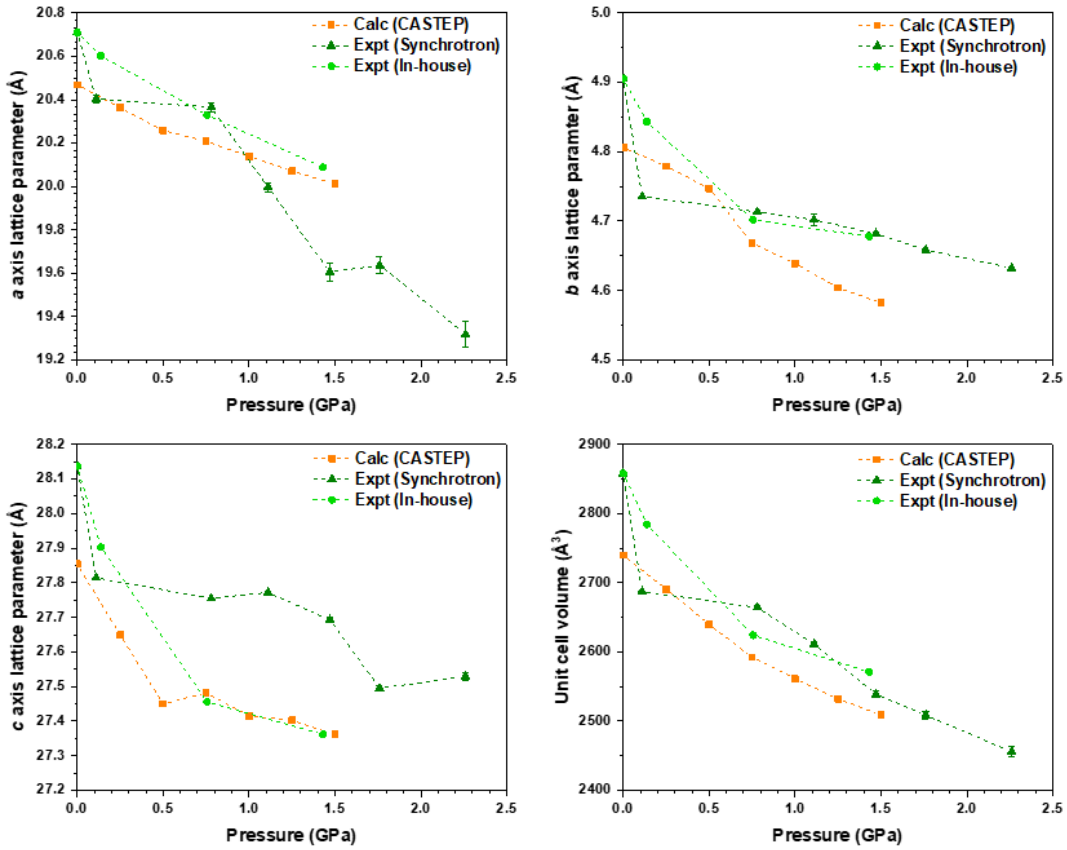

Figure 3.12: Lattice parameters of Pt(bqd-dibutyl)$_2$ across the pressure series collected from in-house diffraction,[1] synchrotron diffraction and computational methods. Error bars show the value of one standard deviation.

Diffraction data and solved structures, all in the *Pna*2$_1$ space group, were obtained for Pt(bqd-dibutyl)$_2$ from the in-house data collections up to 1.43 GPa, after which a reduction in the quality of the diffraction data resulted in no successful indexing or structure solution.[1] Structures were successfully solved for the data from the synchrotron diffraction experiments collected up to 1.76 GPa. Pt(bqd-dibutyl)$_2$ was determined to have remained in the *Pna*2$_1$ space group up to 1.11 GPa, after which indexing and integrating to only the *P*2$_1$ space group was acceptable, indicating that the complex had undergone a phase transition. For the data collected at 1.47, 1.76 and

2.26 GPa the β angle parameter exceeded 93°, with sufficient disparity from the value required for orthorhombic symmetry to justify that a phase transition to the lower symmetry space group had taken place.

Also presented in Figure 3.12 are the calculated unit cell parameters for Pt(bqd-dibutyl)$_2$ under simulated pressures between 0.00 and 1.50 GPa; these calculations were undertaken to help resolve the disparity between the two experimental pressure series. The optimised ambient-pressure structure unit cell volume was *ca.* 4.1% less than that of the experimentally-determined structure, with contribution to the contraction from all unit cell parameters. Across the simulated pressure series, the optimised *a* and *c* axis values fit better with the in-house compression curve than the synchrotron data. A similar result was observed for the computed value of the *b* axis at low pressures, however a larger discrepancy with the experimental values was observed at higher pressure. Since this corresponds to the stacking direction, it could be more prone to over-contraction in the optimisation due to the use of the TS dispersion correction. The volumetric compression curve generated from the output of the CASTEP calculations was generally quite smooth, from which a bulk modulus value of 10.4(8) GPa was determined (Figure 3.13). Therefore, the compressibility of Pt(bqd-dibutyl)$_2$ is statically similar (to 3σ) to that calculated for Pt(bqd)$_2$ but greater than the two Magnus salt complexes.

The majority contribution to the simulated volumetric compression (shown in Figure 3.14) was observed along the *b* axis direction, with 5 % compression between ambient conditions and 1.5 GPa. The Pt···Pt distance decreased from 4.81 Å to 4.58 Å across the simulated pressure series. The compression along the *a* and *c* axis directions was less than 2 % up to 1.50 GPa; compression in these directions appears to be restricted by steric clashing between the *n*-butyl chains. It is possible that the phase transition observed experimentally in the synchrotron pressure series of experiments occurred to facilitate compression along the *a* and *c* axis directions, justified by the sharp decreases observed for these lattice parameters above 1 GPa (Figure 3.12).

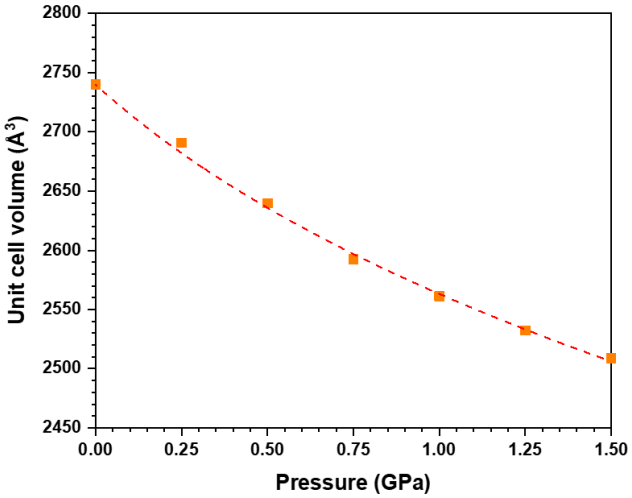

Figure 3.13: Computed unit cell volume across a simulated pressure series for Pt(bqd-dibutyl)$_2$, with the dashed line representing the 3rd-order Birch-Murnaghan equation of state fit.

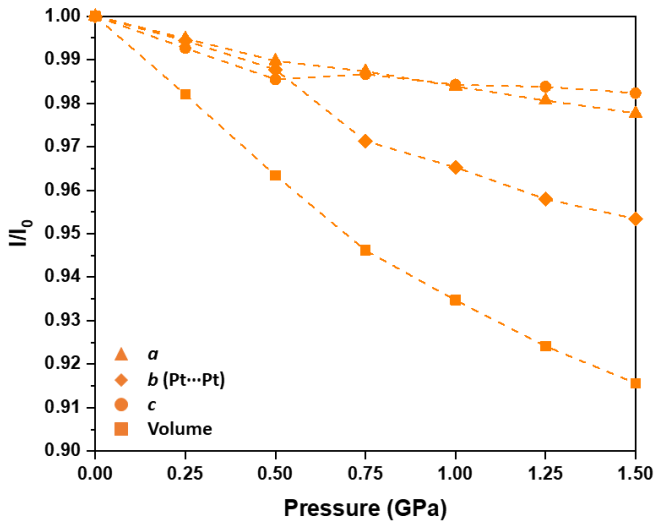

Figure 3.14: Compression curves for the optimised unit cell parameters of Pt(bqd-dibutyl)$_2$, as a fraction of those for the optimised ambient pressure structure throughout the simulated pressure series.

3.5.3: Ambient-pressure solid-state and isolated molecule calculations

In order to interpret the electronic behaviour of all four compounds at ambient pressure, solid-state calculations using a range of pure and hybrid DFT functionals were undertaken. The variety of functionals tested produced a large range of band gap sizes for all four compounds (Table 3.1).

The pure DFT functionals produced the smallest band gaps out of all the functionals tested, with values of less than 0.2 eV obtained for $Pt(bqd)_2$ and the MGS compounds (< 0.2 eV). Thus, the pure DFT functionals predict that these compounds are already in, or close to, the metallic state at ambient conditions; this is contrary to reports in the literature,[22, 29, 30] and highlights the well-documented observation that pure DFT methods underestimate band gap sizes due to the underlying problems with the approximation of electron exchange.[66, 71, 72] On the other hand, the hybrid DFT functionals calculated significantly larger band gap values, in the consistent order of HSE06 < B3LYP < PBE0. All results discussed hereafter will utilise the calculation outputs from the HSE06 functional, unless otherwise stated, due to its known reliability in the literature for estimating band gap sizes.[58, 73]

Table 3.1: Comparison of the ambient pressure band gap sizes obtained from atom-only geometry optimised solid-state calculations for each compound using the range of functionals. Functionals displayed in italics represent pure DFT functionals. *BLYP was used to allow comparison to the previous 1-D study undertaken by Kim and co-workers (2006).[32]

Complex	Functional	Band Gap (eV)
$Pt(bqd)_2$	*PBE*	*0.00*
	B3PW	0.76
	B3LYP	0.79
	HSE06	0.52
	PBE0	1.02
$Pt(bqd\text{-}dibutyl)_2$	*PBE*	*0.52*
	B3LYP	1.48
	HSE06	1.17
	PBE0	1.73
$MagNH_3$	*PBE*	*0.03*
	*BYLP**	*0.00*
	B3LYP	1.72
	HSE06	1.56
	PBE0	2.30
$MagNH_2Me$	*PBE*	*0.15*
	B3LYP	1.85
	HSE06	1.71
	PBE0	2.44

The full electronic band structure of $Pt(bqd)_2$ (shown in Figure 3.15) shows an indirect band gap (X⟶Γ) of 0.52 eV, comparable to the values obtained in the literature (0.25-0.84 eV).[23, 74] Along directions Γ⟶T, W⟶R and Γ⟶X the valence and conduction bands are relatively flat, indicating weak intermolecular interactions, corresponding to paths within the crystallographic layers (i.e. in the *ab* plane). By contrast, the dispersion is significant in the T⟶W and R⟶Γ directions in both frontier bands, indicating stronger interlayer interactions.

The projected density of states (PDOS) and crystalline orbital Hamilton population (COHP) plots are also displayed in Figure 3.15 to provide descriptions of the bands of interest. The former breaks down the contribution to the total density of states for each band from each atom type, whereas the COHP plot combines the density of states and Hamilton population to provide an indication to the strength of interactions between specified atom types. By convention, the COHP plot is plotted using –COHP values, so that bonding and antibonding interactions in each band are represented by positive and negative values, respectively.

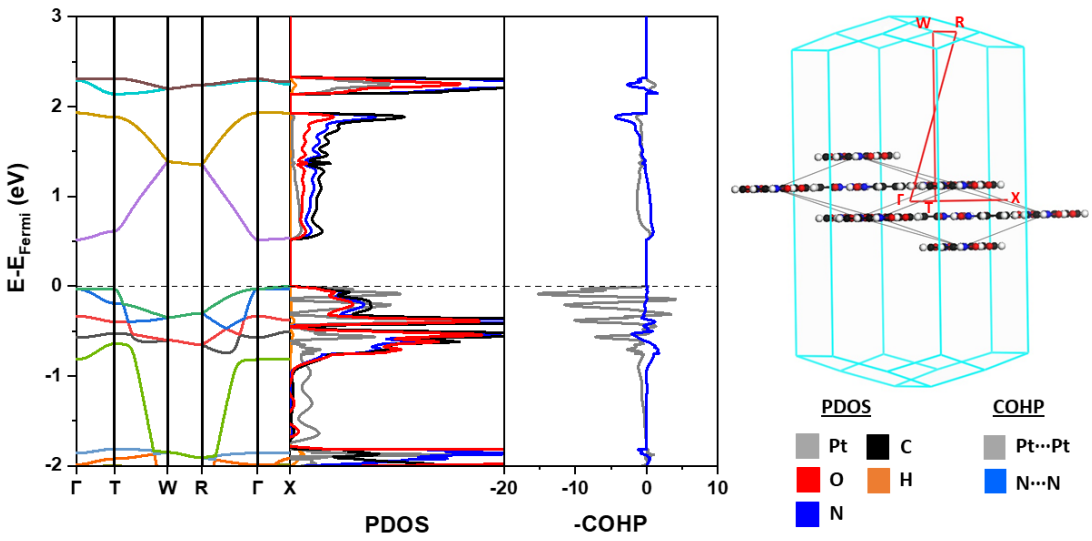

Figure 3.15: LEFT: Electronic band structure, projected density of states (PDOS) and COHP plot of the ambient pressure structure of $Pt(bqd)_2$ (E_{Fermi} = -4.95 eV). The PDOS are coloured to signify the different atomic contributions. The COHP plot is coloured to signify the different interlayer interactions. RIGHT: Reciprocal and real-space lattice of $Pt(bqd)_2$ with outlined Brillouin zone k-point path and k-point positions utilised for electronic band structure generation.

The PDOS indicates that the top of the valence band possesses a mixture of metal and ligand character, while the contribution to the bottom of the conduction band is mainly from ligand orbitals, with only a small contribution from Pt. The COHP plot shows that the top of the valence band is dominated by antibonding interlayer Pt···Pt interactions, whereas the delocalisation of the bottom of the conduction is derived from bonding interlayer N···N interactions and Pt···Pt interactions, both of which switch to antibonding in nature in the LUCO+1 band.

The solid-state calculations were also used to provide a visualisation of crystalline orbitals (COs) of interest; specific orbitals are shown in Figure 3.16. The visualisations and the naming scheme for each orbital are taken from the band ordering at the Γ k-point, the only part of the Brillouin zone for which an interpretation of these bands without an imaginary component can be obtained. However, this ordering does not correctly illustrate the band gap shown in Figure 3.15. Due to its indirect (X⟶Γ) nature, the band gap is actually between the HOCO–1 and LUCO bands. The HOCO–1 consists mainly of the antibonding combination of d_{z^2} orbitals between the Pt centres, with a small contribution from p-orbitals on the ligand. The HOCO consists of antibonding intramolecular interactions between the ligand p_z and Pt $d_{xz/yz}$ orbitals. The LUCO is similar to the HOCO, with the exception of a contribution from the Pt centre coming from its p_z atomic orbital, while the orientation of the neighbouring molecules down the *c* axis appears to facilitate interlayer bonding Pt···Pt and N···N interactions. The visualised frontier orbitals are therefore in agreement with the earlier assignments from the literature and the PDOS/COHP descriptions,[5,11,12] but with the caveat that the direct ligand contribution to interlayer interactions had not been previously identified.

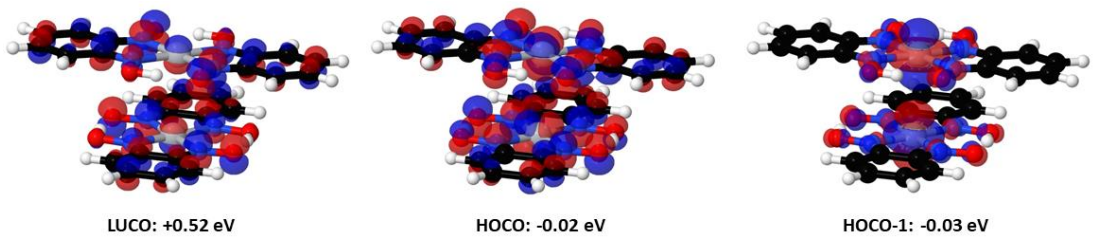

Figure 3.16: Visualisation and Fermi level adjusted energies, at the Γ k-point, of specified crystalline orbitals calculated for the ambient pressure solid-state structure of Pt(bqd)$_2$. Atoms are coloured: Pt, grey; O, red; N, blue; C, black; H, white.

The electronic band structure for Pt(bqd-dibutyl)$_2$ is presented in Figure 3.17. For this optimised ambient-pressure structure, an indirect (U⟶Γ) band gap of 1.17 eV was calculated, and the electronic band structure differs greatly from that calculated for Pt(bqd)$_2$ in that the frontier bands are much more localised (as evident by the lack of k-dependency on band energy). An exception to this is the weak dispersion in the Y⟶S portion of the k-point path for some of the bands, corresponding to the Pt···Pt stacking along the *b* axis direction.

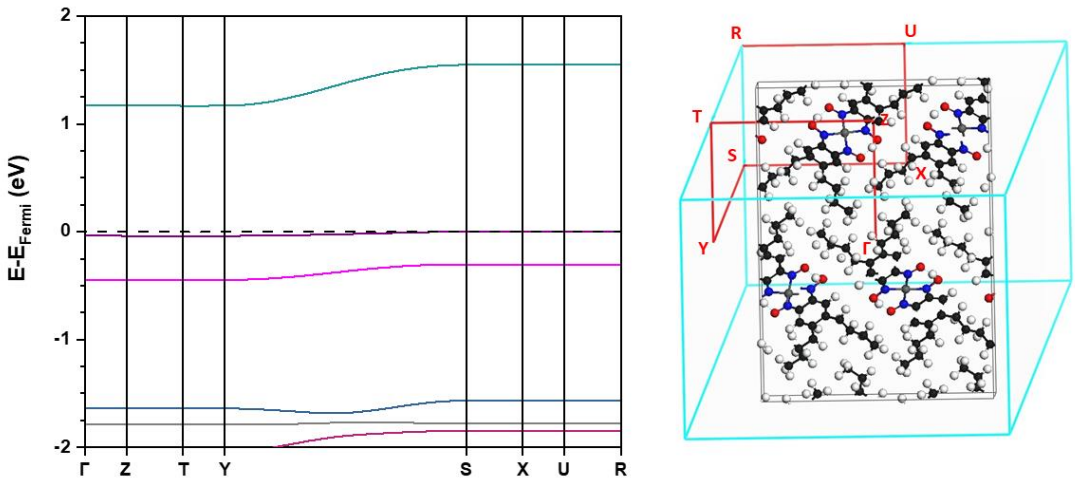

Figure 3.17: Electronic band structure (E_{Fermi} = -4.99 eV) (LEFT) and k-point path (RIGHT) of the ambient pressure structure of Pt(bqd-dibutyl)$_2$.

Specific frontier band COs for Pt(bqd-dibutyl)$_2$ are shown in Figure 3.18. The HOCO depicts an antibonding interaction between the $d_{xz/yz}$ orbitals on the Pt centre and the p_z orbitals on the ligand backbone, similar to that seen in the HOCO of Pt(bqd)$_2$. The

visualised LUCO is also equivalent to that seen for $Pt(bqd)_2$. Also shown in Figure 3.18 is the HOCO-2 orbital, primarily consisting of the Pt d_{z^2} orbital synonymous with the HOCO-1 of $Pt(bqd)_2$ but considerably lower in energy. The Pt d_{z^2} atomic orbital in the HOCO-2 is noticeably tilted away from the plane of the molecule backbone, indicating that there is some interaction between neighbouring molecules along the *b* axis direction.

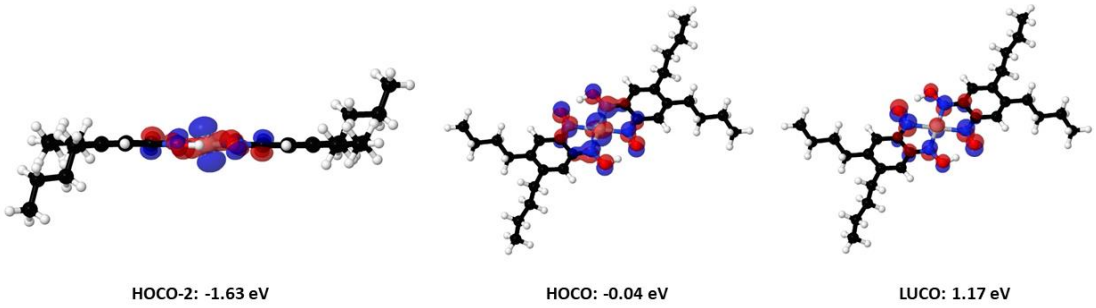

Figure 3.18: Selected CO diagrams from the solid-state calculations on $Pt(bqd\text{-}dibutyl)_2$, with the Fermi-adjusted energies of each orbital at the Γ k-point. Atoms are coloured: Pt, grey; N, blue, O; red, C, black; H, white.

The different order of the COs, and hence nature of the frontier bands, between $Pt(bqd)_2$ and $Pt(bqd\text{-}dibutyl)_2$ is a point that needs further clarification. Thus, isolated molecule calculations on both compounds were undertaken to describe the nature and ordering of molecular orbitals (MOs), and elucidate how the COs are formed from combination of MOs between neighbouring molecules. Figure 3.19 shows a selection of MOs from the isolated molecule calculations on both $Pt(bqd)_2$ and $Pt(bqd\text{-}dibutyl)_2$ which will form the focus of discussion, alongside Figures 3.20 and 3.21 which shows the relationship between the MOs and COs of each compound.

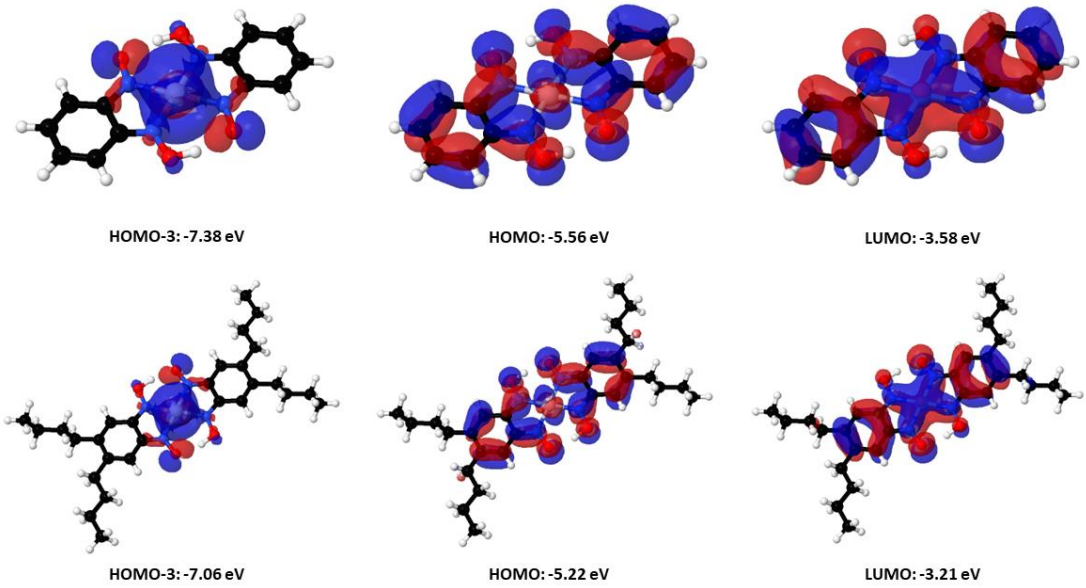

Figure 3.19: Visualisations and absolute energies of certain molecular orbitals for Pt(bqd)$_2$ (top row) and Pt(bqd-dibutyl)$_2$ (bottom row) obtained from isolated molecule calculations. Atoms are coloured: Pt, grey; O, red; N, blue; C, black; H, white.

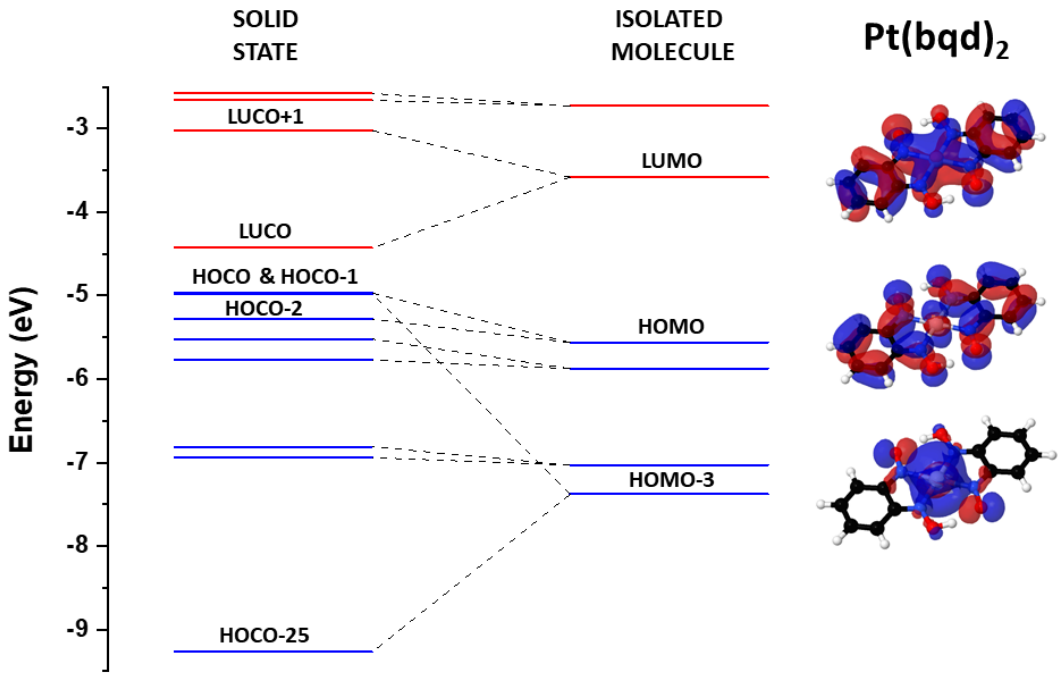

Figure 3.20: Energies of selected isolated molecule molecular orbitals (from Gaussian09 calculations) (isocontour value of 0.02) in Pt(bqd)$_2$ and the crystalline orbitals (from CRYSTAL17 calculations) they contribute to in the solid state. The absolute energies of the crystalline orbitals are shown at the Γ point, with the orbitals between HOCO-6 and HOCO-25 omitted for clarity. Occupied orbitals/bands are shown in blue, unoccupied orbitals/bands in red.

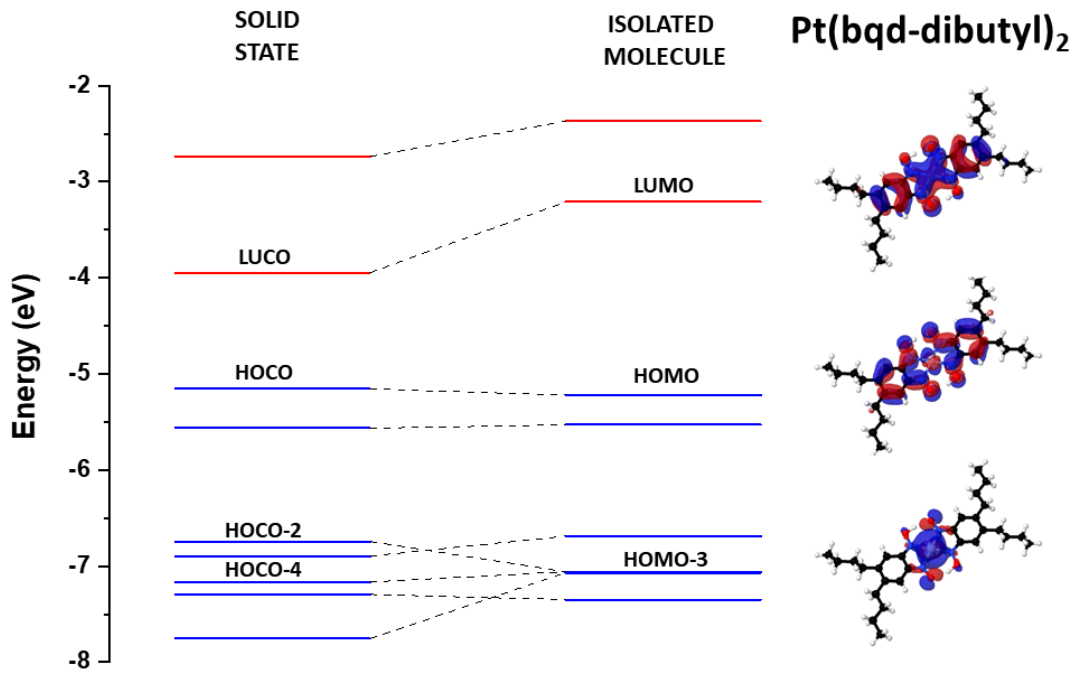

Figure 3.21: Energies of selected isolated molecule molecular orbitals (from Gaussian09) (isocontour value of 0.02) in Pt(bqd-dibutyl)$_2$ and the crystalline orbitals (from CRYSTAL17 calculations) they contribute to in the solid state. The absolute energies of the crystalline orbitals are shown at the Γ point. Occupied orbitals/bands are shown in blue, unoccupied orbitals/bands in red.

The isolated molecule calculations have shown that the nature of the frontier MOs are very similar between the two compounds, with the majority of the orbital descriptions being confined to the ligand backbone and hence the ligand modification has had a negligible effect. The HOMOs consist of π^* interactions between the Pt $d_{xz/yz}$ and ligand p_z orbitals, synonymous with the HOCO for both compounds; the nature of this orbital does not seem to facilitate any intermolecular interaction and hence its energy is not greatly affected by the solid-state packing. The HOMO-3 for Pt(bqd)$_2$ and Pt(bqd-dibutyl)$_2$, consisting mainly of the atomic Pt d_{z^2} orbitals for both compounds, sit around 1.8 eV below the HOMO. In Pt(bqd)$_2$, the stacking of the metal centres in the solid state causes strong σ interactions between the HOMO-3 on neighbouring molecules; the bonding combination results in the low lying HOCO-25, whereas the antibonding combination results in the HOCO-1 similar in energy to the HOCO. The solid-state packing in Pt(bqd-dibutyl)$_2$, on the other hand, results in less

direct orbital overlap between the Pt centres stacked along the *b* axis, and hence the interactions along this direction are incredibly weak. The bonding and antibonding combinations of neighbouring HOMO-3 orbitals result in the HOCO-4 and HOCO-2, with the latter over 1.6 eV away from the HOCO. The LUMO for both compounds consists of π interactions between the metal and ligand p_z orbitals, with antibonding nodes throughout the ligand backbone. Therefore, the alignment of the p_z orbitals between stacked Pt centres in $Pt(bqd)_2$ causes a bonding and antibonding combination, which forms the LUCO and LUCO+1 respectively; the energy difference between these orbitals is relatively small (1.4 eV), due to presence of bonding intermolecular N···N interactions regardless of the Pt···Pt combination. This interaction is weaker than that seen for the combination of the Pt d_{z^2} orbitals, but it is still sufficient to form a relatively delocalised LUCO band. In $Pt(bqd\text{-}dibutyl)_2$, the interaction between the between neighbouring LUMO orbitals is very weak, and can only be contributed to overlap between the slipped ligand backbones; therefore, there is little energy difference between the LUMO and LUCO, thus resulting in a much larger band gap than observed for $Pt(bqd)_2$.

Due to the similar ordering of the molecular orbitals, it could be mistaken that $Pt(bqd)_2$ and $Pt(bqd\text{-}dibutyl)_2$ would have similar electronic properties, especially since the ligand modification does not contribute to the frontier orbitals. However, the nature of the solid-state packing, and hence how the MOs are able to combine to form COs, greatly influences the ordering of orbitals and extent of delocalisation within the solid-state electronic band structure. This results in $Pt(bqd\text{-}dibutyl)_2$ having an ambient-pressure band gap of over twice that of $Pt(bqd)_2$, with very little electronic communication from the frontier bands.

The complete electronic band structure obtained for the ambient structure of $MagNH_3$ (Figure 3.22) revealed a band gap measuring 1.57 eV, larger than that obtained from the previous pure DFT study reported for the 1-D $MagNH_3$ model (*ca.* 1 eV)[33] and that

calculated for $Pt(bqd)_2$ (0.5 eV). The top of the valence band is highly variable along the Γ⟶Z, A→M and R→X portions of the k-point path, representing the Pt···Pt stacking direction. The band flattens along the other parts of the k-point path, reflecting the lack of inter-column interaction associated with this band in the *a*/*b* axes directions. The bottom of the conduction band is mostly k-invariant in its entirety, which suggests it consists of a more localised orbital and is thus unaffected by interactions from neighbouring molecules in all directions throughout the unit cell.

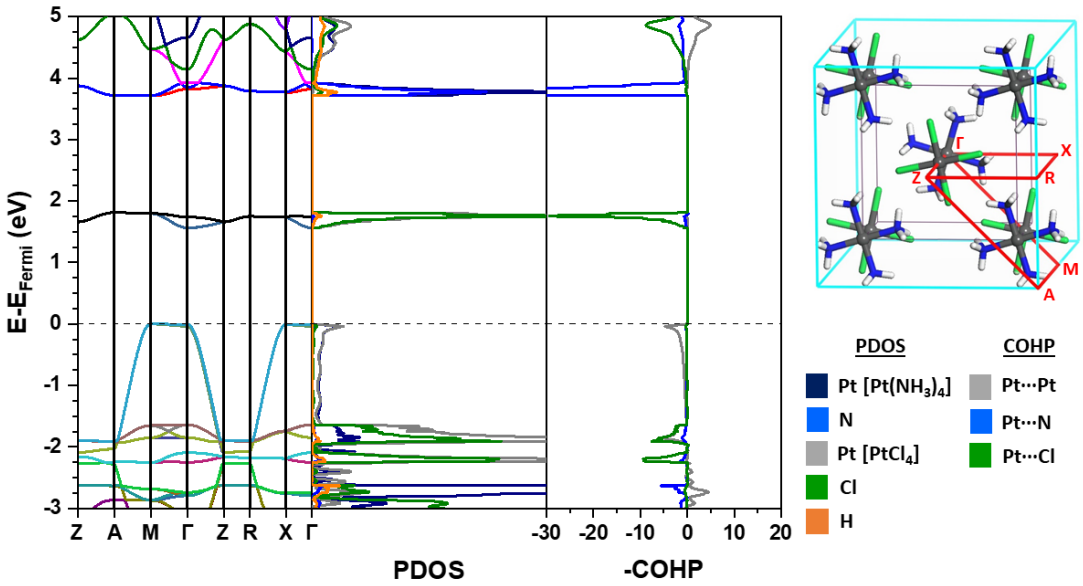

Figure 3.22: LEFT: Electronic band structure, projected density of states (PDOS) and COOP plot of the ambient pressure structure of $MagNH_3$ (E_{Fermi} = -4.85 eV). The PDOS are coloured to signify the contribution from different fragments of the compound and the COHP plot is coloured to signify different interactions throughout the solid-state structure. RIGHT: Real space (grey) and reciprocal (light blue) lattices of $MagNH_3$, with the Brillouin zone path used in the electronic band structure coloured in red.

The PDOS and COHP plots showed that the contribution to the top of the valence band is mainly from an antibonding interaction between the Pt atoms on each salt component, whereas the bottom of the conduction band consists of antibonding interactions between the atoms exclusively in the $[PtCl_4]^{2-}$ component. A closer look at the COHP in the region at the bottom of the conduction band revealed a weak

antibonding Pt···N interaction on the $[Pt(NH_3)_4]^{2+}$ component and an even weaker intra-chain bonding Pt···Pt interaction.

A visualisation of the frontier COs (Figure 3.23) showed good agreement with the PDOS and COHP descriptions and those already revealed in the pure DFT study on the 1-D $MagNH_3$ model, indicating that the change in functional has not caused any unexpected band reordering.[33] In a similar manner to $Pt(bqd)_2$ and $Pt(bqd\text{-}dibutyl)_2$, the MOs of a single dimer of $MagNH_3$ (Figure 3.24) were calculated to elucidate their contribution to the COs upon the formation of the infinite salt chains in the solid state (Figure 3.25). The optimisation of the isolated $[Pt(NH_3)_4][PtCl_4]$ dimer resulted in a slight distortion from the square-planar geometry of both units, with the trans ∠N-Pt-N and ∠Cl-Pt-Cl angles decreasing to 172.6° and 175.0° respectively. Furthermore, the Pt···Pt distance had decreased to 3.00 Å and the N-Pt···Pt-Cl torsion angle had widened to -42.4°, facilitating a shorter (2.3 Å) N-H···Cl contact.

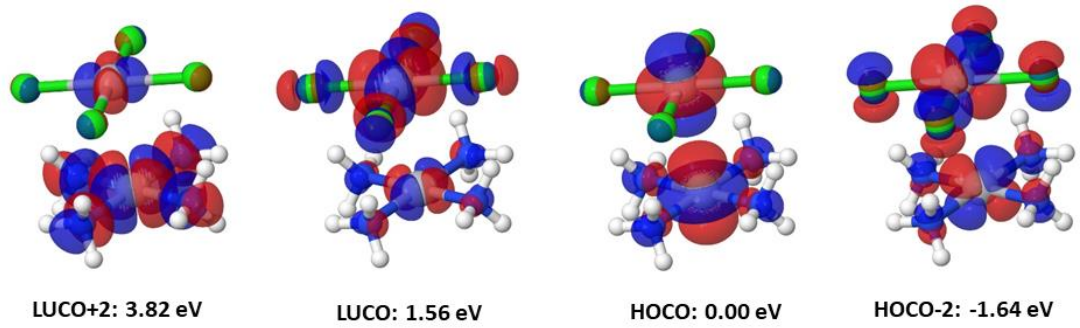

Figure 3.23: Selected crystalline orbitals of $MagNH_3$, with their respective Fermi level adjusted energies obtained at the Γ k-point. Atoms are coloured: Pt (grey), Cl (green), N (blue), H (white).

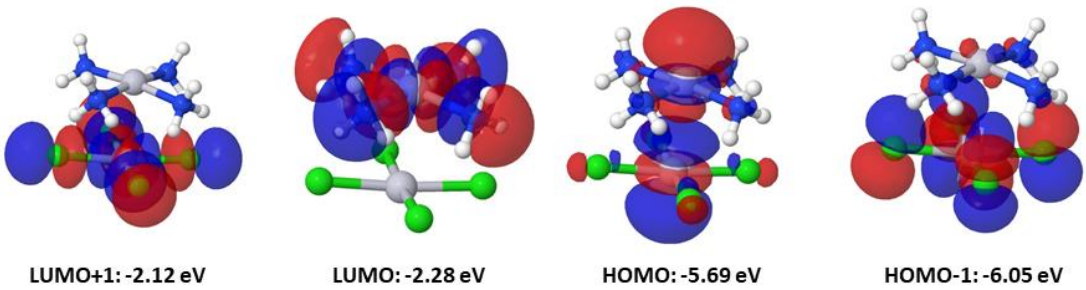

Figure 3.24: Selected molecular orbitals of $MagNH_3$, with their respective Fermi level adjusted energies obtained at the Γ k-point. Atoms are coloured: Pt (grey), Cl (green), N (blue), H (white).

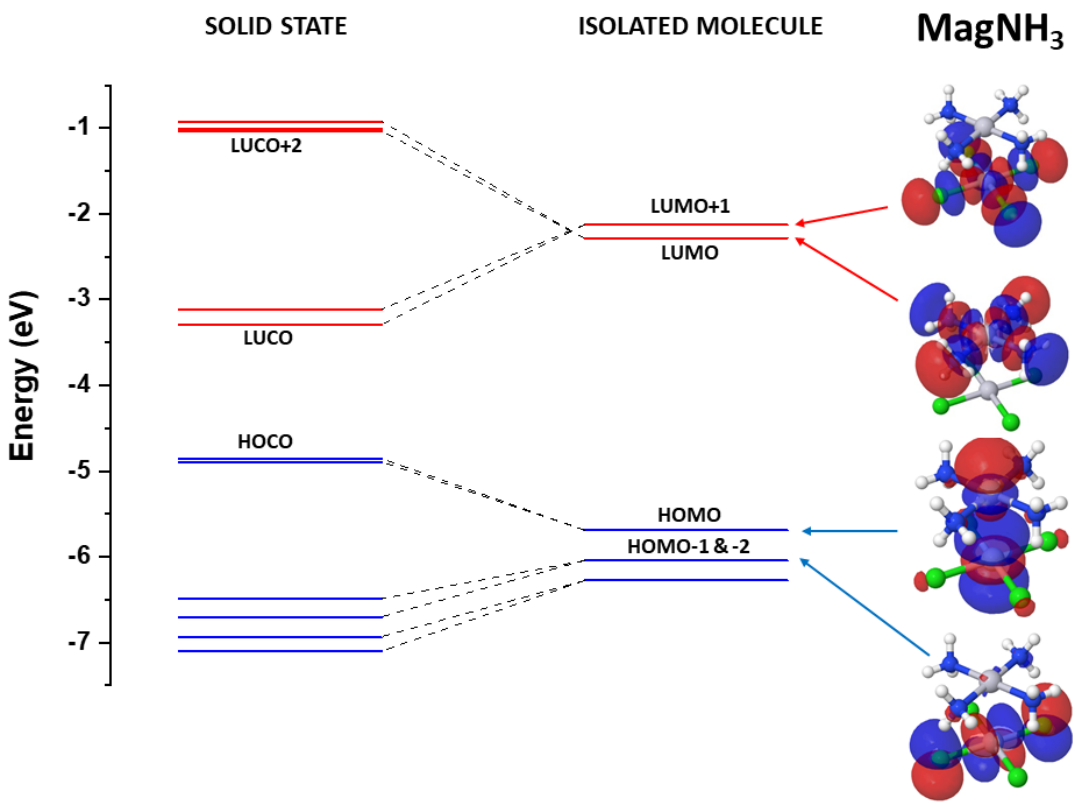

Figure 3.25: Absolute energies of selected isolated molecule molecular orbitals (from Gaussian09 calculations) (isocontour value of 0.02) in $MagNH_3$ and crystalline orbitals (from CRYSTAL17 calculations). The absolute energies of the crystalline orbitals are shown at the Γ k-point. Occupied orbitals/bands are shown in blue, unoccupied orbitals/bands in red.

From Figure 3.25, it is evident that, unlike $Pt(bqd)_2$, the construction of the COs from MOs did not result in a substantial reordering of the orbital hierarchy because the chains in the solid state are just an extended form of the single $[Pt(NH_3)_4][PtCl_4]$ component with two Pt centres. The HOMO orbital of $MagNH_3$ is therefore already attributed to the overlap between d_{z^2} orbitals on neighbouring Pt atoms, responsible for constructing the essentially degenerate HOCO and HOCO-1 bands in the solid state. Similarly, the degenerate HOMO-1 and HOMO-2 orbitals, representing the π* interaction between Pt $d_{xz/yz}$ and Cl p_z orbitals, form the HOCO-2 to HOCO-5 bands in the solid state. The LUMO and LUMO+1 orbitals consist of the σ* interaction isolated to the $[Pt(NH_3)_4]^{2+}$ and $[PtCl_4]^{2-}$ components respectively, which swap order in the solid state. Attempts have been made to attribute this switch in order of these orbitals to a change in the calculated Pt-N and Pt-Cl bond lengths or the atomic

contribution to the orbitals in both the isolated molecule and solid states, with the latter shown in Table 3.2. The change in bond lengths between the optimised isolated molecule and solid-state structures, however, was minimal, calculated as +0.037 Å and +0.006 Å for Pt-N and Pt-Cl respectively. While the correct trends in the change of atomic contributions from the isolated molecule to the solid state were seen for both interactions, namely an increase in total contribution from Pt and N for the Pt-N σ* interaction thus equating to a destabilisation of the orbital and vice versa for the Pt-Cl σ* interaction, the change in values is fairly minimal. Therefore, the energy difference between the orbitals calculated for the isolated molecule and solid-state models is more likely due to differences between the functional and basis sets employed for each model.

Table 3.2: Atomic contribution to the orbitals representing the Pt-N and Pt-Cl σ* interactions for the optimised dimer (from the isolated molecule calculation) and the solid-state calculations on $MagNH_3$, and the resulting % difference.

Atom Type	Pt-N σ* interaction (LUMO→LUCO+2)			Pt-Cl σ* interaction (LUMO+1→LUCO)		
	Isolated Dimer	Solid state	Difference	Isolated Dimer	Solid State	Difference
Pt in $[Pt(NH_3)_4]^{2+}$	**55.2 %**	**53.3 %**	**-1.9 %**	0.3 %	1.0 %	+0.7 %
Pt in $[PtCl_4]^{2-}$	0.3 %	0.2 %	-0.1 %	**49.1 %**	**52.9 %**	**+3.8 %**
N	**35.0 %**	**37.8 %**	**+2.8 %**	0.1 %	0.4 %	+0.3 %
Cl	0.2 %	2.5%	+2.3 %	**50.2 %**	**42.5 %**	**-7.7 %**
H	9.2 %	6.3 %	-2.9 %	0.3 %	3.1 %	+2.8 %

The ambient pressure electronic band structure, PDOS and COHP plots, and hence description of the frontier orbitals, for $MagNH_2Me$ (shown in Figures 3.26 and 3.27) showed a strong similarity with those already discussed for $MagNH_3$, with the exception of a slightly larger band gap, measuring 1.71 eV. A close examination of the COHP plot showed a weak antibonding Pt···Pt interaction in the region of the band associated with the LUCO, differing slightly from that observed for $MagNH_3$. However, it is apparent that the modest ligand modification was not significant

enough to alter the ordering of the bands close to the band gap, matching the prediction in the previous computational study that an alkyl substitution of the ammonia ligand would not alter the conduction band.[33]

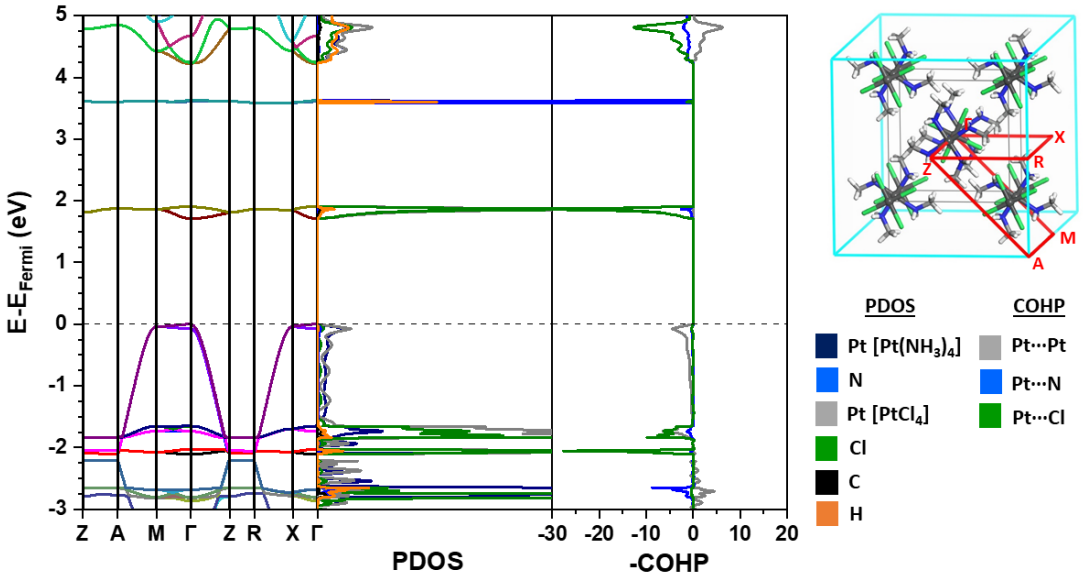

Figure 3.26: LEFT: Electronic band structure, projected density of states (PDOS) and COOP plot of the ambient pressure structure of MagNH$_2$Me (E$_{Fermi}$ = -4.63 eV). The PDOS are coloured to signify the contribution from different fragments of the compound and the COHP plot is coloured to signify different interactions throughout the solid-state structure. RIGHT: Real space (grey) and reciprocal (light blue) lattices of MagNH$_3$, with the Brillouin zone path used in the electronic band structure coloured in red.

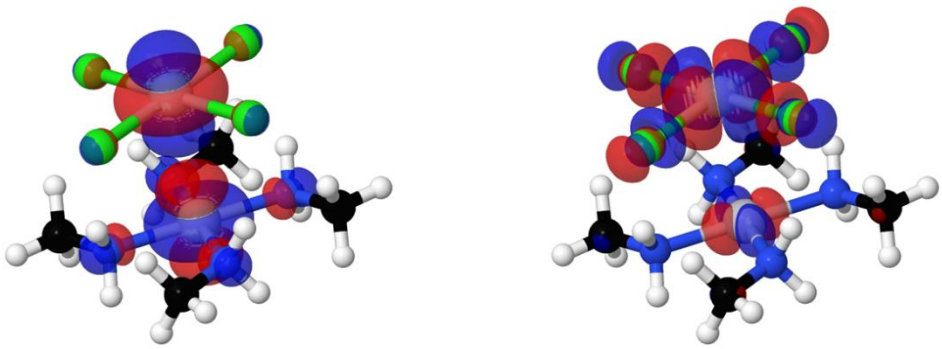

Figure 3.27: Highest occupied (left) and lowest unoccupied (right) crystalline orbitals of MagNH$_2$Me, with their respective Fermi level adjusted energies obtained at the Γ k-point. Atoms are coloured: Pt(grey), Cl (green), N (blue), C (black), H (white).

3.5.4: High-pressure solid-state calculations

The solid-state calculations were repeated for each compound at every pressure point throughout their respective pressure series, in order to examine any changes to the band structures, and thus band gaps, and hence provide a theoretical understanding of the electronic response to the application of pressure. Figure 3.28 shows the change in the energies of the HOCO and LUCO bands, and thus the band gap value, for $Pt(bqd)_2$, while Figures 3.29 and 3.30 show the electronic band structure, PDOS and COHP plots for $Pt(bqd)_2$ at 1.03 GPa and 2.38 GPa respectively. The trend in both the HOCO and LUCO energies in Figure 3.28 might seem to contradict to what is observed in the band structures, with the latter seemingly only showing a change in the LUCO energy. However, it should be noted that Figure 3.28 shows the absolute band energy values, whereas in the band structures the energies of the bands have been adjusted by the value of the Fermi energy so that the highest energy point of the HOCO always sits at 0 eV which masks any change in the HOCO energy.

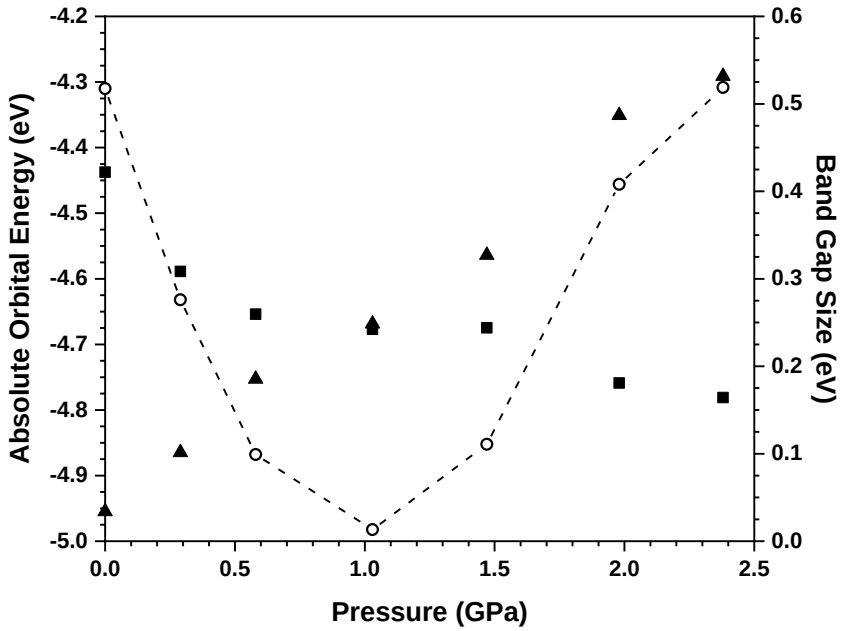

Figure 3.28: Left ordinate: absolute energies of the HOCO (triangle) and LUCO (square) of $Pt(bqd)_2$, as defined in the ambient pressure structure (Figure 3.15), across the pressure series. Right ordinate: corresponding band gap energies (open circles), calculated by the HOCO-LUCO energy difference.

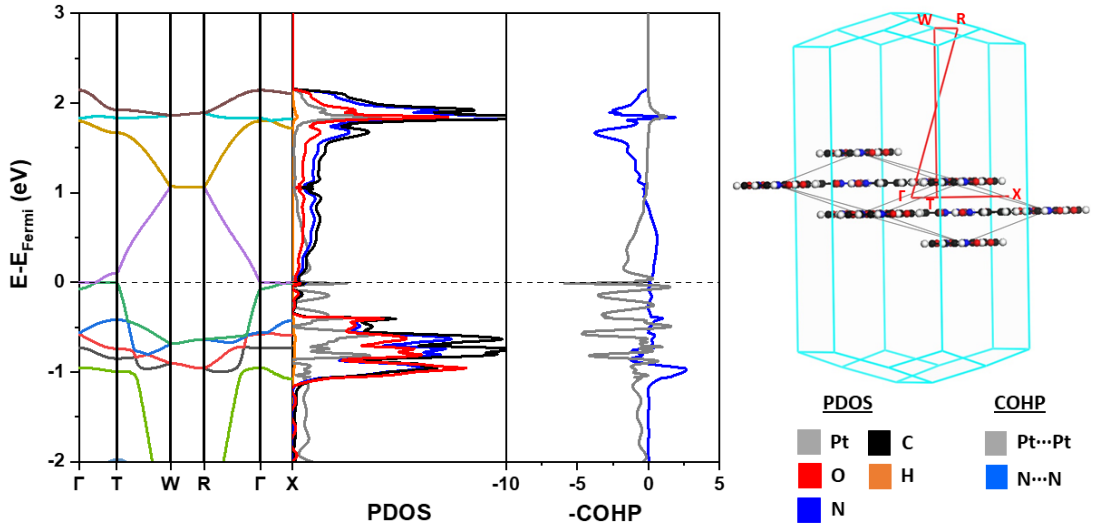

Figure 3.29: LEFT: Computed band structure, PDOS, broken down onto atomic contributions, and the COHP plot showing Pt···Pt interaction and interlayer N···N interaction for Pt(bqd)$_2$ at 1.03 GPa. (E_{Fermi} = -4.67 eV). RIGHT: Real space (grey) and reciprocal (light blue) lattices of Pt(bqd)$_2$, with the Brillouin zone path used in the electronic band structure coloured in red.

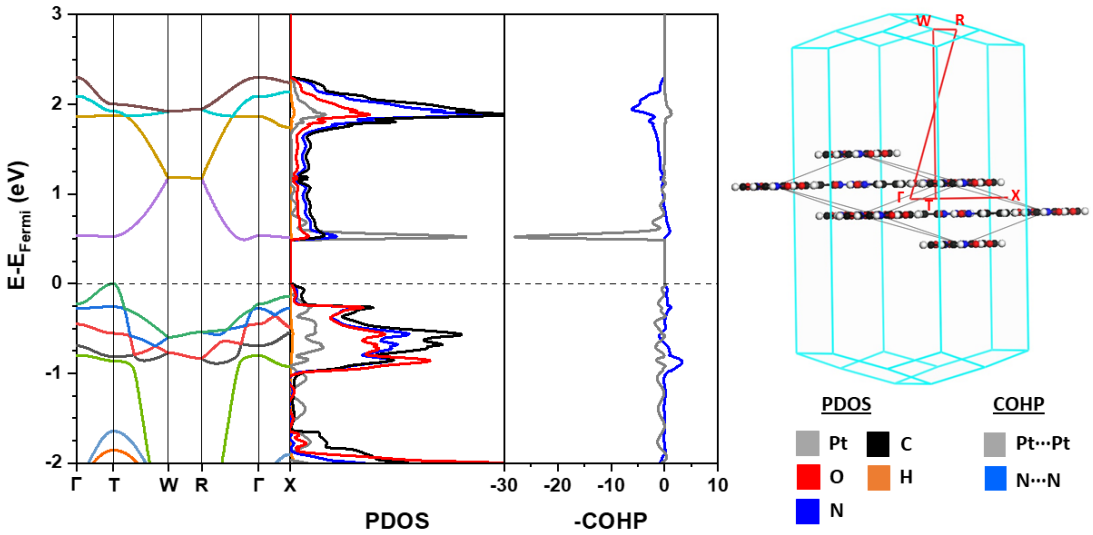

Figure 3.30: LEFT: Computed band structure, PDOS, broken down onto atomic contributions, and the COHP plot showing Pt···Pt interaction and interlayer N···N interaction for Pt(bqd)$_2$ at 2.38 GPa (E_{Fermi} = -4.78 eV). RIGHT: Real space (grey) and reciprocal (light blue) lattices of Pt(bqd)$_2$, with the Brillouin zone path used in the electronic band structure coloured in red.

The band gap of Pt(bqd)$_2$ decreased up to 1 GPa, by which point the band gap had almost completely closed and the metallic state had formed. The contribution to the closure of the band gap was from both of the frontier orbitals responding to compression along the *c* axis direction; the HOCO continuously destabilised due to

the strengthening antibonding interlayer Pt···Pt interaction whereas the LUCO band stabilised due the strengthening of the bonding interlayer N···N and Pt···Pt interactions. After 1 GPa, due to further compression of the Pt···Pt stacking distance, the HOCO and LUCO bands continued to destabilise and stabilise respectively. As a result, the band gap for $Pt(bqd)_2$ reopened, increasing to just over 0.5 eV by the final pressure point of 2.38 GPa. This trend in band gap size across the pressure series matches, and hence explains, the experimental resistivity behaviour in which minimum resistivity was observed at around 1 GPa, with resistivity increasing with increasing pressures thereafter.[29]

Analysed in a similar manner, the absolute energies of the HOCO and LUCO bands, and hence the resulting band gap, across the pressure series for both $MagNH_3$ and $MagNH_2Me$ are presented in Figure 3.31. Just by considering the ambient pressure points, it is evident that the separation between the LUCO energies for the two compounds is larger than expected, given the separation between the HOCO energies. This larger LUCO separation is caused by the combination of the stabilisation of the $MagNH_3$ LUCO by the weakly bonding Pt···Pt interaction and the destabilisation of the $MagNH_2Me$ LUCO by the weakly antibonding Pt···Pt interaction (Figure 3.32) as discussed briefly in the previous section, hence resulting in a slightly larger band gap for $MagNH_2Me$. The nature of these interactions are revealed through the COHP plots for the LUCO band for the optimised ambient-pressure structure of both compounds, represented by the emboldened lines in Figure 3.32.

Throughout the majority of their respective series the band gap for both complexes were observed to close gradually, facilitated almost exclusively by the destabilisation of the HOCO band (Figure 3.31). The LUCO band energy is almost immune in its response to pressure, only varying slightly due to the strengthening of the weak Pt···Pt interactions, caused by compression along the *c* axis direction; the series of overlaid COHP plots for the LUCO and LUCO+1 bands in Figure 3.32 show how the

bonding and antibonding nature of the Pt···Pt interactions in $MagNH_3$ and $MagNH_2Me$ respectively are moderately enhanced throughout the pressure series.

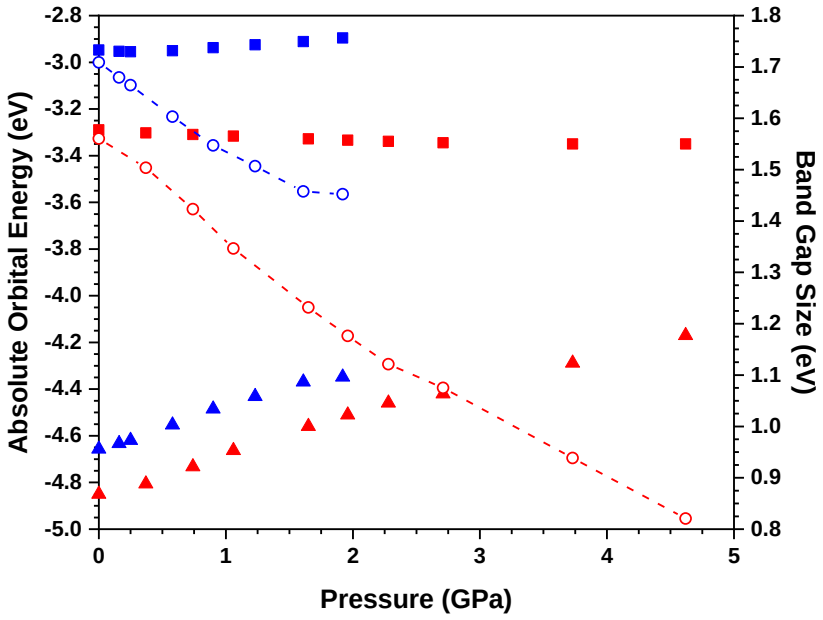

Figure 3.31: Left ordinate: absolute energies of the HOCO (triangle) and LUCO (square) of $MagNH_3$ (red) and $MagNH_2Me$ (blue), across the pressure series. Right ordinate: variation in band gap (open circles) with pressure defined as the difference between the HOCO and LUCO energies.

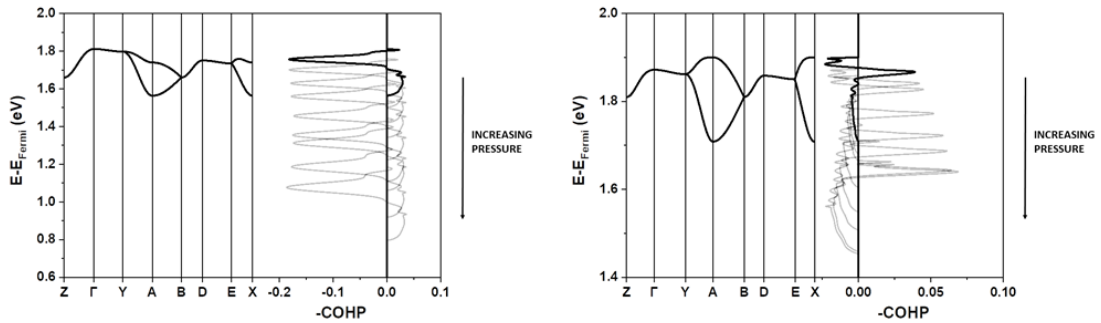

Figure 3.32: Variation in COHP plots for the intra-chain Pt···Pt interaction in the LUCO and LUCO+1 throughout the pressure series for $MagNH_3$ (left) and $MagNH_2Me$ (right), with the ambient pressure positions of the LUCO and LUCO+1 bands shown for reference. The emboldened line in the COHP plot represents the interaction for the LUCO and LUCO+1 bands in the ambient pressure structure, while the grey lines show how the COHP plot changes throughout the pressure series.

By 4.62 GPa, the band gap for $MagNH_3$ had decreased to 0.82 eV, with the electronic band structure, PDOS and COHP plots (shown in Figure 3.33) indicating no

significant changes in the band ordering or band description compared to that observed at ambient conditions (Figure 3.22). The band gap for $MagNH_2Me$ had decreased gradually to 1.46 eV at 1.61 GPa, at a slightly slower rate than that observed for $MagNH_3$ due to the lower anisotropy of the volumetric compression. However, after 1.61 GPa, the band gap compression almost complete plateaued, attributed to the minimal *c* axis compression above 1.61 GPa, prior to the phase transition occurring. Similar to $MagNH_3$, the electronic band structure of $MagNH_2Me$ at 1.92 GPa (Figure 3.34) showed no significant changes to that observed at ambient conditions.

Since a solved structure for the *C*2/*c* phase of $MagNH_2Me$ was not obtained, the electronic band structure after the phase transition has not been computed, and hence the effect of the phase transition on the electronic properties is not yet known.

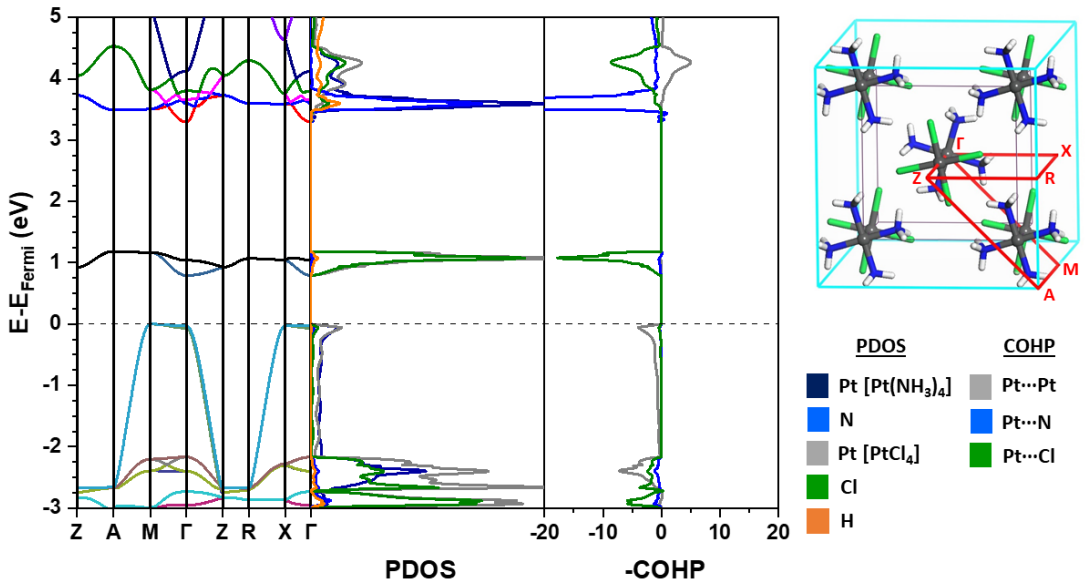

Figure 3.33: LEFT: Electronic band structure, projected density of states (PDOS) and COHP plot of the 4.62 GPa structure of $MagNH_3$ (E_{Fermi} = -4.14 eV). RIGHT: Real space (grey) and reciprocal (light blue) lattices of $MagNH_3$, with the Brillouin zone path used in the electronic band structure coloured in red.

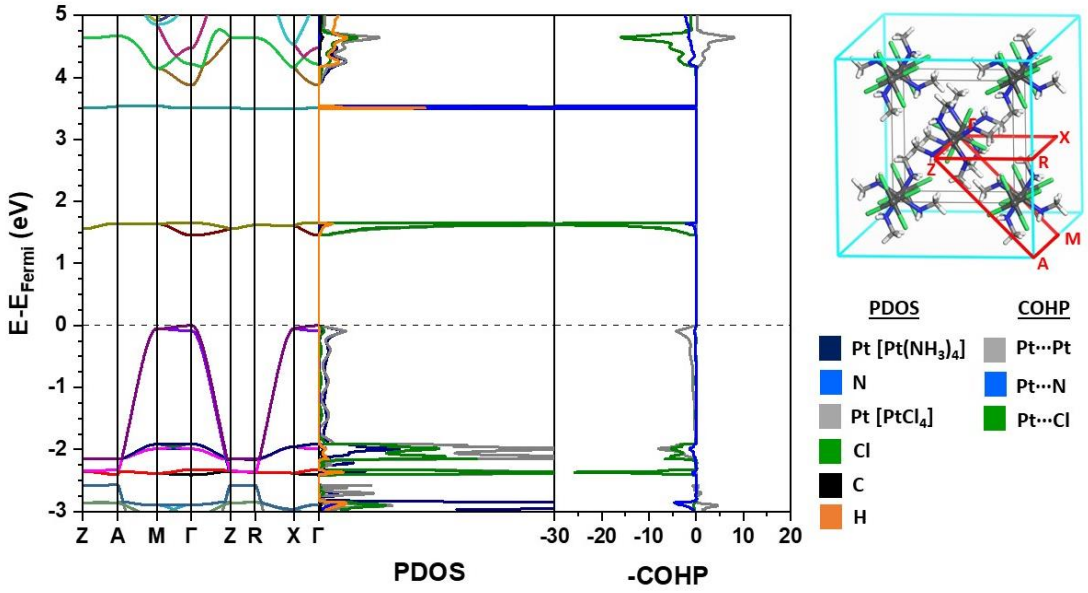

Figure 3.34: Computed electronic band structure, projected density of states (PDOS) and COHP plot of the 1.92 GPa structure of MagNH$_2$Me (E_{Fermi} = -4.35 eV). RIGHT: Real space (grey) and reciprocal (light blue) lattices of MagNH$_2$Me, with the Brillouin zone path used in the electronic band structure coloured in red.

As discussed previously, the trend in the band gap response to pressure from the solid-state calculations for Pt(bqd)$_2$ replicated the experimental behaviour, in terms of its conductivity response to pressure. Consideration must now be given to whether the experimental behaviour for MagNH$_3$ has also been replicated correctly. Across the entire pressure series, using the data plotted in Figure 3.31, an average rate of compression of -0.16 eV GPa^{-1} was determined for MagNH$_3$. If this average band gap compression rate was extrapolated to higher pressures, it is predicted that the metallic state of MagNH$_3$ would occur at 9.8 GPa, in good agreement where the maximum conductivity was observed experimentally.[22]

This methodology of predicting the pressure required to form the metallic state is, however, an oversimplification; the rate of structural compression is not constant throughout the pressure series but rather it decreases with increasing pressure (Figure 3.9). Due to the slowdown in structural compression across the pressure series, the rate of band gap compression between 0.00 GPa and 1.96 GPa was

consistently calculated as -0.20 eV GPa^{-1}, which then decreased to -0.13 eV GPa^{-1} between 1.96 and 4.62 GPa. If this trend continued at even higher pressures as expected, the pressure required to form the metallic state, according to the HSE06 functional, would therefore exceed 10 GPa. Nevertheless, the magnitude of the pressure required to form the metallic state would be in good agreement with that observed experimentally, and the results from this study verify the stark contrast in pressures required to form maximum conductivity state of $Pt(bqd)_2$ and $MagNH_3$ previously discussed in the literature.

It should be noted that all three hybrid DFT functionals revealed a similar average rate of band gap compression in $MagNH_3$ up to 4.62 GPa (Table 3.3). However, due to the higher ambient band gaps calculated for the ambient pressure structure, B3LYP and PBE0 predict that the metallic state would be formed at 10.7 GPa and 13.1 GPa respectively, before even considering the slowdown in structural and band gap compression at higher pressures. The results from the HSE06 functional, based upon the extent of results currently in the literature, have produced results which best fit the known experimental behaviour of $MagNH_3$, thus further verifying its reliability in determining semi-conductor band gaps.

Table 3.3: Computed ambient pressure and high pressure (4.62 GPa) band gaps in $MagNH_3$, with the calculated average rate of band gap compression across the entire pressure range and metallic state formation pressure if the average rate was extrapolated to higher pressures.

Functional	Calculated Ambient-Pressure Band Gap (eV)	Calculated Band Gap (eV) at 4.62 GPa	Average of Rate of Band Gap Compression (eV GPa^{-1})	Predicted Pressure of Metallic State Formation (GPa)
PBE0	2.296	1.485	-0.18	13.08
B3LYP	1.715	0.972	-0.16	10.66
HSE06	1.560	0.821	-0.16	9.75

A different way of considering the rate of band gap compression is with respect to the change in the Pt···Pt stacking distance, as displayed in Figure 3.35, rather than with respect to pressure.

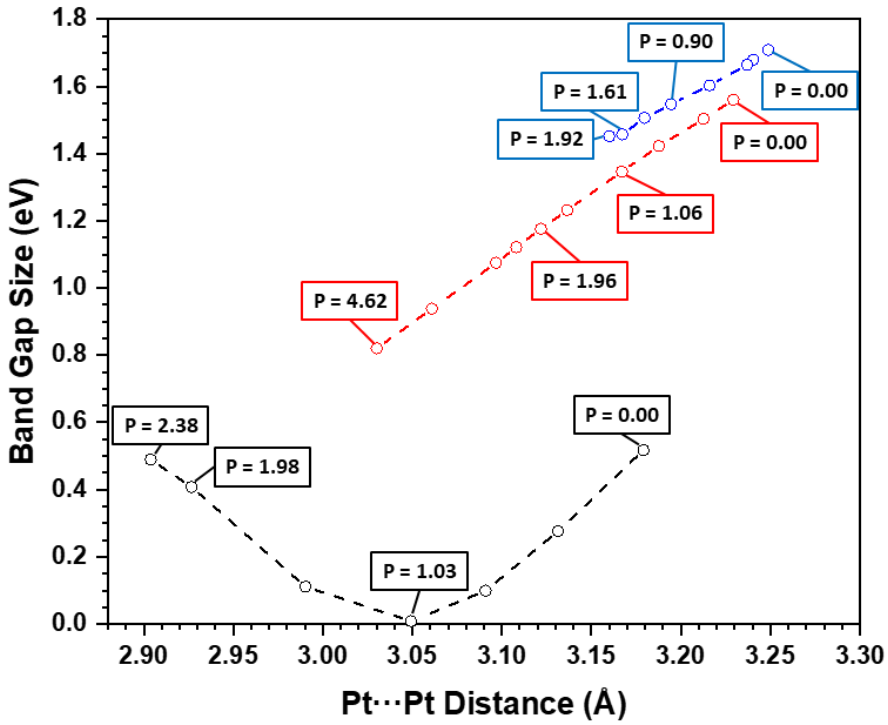

Figure 3.35: Trend in the band gap values with respect to intra-chain Pt···Pt stacking distance throughout the pressure series of $Pt(bqd)_2$ (black), $MagNH_3$ (red) and $MagNH_2Me$ (blue). Larger Pt···Pt distances indicate lower pressures. Certain pressure values are marked; all values have pressure units of GPa.

The trend of band gap values with respect to Pt···Pt stacking distances in $MagNH_3$ is almost linear, with an average rate of compression of -3.72 eV $Å^{-1}$ across the entire pressure series, indicating that the Pt···Pt distance would need to contract by 0.42 Å in total in order to form the metallic state, hence from 3.23 Å to 2.81 Å. To investigate this hypothesis, a further calculation was undertaken, utilising one of the geometry optimised structures for $MagNH_3$ as the input model, but with the *c* axis parameter shortened to 5.52 Å, hence resulting in a Pt···Pt distance of 2.76 Å, slightly exceeding the amount of contraction expected to form the metallic state. As seen in the electronic band structure computed for this structure (Figure 3.36), the extent of *c* axis

contraction has caused the HOCO and LUCO to intersect at around the Γ k-point. Therefore, $MagNH_3$ has clearly formed the metallic state with this extent of Pt···Pt compression. The different pressures required to form the metallic or highest-conductivity state between the various studies must stem from the varying compressibility between the powder and crystal samples of $MagNH_3$.[21, 22]

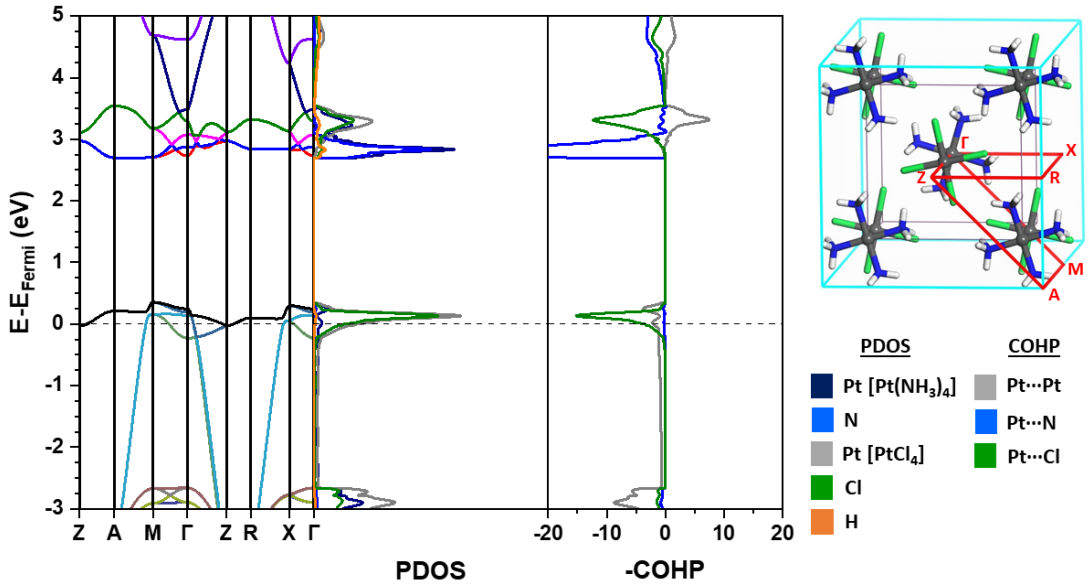

Figure 3.36: Electronic band structure, projected density of states (PDOS) and COOP plot of the theoretical structure of $MagNH_3$ where a = 8.77 Å, c = 5.52 Å (E_{Fermi} = -3.60 eV). RIGHT: Real space (grey) and reciprocal (light blue) lattices of $MagNH_2Me$, with the Brillouin zone path used in the electronic band structure coloured in red.

Returning to the change in band gap value with respect to the Pt···Pt stacking distance in Figure 3.35, it can be seen that $MagNH_2Me$ compresses at a rate of -3.08 eV $Å^{-1}$ between ambient and 1.61 GPa. This slightly slower rate compared to that observed across a similar pressure range for $MagNH_3$ can be attributed to the slight destabilisation of the LUCO across the pressure series offsetting the HOCO destabilisation, as discussed previously. The lack of Pt···Pt contraction and thus lack of band gap compression observed between 1.61 and 1.92 GPa, indicating the inherent rigidity of the structure prior to the phase transition, is readily apparent in Figure 3.35.

Figure 3.35 also clearly highlights the difference in band gap behaviour between $Pt(bqd)_2$ and the MGS complexes. Despite having only slightly shorter interlayer Pt···Pt distances at ambient pressure, a faster rate of band gap compression in $Pt(bqd)_2$ prior to the formation of the metallic state was observed (-3.94 eV $Å^{-1}$), as a result of the HOCO and LUCO both responding to pressure, before the band gap reopens at a slightly slower rate above 1 GPa.

Lastly, the solid-state calculations on the $Pt(bqd\text{-}dibutyl)_2$ structure optimised at the simulated pressure of 1.50 GPa computed a band gap of 1.05 eV, with little change in the nature of the bands electronic band structure, other than slightly greater extents of delocalisation observed in the Y⟶S portions of the k-point path as a result of contraction of the *b* axis direction facilitating stronger intermolecular interactions. The calculations have hence shown that, despite showing considerable volumetric compression with contribution from all three unit cell parameters, the material exhibits a minimal piezoresistive response. This stems from the non-planar packing arrangement in the solid-state resulting in negligible intermolecular interactions. The modification, while achieving its aim of producing a material with better film processability, has unfortunately completely disrupted the desired electronic behaviour.

3.6 Conclusions

The literature previously alluded to the need for short, and compressible, metal···metal stacking, with direct metal···metal orbital overlap, facilitated by the crystal packing, to cause the necessary insulator-metal transition for piezoresistive application. Based upon these criteria, $Pt(bqd)_2$ and $MagNH_3$ should exhibit similar piezoresistive properties. But while fairly modest pressures of *ca.* 1 GPa allow the former to switch from an insulating to a metallic state, the latter resolutely remains an insulator until *ca.* 10 GPa. Further factors must therefore be at play. To that end this work has shown that a synergistic relationship between the extent of anisotropy in the volumetric compression and the delocalisation of the frontier bands is also a key criterion for consideration.

$Pt(bqd)_2$ displayed the greatest extent of volumetric compression anisotropy in favour of the Pt···Pt stacking direction out of the four compounds investigated, and the interlayer interactions in both frontier bands facilitated both a small band gap and fast band gap compression, which allows the material to form the metallic state by 1 GPa. $MagNH_3$, on the other hand, despite having a highly delocalised HOCO band, suffers from a highly localised LUCO band, confined to the $[PtCl_4]^{2-}$ component, and hence, combined with its lower volumetric anisotropy, possesses a large ambient pressure band gap which compresses more slowly.

The modest NH_3 to NH_2CH_3 modification to form $MagNH_2Me$, despite having no effect on the ambient pressure structure, was shown to cause a noticeable negative impact on the structural and electronic response to pressure. The larger ligand group reduced the rigidity of the structure, resulting in more compression in the *ab* plane, hence lowering the rate of Pt···Pt stacking and band gap compression, and ultimately resulting in a potentially irreversible and disruptive phase transition.

The larger modification of the addition of the *n*-butyl groups on to the BQD ligand backbone to form Pt(bqd-dibutyl)$_2$ had an immediate adverse effect; the desired crystal packing was completely disrupted. The solid-state calculations revealed that while weak Pt···Pt interactions can be observed, and the material was calculated to have a lower bulk modulus than the other three compounds, the lack of direct Pt···Pt orbital overlap resulted in a very poor piezoresistive response.

This all-encompassing study on four transition metal complexes has been successful in firstly providing a clear explanation on the contrasting piezoresistive response of Pt(bqd)$_2$ and MagNH$_3$ and, secondly, revealed the effect on the piezoresistive properties of these materials by modest and more considerable ligand modifications. This work has thus added considerably to the current understanding on the piezoresistive response of these class of materials, and thus will allow for a more detailed procedure to be devised when investigating future candidate materials. Undertaking solid-state calculations on the ambient-pressure structures of new materials will give a good indication of its piezoresistivity, by examining the band gap size and extent of frontier band delocalisation, behaviour which isolated molecule calculations might not capture, before committing to time intensive high-pressure diffraction or conductivity studies. Pt(bqd)$_2$ appears to be the best known candidate material from this class of compounds, and thus modest modifications to improve its processability should be a priority. Due to the rotated interlayer relationship of molecules in Pt(bqd)$_2$, it is possible that the addition of methyl groups will provide a degree of improvement in processability without disrupting the crystal packing.

3.7 References

1. E. Broadhurst, MChem Project Report, University of Edinburgh, 2018.
2. G. E. Moore, *Proc. Ieee*, 1998, **86**, 82-85.
3. G. Baccarani, M. R. Wordeman and R. H. Dennard, *Ieee Trans. Electron Devices*, 1984, **31**, 452-462.
4. T. N. Theis and P. M. Solomon, *Science*, 2010, **327**, 1600-1601.
5. T. N. Theis and P. M. Solomon, *Proc. Ieee*, 2010, **98**, 2005-2014.
6. International Business Machines Corporation, US Pat., 7 848 135 B2, 2010.
7. D. Newns, B. Elmegreen, X. H. Liu and G. Martyna, *J. Appl. Phys.*, 2012, **111**.
8. I. B. Magdau, X. H. Liu, M. A. Kuroda, T. M. Shaw, J. Crain, P. M. Solomon, D. M. Newns and G. J. Martyna, *Appl. Phys. Lett.*, 2015, **107**, 073505.
9. P. M. Solomon, B. A. Bryce, M. A. Kuroda, R. Keech, S. Shetty, T. M. Shaw, M. Copel, L. W. Hung, A. G. Schrott, C. Armstrong, M. S. Gordon, K. B. Reuter, T. N. Theis, W. Haensch, S. M. Rossnagel, H. Miyazoe, B. G. Elmegreen, X. H. Liu, S. Trolier-McKinstry, G. J. Martyna and D. M. Newns, *Nano Letters*, 2015, **15**, 2391-2395.
10. D. M. Newns, G. J. Martyna, B. G. Elmegreen, X. H. Liu, T. N. Theis and S. Trolier-McKinstry, in *Micro- and Nanotechnology Sensors, Systems, and Applications IV*, eds. T. George, M. S. Islam and A. Dutta, Proceedings of SPIE, 2012, vol 8373, 04.
11. D. M. Newns, B. G. Elmegreen, X. H. Liu and G. J. Martyna, *MRS Bull.*, 2012, **37**, 1071-1076.
12. D. M. Newns, B. G. Elmegreen, X. H. Liu and G. J. Martyna, *Adv. Mater.*, 2012, **24**, 3672-3677.
13. R. Guo, L. E. Cross, S. E. Park, B. Noheda, D. E. Cox and G. Shirane, *Phys. Rev. Lett.*, 2000, **84**, 5423-5426.
14. Jayarama.A, Narayana.V, E. Bucher and R. G. Maines, *Phys. Rev. Lett.*, 1970, **25**, 1430-1433.
15. Jayarama.A, Narayana.V, E. Bucher and R. G. Maines, *Phys. Rev. Lett.*, 1970, **25**, 368-370.
16. M. A. Kuroda, Z. P. Jiang, M. Povolotskyi, G. Klimeck, D. M. Newns and G. J. Martyna, *Phys. Rev. B*, 2014, **90**, 245124.
17. A. Sousanis, P. F. Smet and D. Poelman, *Materials*, 2017, **10**, 953.
18. D. Poelman, C. Detavernier, P. F. Smet and A. Sousanis, *Sensors.*, 2019, **19**, 4390.
19. D. Poelman, P. F. Smet and A. Sousanis, *Nanomaterials.*, 2019, **9**, 1513.

20. V. Kanchana, G. Vaitheeswaran, G. Santi, W. M. Temmerman, A. Svane, Z. Szotek, P. Strange and L. Petit, *Phys. Rev.*, 2005, **71**.
21. L. V. Interrante and F. P. Bundy, *J. Chem Soc. D*, 1970, **10**, 584-586.
22. L. V. Interrante and F. P. Bundy, *Inorg. Chem.*, 1971, **10**, 1169-1174.
23. M. Megnamisibelombe, *J. Solid State Chem.*, 1977, **22**, 151-156.
24. I. Shirotani, Y. Inagaki, W. Utsumi and T. Yagi, *J. Mater. Chem.*, 1991, **1**, 1041-1043.
25. K. Takeda, I. Shirotani and K. Yakushi, *Chem. Mater.*, 2000, **12**, 912-916.
26. M. Megnamisibelombe, *J. Solid State Chem.*, 1979, **27**, 389-396.
27. C. F. Macrae, P. R. Edginston, P. McCabe, E. Ridcock, G. P. Shields, R. Taylor, M. Towler, J. Van der Streck, *J. Appl. Cryst.*, 2006, **39**, 453-457.
28. I. Shirotani, A. Kawamura, K. Suzuki, W. Utsumi and T. Yagi, *Bull. Chem. Soc. Jpn.*, 1991, **64**, 1607-1612.
29. K. Takeda, I. Shirotani, C. Sekine and K. Yakushi, *J. Phys.: Condens. Matter*, 2000, **12**, L483-L488.
30. K. Takeda, I. Shirotani and K. Yakushi, *Synth. Met.*, 2003, **133**, 415-416.
31. K. Takeda, I. Shirotani, J. Hayashi, H. Fukuda and K. Ito, *Mol. Cryst. Liq. Cryst.*, 2006, **452**, 113-122.
32. M. Atoji, J. W. Richardson and R. E. Rundle, *J. Am. Chem. Soc*, 1957, **79**, 3017-3020.
33. E. G. Kim, K. Schmidt, W. R. Caseri, T. Kreouzis, N. Stingelin-Stutzmann and J. L. Bredas, *Adv. Mater.*, 2006, **18**, 2039-2043.
34. K. Burke, *J. Chem. Phys.*, 2012, **136**, 150901.
35. W. T. Pollard and R. A. Friesner, *J. Chem. Phys.*, 1993, **99**, 6742-6750.
36. M. E. Cradwick, D. Hall and R. K. Phillips, *Acta Crystallogr. B*, 1971, **B 27**, 480-484.
37. Bruker (2012). SAINT. Bruker AXS Inc., Madison, Wisconsin, USA.
38. G. M. Sheldrick, University of Göttingen, Germany, 2008.
39. CrysAlisPro, Oxford Diffraction/Aligent Technologies UK Ltd, Yarnton, UK
40. A. Altomare, G. Cascarano, G. Giacovazzo, A. Guagliardi, M. C. Burla, G. Polidori and M. Camalli, *J. Appl. Crystallogr*, 1994, **27**, 435-435.
41. P. W. Betteridge, J. R. Carruthers, R. I. Cooper, K. Prout and D. J. Watkin, *J. Appl. Crystallogr*, 2003, **36**, 1487-1487.
42. T. J. Kistenmacher and R. Destro, *Inorg. Chem.*, 2983, **22**, 2104-2110.
43. S. A. Moggach, D. R. Allan, S. Parsons and J. E. Warren, *J. Appl. Crystallogr*, 2008, **41**, 249-251.

44. G. J. Piermarini, S. Block, J. D. Barnett and R. A. Forman, *J. Appl. Phys.*, 1975, **46**, 2774-2780.

45. H. Nowell, S. A. Barnett, K. E. Christensen, S. J. Teat and D. R. Allan, *J. Synchrotron Radiat.*, 2012, **19**, 435-441.

46. A. Tkatchenko and M. Scheffler, *Phys. Rev. Lett.*, 2009, **102**, 073005.

47. A. Tkatchenko, R. A. DiStasio, R. Car and M. Scheffler, *Phys. Rev. Lett.*, 2012, **108**, 236402.

48. M. J. Frisch, G. W. Trucks, H. B. Schlegel, G. E. Scuseria, M. A. Robb, J. R. Cheeseman, G. Scalmani, V. Barone, B. Mennucci, G. A. Petersson, H. Nakatsuji, M. Caricato, H. X. Li, P. Hratchian, A. F. Izmaylov, J. Bloino, G. Zheng, J. L. Sonnenberg, M. Hada, M. Ehara, K. Toyota, R. Fukuda, J. Hasegawa, M. Ishida, T. Nakajima, Y. Honda, O. Kitao, H. Nakai, T. Vreven, J. A. Montgomery, Jr., J. E. Peralta, F. Ogliaro, M. Bearpark, J. J. Heyd, E. Brothers, K. N. Kudin, V. N. Staroverov, R. Kobayashi, J. Normand, K. Raghavachari, A. Rendell, J. C. Burant, S. S. Iyengar, J. Tomasi, M. Cossi, N. Rega, J. M. Millam, M. Klene, J. E. Knox, J. B. Cross, V. Bakken, C. Adamo, J. Jaramillo, R. Gomperts, R. E. Stratmann, O. Yazyev, A. J. Austin, R. Cammi, C. Pomelli, J. W. Ochterski, R. L. Martin, K. Morokuma, V. G. Zakrzewski, G. A. Voth, P. Salvador, J. J. Dannenberg, S. Dapprich, A. D. Daniels, Ö. Farkas, J. B. Foresman, J. V. Ortiz, J. Cioslowski and D. J. Fox, GAUSSIAN09, Gaussian Inc., Wallingford, C.T., 2009.

49. N. M. O'Boyle, A. L. Tenderholt and K. M. Langner, *J. Comput. Chem.*, 2008, **29**, 839-845.

50. P. J. Stephens, F. J Devlin, C.F. Chabalowski and M. J. Frisch, *J. Phys. Chem.*, 1994, **98**, 11623.

51. R. Dovesi, R. Orlando, B. Civalleri, C. Roetti, V. R. Saunders and C. M. Zicovich-Wilson, *Z. Kristallogr. Cryst. Mater.*, 2005, **220**, 571-573.

52. R. Dovesi, A. Erba, R. Orlando, C. M. Zicovich-Wilson, B. Civalleri, L. Maschio, M. Rerat, S. Casassa, J. Baima, S. Salustro and B. Kirtman, *Wiley Interdiscip. Rev. Comput. Mol. Sci.* 2018, **8**, e1360.

53. M. F. Peintinger, D. V. Oliveira and T. Bredow, *J. Comput. Chem.*, 2013, **34**, 451-459.

54. J. Heyd, J. E. Peralta, G. E. Scuseria and R. L. Martin, *J. Chem. Phys.*, 2005, **123**, 174101.

55. C. Gatti, V. R. Saunders and C. Roetti, *J. Chem. Phys.*, 1994, **101**, 10686-10696.

56. D. Andrae, U. Haussermann, M. Dolg, H. Stoll and H. Preuss, *Theor. Chim. Acta*, 1991, **78**, 247-266.

57. K. Doll, *Surf. Sci.*, 2004, **573**, 464-473.

58. J. P. Perdew, K. Burke and M. Ernzerhof, *Phys. Rev. Lett.*, 1996, **77**, 3865-3868.

59. A. D. Becke, *J. Chem. Phys.*, 1993, **98**, 5648-5652.

60. J. Heyd, G. E. Scuseria and M. Ernzerhof, *J. Chem. Phys.*, 2003, **118**, 8207-8215.

61. J. Heyd, G. E. Scuseria and M. Ernzerhof, *J. Chem. Phys.*, 2006, **124**, 219906.

62. C. Adamo and V. Barone, *J. Chem. Phys.*, 1999, **110**, 6158-6170.

63. A. D. Becke, *Phys. Rev. A*, 1988, **38**, 3098-3100.

64. C. T. Lee, W. T. Yang and R. G. Parr, *Phys. Rev. B*, 1988, **37**, 785-789.

65. A. A. L. Michalchuk, P. T. Fincham, P. Portius, C. R. Pulham and C. A. Morrison, *J. Phys. Chem. C*, 2018, **122**, 19395-19408.

66. A. J. Garza and G. E. Scuseria, *J. Phys. Chem. Lett.*, 2016, **7**, 4165-4170.

67. A. V. Krukau, O. A. Vydrov, A. F. Izmaylov and G. E. Scuseria, *J. Chem. Phys.*, 2006, **125**, 224106.

68. H. J. Monkhorst and J. D. Pack, *Phys. Rev. B*, 1976, **13**, 5188-5192.

69. R. Dovesi, V. R. Saunders, C. Roetti, R. Orlando, C. M. Zicovich-Wilson, F. Pascale, B. Civalleri, K. Doll, N. M. Harrison, I. J. Bush, P. D'Arco, M. Llunel, Y. Noël, L. Maschio, A. Erba, M. Rérat and S. Casassa, *CRYSTAL17 User's Manual*, accessed January 2019.

70. F. Birch, *Phys. Rev.*, 1947, **71**, 809-824.

71. J. P. Perdew and M. Levy, *Phys. Rev. Lett.*., 1983, **51**, 1884-1887.

72. P. J. Hasnip, K. Refson, M. I. J. Probert, J. R. Yates, S. J. Clark and C. J. Pickard, *Philos. Trans. R. Soc. A*, 2014, **372**, 20130270.

73. A. A. L. Michalchuk, S. Rudic, C. R. Pulham and C. A. Morrison, *Phys. Chem. Chem. Phys.*, 2018, **20**, 29061-29069.

74. I. Shirotani, T. Kudo, N. Sato, H. Yamochi and G. Saito, *J. Mater. Chem.*, 1995, **5**, 1357-1362.

Chapter 4

Investigating the Structural and Electronic Band Structure Response to Pressure of Au-dithiolene Mott Insulator Polymorphs

4.1 Synopsis

This chapter continues with the material application outlined in Chapter 3, in facilitating conductivity through a material by the application of pressure. However, this chapter will focus on the investigation of radical Au-based complexes, rather than the closed-shell Pt systems in Chapter 3, and thus, while involving similar complementary analysis techniques of synchrotron X-ray diffraction and solid-state calculations, a different method of pressure-conductivity switch must be considered.

4.2 Disclaimer

All synthetic and crystallisation work of the $Au(bpedt)_2$ samples was undertaken by Asato Mizuno (obtained PhD from Nagoya University in 2018) and Dr Helen Benjamin (formerly based at the University of Edinburgh), following the procedures outlined in the literature.[1]

4.3 Introduction

The work in this chapter follows on from the work presented in Chapter 3, in that a similar material application, namely the response of the conductive properties of the material of interest to the application of pressure, will be explored. However, rather than considering closed-shell systems as seen in Chapter 3, this chapter will focus on Au compounds containing an odd number of electrons per molecule. As a result, while the methods of investigation are similar to those used in Chapter 3, careful consideration must be given to the fact that there is a different mechanism underlying the pressure-conductivity switch. This will be introduced prior to a discussion of the specific materials of interest.

Conductivity in closed-shell systems is facilitated by the charge transfer between the spatially-independent HOCO and LUCO bands, thus the nature of these bands and the band gap rate of compression formed the key points of focus within the pressure series studied in Chapter 3. In the case of open-shell systems, the description is more complicated, as the highest occupied component of the valence band is only partially occupied. According to band theory, this should mean that all open-shell systems would be metallic, with the unpaired electrons being delocalised throughout the solid;[2] given that many open-shell systems do not display metallic behaviour, this is clearly an oversimplification.[3] Band theory does not take into account electron correlation effects, more specifically the Coulombic repulsion between spatially-close electrons,[3, 4] which can result in the unpaired electrons becoming localised on a particular site, with an energy barrier restricting the movement of electrons between sites.[2, 3] This energy barrier is often sufficiently large to prohibit the excitation of electrons at low temperatures, and thus these materials normally display insulator behaviour. These materials, referred to as Mott insulators, can however undergo insulator-metal transitions by various mechanisms,[5] such as by the application of temperature,[6-8] pressure,[9-13] or by irradiation.[14, 15] The mechanism of conductivity in these materials is described by the movement, or "hopping", of an unpaired electron from one site to another or, in other words, by the oxidation of one site and reduction of another.[2, 3]

The hopping of electrons between sites has two associated energy terms. The first, commonly known as the transfer (t) or resonance (β) integral, relates to the kinetic energy acting on electrons, which allows them to hop between sites.[3] The second energy term is the Coulombic barrier, **U**, caused by the interaction between electrons in close contact on a particular site.[3] The effect of these two competing energy terms can be seen in the computed band structures of these materials; a simplified schematic example is shown in Figure 4.1. The highest level in the valence band, sitting below

the Fermi level, represents the semi-occupied crystalline orbitals (SOCOs) responsible for the highly-localised sites of each unpaired electron. The band representing the equivalent unoccupied component for each site is found in the conduction band, above the Fermi energy, with the separation energy between the midpoints of the two bands defined by **U**.[3] By convention, these two parts of the band structure are referred to as the lower and upper Hubbard (sub-)bands respectively,[3, 16, 17] and the minimum energy separation between them is thus defined as the sub-band gap. The bandwidth, ***W***, of each of the sub-bands is also marked on Figure 4.1, which describes the extent of delocalisation present in each of the sub-bands and is thus related to the extent of orbital overlap between neighbouring sites, the number of neighbouring sites and the transfer integral ***t***.[3]

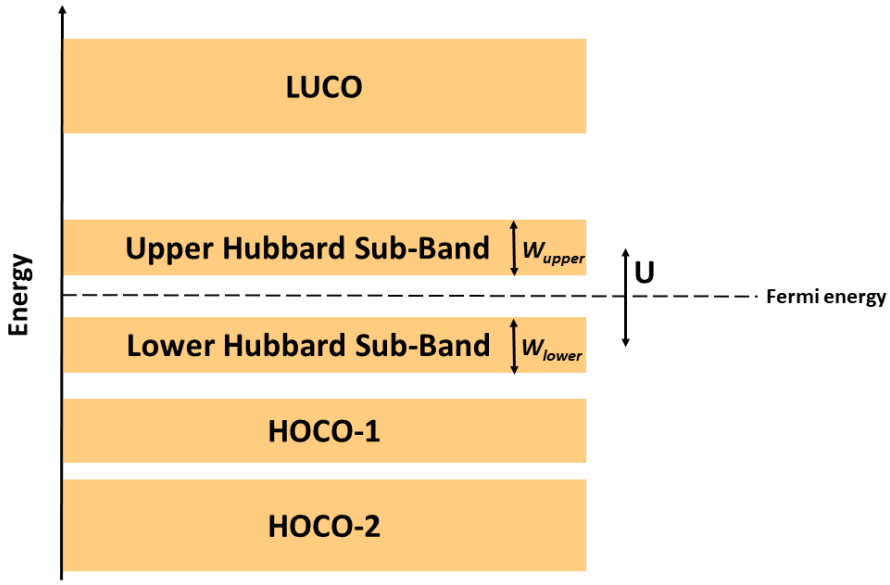

Figure 4.1: Generic band structure diagram of an open-shell system in the non-conductive state, highlighting the splitting of the SOCO band into the lower and upper Hubbard sub-bands by the Coulombic barrier, U, and the dispersion of the bands described by the bandwidth, W.

One method of facilitating an insulator-metal transition, commonly referred to as a Mott-Hubbard transition, in these materials is by 'bandwidth-control', in other words by decreasing the relative interaction strength **U**/***t*** of the two energy terms.[18] The size of the Coulombic barrier is generally an intrinsic property of the material, determined

by the chemical nature of the localised site of the unpaired electron, and therefore it is difficult to decrease **U**/***t*** by considerably decreasing **U** without substantial alterations in molecular conformation or intramolecular connectivity.[3] However, increasing the extent of orbital overlap between neighbouring molecules, by decreasing the intermolecular separation in the solid state, will cause ***W*,** and thus ***t***, to increase.[3] This behaviour can be controlled by the application of pressure. Once the bandwidths have sufficiently increased, thereby reducing **U**/***t***, the conductive state will be formed. This therefore rationalises a pathway towards the design of new responsive materials; with an appropriate relationship between **U** and ***W***, they should possess a clear sub-band gap at ambient conditions to resist excitation by thermal means, but not so large as to be unsurmountable without resort to extremely high pressures to form the metallic state.

Some of the most-studied examples of transition metal complexes which display Mott insulator and Mott-Hubbard transition behaviour include transition metal oxides, such as vanadium oxides and Cu(II) d^9 cuprates.[7, 15, 19-24] However, due to 5d orbitals being more radially extended than their 3d and 4d counterparts,[3] there is growing interest in Mott insulators containing 3rd row transitional metals, with the expectation this will lead to smaller **U** and larger ***W*** values. As a result, there have been recent publications concerning Au-based Mott insulators.[25-34]

4.3.1 Introduction to Au(bepdt)$_2$

The work in this chapter will specifically focus on the *trans* isomer of an asymmetric Au-dithiolene complex, Au(bpedt)$_2$, where bpedt refers to the bidentate ligand system (1-((1,1-biphenyl)-4-yl-)-ethylene-1,2-dithiolene. The molecular structure of Au(bpedt)$_2$ (Figure 4.2A) consists of an almost square planar metal environment with ∠S-Au-S values ranging between 88° and 92°, with a twist of *ca.* 5° between the two Au-dithiolene rings (Figure 4.2B).[1] Furthermore, the torsion angles between

neighbouring Au-dithiolene and phenyl rings (*ca.* 19° and 22°) and neighbouring phenyl rings (*ca.* 3° and 7°), as shown in Figure 4.2C, suggest that delocalisation throughout the entire ligand system will be limited. $Au(bpedt)_2$ has been shown to crystallise in the $P2_1/c$ space group, hereafter referred to as phase **1**, with a structure published from diffraction data collected at 120 K (a = 6.1872(6) Å, b = 7.2049(18) Å, c = 51.832(13) Å, β = 92.775(2)°; CSD refcode: TUBSCH) (Figure 4.3A).[1]

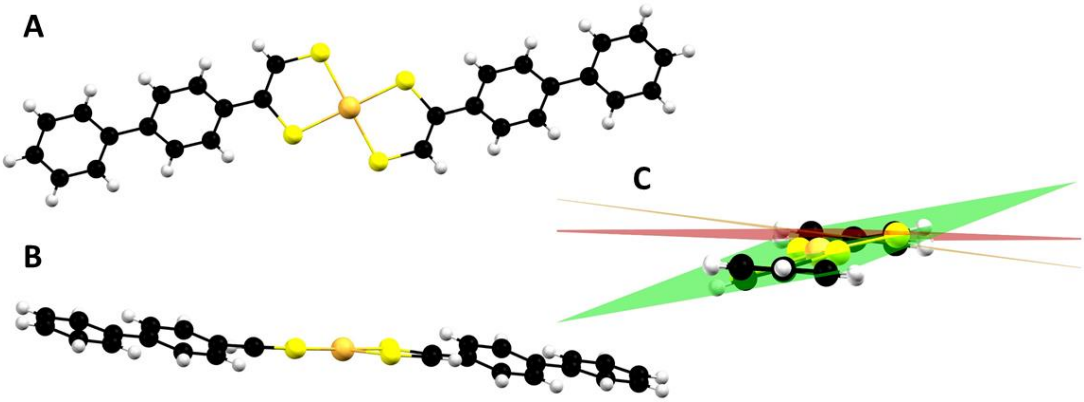

Figure 4.2: Molecular structure of $Au(bpedt)_2$ (A), side on view showing twisting around Au metal centre (B), and end-on-view showing twisting between one set of neighbouring dithiolene (green), inner phenyl (orange) and outer phenyl (red) ring planes, adapted from cifs from the literature.[1] Atoms are coloured: Au (orange), S (yellow), C (black), H (grey). Images created using Mercury.[35]

Figure 4.3 shows the known crystal packing of $Au(bpedt)_2$; it does not facilitate any direct overlap between the metal centres on neighbouring molecules, unlike that seen for $Pt(bqd)_2$ or the Magnus green salts in Chapter 3. However, two specific directions of intermolecular interactions in the solid state have been identified,[1] which have been indicated in Figure 4.3B. The first, indicated by the green dashed lines, hereafter referred to as the chain interaction, is the zigzag interaction between the Au-dithiolene centres as a result of the herringbone arrangement of molecules down the *b* axis direction. While this interaction results in a long Au···Au contact distance of over 5 Å, shorter intermolecular Au···S and S···S contacts, shown in Figure 4.3C, on the order of 3.5-4.5 Å are present.

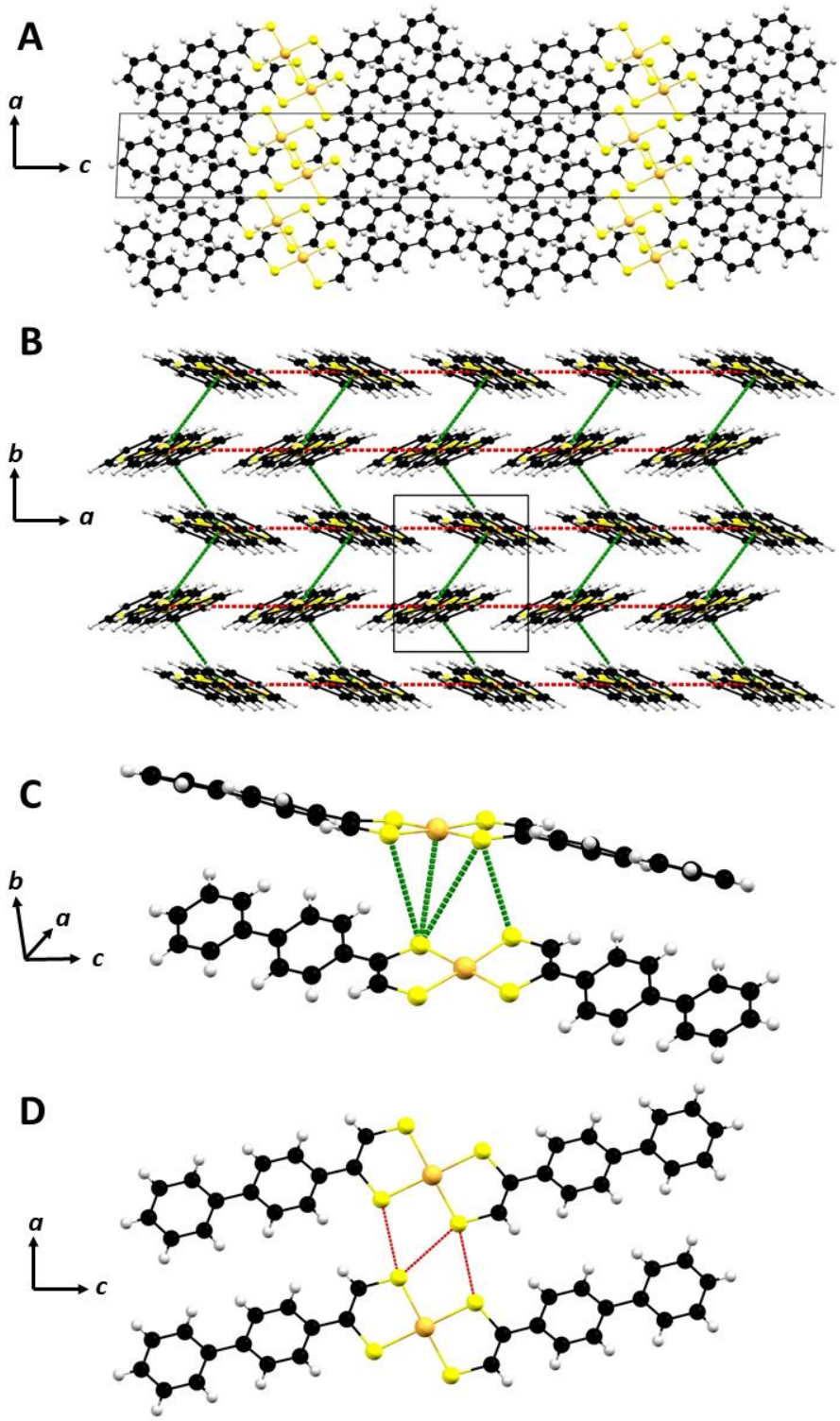

Figure 4.3: Packing diagram of $Au(bpedt)_2$ showing contents in and around the unit cell in the ac plane (A); packing diagram in the ab plane, with interactions (red and green dashed lines) between Au and dithiolene rings along the a and b axis directions (B); shortest intermolecular Au···Au and S···S interactions along the a axis (C); shortest intermolecular S···S interactions along the b axis (D). Images created using Mercury.[35]

The second interaction, indicated by the red dashed lines in Figure 4.3B, resembles the interaction between neighbouring molecules along the *a* axis direction, in which neighbouring Au-dithiolene rings are more co-planar, resulting in intermolecular Au···Au and S···S interactions on the order of 6.2 Å and 3.4 Å respectively (Figure 4.3D). These S···S interactions in particular have been identified as very short in the context of dithiolene complexes in the literature,[1] and thus might be able to facilitate sufficient delocalisation in the Hubbard sub-bands to allow a Mott-Hubbard transition to take place upon the application of pressure. The *c* axis direction can be thought of as the insulating direction, given it consists of stacking of the biphenyl components of the ligand system and thus does not facilitate any short Au···Au, Au···S or S···S intermolecular interactions.

Investigation of the electronic properties of this material using experimental methods has shown that it exhibits semi-conductive behaviour, with a low thermal activation energy of 0.11 eV, and thus points to $Au(bpedt)_2$ acting as a Mott insulator.[1] The response of its electronic properties to pressure however has not yet been evaluated, and therefore it remains unknown if a Mott-Hubbard transition under the application of pressure can be facilitated.

The structural response to the application of pressure however has been investigated using high-pressure diffraction experiments on an in-house laboratory diffractometer; Figure 4.4 shows the unit cell parameter compression up to 1.6 GPa.[36] These experiments revealed the majority of compression could be attributed to the *a* and *b* direction, more so for the latter,[36] and thus resulted in contraction of the S···S intermolecular contact distances previously highlighted along these directions. By contrast, the contraction along the *c* axis direction was minimal, due to the steric clashing between phenyl groups. Volumetric compression of around 12% was achieved by 1.6 GPa, after which point no suitable diffraction data was obtained.[36]

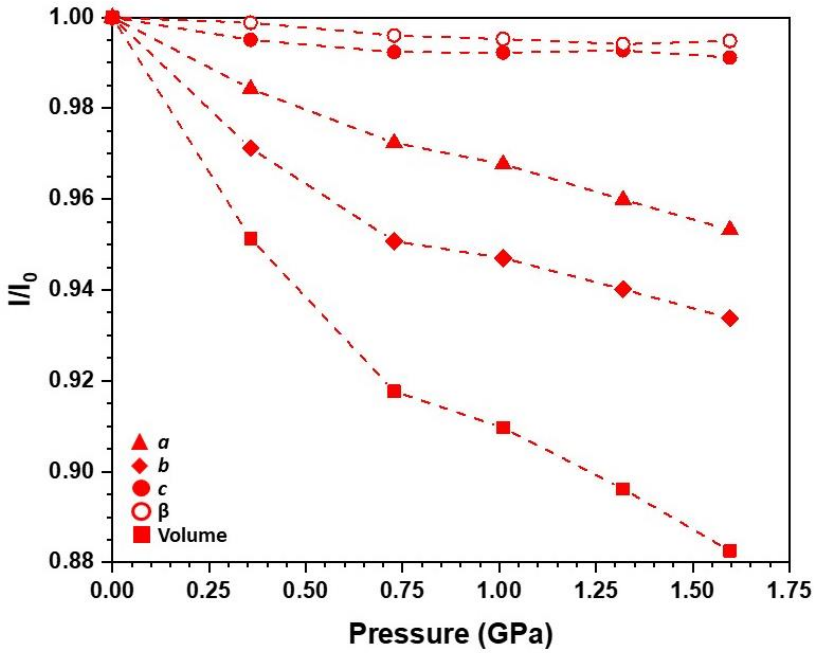

Figure 4.4: Compression curves for Au(bpedt)$_2$ up to 1.6 GPa for the unit cell parameters, adapted from the results reported by E. Broadhurst.[36] Error bars are smaller than symbols used.

While the quality of the data and compression trends obtained was promising, the structural changes that occur above 1.6 GPa are unknown. Furthermore, there appeared to be two clear regimes in the volumetric compression curve, with a stark change in its gradient at around 0.7 GPa, coinciding with a similar change in the rate of compression along the *b* axis. This required further investigation, utilising higher-intensity synchrotron radiation, with the hope that a newly synthesised batch of single crystals would be of better quality in order to study the structural response to even higher pressures. Upon preparation of the new batch of single crystals, however, a preliminary diffraction experiment on the in-house laboratory diffractometer suggested that the sample had not crystallised in the expected space group, thus highlighting that a different polymorph might have been obtained.

4.3.2 Aim of research

Given the surprising potential discovery of a previously unknown polymorph of $Au(bpedt)_2$ (which will hereafter be referred to as polymorph **2**), despite utilising the same crystallisation method (electrochemical oxidation) as for the published structure, the first objective was to utilise synchrotron X-ray diffraction experiments to ascertain the structure of polymorph **2**, and then study its structural response to pressure. These results could be directly compared to the crystal packing and intermolecular interactions identified for the known polymorph **1**. Solid-state calculations would then be undertaken on both polymorphs, to determine their electronic band structures throughout the pressure series, and therefore to ascertain if the two polymorphs possess different electronic responses to pressure as a result of the different crystal packing.

4.4 Methods

4.4.1: High-pressure X-ray crystallography

High-pressure diffraction experiments were undertaken on a single crystal of **2**, loaded in a modified Merrill-Bassett diamond anvil cell alongside a ruby crystal (acting as the in-situ pressure calibrant) and the hydrostatic pressure transmitting medium Fluorinert FC-70 (perfluorotri-N-pentylamine).[37, 38]

High-pressure data were at the Diamond Light Source I19 (EH2) beamline,[39] utilising a Newport 4-circle κ-geometry diffractometer installed with a Pilatus 300 K detector, and tuneable monochromatic X-ray radiation set to 0.4859 Å (25.5 keV). Data were collected using a series of ω scans, adapted to avoid shading of the detector from the cell body, with a step size and exposure time of 0.2° and 0.2 s respectively, at various pressures between 0.11 GPa and 1.18 GPa. Data reduction (integration and absorption correction) was undertaken using the CrysAlisPro software suite.[40]

The structure solutions for all high-pressure data was carried out using CRYSTAL.[41] The structure for the diffraction data for the lowest pressure point was solved using Sir92,[42] and was then used as the input model for the diffraction data collected at the higher pressure points. All 1,2 and 1,3 distances for the ligand systems were restrained and planar restraints were applied to each of the phenyl groups and each Au-dithiolene ring. All torsion angles and metal-ligand bond distances were allowed to freely refine. Vibrational and thermal similarity restraints were also applied to the non-metal atoms on the ligand system. Data was refined against F^2 with isotropic atomic displacement refinement for non-hydrogen atoms.

4.4.2: DFT and hybrid DFT solid-state calculations

All solid-state calculations were performed using CRYSTAL17,[43, 44] where pure DFT and hybrid DFT functionals were implemented with crystalline orbitals built from linear combinations of atomic orbitals, developed from Gaussian-type functions for solid-state periodic systems. Triple zeta valence with polarization quality basis sets were used for all ligand atoms (S, C and H),[45] while the Au atoms were modelled using the energy-consistent relativistic pseudopotential as developed by Andrae *et al* (to treat the core electrons);[46] the remaining [8s7p6d] valence electrons were treated explicitly with optimised basis sets, as described by Doll et *al*.[47]

The starting position of the radical electron on each molecule at the start of the single-point energy or geometry optimisation calculations was always positioned on the Au atom, with the spin configuration locked for at least 3 self-consistent field (SCF) cycles, ensuring that the total number of SCF cycles outnumbered the number of cycles for which the spin state was locked. Due to defining the starting position and spin state (α, up, or β, down) of the radical electron on each molecule, the cell symmetry was required to be reduced to *P*1, thus every atom in the unit cell was spatially independent, increasing the computational resources required to study the material.

As will be discussed in Section 4.5.1, polymorph **2** of Au(bpedt)$_2$ is structurally distinctive from the previously-known polymorph, **1**, with a much smaller unit cell and only two molecules, thus two Au centres, per unit cell. This results in half the number of possible spin configurations per unit cell (one antiferromagnetic (AFM) and one ferromagnetic (FM); Figure 4.5) and half the total number of atomic coordinates requiring optimisation for **2**, compared to **1**. Therefore, the properties of interest of phase **2**, including full electronic band structures, were calculated from an atomistically-optimised structural model, stemming from optimised wavefunctions and k-point grid samplings, using the experimentally-determined atomic coordinates

as the starting model. The structural optimisations were undertaken with Monkhorst-Pack nets[48] of 4 × 4 × 4 using the B3LYP,[49] HSE06,[45, 50, 51] and PBE0 functionals,[52] and 8 × 8× 8 for the PBE functional,[53] corresponding to a maximum grid spacing of *ca.* 0.04 $Å^{-1}$ and 0.02 $Å^{-1}$ respectively and to 36 and 260 k-points in the irreducible BZ respectively, such that the total energy difference obtained by using larger Monkhorst-Pack nets was smaller than 10^{-7} Hartree.

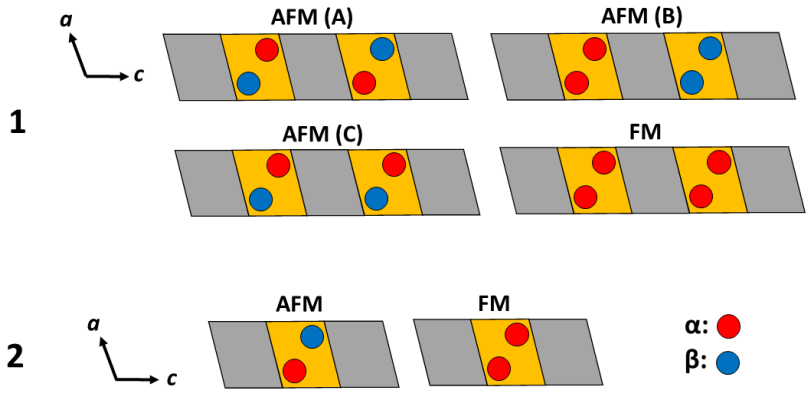

Figure 4.5: Schematic indicating the spin configurations tested for each unit cell of the two phases (1 and 2) of Au(bpedt)$_2$. Orange sections indicate the conductive layer down the ab plane, whereas grey sections indicate the insulating layer along the c axis directions. Circles represent the radical electron site on each molecule.

The optimisation calculations on **2** were originally undertaken with optimisation of both the unit cell parameters and atomic coordinates; however, excessive contraction of the unit cell due to the inclusion of the required D3 dispersion correction was observed, and therefore the results of atom-only optimisations, in which the unit cell parameters remained constrained to the experimental values, will be discussed herein. All other optimisation criteria were used as default for CRYSTAL17 (default total energy convergence threshold during optimisation (TOLDEE) of 10^{-7} Hartree, tolerance of the RMS of the gradient (TOLDEG) of $3x10^{-4}$ Hartree and tolerance of the RMS of the atomic displacements (TOLDEE) of $1.2x10^{-3}$ Hartree).[54]

As will be discussed in Sections 4.5.2 and 4.5.3, properties of interest were also calculated for **1**, using the same array of functionals as for **2**. However, due to the

higher number of spatially independent atoms in the unit cell, geometry optimisation calculations were beyond the computational resources available for this investigation. Therefore, all calculation results shown for **1** were produced from single-energy calculations on the experimentally determined structures, without optimisation of the k-point sampling. The wavefunction optimisation and single point energy calculations were thus only undertaken with a Monkhorst-Pack net[47] of 4 × 4 × 4 for all five functionals, corresponding to 36 k-points in the irreducible BZ and a maximum grid spacing of *ca.* 0.04 $Å^{-1}$, for all four possible spin configurations (three AFM, one FM; Figure 4.5). Therefore, the spin configurations studied only take into account those possible between sites within each unit cell and do not take consider spin configurations formed between sites across neighbouring unit cells. Studying all possible spin configurations that transcend unit cell boundaries would require supercell models to be devised, thus increasing the number of molecules in each model and increasing the number of models to be studied, considerably increasing the complexity of the problem at hand.

Previous work, in the literature and in Chapter 3, have shown that HSE06 is the most appropriate with respect to determining the optimised unit cell parameters and size of the electronic band gap,[55-57] and thus the main focus of the results section will be on the output from the calculations using the HSE06 functional.

4.4.3: Isolated molecule (Gaussian) calculations

Hybrid DFT calculations for $Au(bpedt)_2$ were performed using the Gaussian09 package,[58] undertaken using the unrestricted hybrid UB3LYP functional,[49] with the SDD basis set and effective core potentials for Pt and the 6-311G** basis sets for the H, C and S atoms. The initial atomic coordinates were taken from one molecule of the ambient pressure structure of polymorph **1**.[36]

4.5 Results and Discussion

4.5.1 X-ray crystallography

The high-pressure diffraction experiments undertaken using synchrotron radiation revealed that the newly synthesised batch of single crystals of $Au(bpedt)_2$ were indeed of a previously-undiscovered polymorph. Phase **2** of the $Au(bpedt)_2$ was determined to be crystallised in the $P2_1$ space group (a = 11.67(3) Å, b = 7.4328(16) Å, c = 14.529(8) Å, β = 113.00(16)°), with two Au centres per unit cell.

Due to the subpar quality of crystals available, the diffraction data obtained during the series of synchrotron diffraction experiments on **2** suffered from relatively low intensity ($I/\sigma < 5$) and high R_{int} values (> 14 %) throughout the pressure series. Furthermore, a suitable single crystal of **2** has not been obtainable since the beamtime session to record diffraction data, and thus solve the structure, at ambient pressure. Therefore, all discussion in terms of the rate of compression of **2** is with respect to the structure obtained from the diffraction data collected at the lowest pressure point of 0.11 GPa.

The crystal packing of **2** (Figure 4.6A) is similar to that of **1** in that there is a herringbone arrangement between neighbouring molecules, with zig-zag stacking of molecules down the *b*-axis direction. This stacking along the *b* axis direction results in a similar array of intermolecular Au···S and S···S contacts as to that seen in **1**, with the shortest being on the order of 3.6-4.4 Å (Figures 4.6B and 4.6C). The main difference between the crystal packing of **1** and **2** stems from the inter-chain relationship; **2** completely lacks short S···S contacts in the *a* axis direction, thus possessing insulating layers along both the *a* and *c* axis direction. Since S···S interactions have been cited as the possible source of electronic communication in this

material,[1] a piezoresistive response should be possible for **2**. Nevertheless, its structural and band structure response to pressure requires comparison to that of **1** to understand how the extent and directionality of these S···S interactions influences the property behaviour of these materials.

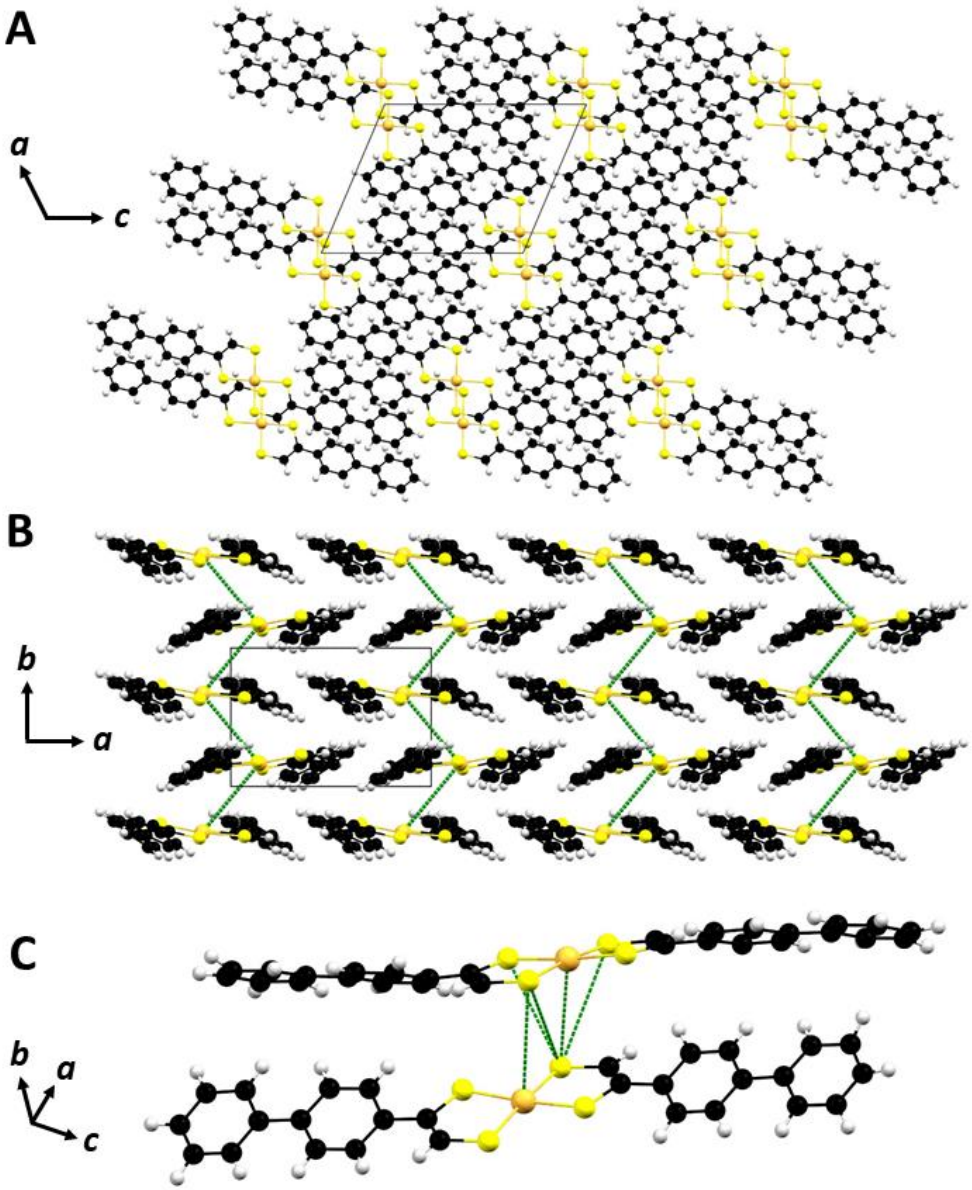

Figure 4.6: Crystal packing of Au(bpedt)$_2$ in the P2$_1$ phase, as viewed along the ac (A) and ab (B) planes. Interactions between neighbouring Au and dithiolene rings along the b axis are shown with the green dashed lines in (B), while (C) highlights the shortest intermolecular Au···S and S···S interactions between molecules stacked mostly down the b axis direction. Images created using Mercury.[35]

Upon the application of increasing pressure up to 1.18 GPa, compression was observed along all three unit cell directions, after which the diffraction quality dropped considerably and indexing could not be successfully obtained. The quality of the diffraction data meant structure refinements could only be obtained successfully for the pressure points up to 0.85 GPa inclusive. Figure 4.7 shows the change in the unit cell parameters across the pressure series, as well as the comparative compression with respect to the values obtained at 0.11 GPa.

Despite the inconsistent compression trends and, in some cases, large standard deviations observed for the individual unit cell parameters, the pressure series has produced a relatively smooth volumetric compression curve for **2**, with around 7 % compression observed between 0.11 and 1.18 GPa. This rate of compression is slightly less than that observed for **1** (*ca.* 8%) within a similar pressure range. However, the apparent agreement between the rate of volumetric compression in the two polymorphs hides the varying contributions from compression along each of the unit cell parameters. As discussed in section 4.3, the greatest contribution to the overall compression of **1** was attributed to the *b* axis direction (Figure 4.3) throughout the entire pressure series.[36] While this is the case for **2** at lower pressures, a rapid decrease in the *a* axis parameter above 0.25 GPa results in it displaying a statistically similar rate of compression as in the *b* axis direction at 0.85 GPa and 1.18 GPa.

It is readily apparent that the poor crystal quality has severely hindered any definite conclusions that can be drawn from this high-pressure diffraction study. Higher quality crystals would be required if the structural response of **2** was to be investigated further. Moreover, the unexpected polymorphism of this material, and thus relationship between the two polymorphs, is an avenue for future investigations, given that they can be produced by following the same electrochemical crystallisation process. The discovery of **2** however has provided an opportunity for the electronic properties of the two polymorphs to be compared by solid-state calculations.

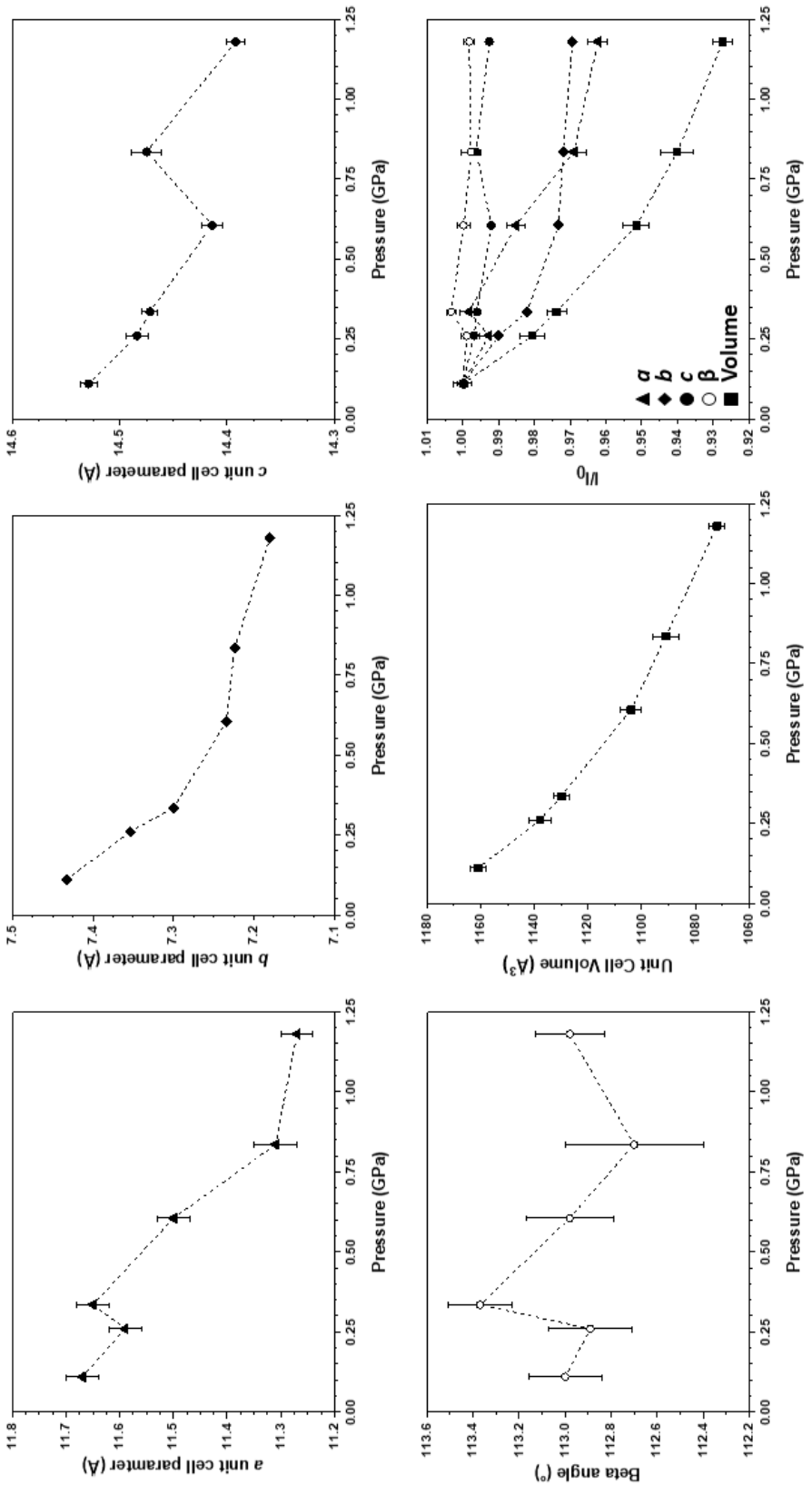

Figure 4.7: Absolute values of the unit cell parameters of polymorph 2 of Au(bpedt)$_2$ across the pressure series, and compression of each unit cell parameter relative to the values obtained at 0.11 GPa (graph in lower right). Triangles, diamonds, filled circles, open circles and squares represent compression along the a, b, and c axis directions, in the β angle and in the unit cell volume respectively.

4.5.2 Ambient-pressure/lowest-pressure solid-state calculations

Table 4.1 shows the calculated energies for each spin configuration tested for both phases, along with the starting and ending spin density across the entire unit cell. The AFM(A) and AFM(C) systems of **1** converged to essentially the same energy value (to two decimal places), which is unsurprising since the spin configuration down the *b* axis is essentially the same (Figure 4.5). This therefore shows that the phenyl groups sufficiently separate the chains to prohibit communication between sites along the *c* axis direction, as suggested in the literature.[1] The FM configuration was shown to be less energetically stable, calculated as 10.7 kJ mol^{-1} higher in energy than the AFM(A) and AFM(C) configurations, but still maintained its starting spin configuration throughout the calculation. This energy difference is considerably larger than the lone example for this class of materials found in the literature (5 meV, 0.48 kJ mol^{-1}),[30] and exceeds the thermal energy available at 298 K (2.48 kJ mol^{-1}); thus, **1** is favoured to display the AFM(A/C) spin configuration. The AFM(B) configuration, despite having a spin value of 0 across the unit cell, consists of two isolated chains of ferromagnetically-related spins (Figure 4.5), and thus was seen to behave midway between the other configurations. Its wavefunction converged at an energy 5.3 kJ mol^{-1} higher than the other AFM configurations, and its spin density changed from 0 to -1, indicating a final configuration in which spins on neighbouring molecules along one half of the chains converted to an anti-parallel relationship.

The calculations on **2** revealed an energy difference of 3.6 kJ mol^{-1} (37 meV) between the AFM and FM configurations (Table 4.1), much smaller than that observed for **1**, but still in favour of the antiferromagnetic state. The total energy per molecule in the lowest energy configurations suggest that **2** is the more stable polymorph; however, since the values calculated for **1** were determined without optimisation of the k-point sampling, this result should be treated with caution.

Table 4.1: Summary of single-point energy calculations (phase 1) and atom-only geometry optimisation calculations (phase 2) of Au(bpedt)$_2$ indicating the energy difference between different spin configurations.

	Total Energy (With Dispersion Correction (eV)	Energy Difference to Lowest Energy Phase (kJ mol^{-1})	Starting Total Spin Across Unit Cell	Ending Total Spin Across Unit Cell
PHASE 1				
AFM (A)	-305415.92	0.00	0	0
AFM (B)	-305415.86	+5.33	0	-1
AFM (C)	-305415.92	0.00	0	0
FM	-305415.81	+10.67	2	2
PHASE 2				
AFM	-152718.76	0.00	0	0
FM	-152718.72	+3.56	1	1

During the wavefunction optimisation of both polymorphs, the spin density of the unpaired electron was seen to shift from its starting position on the metal centre. In all cases, the final spin density on the Au metal centre never exceeded 3 %, with the majority found residing on the dithiolene rings; this is in good agreement with the results of isolated molecule calculations (Table 4.2) and the already published work on this material.[1] The site of the paired electron is not heavily delocalised across the whole molecule, but its strong presence on the sulfur atoms means the S···S contact distances previously highlighted must play an important role, not just in terms of the crystal packing, but also on whether electron hopping is able to be facilitated.

Table 4.2: Final total calculated % spin distribution across the various atom types in Au(bpedt)$_2$ in its lowest energy AFM and FM configurations in the solid state in both polymorphs, compared to that obtained for the isolated molecule. Negative values indicate spin density residing on the atom type is antiparallel to the assigned spin.

Atom Type	PHASE 1		PHASE 2		Isolated
	AFM	FM	AFM	FM	Molecule
Au	2.2 %	2.3 %	2.3 %	2.2 %	-1.5 %
S	65.8 %	66.2 %	63.0 %	62.7 %	70.7 %
C (dithiolene rings)	27.6 %	26.7 %	28.1 %	27.6 %	25.4 %
C (phenyl rings)	5.5 %	5.9 %	7.6 %	8.7 %	6.7 %
H (all)	-0.8 %	-1.1 %	-0.9 %	-1.3 %	-1.3 %

Figures 4.6 to 4.9 show the calculated electronic band structures, BZ k-point paths, PDOS and COHP plots for the lowest energy AFM configuration of **1**, the only FM configuration of **1**, and both configurations of **2**. Additional complications are caused by the production of separate band structures, PDOS and COHP plots for the α and β states. Therefore, the electronic band structures, PDOS and COHP plots for the α and β states have been overlaid.

In the AFM configuration band structures there is direct overlap between α and β states, and thus each grey line at the top of the valence band and bottom of the conduction band in the band structure for **1** actually consists of four overlapping bands (two α and two β), each holding one electron. In the band structure for the FM configuration of **1**, the α and β states do not directly overlap; each red line in the band structure represents two overlapping α bands and blue lines represent two overlapping β bands, with one electron occupying each band. The left-hand and right-hand sections of the PDOS plots represent the α and β states respectively. The sign of the COHP values have been altered so that, for both the α and β states, antibonding and bonding interactions are designated by negative and positive values respectively. In the COHP plots, a range of intramolecular ($A_i \cdots B_i$) and intermolecular ($A_i \cdots B_j$) interactions have been examined, with A and B representing the two interacting atom types; A and B are the same in some cases.

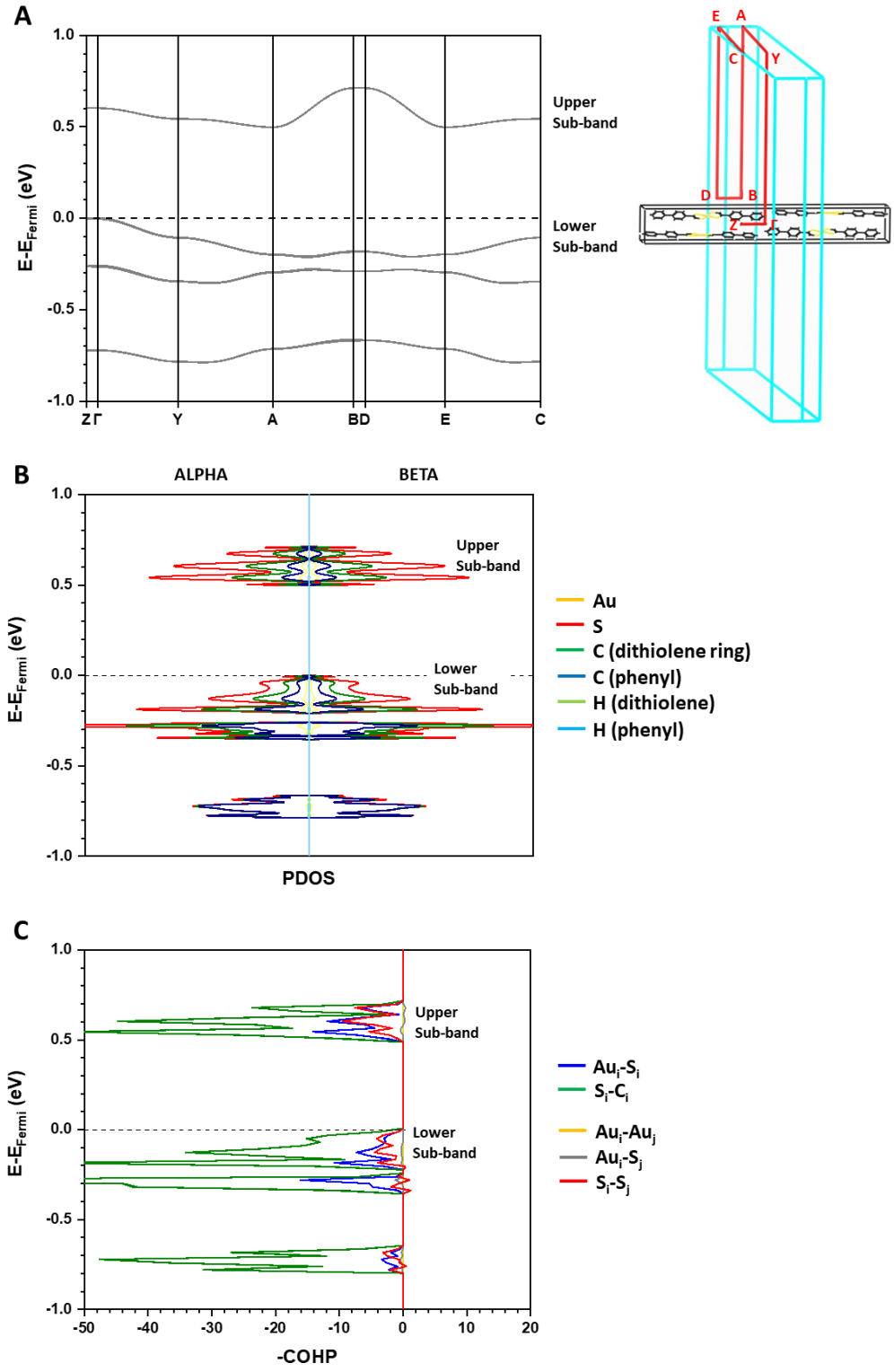

Figure 4.8: Electronic band structure and k-point path (A), projected density of states (B) and COHP plot (C) of the non-optimised ambient-pressure structure of Au(bpedt)$_2$ (1) in the AFM(C) state. In the electronic band structure, the bands are coloured grey to indicate the overlap between, and degeneracy of, the equivalent alpha and beta states.

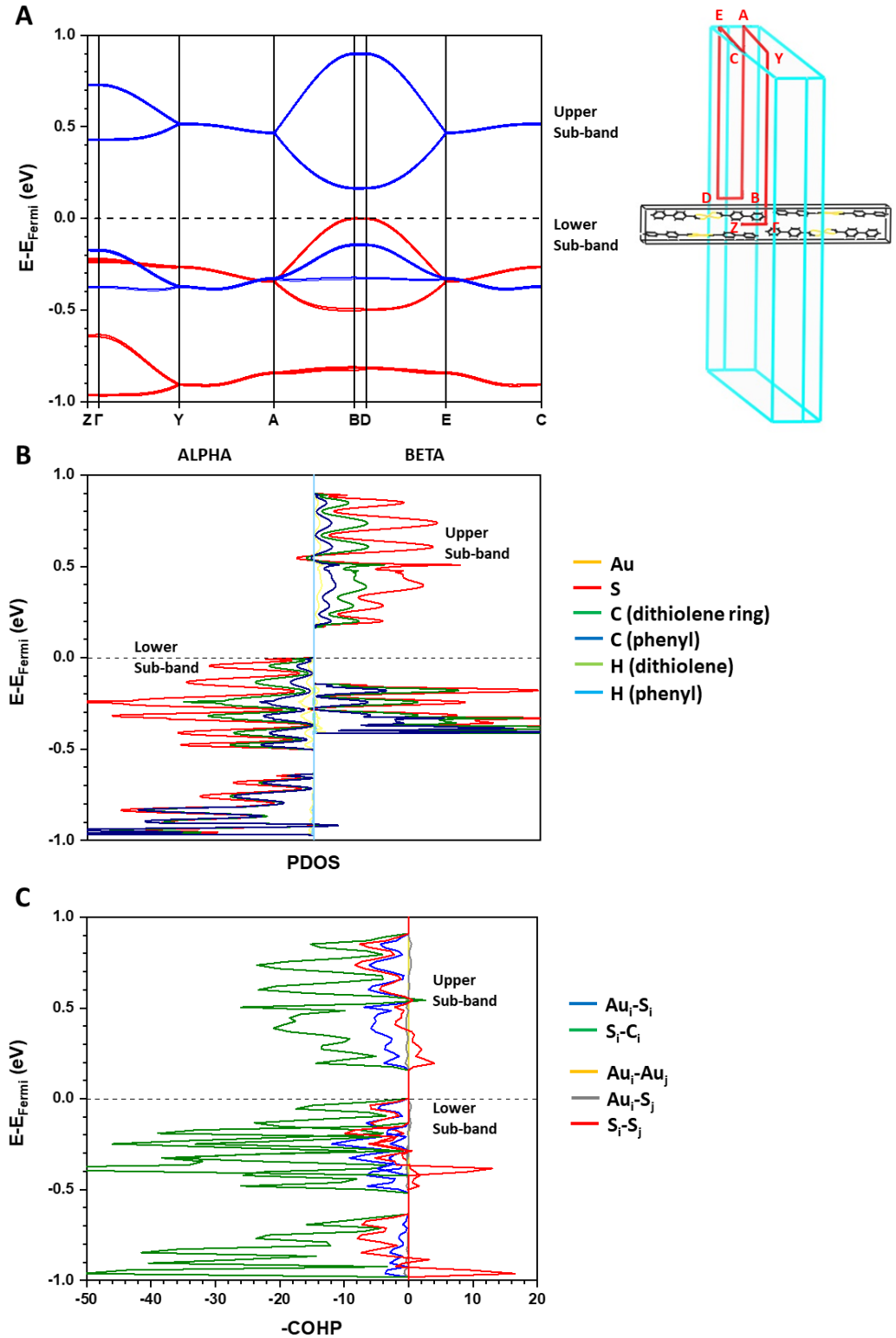

Figure 4.9: Electronic band structure and k-point path (A), projected density of states (B) and COHP plot (C) of the non-optimised ambient-pressure structure of Au(bpedt)$_2$ (1) in the FM state. In the electronic band structure, the bands representing the alpha and beta states are coloured red and blue respectively.

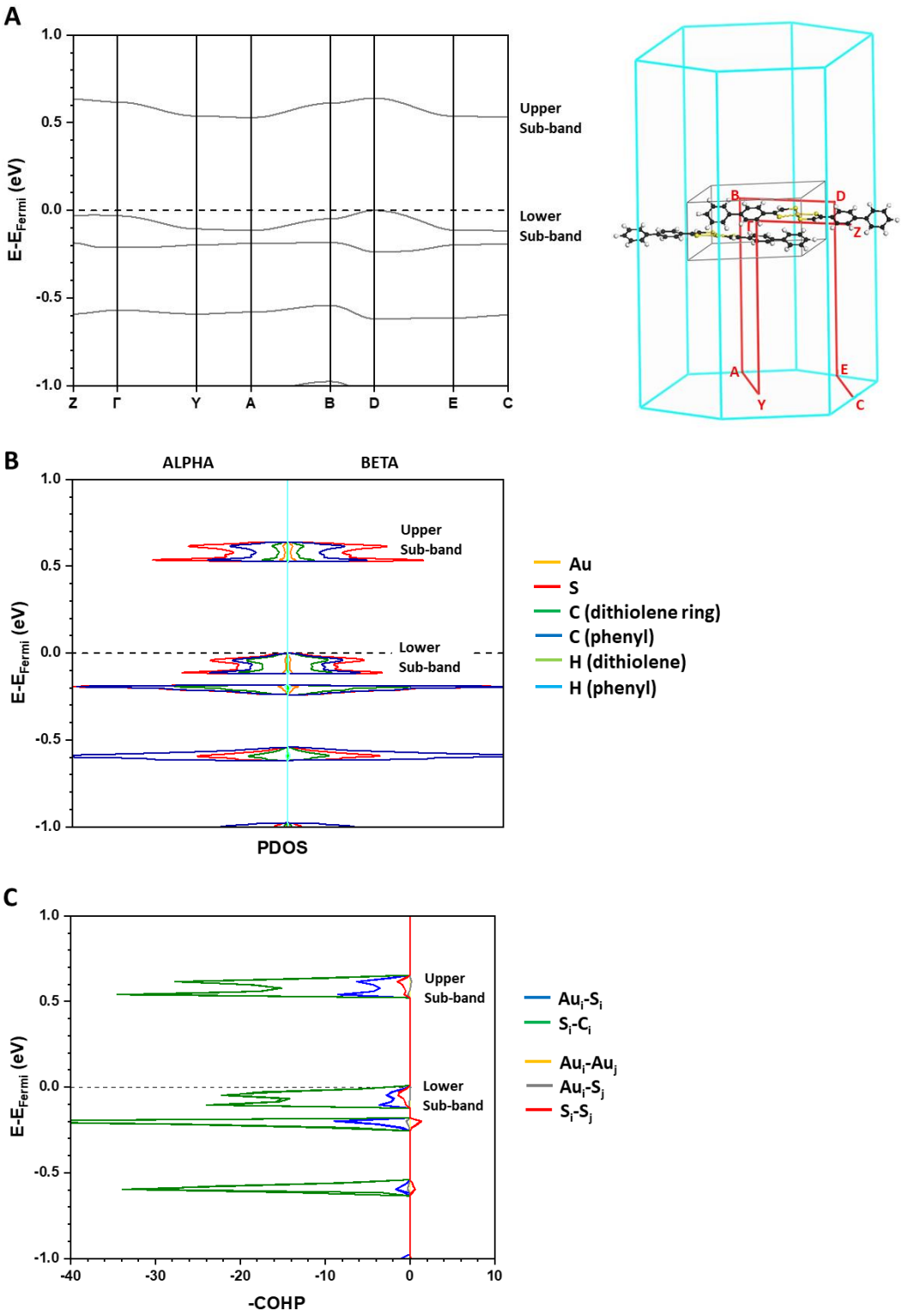

Figure 4.10: Electronic band structure and k-point path (A), projected density of states (B) and COHP plot (C) of the optimised 0.11 GPa structure of Au(bpedt)$_2$ (2) in the AFM state. In the electronic band structure, the bands are coloured grey to indicate the overlap between, and degeneracy of, the equivalent alpha and beta states.

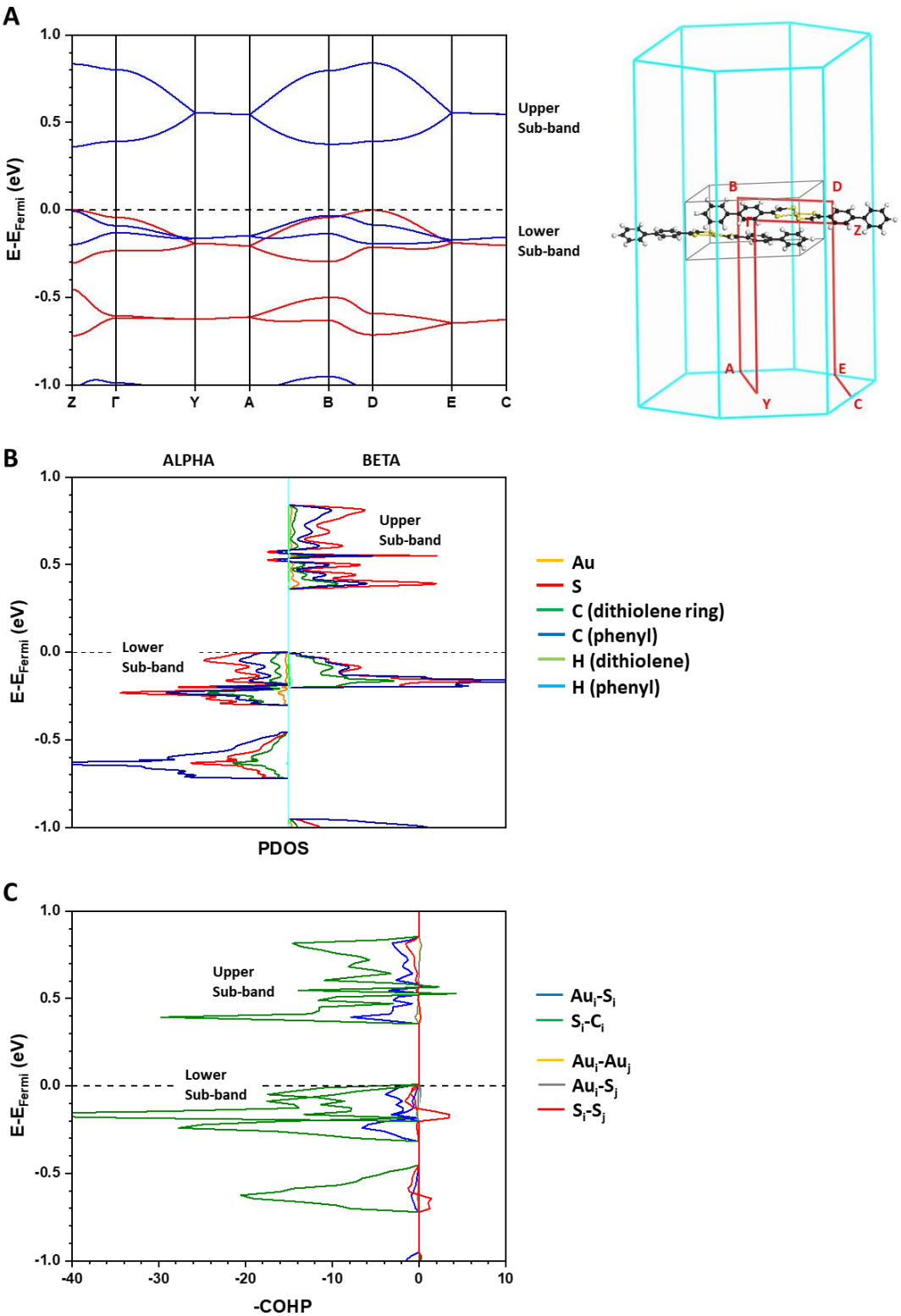

Figure 4.11: Electronic band structure and k-point path (A), projected density of states (B) and COHP plot (C) of the optimised 0.11 GPa structure of Au(bpedt)$_2$ (2) in the FM state. In the electronic band structure, the bands representing the alpha and beta states are coloured red and blue respectively.

The first important observation is that the calculated band structures for both phases show the presence of Hubbard sub-bands; the highest occupied bands consist of half of the unpaired electron α and β states in the AFM configurations and only α states in the FM configurations, while the lowest unoccupied bands represent the remaining half of the α and β states in the AFM configurations and only β states in the FM configurations. As expected for Hubbard sub-bands, the shape of the bands, in terms of the extent of delocalisation along the BZ k-point path, and the atomic contributions to the PDOS show that these bands are spatially similar.

The majority of delocalisation in the sub-bands of both polymorphs is seen along the reciprocal *b* axis direction, namely Γ⟶Y, A⟶B and D⟶E, indicating that the strongest intermolecular interactions are along this direction, with some delocalisation also observed along the reciprocal *a* axis direction for **1**. The sub-bands mainly consist of contribution from the S and C atoms in the dithiolene rings, in good agreement with the atomic contribution to the unpaired spin density previously discussed (Table 4.2). The COHP plots show that the main contribution to the sub-bands are from intramolecular interactions. Nevertheless, there is evidence of weak intermolecular interactions, mostly from S···S contacts, which is unsurprising given the crystal packing does not facilitate significant overlap between Au centres. These results justify the identification of the S···S contacts along the *a* and *b* directions, especially the latter in the case of **1**, from the structures obtained from the diffraction experiments, and their importance for facilitating conductivity in the two polymorphs, given they are the largest contributors towards connectivity between the localised sites.

The hybrid DFT HSE06 functional calculated that for all possible spin configurations of both phases, $Au(bpedt)_2$ can be described as a Mott insulator with a non-zero band gap at the lowest pressure in their respective pressure series. The sub-band gap for **1** in the AFM(C) configuration was calculated as 0.53 eV, with narrow $\boldsymbol{W}$ values of

0.21 eV (Table 4.3). On the other hand, the ***W*** values calculated for FM configuration were much larger, thus resulting in a smaller sub-band gap of 0.13 eV. The larger bandwidths in the FM configuration stems from a splitting of the bands, compared to the AFM configuration in which all bands within the same energy level overlap completely, the explanation for which has not yet been determined. Whilst possessing a similar **U** value to **1**, the ***W*** values of **2** are lower for both spin configurations (Table 4.3), hence resulting in larger sub-band gaps of 0.53 eV and 0.36 eV for the AFM and FM configurations respectively. The difference in the bandwidths between the two polymorphs stems mainly from the differing extents of delocalisation along the *b* axis direction; it appears that the specific crystal packing in **1** facilitates molecular arrangements that in turn allow for more extensive S··· orbital overlap.

Table 4.3: Calculated U, W and sub-band gap values for the lowest energy spin configurations of both polymorphs for their lowest pressure structures.

Polymorph	Spin Configuration	U (eV)	*W* (eV)		Sub-band Gap (eV)
			Lower	Upper	
1	AFM	0.71	0.21	0.21	0.50
	FM	0.75	0.50	0.74	0.13
2	AFM	0.65	0.12	0.11	0.53
	FM	0.75	0.30	0.48	0.36

An experimental activation energy for **1** of 0.11 eV has previously been reported,[1] thus corresponding to a sub-band gap of double that value;[59] the calculated sub-band gaps for the AFM configurations of both phases are therefore in reasonable agreement with this value, although the calculations appear to show Au(bpedt)$_2$ to be a stronger Mott insulator than observed experimentally. Nevertheless, these calculations have provided a more accurate representation of this material as a Mott insulator compared to previous calculations using Extended Hückel Theory which predicted the material to exhibit the metallic state at ambient conditions,[1, 60] due to limitations of the latter method in not treating electron correlation explicitly.[61, 62]

4.5.3 High-pressure solid-state calculations

Similar hybrid DFT calculations were undertaken on higher-pressure structures of **1** and **2** to determine the response of the bandwidths and sub-band gap to the application of pressure. The calculated bandwidths and sub-band gaps of **1** and **2** at various pressure points throughout their respective pressure series are presented in Figure 4.12. The value of **U** throughout the pressure series is also shown in the graph, determined by calculating the energy difference between the midpoint of each Hubbard sub-band, as shown in Figure 4.1.

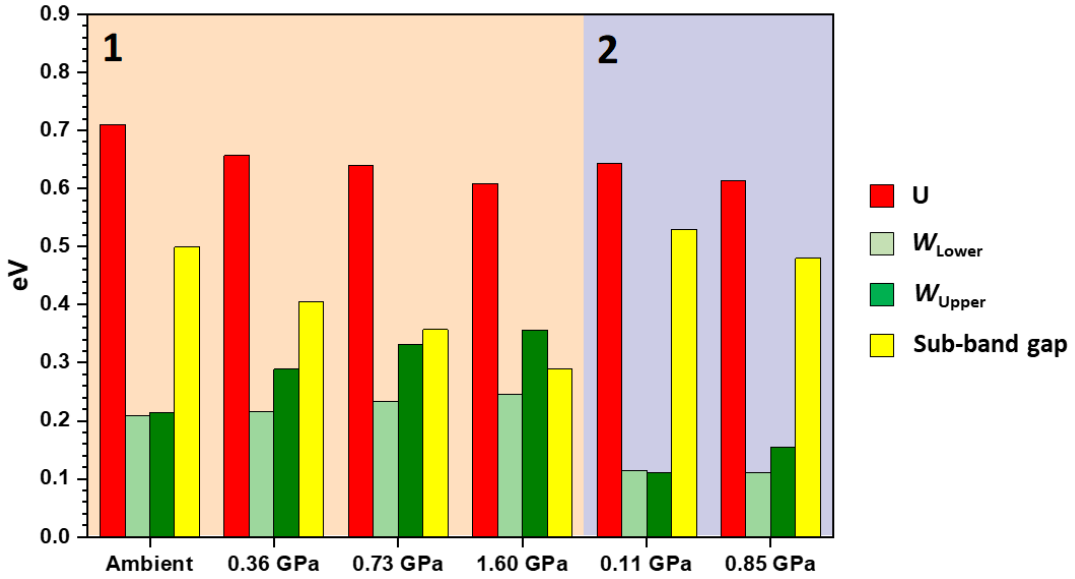

Figure 4.12: U, W and sub-band gap values for the lowest energy AFM configuration of both phases of Au(bpedt)$_2$ throughout their respective pressure series.

In general, the bandwidth values of the upper and lower sub-bands were seen to increase across the pressure series; this is expected result, as compression of the solid-state structure would lead to smaller intermolecular separation and thus enhance intermolecular orbital overlap. Furthermore, the **U** values were determined to decrease throughout the pressure series for both polymorphs, thus indicating that compression of the material resulted in a decrease in on-site repulsion. Both of these

trends lead to the desired result of sub-band gap compression across the pressure series for both polymorphs.

The sub-band gap for the lowest energy AFM configuration of **1** decreased from 0.50 eV to 0.29 eV between ambient and 1.60 GPa; based upon these results the Mott-Hubbard transition would not occur until around 4 GPa, however this has not taken into account any slowing of the rate of volumetric compression at higher pressure. The rate of change in the sub-band gap over this pressure range was consistent between all three hybrid DFT functionals used, with the difference between the functionals solely originating from the value of the ambient pressure sub-band gap. Therefore, if the HSE06 functional was indeed overestimating the sub-band gap in this case, and the experimental band gap was instead considered, the extent of compression observed would see the metallic state formed at around 1.60 GPa.

On the other hand, **2** displayed a very poor response to pressure, with the sub-band gap only decreasing from 0.53 eV to 0.48 eV between 0.11 GPa and 0.85 GPa, with almost no increase in the bandwidth of the lower sub-band. While **2** was shown to exhibit slightly lower compression than **1**, both volumetrically and along the directions associated with S···S interactions, this is not expected to account for such a large discrepancy in the bandwidth responses between the two polymorphs. **1** appears intrinsically to possess greater delocalisation in its band structure, seemingly from a greater extent of orbital overlap derived from shorter S···S contacts and more favourable intermolecular arrangements.

The FM configurations for both phases revealed stronger responses to pressure, with **1** actually forming the metallic state by 0.73 GPa with the sub-band gap closing completely, facilitated by relatively large increases in the bandwidths of both sub-bands. While this result is promising, the energy hierarchy between spin configurations was seen to increase with increasing pressure, to *ca.* 19 kJ mol^{-1} and

5 kJ mol^{-1} for **1** and **2** respectively. Therefore, it is highly unlikely to observe a Mott-Hubbard transition experimentally originating from the FM spin configurations. Furthermore, to emphasise the instability of the FM configuration of **1**, its spin multiplicity was seen to decrease gradually with increasing pressure, reaching a value of *ca.* 1.5 at 1.60 GPa, thus equating to a 70 % decrease in the extent of ferromagnetism compared to that calculated for the optimised wavefunction of the ambient-pressure structure.

The stronger overall response in the bandwidth size to pressure seen in **1** across both types of spin configuration is not surprising, given that it possesses the greater number of intermolecular interactions between neighbouring Au-dithiolene components, with two directions of short S···S contacts facilitated by the nature of the crystal packing, and it has been shown to exhibit faster unit cell compression, compared to the results observed for **2**. However, given the discrepancy between the experimental and calculated sub-band gaps, it is unknown if **1** can undergo an antiferromagnetic insulator-to-metal transition below 2 GPa; more detailed calculations and further experimental work will be required to determine its true behaviour.

4.6 Conclusions

Utilising the complementary techniques of high-pressure synchrotron X-ray diffraction and solid-state hybrid DFT calculations, the structural and electronic band structure response to pressure of two phases of $Au(bpedt)_2$ have been characterised, up to 1.60 GPa and 0.85 GPa for the $P2_1/c$ and previously-unknown $P2_1$ phases respectively. The investigation has revealed that the former undergoes greater unit cell compression and survives to higher pressure and, as a result of this and the nature of the crystal packing allowing a greater number of weak intermolecular interactions, it displayed a stronger electronic response, in terms of the rate of sub-band gap compression *via* bandwidth enlargement. However, these results must be viewed with caution. Firstly, the diffraction experiments on the $P2_1$ phase was negatively affected by poor crystal quality, and thus a clear ordering of unit cell parameter compression could not be established and diffraction could not be obtained above 1.2 GPa; therefore, definite comparisons to the $P2_1/c$ phase cannot be made. Secondly, the size of the $Au(bpedt)_2$ system and the need to reduce the system symmetry to $P1$ in order to study all possible spin configurations meant that the electronic band structures could only be calculated from single-point energy calculations in the case of the $P2_1/c$ phase, with full or atom-only geometry optimisation calculations being beyond the computational resources available for this investigation. However, the results obtained in this work have left a sufficient amount of promise and scope for future work. Based upon the rate of sub-band gap compression, it is not unreasonable that the $P2_1/c$ phase could undergo a Mott-Hubbard transition by 2 GPa, and therefore high-pressure conductivity measurements will need to be undertaken to ascertain if this can be achieved experimentally. Furthermore, the reasoning for the existence of two polymorphs, despite stemming from the same electro-oxidation/crystallisation procedure must be considered, since this might also present similar complications in derivative compounds of $Au(bpedt)_2$ or other Au-based Mott insulator materials.

4.7 References

1. A. Mizuno, H. Benjamin, Y. Shimizu, Y. Shuku, M. M. Matsushita, N. Robertson and K. Awaga, *Adv. Funct. Mater.*, 2019, **29**, 1904181.
2. N. F. Mott, *Rev. Mod. Phys.*, 1968, **40**, 677-683.
3. P. Fazekas, *Lecture notes on electron correlation and magnetism*, World Scientific, Singapore and London, 1999.
4. M. Imada, A. Fujimori and Y. Tokura, *Rev. Mod. Phys.*, 1998, **70**, 1039-1263.
5. N. Mott, *Phys. Today*, 1978, **31**, 42-47.
6. Y. Tokura, Y. Okimoto, S. Yamaguchi, H. Taniguchi, T. Kimura and H. Takagi, *Phys. Rev. B*, 1998, **58**, R1699-R1702.
7. M. M. Qazilbash, M. Brehm, B. G. Chae, P. C. Ho, G. O. Andreev, B. J. Kim, S. J. Yun, A. V. Balatsky, M. B. Maple, F. Keilmann, H. T. Kim and D. N. Basov, *Science*, 2007, **318**, 1750-1753.
8. S. J. Moon, H. Jin, W. S. Choi, J. S. Lee, S. S. A. Seo, J. Yu, G. Cao, T. W. Noh and Y. S. Lee, *Phys. Rev. B*, 2009, **80**, 195110.
9. Y. Okada, T. Arima, Y. Tokura, C. Murayama and N. Mori, *Phys. Rev. B*, 1993, **48**, 9677-9683.
10. F. Nakamura, T. Goko, M. Ito, T. Fujita, S. Nakatsuji, H. Fukazawa, Y. Maeno, P. Alireza, D. Forsythe and S. R. Julian, *Phys. Rev. B*, 2002, **65**, 220402.
11. P. Limelette, P. Wzietek, S. Florens, A. Georges, T. A. Costi, C. Pasquier, D. Jerome, C. Meziere and P. Batail, *Phys. Rev. Lett.*, 2003, **91**, 016401.
12. J. R. Patterson, C. M. Aracne, D. D. Jackson, V. Malba, S. T. Weir, P. A. Baker and Y. K. Vohra, *Phys. Rev. B*, 2004, **69**, 220101.
13. V. T. Phuoc, C. Vaju, B. Corraze, R. Sopracase, A. Perucchi, C. Marini, P. Postorino, M. Chligui, S. Lupi, E. Janod and L. Cario, *Phys. Rev. Lett.*, 2013, **110**, 037401.
14. M. Eckstein and P. Werner, *Phys. Rev. Lett.*, 2013, **110**, 126401.
15. H. Okamoto, T. Miyagoe, K. Kobayashi, H. Uemura, H. Nishioka, H. Matsuzaki, A. Sawa and Y. Tokura, *Phys. Rev. B*, 2011, **83**, 125102.
16. T. Giamarchi, *Physica B*, 1997, **230**, 975-980.
17. N. Mott, *J. Solid State Chem.*, 1990, **88**, 5-7.
18. S. J. Moon, H. Jin, K. W. Kim, W. S. Choi, Y. S. Lee, J. Yu, G. Cao, A. Sumi, H. Funakubo, C. Bernhard and T. W. Noh, *Phys. Rev. Lett.*, 2008, **101**, 195110.
19. C. N. Berglund and H. J. Guggenheim, *Phys. Rev.*, 1969, **185**, 1022-1033.

20. C. N. Berglund and A. Jayaraman, *Phys. Rev.*, 1969, **185**, 1034-1039.
21. M. S. Laad, L. Craco and E. Muller-Hartmann, *Phys. Rev. B*, 2006, **73**, 045109.
22. M. K. Liu, H. Y. Hwang, H. Tao, A. C. Strikwerda, K. B. Fan, G. R. Keiser, A. J. Sternbach, K. G. West, S. Kittiwatanakul, J. W. Lu, S. A. Wolf, F. G. Omenetto, X. Zhang, K. A. Nelson and R. D. Averitt, *Nature*, 2012, **487**, 345-348.
23. L. Craco, *Phys. Rev. B*, 2009, **79**, 085123.
24. T. Yanagisawa and M. Miyazaki, *Europhys. Lett.*, 2014, **107**, 27004.
25. A. J. Schultz, H. H. Wang, L. C. Soderholm, T. L. Sifter, J. M. Williams, K. Bechgaard and M. H. Whangbo, *Inorg. Chem.*, 1987, **26**, 3757-3761.
26. N. C. Schiodt, T. Bjornholm, K. Bechgaard, J. J. Neumeier, C. Allgeier, C. S. Jacobsen and N. Thorup, *Phys. Rev. B*, 1996, **53**, 1773-1778.
27. O. J. Dautel, M. Fourmigue, E. Canadell and P. Auban-Senzier, *Adv. Funct. Mater.*, 2002, **12**, 693-698.
28. W. Suzuki, E. Fujiwara, A. Kobayashi, Y. Fujishiro, E. Nishibori, M. Takata, M. Sakata, H. Fujiwara and H. Kobayashi, *J. Am. Chem. Soc*, 2003, **125**, 1486-1487.
29. S. Kokatam, K. Ray, J. Pap, E. Bill, W. E. Geiger, R. J. LeSuer, P. H. Rieger, T. Weyhermuller, F. Neese and K. Wieghardt, *Inorg. Chem.*, 2007, **46**, 1100-1111.
30. N. Tenn, N. Bellec, O. Jeannin, L. Piekara-Sady, P. Auban-Senzier, J. Iniguez, E. Canadell and D. Lorcy, *J. Am. Chem. Soc*, 2009, **131**, 16961-16967.
31. G. Yzambart, N. Bellec, G. Nasser, O. Jeannin, T. Roisnel, M. Fourmigue, P. Auban-Senzier, J. Iniguez, E. Canadell and D. Lorcy, *J. Am. Chem. Soc*, 2012, **134**, 17138-17148.
32. P. Stoliar, P. Diener, J. Tranchant, B. Corraze, B. Briere, V. Ta-Phuoc, N. Bellec, M. Fourmigue, D. Lorcy, E. Janod and L. Cario, *J. Phys. Chem. C*, 2015, **119**, 2983-2988.
33. A. Filatre-Furcate, T. Roisnel, M. Fourmigue, O. Jeannin, N. Bellec, P. Auban-Senzier and D. Lorcy, *Chem. Eur. J.*, 2017, **23**, 16004-16013.
34. B. Briere, J. Caillaux, Y. Le Gal, D. Lorcy, S. Lupi, A. Perucchi, M. Zaghrioui, J. C. Soret, R. Sopracase and V. T. Phuoc, *Phys. Rev. B*, 2018, **97**, 035101.
35. C. F. Macrae, P. R. Edginston, P. McCabe, E. Ridcock, G. P. Shields, R. Taylor, M. Towler, J. Van der Streck, *J. Appl. Cryst.*, 2006, **39**, 453-457.
36. E. Broadhurst, MChem Project Report, University of Edinburgh, 2018.
37. S. A. Moggach, D. R. Allan, S. Parsons and J. E. Warren, *J. Appl. Crystallogr*, 2008, **41**, 249-251.
38. G. J. Piermarini, S. Block, J. D. Barnett and R. A. Forman, *J. Appl. Phys.*, 1975, **46**, 2774-2780.
39. H. Nowell, S. A. Barnett, K. E. Christensen, S. J. Teat and D. R. Allan, *J. Synchrotron Radiat.*, 2012, **19**, 435-441.

40. CrysAlisPro, Oxford Diffraction/Aligent Technologies UK Ltd, Yarnton, UK
41. P. W. Betteridge, J. R. Carruthers, R. I. Cooper, K. Prout and D. J. Watkin, *J. Appl. Crystallogr*, 2003, **36**, 1487-1487.
42. A. Altomare, G. Cascarano, G. Giacovazzo, A. Guagliardi, M. C. Burla, G. Polidori and M. Camalli, *J. Appl. Crystallogr*, 1994, **27**, 435-435.
43. R. Dovesi, R. Orlando, B. Civalleri, C. Roetti, V. R. Saunders and C. M. Zicovich-Wilson, *Z. Kristallogr. Cryst. Mater.*, 2005, **220**, 571-573.
44. R. Dovesi, A. Erba, R. Orlando, C. M. Zicovich-Wilson, B. Civalleri, L. Maschio, M. Rerat, S. Casassa, J. Baima, S. Salustro and B. Kirtman, *Wiley Interdiscip. Rev. Comput. Mol. Sci.* 2018, **8**, e1360.
45. J. Heyd, J. E. Peralta, G. E. Scuseria and R. L. Martin, *J. Chem. Phys.*, 2005, **123**, 174101.
46. D. Andrae, U. Haussermann, M. Dolg, H. Stoll and H. Preuss, *Theor. Chim. Acta*, 1990, **77**, 123-141.
47. K. Doll, P. Pyykko and H. Stoll, *J. Chem. Phys.*, 1998, **109**, 2339-2345.
48. H. J. Monkhorst and J. D. Pack, *Phys. Rev. B*, 1976, **13**, 5188-5192.
49. P. J. Stephens, F. J. Devlin, C. F. Chabalowski and F. J. Frisch, *J. Phys. Chem.*, 1994, **98**, 11623.
50. J. Heyd, G. E. Scuseria and M. Ernzerhof, *J. Chem. Phys.*, 2003, **118**, 8207-8215.
51. J. Heyd, G. E. Scuseria and M. Ernzerhof, *J. Chem. Phys.*, 2006, **124**, 219906.
52. C. Adamo and V. Barone, *J. Chem. Phys.*, 1999, **110**, 6158-6170.
53. J. P. Perdew, K. Burke and M. Ernzerhof, *Phys. Rev. Lett.*, 1996, **77**, 3865-3868.
54. R. Dovesi, V. R. Saunders, C. Roetti, R. Orlando, C. M. Zicovich-Wilson, F. Pascale, B. Civalleri, K. Doll, N. M. Harrison, I. J. Bush, P. D'Arco, M. Llunel, Y. Noël, L. Maschio, A. Erba, M. Rérat and S. Casassa, *CRYSTAL17 User's Manual*, accessed January 2019.
55. A. A. L. Michalchuk, P. T. Fincham, P. Portius, C. R. Pulham and C. A. Morrison, *J. Phys. Chem. C*, 2018, **122**, 19395-19408.
56. A. J. Garza and G. E. Scuseria, *J. Phys. Chem. Lett.*, 2016, **7**, 4165-4170.
57. A. V. Krukau, O. A. Vydrov, A. F. Izmaylov and G. E. Scuseria, *J. Chem. Phys.*, 2006, **125**, 224106.
58. M. J. Frisch, G. W. Trucks, H. B. Schlegel, G. E. Scuseria, M. A. Robb, J. R. Cheeseman, G. Scalmani, V. Barone, B. Mennucci, G. A. Petersson, H. Nakatsuji, M. Caricato, H. X. Li, P. Hratchian, A. F. Izmaylov, J. Bloino, G. Zheng, J. L. Sonnenberg, M. Hada, M. Ehara, K. Toyota, R. Fukuda, J. Hasegawa, M. Ishida, T. Nakajima, Y. Honda, O. Kitao, H. Nakai, T. Vreven, J. A. Montgomery, Jr., J. E. Peralta, F. Ogliaro, M. Bearpark, J. J. Heyd, E. Brothers, K. N. Kudin, V. N. Staroverov, R. Kobayashi, J. Normand, K. Raghavachari, A. Rendell, J. C. Burant, S. S. Iyengar, J. Tomasi, M. Cossi, N. Rega, J.

M. Millam, M. Klene, J. E. Knox, J. B. Cross, V. Bakken, C. Adamo, J. Jaramillo, R. Gomperts, R. E. Stratmann, O. Yazyev, A. J. Austin, R. Cammi, C. Pomelli, J. W. Ochterski, R. L. Martin, K. Morokuma, V. G. Zakrzewski, G. A. Voth, P. Salvador, J. J. Dannenberg, S. Dapprich, A. D. Daniels, Ö. Farkas, J. B. Foresman, J. V. Ortiz, J. Cioslowski and D. J. Fox, GAUSSIAN09, Gaussian Inc., Wallingford, C.T., 2009.

59. J. S. Blakemore, *Solid state physics*, W.B. Saunders, Philadelphia, 1969.

60. R. Hoffmann, *J. Chem. Phys.*, 1963, **39**, 1397-1412.

61. M. H. Whangbo, *Theor. Chem. Acc.*, 2000, **103**, 252-256.

62. A. Mailman, S. M. Winter, X. Yu, C. M. Robertson, W. J. Yong, J. S. Tse, R. A. Secco, Z. X. Liu, P. A. Dube, J. A. K. Howard and R. T. Oakley, *J. Am. Chem. Soc*, 2012, **134**, 9886-9889.

Chapter 5

Investigating the High-Pressure Structural Response and Energy Hierarchy of Solid-State Intermolecular Interactions of 1,3,5-triathia-2,4,6-triazapentalenyl

5.1 Synopsis

This chapter will focus on a heterocyclic open-shell system which exhibits magnetic bistability upon exposure to varying temperature or light, which offers control of magnetic properties over a wide hysteresis loop. Herein, high-pressure X-ray diffraction experiments were undertaken to investigate whether the structural phase transition facilitated by temperature can also be observed under the application of pressure. Results were complemented by semi-empirical PIXEL calculations to provide an energy hierarchy of the intermolecular interactions in this material at ambient-pressure and high-pressure conditions.

5.2 Disclaimer

The crystal samples of 1,3,5-triathia-2,4,6-triazapentalenyl (TTTA) for this work were provided by Asato Mizuno (obtained PhD degree from Nagoya University, Japan, 2015-2018).

5.3 Introduction

Magnetism is another property of materials which can be exploited for its response to the application of external stimuli. There is considerable interest in materials that possesses two structural phases, each with different magnetic properties, which can coexist within a certain range of experimental conditions; this trait is known as bistability, and materials that exhibit this behaviour have been explored for potential application in memory or sensory devices.[1-4] One well-known example of magnetic functional materials are spin-crossover transition metal complexes,[5, 6] in which an external stimulus (temperature, light, or pressure)[7-11] causes a transition of the *d*-electron configuration between high-spin and low-spin configurations, which thus

alters the magnetic properties of the complex and has an associated structural change in the metal coordination geometry and metal-ligand bond lengths.[12] While this phenomenon was first observed in iron dithiocarbamate complexes in the 1930s,[13, 14] the field has since expanded with investigations on various classes of transition metal-based materials, such as metallic grid complexes,[15-19] polymers,[20, 21] and framework materials.[22-25] The field of magnetic materials has also expanded to look at organic molecular magnets,[26, 27] consisting of neutral molecular radicals synthesised with sufficient steric and electronic hindrance so that the unpaired spins remain monomeric, with the aim of achieving changes in magnetism through the ordering or disordering of the unpaired spins throughout the crystal structure as they respond to the external stimuli. One class of organic molecule magnets of considerable interest are the heterocyclic thiazyl π-type radicals which include, but are not limited to, molecules containing the 1,3,2-dithiazolyl (DTA) functional group; these have been shown to exhibit a variety of gradual, abrupt, hysteretic and non-hysteretic spin transition behaviours.[28-35]

One DTA material of interest, which will be sole focus of this chapter, is 1,3,5-triathia-2,4,6-triazapentalenyl, hereafter referred to by the established literature abbreviation TTTA. This planar molecular system consists of two interconnected 5-membered aromatic rings of C, N and S atoms (Figure 5.1A).[36] The radical electron is formally designated onto the N atom on the –S–N–S– moiety, but has been shown to be more delocalised across the entire molecule, primarily on all three atoms of that moiety.[37, 38] TTTA is a molecule of considerable interest and multiple publications have investigated its magnetic properties at various experimental conditions. Firstly, TTTA was shown to display a magnetic phase transition, between a high temperature (HT) paramagnetic phase and low temperature (LT) diamagnetic phase.[37, 38] The magnetic phase transition has an associated structural phase transition, between a $P2_1/c$ polymorph at HT, which is also the phase in which it crystallises at room

temperature (RT), and a $P\bar{1}$ polymorph at LT (Figures 5.1B and 5.1C), with a minimal volumetric difference between the two polymorphs.[37, 38] Both polymorphs are dominated by the presence of columns of π-stacking interactions, with regular π-stacks (···A···A···A···)$_n$ in the $P2_1/c$ polymorph (Figure 5.1B) and with distorted π-stacks which include fully-eclipsed π-dimers (···A-A···A-A···)$_n$ in the $P\bar{1}$ polymorph (Figure 5.1C). The molecules within the eclipsed dimer are not precisely parallel; a shorter contact distance is observed between the overlapping –S–N–S– moieties (3.2739(29) Å) compared to the overlapping –N–S–N– moieties (3.5064(9) Å),[37] which has been attributed to interaction between the unpaired electrons on each molecule, since they are mostly located on the –S–N–S– moieties. (Figure 5.1D).[39]

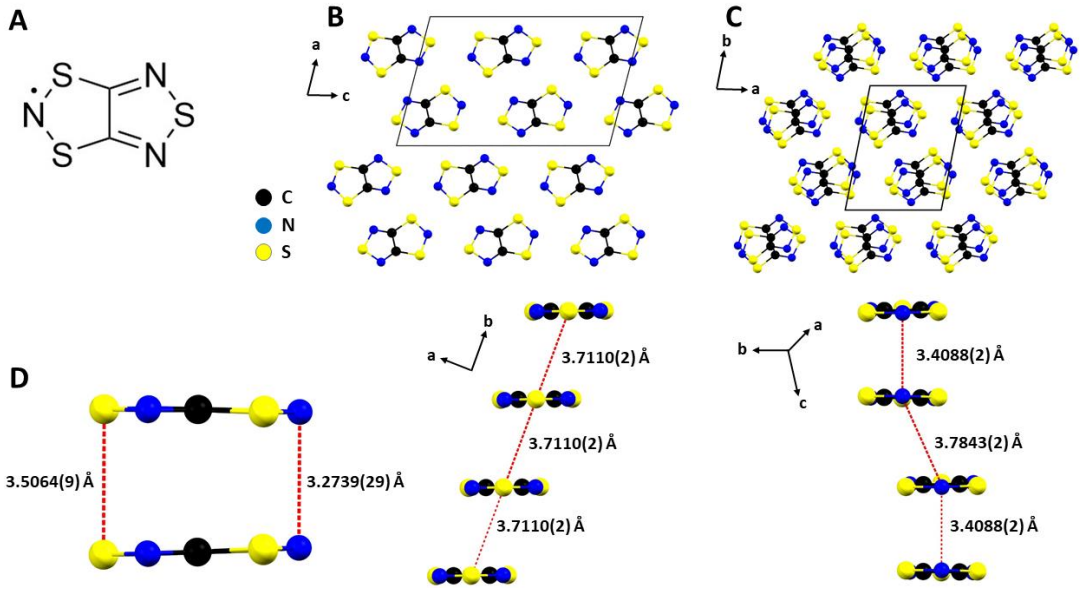

Figure 5.1: A: Molecular structure of TTTA. B: Crystal packing (above) and intra-column molecular separation (below) in the $P2_1/c$ (HT) phase of TTTA (adapted from CSD reference SAXPOW05).[37] C: Crystal packing (above) and intra-column molecular separation in the $P\bar{1}$ (LT) phase of TTTA (adapted from CSD reference SAXPOW06).[37] D: Eclipsed dimer in $P\bar{1}$ (LT) phase, showing slight distortion in parallel arrangement of dimer. Images created using Mercury.[40]

Between the columns of TTTA molecules, formed by the π-stacking interactions, there are multiple types of lateral interactions, generally described by short S···N contact distances that range between 2.9 Å and 3.7 Å, and are thus comparable to their combined van der Waals radii (*ca.* 3.4 Å).[41] That said, there is a considerable difference

between the inter-column arrangements in the two phases; in the $P\bar{1}$ phase, all molecules are approximately parallel with their neighbours with the small deviations from true parallelism caused by the aforementioned shorter intermolecular N···N distances in the eclipsed dimer, whereas in the $P2_1/c$ phase the molecules are stacked in a herringbone arrangement with some inter-column stacking angles of *ca.* 42° (as shown in Figure 5.2).

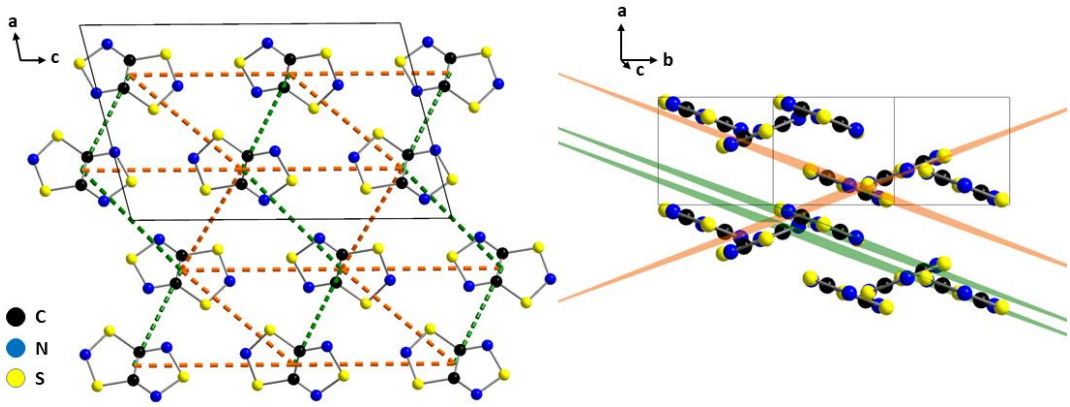

Figure 5.2: Two different views of the packed crystal structure of the P2₁/c phase of TTTA. LEFT: All green lines indicate neighbouring molecules which are parallel, while all orange lines indicate neighbouring molecules which are related by an angle of 41.83(2)°. RIGHT: Examples of each of the angular relationships between neighbouring molecules, with the plane colours indicating the angle between the two molecules. Images created using DIAMOND.[42]

In both phases, the interactions between neighbouring unpaired spins along the π-stacking direction have been deemed to be antiferromagnetic: very strong in the case of eclipsed dimer in the LT phase, and only moderate in the HT phase.[43-45] While the magnetic coupling constants of the inter-column interactions have been calculated to be considerably lower,[41, 43, 44] they have been deemed to be of sufficient energetic strength to stabilise the crystal packing arrangements of both polymorphs and thus cause a wide magnetic hysteresis loop to be exhibited by the material; the HT⟶LT and LT⟶HT transitions occur abruptly at $T_{\downarrow}$ = 230 K and $T_{\uparrow}$ = 305 K respectively, and therefore the material displays magnetic bistability with both polymorphs observable at room temperature (RT).[37] However, neither the intra-column nor the inter-column interactions have been quantified from the perspective of intermolecular energies.

More recent investigations have focused on revealing more intricate details of the behaviour of each polymorph and thus of the phase transition itself. Firstly, at LT the energy minimum is represented by the $P\bar{1}$ polymorph, with the $P2_1/c$ phase acting as the transition state between the degenerate $(\cdots A\text{-}A\cdots A\text{-}A\cdots)_n$ and $(\text{-}A\cdots A\text{-}A\cdots A\text{-})_n$ π-stacking configurations of the $P\bar{1}$ polymorph.[33, 46] However, as highlighted previously, this transition is associated with a major inter-column rearrangement, and thus at lower temperatures the structure is trapped in the $P\bar{1}$ polymorph. This explains the high temperatures required for the LT⟶HT transition. At higher temperatures, the transition to the $P2_1/c$ phase occurs, and that polymorph is stabilised by considerable vibrational entropy caused by pair-exchange dynamics (PED) within the π-stacking columns.[33, 46] In other words, in the $P2_1/c$ phase, the regular π-stacking columns obtained from X-ray crystallography is only representative of the average, and most probable, structure; the material is actually converting between $(\cdots A\text{-}A\cdots A\text{-}A\cdots)_n$ and $(\text{-}A\cdots A\text{-}A\cdots A\text{-})_n$ dimer configurations on the picosecond timescale.[46] However, it should be noted that the dimerisation occurring in the $P2_1/c$ polymorph is different to that in the $P\bar{1}$ phase, given that the inter-column interactions in the $P2_1/c$ phase are being maintained with this PED behaviour.[45] The PED behaviour, along with the strength and nature of the inter-column interactions, has therefore been cited as the cause for the considerably lower HT⟶LT transition temperature, and also has been shown to affect the magnetic coupling constants observed in the $P2_1/c$ phase.[45] Taking the PED behaviour into account, new intra-column coupling constants were calculated (*ca.* -440 cm^{-1}),[45] which were about twice as strong as those determined from the static X-ray crystallographic model,[43, 44] but still considerably less than those calculated for the eclipsed dimer in the $P\bar{1}$ polymorph (*ca.* -2200 cm^{-1}).[45]

The magnetic phase transition has also been observed under photo-irradiation,[47-50] but it has not been obtained under the application of pressure. However, the magnetic

properties of TTTA have been shown to be responsive to pressure, specifically through the gradual suppression of the extent of paramagnetism.[51] By 1.5 GPa, the highest pressure point of the investigation, the paramagnetism was less than 50 % of that observed at ambient pressures.[51] If the rate of suppression, which was consistent throughout the pressure series, was maintained to even higher pressures it is expected that the paramagnetism would be completely supressed by 3 GPa. Another response to pressure was observed in the transition temperatures, which were seen to increase to $T_{\downarrow} \approx 275$ K and $T_{\uparrow} \approx 330$ K by 1.5 GPa.[51] From these results, further increases in pressure would see $T_{\downarrow}$ move to within the range of room temperature. It has been stated in the literature that the magnetic phase transition is driven by the application of pressure,[28] however it has not yet been achieved to completion. Furthermore, it is currently uncertain if the structural component of the phase transition also occurs at a critical pressure, once $T_{\downarrow}$ has increased to a sufficient value.

5.3.1 Aim of research

In light of the fact that currently no structural response of TTTA to pressure has been reported in the literature, the primary objective of this current study was to utilise high-pressure diffraction experiments to investigate if the same structural phase transition observed under photo-irradiation and variable temperature conditions is also enabled by high-pressure. This new-found information would ideally provide a connection to the paramagnetic suppression observed in this material as a response to pressure. Furthermore, semi-empirical PIXEL calculations have been undertaken to determine the energetic hierarchy of the intermolecular interactions in the crystal structures of both polymorphs of TTTA, an alternative perspective to the magnetic interaction hierarchy already reported in the literature.[43-45] By specifically considering the relative strengths of the strongest π-stacking and inter-column interactions, there is the expectation that the claims in the literature regarding the source of the wide magnetic hysteresis behaviour could be clarified.

5.4 Methods

5.4.1 Ambient-pressure X-ray crystallography

Ambient pressure diffraction data was obtained at room temperature from a full sphere collection on a single crystal of TTTA, utilising a series of ω scans, on a Bruker SMART APEX II in-house laboratory diffractometer with monochromated Mo-Kα X-ray radiation (λ=0.71073 Å, 17.4 keV). These sets of data were integrated using the program SAINT, with the SADABS absorption correction.[52, 53] Sir92 was utilised for the structure solutions within CRYSTALS, with all data refined against F^2.[54, 55] All non-hydrogen atoms were refined anisotropically.

5.4.2 High-pressure X-ray crystallography

High-pressure diffraction experiments were undertaken on a single crystal of TTTA, loaded in a modified Merrill-Bassett diamond anvil cell alongside a ruby crystal (acting as the in-situ pressure calibrant) and the hydrostatic pressure transmitting medium Daphne 7474 (a mixture of silicone oil and 2,2,8,8 tetra-alkylsilane).[56-61] The high-pressure diffraction data were obtained on the Diamond Light Source I19 EH2 beamline,[62] utilising a Newport 4-circle κ-geometry diffractometer, installed with Pilatus 300 K detector, and tuneable monochromatic X-ray radiation set to 0.4859 Å (25.5 keV) at various pressures up to 4.56 GPa. Data were collected on a series of ω scans, adapted to avoid shading of the detector from the cell body, with a step size and exposure time of 0.2° and 0.2 s respectively. Data reduction (integration and absorption correction) was undertaken using the CrysAlisPro software suite.[63]

The structure solutions for the high-pressure data was carried out using CRYSTALS.[55] The ambient pressure-structure was used as the input model, with the structure allowed to refine against each high-pressure data set and adjust to the updated unit

cell parameters. All 1,2 and 1,3 distances were restrained. Moreover, planar, vibrational and thermal similarity restraints were applied across the TTTA molecule. The data was refined against F^2 with anisotropic atomic displacement refinement for non-hydrogen atoms in all cases.

5.4.3 PIXEL calculations

Literature structures and structures obtained from the ambient and high-pressure diffraction experiments in this investigation were used as the starting models to calculate the molecular electron density in both polymorphs of TTTA by quantum mechanical calculations using the GAUSSIAN09 program with the literature-established MP2/6-31G** level of theory and basis set combination.[64, 65] The electron density model for each individual structure was then assigned to the PIXEL-C component of the CLP-PIXEL suite,[66, 67] which allowed for the calculation of the dimer and lattice energies. For all the structures investigated, the entire process was streamlined by the MRPixel program,[67] which automated the process of file generation, transferring files to and from the computing cluster required to run the molecular electron density calculations and starting the calculation procedure within PIXEL-C, resulting in the final output files with all lattice and interaction energies calculated and listed.

Interactions were only considered for molecules that had a centroid position at a distance of up to 15 Å from the central reference molecule. The molecular electron density on each molecule was split into cubed pixels, with dimensions of 0.08 Å, which were then later combined into blocks of 3 × 3 × 3 superpixels (in other words, the condensation level of 3 used). This combination of density step size and condensation level, optimised for this system, was in line with those established in the literature.[68]

5.5 Results and Discussion

5.5.1 Ambient-pressure and high-pressure X-ray crystallography

At ambient pressure, the structure of the expected $P2_1/c$ polymorph of TTTA was obtained successfully. The structural response of TTTA to pressure was examined by undertaking a series of synchrotron X-ray diffraction experiments on TTTA at various pressures up to 4.56 GPa. The extent of each unit cell parameter compression was determined by comparing the unit cell parameters at each pressure point with those obtained at ambient pressure; Figure 5.3 shows the compression curves for all unit cell parameters throughout the pressure series.

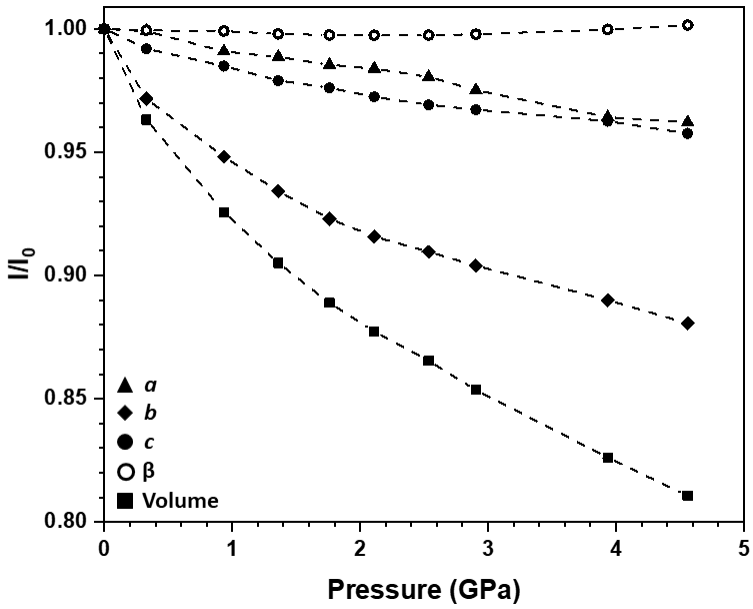

Figure 5.3: Compression curves of each of the unit cell parameters (a, triangle; b, diamond; c, closed circle; beta, open circle; volume, square) of TTTA throughout the pressure series up to 4.56 GPa, in comparison to the unit cell parameters obtained at ambient conditions. Error bars are smaller than the symbols used.

Throughout the entirety of the pressure series, TTTA exhibited very smooth compression, especially in terms of the unit cell volume and *b* axis parameter. Over 19% volumetric compression was observed by 4.56 GPa, after which no further

diffraction reflections were obtained, attributed to surpassing the hydrostatic limit of the pressure transmitting medium.[59, 60] This extent of volumetric compression up to 4.56 GPa equates to a bulk modulus (B) of 9.0(4) GPa, when the pressure-volume data is fitted to the 3rd-order Birch-Murnaghan EoS,[70] which is comparable to those obtained for other molecular spin-crossover materials.[71, 72] The majority of compression was attributed to the *b* axis direction, with it achieving 12 % compression by the final pressure point; this corresponds to a decrease in the *b* axis parameter, and thus in the intermolecular separation in the π-stacking columns, from 3.7100(2) Å to 3.2672(6) Å. The *a* and *c* axis directions, which contribute to the side-by-side and head-to-tail inter-column interactions of TTTA molecules respectively, showed lesser extents of compression, *ca.* 4 % each by 4.56 GPa. At lower pressures the difference in compression between the two axes is larger, in favour of the *c* axis, but the two curves appear to converge towards higher pressures. No significant change was observed in the beta angle across the pressure series.

The main conclusion from the series of high-pressure diffraction experiments is that no structural phase transition was observed to the $P\bar{1}$ phase as seen upon cooling or to a previously-undiscovered polymorph, despite well-exceeding the pressure at which it is hypothesised that the paramagnetism would be completely quenched. Without magnetism data above 1.5 GPa, it is uncertain if the suppression of the paramagnetism continues at the same rate as below 1.5 GPa, but the results of the high-pressure diffraction experiments have clearly proven that the gradual rate of paramagnetic suppression is not associated with a structural phase transition within the pressure range up to 4.6 GPa.

5.5.2 PIXEL calculations on ambient-pressure structures

Utilising the PIXEL method, the energetically-dominant intermolecular interactions within the room-temperature crystal structures of both polymorphs of TTTA have

been determined. In the case of the $P2_1/c$ polymorph, the ambient-pressure structure determined in this study was utilised as the model for electron density calculation. Within the set radius of 15 Å around the central reference molecule, a total of 70 unique interactions were found in the ambient-pressure structure of the $P2_1/c$ phase, over half of which had duplicates due to symmetry. The nine strongest interactions had total energy values stronger than 2.5 kJ mol^{-1}; the component and total energies of each of these interactions are shown in Table 5.1, and Figure 5.4 shows a graphical representation of the dimers representing each of these interactions.

Table 5.1: Intramolecular separation distances, component and total energy terms for the nine strongest interactions calculated for the ambient pressure structure of the $P2_1/c$ phase of TTTA.

Interaction	Intramolecular Centroid Separation (Å)	Coulombic Energy (kJ mol^{-1})	Polarisation Energy (kJ mol^{-1})	Dispersion Energy (kJ mol^{-1})	Repulsion Energy (kJ mol^{-1})	Total Energy (kJ mol^{-1})
1	3.71	-10.8	-8.5	-46.3	47.4	-18.2
2	5.52	-25.4	-8.9	-24.6	41.8	-17.1
3	6.73	-19.5	-6.6	-17.4	26.3	-17.1
4	5.17	-4.6	-2.1	-17.5	13.2	-10.9
5	7.54	-8.8	-4.4	-12.5	16.8	-8.9
6	5.82	-6.8	-5.9	-17.1	22.5	-7.4
7	7.14	-5.1	-3.0	-12.8	14.3	-6.5
8	7.00	-0.1	-0.3	-5.2	1.4	-4.3
9	8.18	-0.4	-0.2	-2.7	0.5	-2.8

Interaction 1 was clearly identified as the π-type dispersion-dominated interaction between slipped overlapping molecules previously identified in the literature responsible for the stacking columns along the *b* axis direction. This interaction was identified as having the strongest magnetic coupling constant by far in $P2_1/c$ phase; however, the PIXEL calculations, which instead calculate the energetic strength of the interactions in the crystal structure, have revealed an interaction energy hierarchy in which the three strongest interactions are very similar in energy. Interactions 2 and 3 have been identified as two different types of inter-column interactions, both of which calculated as having a higher contribution towards the total interaction energy from

the Coulombic energy term, due to the short N···S contact distances, rather than the dispersion energy term as seen for interaction 1. Interaction 2 corresponds to the primary interaction between columns within the unit cell, whereas interaction 3 is the strongest interaction responsible for linking columns between unit cells.

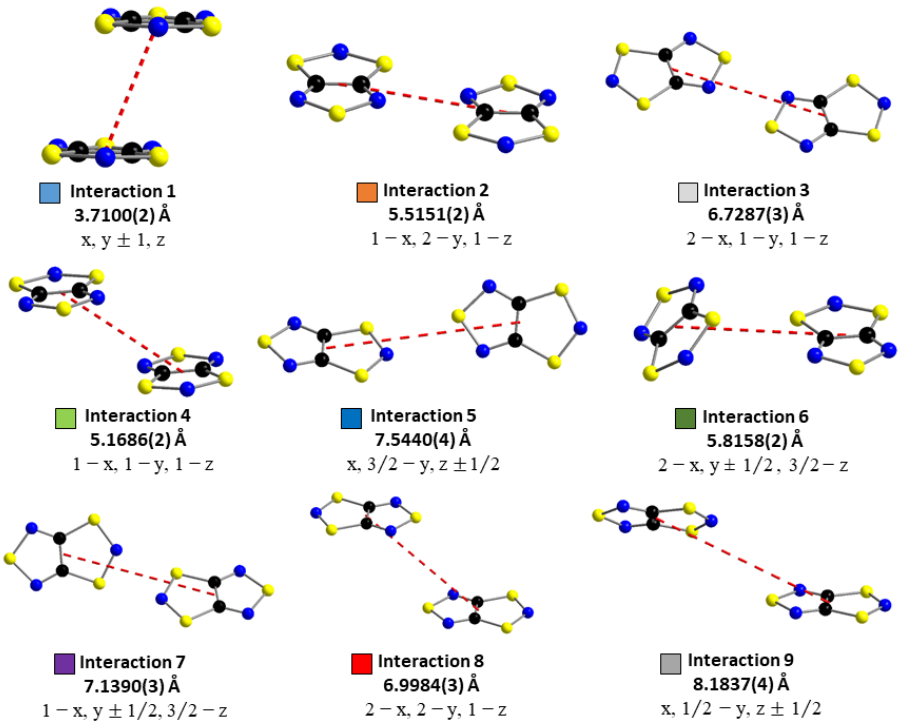

Figure 5.4: Strongest identified intermolecular interactions in the ambient pressure HT phase of TTTA, with colour identifiers to match those used in the energy framework diagram in Figure 5.3. Images created using DIAMOND.[42]

Figure 5.5 shows how the combination of these three interactions alone account for the connectivity between most of the molecules in the crystal structure; the images in this figure are classed as energy frameworks, which show the directionality of intermolecular interactions throughout the crystal structure, with the thickness of the lines indicating the strength of the interactions between the molecule centroids scaled to correspond with the interaction energy. Unlike interaction 1, which is exclusively aligned to the *b* axis direction, interactions 2 and 3 possess contribution from all three axis directions. The only other almost uni-directional interaction is interaction 5,

responsible for linking columns along the *c* axis direction. The five other strongest interactions, which have not been discussed until now, are seen to fill in the gaps between molecules already connected by interactions 1, 2, 3 and 5. The energy frameworks presented in Figure 5.6 show a substantially more complex representation of the crystal structure, once the contribution from all nine of the strongest interactions have been considered.

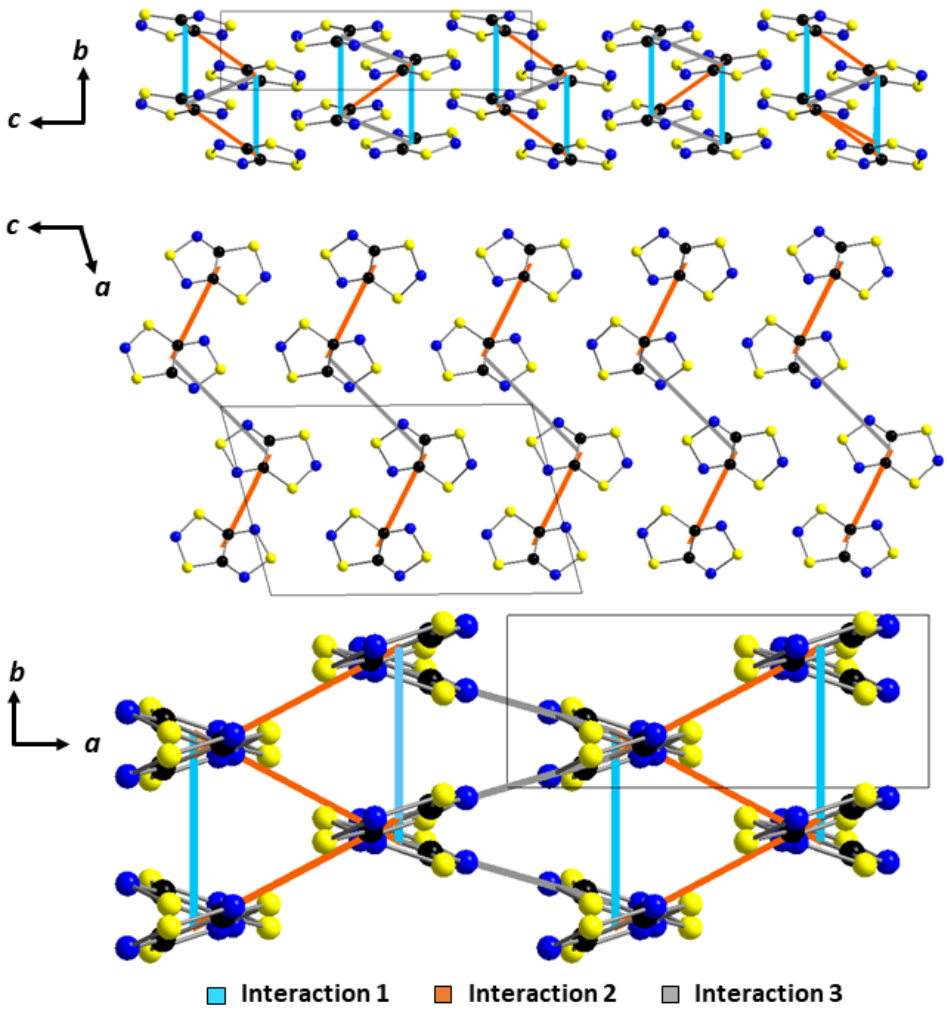

Figure 5.5: Energy framework of the ambient pressure HT phase structure of TTTA, viewing along, or cutting through, various directions of the crystal structure, consisting of only the strongest three interactions, as calculated by the PIXEL method. Interaction rods are coloured to match the interactions shown in Figure 5.4. Images created using DIAMOND.[42]

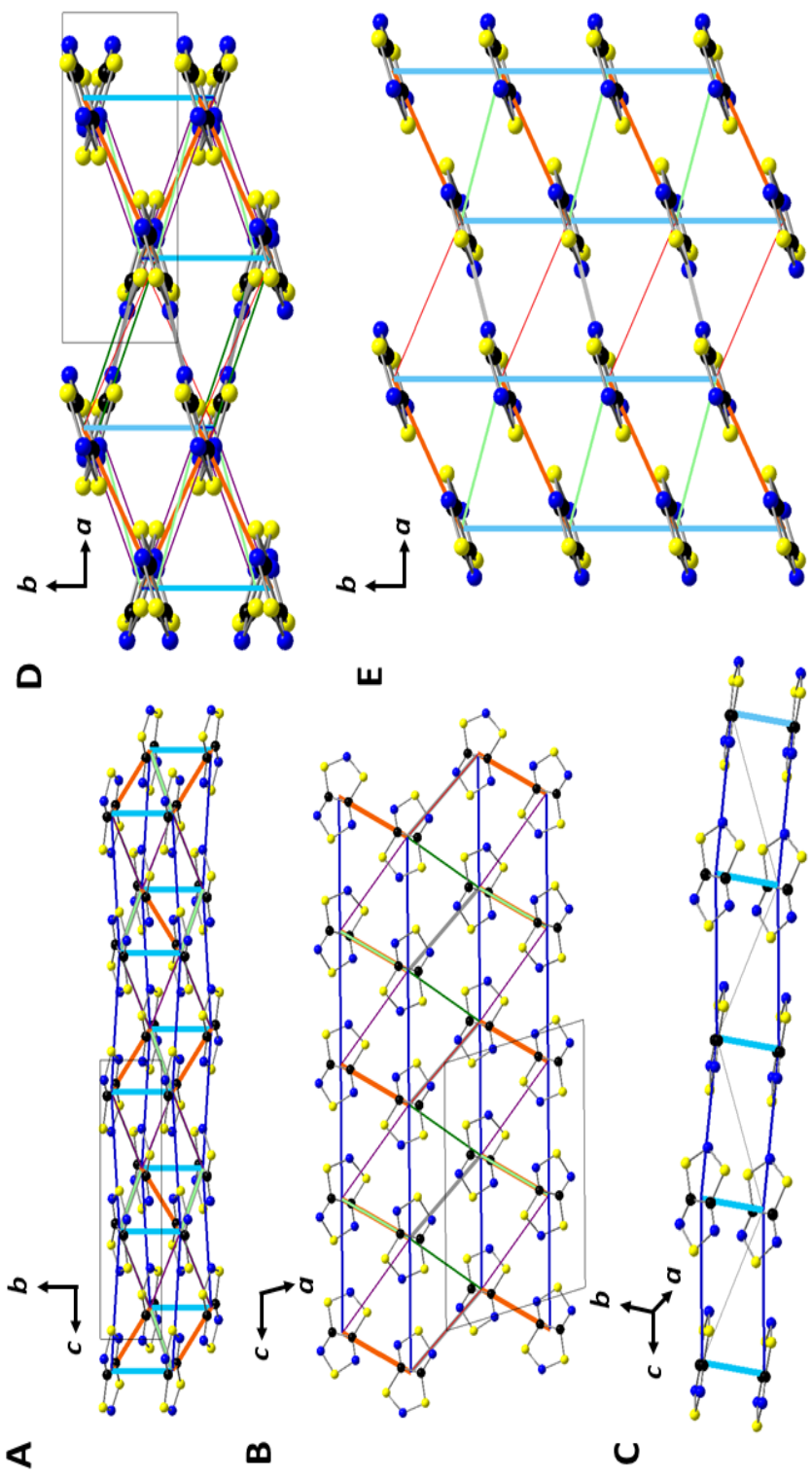

Figure 5.6: Various views of the energy framework of the ambient pressure $P2_1/c$ phase structure of TTTA, consisting of all nine strongest interactions, as calculated by the PIXEL method. Interaction rod thickness is scaled according to the total interaction energy, and are coloured to match the interactions shown in Figure 5.4. A, B and D view the crystal lattice along the a, b, and c axes respectively. C and E show extended segments of the crystal lattice, to provide a clearer view of the combination of inter-column interactions mostly aligned with the bc and ab planes respectively. Images created using DIAMOND.[42]

In the case of the $P\bar{1}$ polymorph, the literature structure obtained at RT (CSD refcode: SAXPOW05) was chosen to be studied.[37] Due to the asymmetric unit containing 2 molecules, this added to the complexity of the calculation through the larger number of interactions accounted for. Within the set radius of 15 Å, 247 unique interactions were observed, 17 of which had a calculated energy stronger than 2.5 kJ mol^{-1}. Table 5.2 and Figure 5.7 show the total and component energy values and visual representations of a selection of these interactions.

Table 5.2: Intramolecular separation distances, component and total energy terms for a selected number of the strongest interactions calculated in the $P\bar{1}$ phase of TTTA.

Interaction	Intramolecular Centroid Separation (Å)	Coulombic Energy (kJ mol^{-1})	Polarisation Energy (kJ mol^{-1})	Dispersion Energy (kJ mol^{-1})	Repulsion Energy (kJ mol^{-1})	Total Energy (kJ mol^{-1})
1	3.784	-10.1	-7.8	-44.1	43.0	-18.9
2	6.656	-22.6	-7.7	-18.6	31.5	-17.4
3	5.417	-34.1	-13.2	-28.9	58.9	-17.2
4	5.112	-2.9	-1.2	-14.8	8.1	-10.8
5	7.531	-6.6	-3.4	-11.3	13.7	-7.5
6	7.531	-4.8	-2.6	-10.0	10.1	-7.3
7	7.538	-4.5	-2.3	-9.5	9.2	-7.2
8	5.912	-7.7	-6.8	-17.8	25.5	-6.8
9	7.202	-4.3	-3.7	-13.2	14.7	-6.6
18	3.409	-26.7	-22.3	-61.7	108.5	-2.2

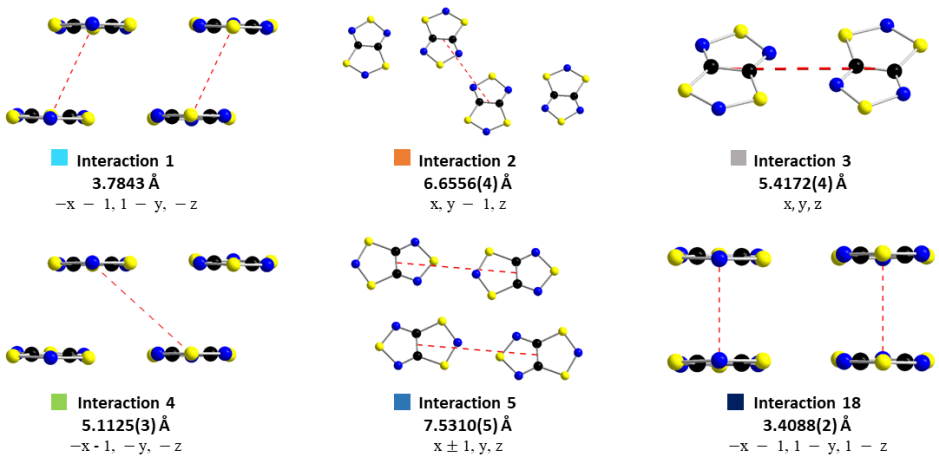

Figure 5.7: Selection of intermolecular interactions in the ambient-pressure $P\bar{1}$ phase of TTTA, with the dashed lines indicating the specific interaction between dimers in the asymmetric unit. C, N and S atoms are coloured black, blue and yellow respectively. Images created using DIAMOND.[42]

Figures 5.8 and 5.9 show the energy framework of the $P\bar{1}$ polymorph constructed of the three strongest interactions (plus interaction 18) and the nine strongest interactions (plus interaction 18) respectively.

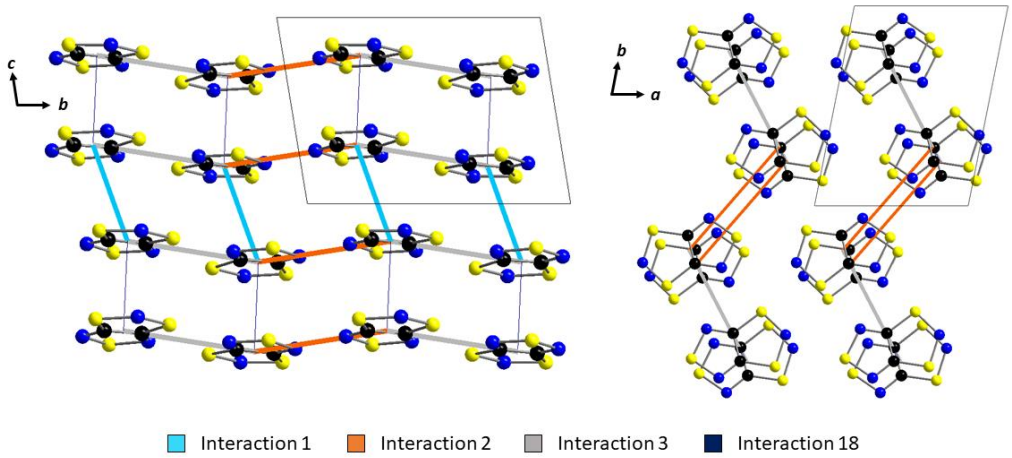

Figure 5.8: Energy frameworks of the $P\bar{1}$ polymorph of TTTA, viewed along the a and b axes, constructed by interactions 1, 2, 3 and 18, as calculated by the PIXEL method, according to the descriptions set in Table 5.2 and Figure 5.7. Images created using DIAMOND.[42]

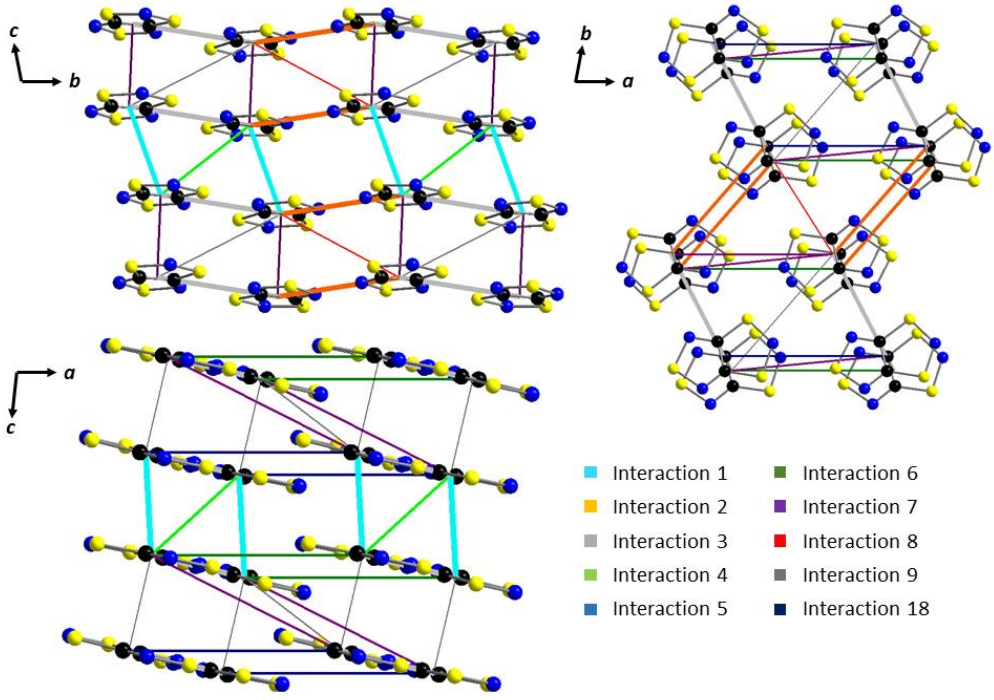

Figure 5.9: Energy frameworks of the $P\bar{1}$ polymorph of TTTA, viewed along the a, b and c axes, constructed by interactions 1-9 and 18, as calculated by the PIXEL method, according to the descriptions set in Table 5.2 and Figure 5.7. Images created using DIAMOND.[42]

The results of the calculation interaction energies in the $P\bar{1}$ polymorph present a similar picture to that observed for the $P2_1/c$ polymorph in that the strongest interaction is the slipped π-stacking interaction, which has a similar net energy value to the strongest inter-column interactions. The interaction representing the eclipsed π-stacked dimer, shown in the literature to be the strongest magnetic interaction across both polymorphs,[44, 45] has been calculated by the PIXEL method to have a weak net interaction energy of -2.2 kJ mol^{-1}. This net energy value hides the large attractive and repulsive energy component terms cancelling each other out due to the direct overlap of the molecules in the dimer, rather than it being an inherently weak interaction such as those seen over very large separation distances. Thus, in a similar manner to the $P2_1/c$ polymorph, describing the crystal structure from the viewpoint of intermolecular energy provides a different perspective on the construction of the $P\bar{1}$ polymorph and highlights the relative strength of the inter-column interactions.

5.5.3 PIXEL calculations on high-pressure structures

Given that structure solutions of the $P2_1/c$ polymorph were successfully obtained up to 4.56 GPa, PIXEL calculations were undertaken on all the high-pressure structures to examine the change in the total lattice energy and individual dimer interaction energies across the pressure series. The total lattice energy values, along with their component energies terms, across the pressure series is shown in Figure 5.10. Throughout the pressure series, the total lattice energy was seen to steadily increase, from -75.4 kJ mol^{-1} to -32.9 kJ mol^{-1} (i.e. becoming less stabilised), driven by the increase in the repulsion energy term outweighing the combined decrease in the attractive energy terms; this is the expected result of the molecules being forced together with increasing pressure. If the current rate of change was maintained, the lattice energy would not cross to a net repulsive value until *ca.* 8 GPa. Figure 5.11 shows the change in the total energy value calculated for each of the nine strongest

interactions in this polymorph, as shown in Figure 5.4, with the change in the dimer separation distance; shorter interaction distances account for higher pressures.

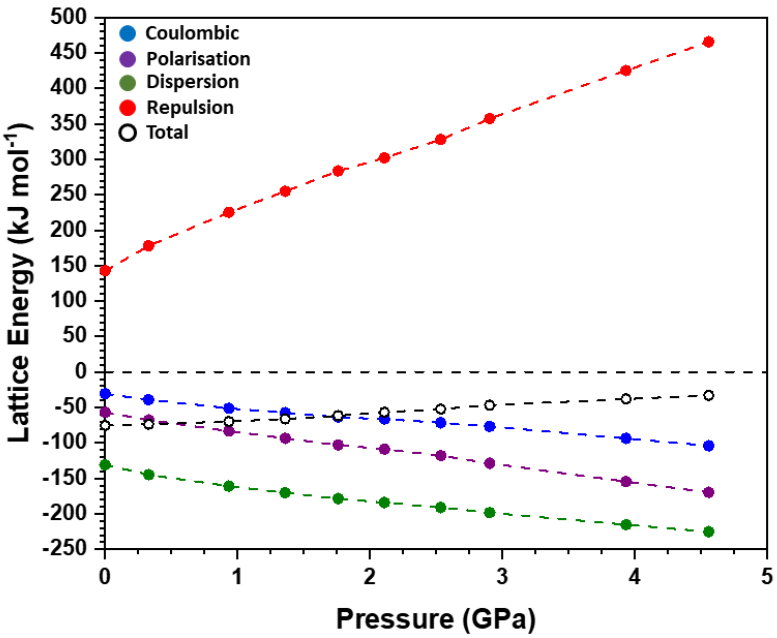

Figure 5.10: Components energy terms and total lattice energy of the P2₁/c phase of TTTA, obtained by PIXEL method calculations on the experimentally-obtained structures from its pressure series.

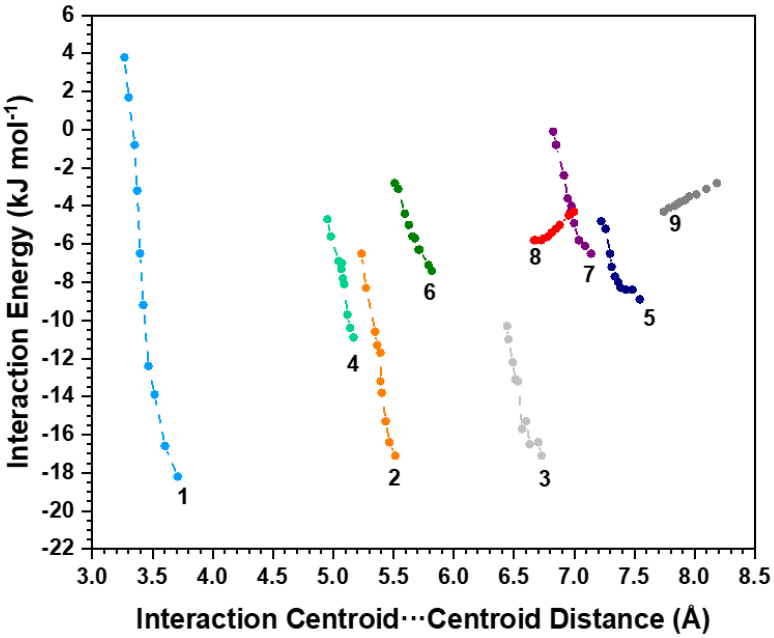

Figure 5.11: Total energies of the nine strongest interactions, as calculated for the ambient-pressure P2₁/c polymorph structure, calculated for every structure obtained from the high-pressure X-ray diffraction experiments. Smaller intermolecular separations generally equate to higher pressures.

As expected, most of the strongest interactions weakened throughout the pressure series, exhibiting a similar trend as that for the lattice energies (Figure 5.10), in that the strengthening of the repulsive energy term outweighed the strengthening of the attractive component energy terms. Interactions 8 and 9 were obvious exceptions, with their respective total interaction energy values decreasing as a response to pressure. The combination of the relatively-long separation distances associated with those interactions and their specific natures, in not facilitating a lot of direct molecular overlap, resulted in comparatively less growth of the repulsion energy term with decreasing intermolecular separation, thus causing a strengthening of the net interaction energy.

The interaction energy hierarchy identified at ambient pressure in the $P2_1/c$ polymorph (Table 5.1) drastically changed order throughout the pressure series; interaction 1, for example, was calculated to be the most responsive interaction to pressure, ultimately becoming the weakest of the nine interactions by the end of the pressure series. This can be directly linked back to the structural response to pressure, in that the *b* axis was the most compressible crystal lattice direction. The separation of molecules in the columns was compressed throughout the pressure series to such an extent that the π-stacking interaction was calculated to become net repulsive by 3.92 GPa. None of the other highlighted interactions reached a net repulsive energy value by the end of the pressure series; however, due to considerable alignment with the *b* axis, most showed a consistent weakening throughout the pressure series. Even interaction 5, which is mostly aligned with the *c* axis, despite showing initially a sluggish response to pressure with a minimal change in energy between 0.30 GPa and 1.35 GPa, showed a strong response at the latter stages of the pressure series. Nevertheless, the fact that all the inter-column interactions returned a net attractive interaction energy even up to the highest pressure of 4.56 GPa could act as an explanation for the lack of structural phase transition observed under pressure.

The stabilisation of the $P2_1/c$ polymorph, as discussed in the introduction, has been attributed to the PED behaviour of the π-stacking columns, the rate of which has been shown to decrease upon decreasing intermolecular separation.[46] Therefore, upon compression of the unit cell by pressure, the $P2_1/c$ polymorph should be destabilised. The inter-column interactions, which have been attributed to be the cause of the anomalously large hysteresis loop, must play a role in resisting the phase transition to the $P\bar{1}$ polymorph, or to any other polymorph, under pressure. Therefore, the gradual suppression of paramagnetism observed under pressure must be caused by an alternative phenomenon, most likely by the gradual decrease in separation along the π-stacking direction causing an increase in the strength of the antiferromagnetic coupling between the neighbouring semi-occupied molecular orbitals.

In order to clarify these claims, further work would be required, such as further molecular dynamics simulations and calculations of magnetic coupling constants utilising the structures of the $P2_1/c$ polymorph obtained at high pressure in this current study, to investigate how the PED behaviour and strength of magnetic interactions are affected by the compression of the unit cell. Furthermore, magnetic experiments up to at least 5 GPa would be necessary to verify the rate of paramagnetic suppression until full diamagnetism is achieved, since this has not yet been observed experimentally.

5.6 Conclusions

This short study has built upon the considerable number of publications already concerning TTTA, by investigating the possibility of a structural phase transition under the application of pressure as well as providing an energetic description of the hierarchy of intermolecular interactions that build up the crystal structures in both the $P\bar{1}$ and $P2_1/c$ phases at ambient conditions and the latter at high-pressure. No structural phase transition was observed under pressure, with smooth compression up to 4.6 GPa, the majority of which was attributed to the π-stacking direction. Therefore, the suppression of the paramagnetism in TTTA as a response to pressure has been hypothesised to simply stem from decreasing intermolecular separation in the π-stacking columns in the $P2_1/c$ phase, given that its gradual nature matches well with the gradual compression of the unit cell observed in this study for the first time.

The PIXEL calculations calculated an energy hierarchy of the intermolecular interactions, revealing that the strongest inter-column interactions are comparable in energy to the slipped π-stacking interactions in both polymorphs. While this seems to contradict the results in the literature concerning the calculated magnetic coupling constants, the two methods are concerned with investigating different properties of the material, and thus are in-fact complementing each other rather than providing contradictory perspectives. The high relative energetic strength of the inter-column interactions calculated in this study have, for the first time, clarified the claims made in the literature regarding the importance of the inter-column interactions in causing the wide magnetic hysteresis. Furthermore, the lack of the structural phase transition under pressure has also been attributed to the strength of the inter-column interactions, especially since they have been shown to not be net repulsive at 4.6 GPa. This work has provided both a strong contribution to the understanding of this already extensively studied material and sufficient scope for future work.

5.7 References

1. J. F. Letard, P. Guionneau and L. Goux-Capes, in *Spin Crossover in Transition Metal Compounds III*, ed P. Gütlich and H. A. Goodwin, 2004, ch 10, pp. 221-249.
2. P. Gamez, J. S. Costa, M. Quesada and G. Aromi, *Dalton Trans.*, 2009, 7845-7853.
3. G. Molnar, L. Salmon, W. Nicolazzi, F. Terki and A. Bousseksou, *J. Mater. Chem. C*, 2014, **2**, 1360-1366.
4. O. Sato, *Nat. Chem.*, 2016, **8**, 644-656.
5. P. Gutlich and H. A. Goodwin, *Spin Crossover in Transition Metal Compounds I*, 2004, **233**, 1-47.
6. A. Bousseksou, G. Molnar, L. Salmon and W. Nicolazzi, *Chem. Soc. Rev.*, 2011, **40**, 3313-3335.
7. J. A. Real, A. B. Gaspar and M. C. Munoz, *Dalton Trans.*, 2005, 2062-2079.
8. S. Decurtins, P. Gutlich, C. P. Kohler, H. Spiering and A. Hauser, *Chem. Phys. Lett.*, 1984, **105**, 1-4.
9. S. Decurtins, P. Gutlich, C. P. Kohler and H. Spiering, *Journal of the Chemical Society-Chem. Commun.*, 1985, 430-432.
10. P. Gutlich, V. Ksenofontov and A. B. Gaspar, *Coord. Chem. Rev.*, 2005, **249**, 1811-1829.
11. J. Linares, E. Codjovi and Y. Garcia, *Sensors*, 2012, **12**, 4479-4492.
12. M. A. Halcrow, *Chem. Soc. Rev.*, 2011, **40**, 4119-4142.
13. L. Cambi and L. Szego, *Ber. Dtsch. Chem. Ges.*, 1931, **64**, 2591-2598.
14. P. Gutlich, Y. Garcia and H. A. Goodwin, *Chem. Soc. Rev.*, 2000, **29**, 419-427.
15. D. M. Bassani, J. M. Lehn, K. Fromm and D. Fenske, *Angew. Chem., Int. Ed.*, 1998, **37**, 2364-2367.
16. E. Breuning, M. Ruben, J. M. Lehn, F. Renz, Y. Garcia, V. Ksenofontov, P. Gutlich, E. Wegelius and K. Rissanen, *Angew. Chem., Int. Ed.*, 2000, **39**, 2504-2507.
17. T. Matsumoto, G. N. Newton, T. Shiga, S. Hayami, Y. Matsui, H. Okamoto, R. Kumai, Y. Murakami and H. Oshio, *Nat. Commun.*, 2014, **5**,3865.
18. M. Steinert, B. Schneider, S. Dechert, S. Demeshko and F. Meyer, *Angew. Chem., Int. Ed.*, 2014, **53**, 6135-6139.
19. J. W. L. Wong, S. Demeshko, S. Dechert and F. Meyer, *Inorg. Chem.*, 2019, **58**, 13337-13345.
20. M. C. Munoz and J. A. Real, *Coord. Chem. Rev.*, 2011, **255**, 2068-2093.
21. O. Kahn and C. J. Martinez, *Science*, 1998, **279**, 44-48.

22. C. Wang, D. M. Liu and W. B. Lin, *J. Am. Chem. Soc*, 2013, **135**, 13222-13234.
23. G. J. Halder, C. J. Kepert, B. Moubaraki, K. S. Murray and J. D. Cashion, *Science*, 2002, **298**, 1762-1765.
24. N. F. Sciortino, F. Ragon, K. A. Zenere, P. D. Southon, G. J. Halder, K. W. Chapman, L. Pineiro-Lopez, J. A. Real, C. J. Kepert and S. M. Neville, *Inorg. Chem.*, 2016, **55**, 10490-10498.
25. K. A. Zenere, S. G. Duyker, E. Trzop, E. Collet, B. Chan, P. W. Doheny, C. J. Kepert and S. M. Neville, *Chem. Sci.*, 2018, **9**, 5623-5629.
26. D. Gatteschi, *Adv. Mater.*, 1994, **6**, 635-645.
27. R. G. Hicks, *Nat. Chem.*, 2011, **3**, 189-191.
28. J. M. Rawson, A. Alberola and A. Whalley, *J. Mater. Chem.*, 2006, **16**, 2560-2575.
29. J. L. Brusso, O. P. Clements, R. C. Haddon, M. E. Itkis, A. A. Leitch, R. T. Oakley, R. W. Reed and J. F. Richardson, *J. Am. Chem. Soc*, 2004, **126**, 8256-8265.
30. J. L. Brusso, O. P. Clements, R. C. Haddon, M. E. Itkis, A. A. Leitch, R. T. Oakley, R. W. Reed and J. F. Richardson, *J. Am. Chem. Soc*, 2004, **126**, 14692-14693.
31. K. Lekin, S. M. Winter, L. E. Downie, X. Z. Bao, J. S. Tse, S. Desgreniers, R. A. Secco, P. A. Dube and R. T. Oakley, *J. Am. Chem. Soc*, 2010, **132**, 16212-16224.
32. A. Alberola, D. J. Eisler, L. Harvey and J. M. Rawson, *CrystEngComm*, 2011, **13**, 1794-1796.
33. S. Vela, M. B. Reardon, C. E. Jakobsche, M. M. Turnbull, J. Ribas-Arino and J. J. Novoa, *Chem. Eur. J.*, 2017, **23**, 3479-3489.
34. T. Francese, J. Ribas-Arino, J. J. Novoa, R. W. A. Havenith, R. Broer, C. de Graaf and M. Deumal, *Phys. Chem. Chem. Phys.*, 2018, **20**, 20406-20416.
35. M. B. Mills, T. Wohlhauser, B. Stein, W. R. Verduyn, E. Song, P. Dechambenoit, M. Rouzieres, R. Clerac and K. E. Preuss, *J. Am. Chem. Soc*, 2018, **140**, 16904-16908.
36. G. Wolmershauser and R. Johann, *Angew. Chem., Int. Ed.*, 1989, **28**, 920-921
37. W. Fujita and K. Awaga, *Science*, 1999, **286**, 261-262.
38. G. D. McManus, J. M. Rawson, N. Feeder, J. van Duijn, E. J. L. McInnes, J. J. Novoa, R. Burriel, F. Palacio and P. Oliete, *J. Mater. Chem.*, 2001, **11**, 1992-2003.
39. W. Fujita, K. Awaga, H. Matsuzaki and H. Okamoto, *Phys. Rev. B*, 2002, **65**, 064434
40. C. F. Macrae, P. R. Edginston, P. McCabe, E. Ridcock, G. P. Shields, R. Taylor, M. Towler, J. Van der Streck, *J. Appl. Cryst.*, 2006, **39**, 453-457.
41. S. S. Batsanov, *Inorg. Mater.*, 2001, **37**, 871-885.
42. K. Brendenburg, DIAMOND, Crystal Impact GbR, Bonn, Germany, 1999.
43. C. S. Clarke, J. Jornet, M. Deumal and J. J. Novoa, *Polyhedron*, 2009, **28**, 1614-1619.

44. C. S. Clarke, J. Jornet-Somoza, F. Mota, J. J. Novoa and M. Deumal, *J. Am. Chem. Soc*, 2010, **132**, 17817-17830.

45. S. Vela, M. Deumal, M. Shiga, J. J. Novoa and J. Ribas-Arino, *Chem. Sci.*, 2015, **6**, 2371-2381.

46. S. Vela, F. Mota, M. Deumal, R. Suizu, Y. Shuku, A. Mizuno, K. Awaga, M. Shiga, J. J. Novoa and J. Ribas-Arino, *Nat. Commun.*, 2014, **5**, 4411.

47. H. Matsuzaki, W. Fujita, K. Awaga and H. Okamoto, *Phys. Rev. Lett.*, 2003, **91**, 017403.

48. P. Naumov, J. P. Hill, K. Sakurai, M. Tanaka and K. Ariga, *J. Phys. Chem. A*, 2007, **111**, 6449-6455.

49. I. Katayama, T. Kon, K. Mitarai and J. Takeda, *Phys. Rev. B*, 2009, **80**, 092103.

50. T. Kon, S. Oguri, I. Katayama, T. Kodaira and J. Takeda, *Phys. Rev. B*, 2009, **79,** 035106.

51. T. Tanaka, W. Fujita and K. Awaga, *Chem. Phys. Lett.*, 2004, **393**, 150-152.

52. Bruker (2012). SAINT. Bruker AXS Inc., Madison, Wisconsin, USA.

53. G. M. Sheldrick, University of Göttingen, Göttingen, Germany, 2008

54. A. Altomare, G. Cascarano, G. Giacovazzo, A. Guagliardi, M. C. Burla, G. Polidori and M. Camalli, *J. Appl. Crystallogr*, 1994, **27**, 435-435.

55. P. W. Betteridge, J. R. Carruthers, R. I. Cooper, K. Prout and D. J. Watkin, *J. Appl. Crystallogr*, 2003, **36**, 1487-1487.

56. L. Merrill and W. A. Bassett, *Rev. Sci. Instrum.*, 1974, **45**, 290-294.

57. S. A. Moggach, D. R. Allan, S. Parsons and J. E. Warren, *J. Appl. Crystallogr*, 2008, **41**, 249-251.

58. G. J. Piermarini, S. Block, J. D. Barnett and R. A. Forman, *J. Appl. Phys.*, 1975, **46**, 2774-2780.

59. S. Klotz, J. C. Chervin, P. Munsch and G. Le Marchand, *J. Phys. D: Appl. Phys.*, 2009, **42**, 075413.

60. K. Murata, K. Yokogawa, H. Yoshino, S. Klotz, P. Munsch, A. Irizawa, M. Nishiyama, K. Iizuka, T. Nanba, T. Okada, Y. Shiraga and S. Aoyama, *Rev. Sci. Instrum.*, 2008, **79**, 085101.

61. S. Sasaki, S. Kato, T. Kume, H. Shimizu, T. Okada, S. Aoyama, F. Kusuyama and K. Murata, *Japanese J. Appl. Phys.*, 2010, **49**, 106702.

62. H. Nowell, S. A. Barnett, K. E. Christensen, S. J. Teat and D. R. Allan, *J. Synchrotron Radiat.*, 2012, **19**, 435-441.

63. CrysAlisPro, Oxford Diffraction/Aligent Technologies UK Ltd, Yarnton, UK.

64. J. D. Dunitz and A. Gavezzotti, *Angew. Chem., Int. Ed.*, 2005, **44**, 1766-1787.

65. M. J. Frisch, G. W. Trucks, H. B. Schlegel, G. E. Scuseria, M. A. Robb, J. R. Cheeseman, G. Scalmani, V. Barone, B. Mennucci, G. A. Petersson, H. Nakatsuji, M. Caricato, H. X. Li, P. Hratchian, A. F. Izmaylov, J. Bloino, G. Zheng, J. L. Sonnenberg, M. Hada, M. Ehara, K. Toyota, R. Fukuda, J. Hasegawa, M. Ishida, T. Nakajima, Y. Honda, O. Kitao, H. Nakai, T. Vreven, J. A. Montgomery, Jr., J. E. Peralta, F. Ogliaro, M. Bearpark, J. J. Heyd, E. Brothers, K. N. Kudin, V. N. Staroverov, R. Kobayashi, J. Normand, K. Raghavachari, A. Rendell, J. C. Burant, S. S. Iyengar, J. Tomasi, M. Cossi, N. Rega, J. M. Millam, M. Klene, J. E. Knox, J. B. Cross, V. Bakken, C. Adamo, J. Jaramillo, R. Gomperts, R. E. Stratmann, O. Yazyev, A. J. Austin, R. Cammi, C. Pomelli, J. W. Ochterski, R. L. Martin, K. Morokuma, V. G. Zakrzewski, G. A. Voth, P. Salvador, J. J. Dannenberg, S. Dapprich, A. D. Daniels, Ö. Farkas, J. B. Foresman, J. V. Ortiz, J. Cioslowski and D. J. Fox, GAUSSIAN09, Gaussian Inc., Wallingford, C.T., 2009.

66. A. Gavezzotti, CLP-PIXEL Suite, University of Milan, Milan, Italy, 2008.

67. A. Gavezzotti, *Mol. Phys.*, 2008, **106**, 1473-1485.

68. M. G Reeves, P. A. Wood and S. Parsons, *J. Appl. Crystallogr.*, 2020, **53**, 1154-1162.

69. A. Gavezzotti, *Molecular aggregation : structure analysis and molecular simulation of crystals and liquids*, Oxford University Press, Oxford, 2007.

70. F. Birch, *Phys. Rev.*, 1947, **71**, 809-824.

71. M. Mikolasek, M. D. Manrique-Juarez, H. J. Shepherd, K. Ridier, S. Rat, V. Shalabaeva, A. C. Bas, I. E. Collings, F. Mathieu, J. Cacheux, T. Leichle, L. Nicu, W. Nicolazzi, L. Salmon, G. Molnar and A. Bousseksou, *J. Am. Chem. Soc*, 2018, **140**, 8970-8979.

72. G. Molnar, M. Mikolasek, K. Ridier, A. Fahs, W. Nicolazzi and A. Bousseksou, *Ann. Phys-Berlin*, 2019, **531**, 1900076.

Chapter 6

Investigating Phase Transition Behaviour and Selective Gas Uptake in Sc_2BDC_3 Metal-Organic Framework

6.1 Synopsis

This chapter focuses on a distinctively different class of functional material, namely metal-organic frameworks (MOFs), and their application for selective gas uptake. Unlike the other chapters, only computational methods, in the form of classical-based simulations, have been employed herein, but the extensive results gained have provided valuable information on quantifying interaction energies to explain the phase transition behaviour and apparent selectivity for CO_2 adsorption over CH_4 in a small pore Sc-based MOF.

6.2 Disclaimer

The experimental structure solutions of Sc_2BDC_3, used as starting models for the simulations reported herein, were provided courtesy of Dr. Stephen Moggach (now based at the University of Western Australia). The DFT calculations reported in section 6.3.4, undertaken to determine the energy difference between the two phases of Sc_2BDC_3 and determine guest-framework interaction energies, were carried out by Prof. Carole Morrison (University of Edinburgh), building upon the work featured in the MChemX final year project report of Jamie McHardy (both of University of Edinburgh).[1] Determination of the guest molecule adsorption correlation lengths was carried out by Dr. Gaël Donval (University of Bath).

6.3 Introduction

Metal-organic frameworks (MOFs) are a highly versatile class of material that often have large internal surface areas and pores sizes,[2, 3] rendering them suitable for a wide variety of applications in catalysis,[4] sensors,[5, 6] hosting reactive species,[7] and gas storage/separation.[8-15] In the latter case, most investigations on gas uptake in MOFs

have relied heavily on results gathered from gravimetric or volumetric adsorption isotherms. While these provide valuable preliminary information on guest uptake selectivity, they cannot provide structural information on the framework nor can they determine where the guest molecules reside within the material. Identifying where the adsorption sites are, quantifying the strength of guest/host binding, and understanding how seemingly small perturbations in the framework structure can change pore size and shape, which in turn affect uptake, selectivity and adsorption site location, can aid the development of new MOFs with enhanced gas adsorption and separation performance.

In-situ crystallographic techniques can provide direct evidence of adsorption, with defined atomic positions for guest molecules.[16-20] This is challenging work, however, with only *ca.* 2.3 % of the structural entries logged in the MOF subset of the Cambridge Structural Database (CSD) having been structurally characterised with the inclusion of adsorbed gas molecules, as of January 2020.[21, 22] Furthermore, the majority of these can be attributed to just one publication concerning variable temperature powder diffraction on a series of CPO-27 frameworks, which is responsible for over 1,800 entries into the database.[23] Only *ca.* 320 entries in the database refer to samples obtained from single crystals, with 147 and 28 of those containing adsorbed CO_2 and CH_4 respectively; only around 50 of those pertain to structures collected between 283 K and 303 K. For gas mixtures, only one report is known which used X-ray diffraction as the primary characterisation technique, specifically on the CO_2/CH_4 gas uptake by the powder form of a MIL-53(Cr) 'breathing' structure, which showed that a narrow-pore to large-pore phase transition which occurs under CO_2 uptake can be attenuated depending on the composition of the CO_2/CH_4 gas mixture applied to the material.[24] In a more recent publication, Long and co-workers briefly commented on the need for further prioritisation of structural characterisation of MOFs under adsorption of gas mixtures.[25]

Gas loading into MOF single crystals can be explored using DACs, but problems of low structure completeness arise due to data loss from both the shading of the detector from the body of the DAC and due to sample reflections being obscured by signals arising from the anvils and gasket material. Moreover, since DACs have a relatively high minimum loading pressure, (*ca*. 1 kbar), it is difficult to study materials at low pressures. This could lead to important subtle structural changes occurring at lower pressures being overlooked. Capillary gas cell methods are an alternative which allow for single crystals to be studied in a similar manner to that of a standard single crystal diffraction measurement, whilst surrounding the material in a gaseous environment at relatively low gas loadings.[26, 27]

One MOF which has been studied for its various properties and adsorption capabilities using capillary gas cell techniques is scandium terephthalate $Sc_2(O_2CC_6H_4CO_2)_3$,[28-32] hereafter denoted by the abbreviation Sc_2BDC_3, where BDC = 1,4-benzenedicarboxylate. The staggered chains of ScO_6 octahedra, with each Sc(III) ion coordinated to six different μ^4-bridging BDC ligands, form a framework consisting of narrow 1-D triangular channels *ca*. 4 Å in diameter. Sc_2BDC_3 crystallises at 298 K in the orthorhombic space group *Fddd*, resulting in symmetrical equivalence between all porous channels (Figure 6.1).[30]

The central linker in the *Fddd* phase, denoted group 1, lies directly parallel to the channel direction, whereas the side linker groups, group 2, are tilted away from the channel direction by *ca.* 8° (Figure 6.2).[30] The framework undergoes a reversible phase transition to the monoclinic *C*2/*c* space group below 225 K, facilitated by the rotation of the group 2 linkers (to 3.6(1)° and 12.0(2)° for groups 2a and 2b respectively at 170 K) to form symmetry-inequivalent porous channels (Figure 6.2).[32]

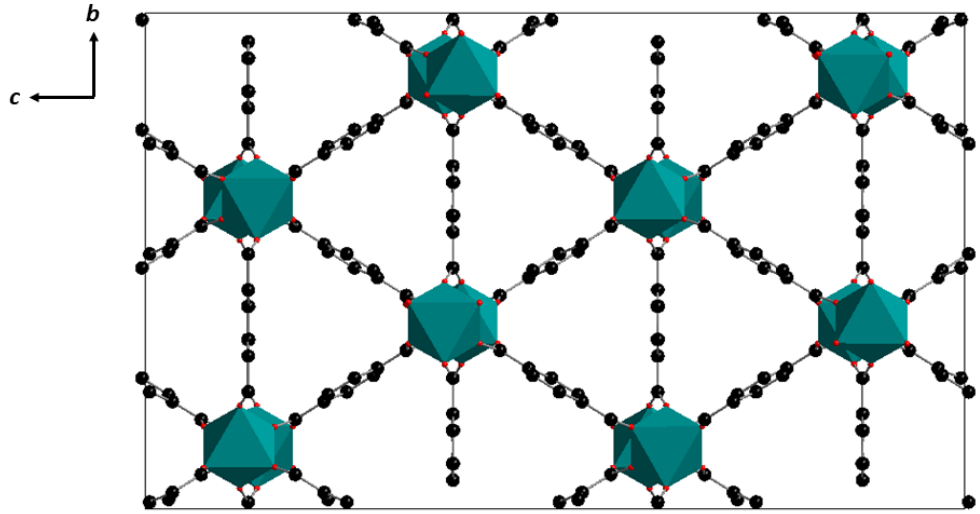

Figure 6.1: Unit of the Fddd phase of Sc_2BDC_3, indicating the construction of the triangular 1-D porous channels. ScO_6 octahedra are represented by the green polyhedral; O and C atoms are coloured red and black respectively. H atoms have been removed for clarity. Image created using DIAMOND.[33]

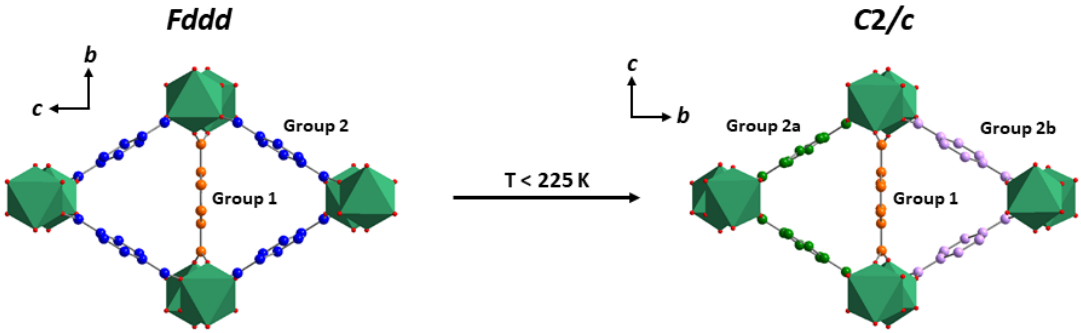

Figure 6.2: Structures of Sc_2BDC_3, adapted from the results reported by Mowat et al,[32] summarising the result of the phase transition behaviour on the nature of the porous channels. ScO_6 octahedra are represented by the green polyhedra, O atoms are coloured red, BDC linker C atoms are coloured according to symmetry equivalence, H atoms have been removed for clarity. Images were created using DIAMOND.[33]

The structure of the Sc_2BDC_3 and location of adsorbed guest molecules under various CO_2 and CH_4 loadings have been identified using synchrotron X-ray diffraction experiments incorporating capillary gas cell, < 240 K and at room temperature (RT),[30, 34] and DAC cryogenic gas loading techniques.[35] The main results from those studies, alongside results from some preliminary DFT calculations, are outlined in the next four sub-sections to provide context for the work carried out in this chapter.

6.3.1 CO_2 adsorption in Sc_2BDC_3

The results from the various X-ray diffraction/gas adsorption studies on Sc_2BDC_3, including changes in the framework structure, overall CO_2 uptake and CO_2 adsorption site occupancies are summarised across Table 6.1 and Figure 6.3.

The study undertaken at 235 K revealed that for the only pressure point measured at 1 bar of CO_2 the Sc_2BDC_3 framework had undergone the *Fddd*→*C*2/*c* phase transition,[30] facilitated by a similar rotation of the group 2 linkers as observed in the variable temperature study.[32] Two different CO_2 adsorption sites were determined, one in each type of porous channel (Figure 6.3), with a total CO_2 loading of 3.4 mmol g^{-1}.[30] Site 1 was identified in the channel formed by the group 1 and 2a linkers, parallel to the phenyl ring of the central linker group. Site 2 was identified in the channel formed by the group 1 and group 2b linkers, disordered across two symmetrically equivalent positions situated close, and parallel to, the group 2b phenyl rings.

A currently-unpublished follow-up study investigated CO_2 uptake in Sc_2BDC_3 at RT at various pressures between 1.2 and 10.0 bar.[34] At 1.2 bar, the framework had remained in the *Fddd* phase and two CO_2 adsorption sites, similar to those denoted as site 1 and site 2 in the *C*2/*c* phase at 235 K,[30] were observed (Figure 6.3). However, due to the higher symmetry of the *Fddd* phase, both sites were located in every porous channel. Upon increasing CO_2 pressure, the occupancies of both sites in the *Fddd* phase increased gradually with no clear binding hierarchy until 2.5 bar when the occupancy of site 1 appears to be slightly favoured. The group 2 linker rotation decreased gradually from 7.6(1)° to 5.5(2)° across this pressure range, highlighting the subtle response in the framework structure to CO_2 uptake. At 1.75 bar, a twinning of the reflections in the diffraction pattern was observed, providing evidence of a phase transition occurring within the framework structure. However, due to lack of

separation between the two domains, the structure continued to be solved in the *Fddd* phase up to 2.5 bar inclusive.

Table 6.1: Summary of results from the various X-ray diffraction experiments studying the adsorption of CO_2 in Sc_2BDC_3 under various experimental conditions.

Study by Miller *et al.* (2009).[30] Method: Capillary Gas Cell

Pressure (bar)	Space Group	Group 2 Linker Rotation (°)	Site Occupancy			Molecules per unit cell	CO_2 Uptake (mmol g^{-1})
			Site 1	Site 2	Site 3		
0[a]	*Fddd*	7.9(1)	-	-	-	0.00	0.00
1.00[b]	*C2/c*	5.8(1) (a) 13.8(2) (b)	1.00	0.50	-	8.00	3.44

Study by Sotelo (2015).[34] Method: Capillary Gas Cell

Pressure (bar)	Space Group	Group 2 Linker Rotation (°)	Site Occupancy			Molecules per unit cell	CO_2 Uptake (mmol g^{-1})
			Site 1	Site 2	Site 3		
0[a]		7.6(1)	-	-	-	0.00	0.00
1.20[a]		6.6(1)	0.11(1)	0.13(1)	-	5.95	1.28
1.50[a]		6.4(1)	0.13(1)	0.14(1)	-	6.61	1.42
1.75[a]	*Fddd*	6.1(1)	0.15(1)	0.16(1)	-	7.31	1.57
2.00[a]		5.8(1)	0.17(1)	0.17(1)	-	8.14	1.75
2.20[a]		5.6(1)	0.18(1)	0.18(1)	-	8.58	1.84
2.50[a]		5.5(2)	0.24(3)	0.18(1)	-	9.42	2.02
3.00[a]		1.7(2) (a) 8.8(2) (b)	0.39(3)	0.32(2)	0.18(2)	4.81	2.07
6.00[a]	*C2/c*	2.6(1) (a) 10.1(2) (b)	0.55(2)	0.38(2)	0.17(2)	5.40	2.32
10.00[a]		4.3(1) (a) 10.9(2) (b)	0.68(2)	0.59(3)	0.15(3)	8.04	3.45

Study by Sotelo *et al* (2015).[35] Method: Cryogenic loading of DAC

Pressure (bar)	Space Group	Group 2 Linker Rotation (°)	Site Occupancy			Molecules per unit cell	CO_2 Uptake (mmol g^{-1})
			Site 1	Site 2	Site 3		
2,000[a]	*C2c*	6.2(2) (a) 16.9(3) (b)	0.96(3)	0.83(3)	1.00	14.48	6.22

[a] collected at 298 K

[b] collected at 230 K

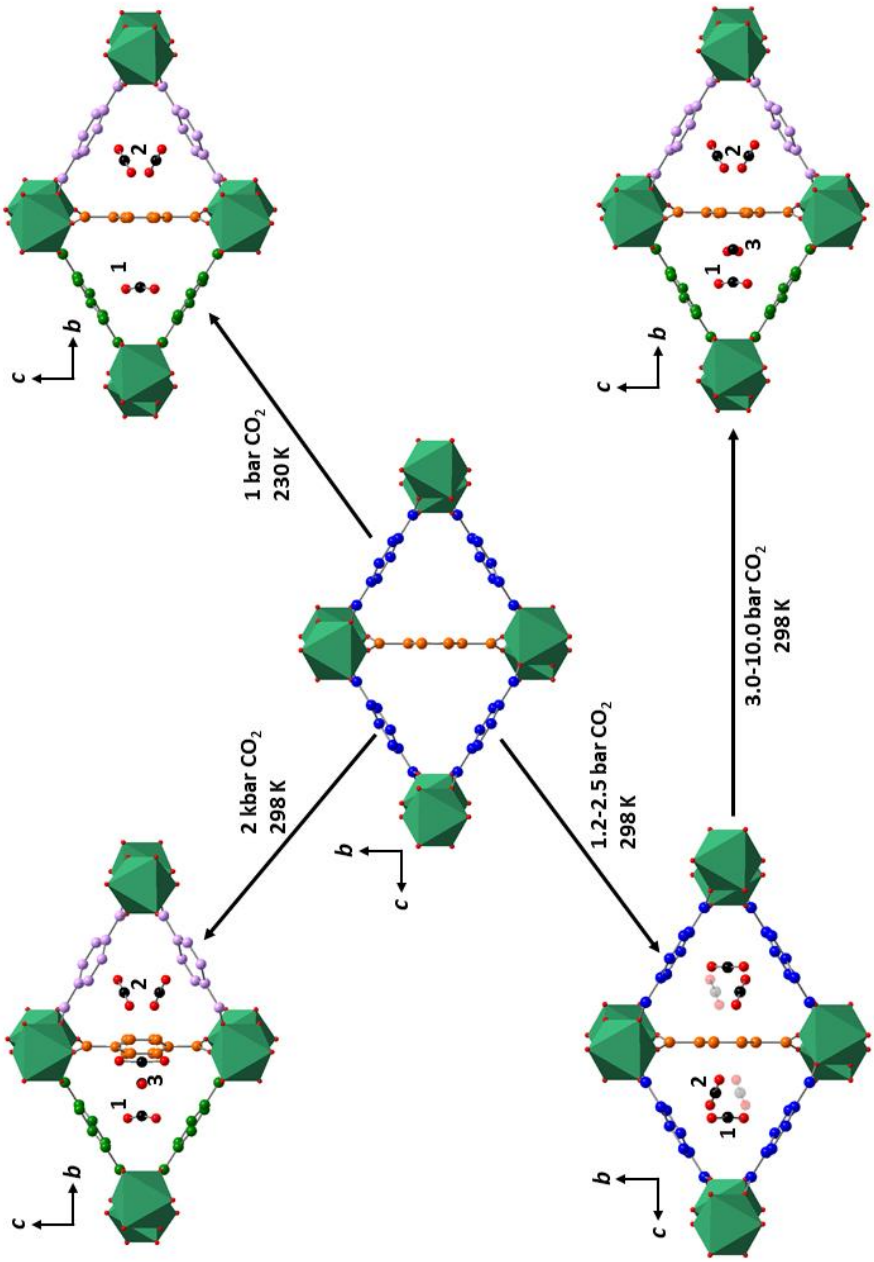

Figure 6.3: Structures of Sc_2BDC_3 framework, adapted from various gas adsorption studies,[30, 34, 35] summarising the phase transition behaviour and CO_2 adsorption site positions under a variety of experimental conditions. ScO_6 octahedra are represented by the green polyhedra, O atoms are coloured red, C atoms on the BDC linker groups are coloured according to symmetry equivalence, C on the CO_2 guest molecules coloured black, H atoms removed for clarity. Image created using DIAMOND.[33]

By 3 bar, the domains were sufficiently separated, allowing both domains to be isolated, facilitating the data to be resolved for the *C*2/*c* structure, with large deviations of −3.7° and +3.3° in the group 2a and 2b linker rotation angles respectively from those measured at 2.5 bar. With increasing pressure up to 10.0 bar, the linker rotation angles increased further to 4.3(1)° and 10.9(2)° respectively. Both sites 1 and 2 were, as expected, identified in the *C*2/*c* phase and their refined occupancies increased between 3 and 10 bar, with site 2 exceeding 50% occupancy at 10 bar. This latter observation contradicted a previous claim that the distance between the neighbouring site 2 positions (~2 Å) was too short to allow simultaneous occupation.[30] Moreover, a previously unobserved third adsorption site was located in the *C*2/*c* phase, hereafter known as site 3, in the same channel as site 1 but closer to the central linker wall (Figure 6.2). CO_2 molecules positioned here are aligned along the channel direction, but staggered midway between neighbouring site 1 molecules with an O···O contact distance of 2.89(7) Å. The discovery of a third adsorption site in Sc_2BDC_3 at RT at around 2 mmol g^{-1} is rather surprising given it was not observed at a CO_2 uptake of *ca.* 3.4 mmol g^{-1} of at 235 K. Between 3 and 10 bar, the increase in CO_2 uptake to 3.45 mmol g^{-1} was attributed to increased occupancy of sites 1 and 2, whereas site 3 occupancy did not change, hence indicating a clear binding site hierarchy in the *C*2/*c* phase.

Temperature appears to have a substantial influence on the extent of CO_2 uptake, with similar gas loadings observed at 1 bar and 235 K and at 10 bar and RT.[30, 34] However, the study at RT clearly revealed CO_2 uptake was possible in the *Fddd* phase, and hence the phase transition is not a prerequisite to CO_2 adsorption. Moreover, both studies observed CO_2 loadings of only around 50 % of the observed maximum CO_2 loading of 6.5 mmol g^{-1}, obtained from adsorption isotherms at 150 K;[30] the number of adsorption sites in the study at RT however would be sufficient to obtain this maximum loading, assuming full occupancy of all the sites was possible.

A later investigation, which utilised cryogenic loading of CO_2 into the framework using DACs to investigate high-pressure guest uptake in Sc_2BDC_3, verified this hypothesis, observing a CO_2 uptake of 6.2 mmol g^{-1} in the *C*2/*c* phase at 2 kbar, with the filling of all three adsorption sites to almost 100% occupancy, with disorder of site 3 across two positions (Figure 6.3).[35] Further structural variations in the framework and the adsorption site positions were observed at these high pressures, seemingly to facilitate the much higher CO_2 loading, such as greater separation of neighbouring site 2 distances (from 2.05 Å at 10 bar to 2.45 Å at 2 kbar), further rotation of the group 2a and 2b linkers (to 6.32° and 16.95° respectively) and disorder of the group 1 linker.

6.3.2 CH_4 adsorption in Sc_2BDC_3

Similar studies investigating CH_4 uptake in Sc_2BDC_3 have been undertaken. Figure 6.4 shows the position of CH_4 adsorption sites within the porous channels of Sc_2BDC_3, while Table 6.2 summarises the results across the various pressure studies. The CH_4 adsorption sites have been named here according to the similarity of their positions in the porous channel as to those identified for CO_2, regardless of framework symmetry.

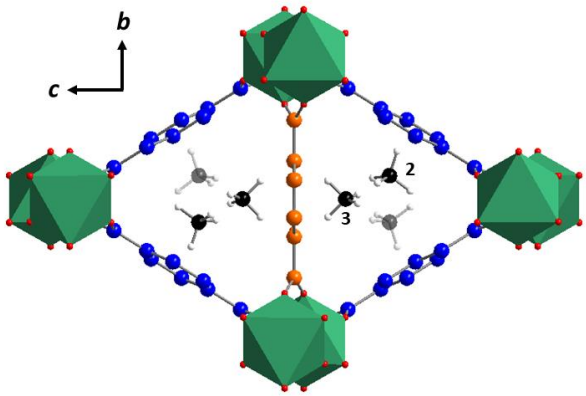

Figure 6.4: Structure of the Fddd phase of Sc_2BDC_3, adapted from the various previous studies,[30, 34, 35] with the inclusion of the observed CH_4 adsorption sites, labelled accordingly by site. Image created using DIAMOND.[33]

Table 6.2: Refined occupancies and CH_4 uptake value in Sc_2BDC_3, obtained experimentally from the in-situ diffraction gas study up to 4.6 bar.

Study by Miller *et al.* (2009).[30] Method: Capillary Gas Cell

Pressure (bar)	Space Group	Group 2 Linker Rotation (°)	Site Occupancy		Molecules per unit cell	CH_4 Uptake (mmol g^{-1})
			Site 2	Site 3		
0.0[a]	*Fddd*	7.9(1)	-	-	0.00	0.00
9.0[b]	*Fddd*	6.7(1)	0.125	0.25	8.00	1.72

Study by Sotelo (2015).[34] Method: Capillary Gas Cell

Pressure (bar)	Space Group	Group 2 Linker Rotation (°)	Site Occupancy		Molecules per unit cell	CH_4 Uptake (mmol g^{-1})
			Site 2	Site 3		
0[a]	*Fddd*	7.8(1)	-		0.00	0.00
1.1[a]		7.7(1)	-		0.00	0.00
4.6[a]		7.8(1)	-	0.11(2)	1.76	0.38
4.6[b]		7.7(0)	0.12(1)	0.31(1)	9.86	2.12

Study by Sotelo *et al.* (2016).[35] Method: Cryogenic DAC loading

Pressure (bar)	Space Group	Group 2 Linker Rotation (°)	Site Occupancy		Molecules per unit cell	CH_4 Uptake (mmol g^{-1})
			Site 2	Site 3		
3,000[a]	*Fddd*	8.8(1)	0.68(2)	0.91(3)	36.32	7.80
10,000[a]	*Fddd*	11.9(2)	1.00	1.00	48.00	10.31

[a] data collected at 290-298 K

[b] data collected at 230 K

Unlike in the case of CO_2 adsorption, the framework remained in the *Fddd* phase upon CH_4 adsorption at 230 K.[30] At the only reported pressure point of 9 bar of CH_4, two low occupancy adsorption sites were identified in similar positions to sites 2 and 3 observed under CO_2 adsorption (Figure 6.4), with a total CH_4 loading of 1.72 mmol g^{-1}. Even lower CH_4 uptake was observed in the unpublished study undertaken at RT,[34] with significant uptake being first observed at 4.6 bar, at which point only the site 3 position could be identified. Decreasing the temperature to 230 K whilst maintaining the pressure at 4.6 bar allowed occupancy of CH_4 in site 2 to observed, with a total CH_4 uptake of 2.12 mmol g^{-1},[34] exceeding the amount of CH_4 loading seen at 9 bar and 230 K.[30] The amount of CH_4 uptake observed in both studies was however low

compared to the maximum uptake of 6.8 mmol g^{-1} calculated from full occupancy of sites 2 and 3,[30] suggesting that very high pressures would be required achieve this extent of loading.

A cryogenic-loading high-pressure study actually observed an even higher CH_4 uptake than was suggested from publications of earlier studies,[30] obtaining 10.3 mmol g^{-1} in the *Fddd* phase of Sc_2BDC_3 at 10 kbar.[35] This was achieved by the 100% occupancy of both types of CH_4 adsorption site and by greater separation between neighbouring site 2 positions (3.58(2) Å in the 10 kbar structure, compared to 3.04(7) Å in the 4.6 bar structure collected at 230 K). This thus allowed the disordered site 2 positions to become distinctive adsorption sites, something which was not observed in the previous gas cell studies.[30, 34] This hyper-filling of the porous channels facilitated greater structural changes in the framework with a significant increase in the rotation of the group 2 linkers relative to the channel directions, to 8.8(1)° and 11.9(2)° at 3 kbar and 10 kbar respectively, prior to the structure distorting and undergoing phase transitions to obtain higher density framework structures at 13 kbar and 25 kbar.[35]

6.3.3 Gas mixture adsorption in Sc_2BDC_3

The results of pure gas adsorption studies would suggest that Sc_2BDC_3 exhibits selective uptake for CO_2 over CH_4. This desirable property was investigated by X-ray diffraction in a currently-unpublished study, by subjecting the framework to 80:20 and 50:50 CH_4/CO_2 gas mixtures, up to total pressures of *ca.* 4.5 bar at 298 K.[34] Table 6.3 shows a summary of the structural changes and extent of gas uptake throughout both pressure series.

Under exposure to either gas mixture, Sc_2BDC_3 behaved as if under pure CO_2 uptake, with no evidence of CH_4 uptake at any pressure.[34] In both studies, the refined site

occupancies at each partial pressure of CO_2 slightly exceeded those observed in the pure CO_2 study.[34] The phase transition to the *C*2/*c* phase was only observed in the 50:50 mixture study at the final pressure point of 4.29 bar, equating to a partial pressure of CO_2 of just over 2 bar, marking the point at which the phase transition was observed in the pure study at RT,[34] with a similar binding site hierarchy as seen previously. These results therefore appear to confirm the selectivity of Sc_2BDC_3 for uptake of CO_2 over CH_4; however, the selectivity was not investigated at higher pressures, and thus it is unknown if this desirable property is maintained.

Table 6.3: Refined occupancies and subsequent uptake of CO_2 in Sc_2BDC_3, space group of the framework structure and extent of Group 2 linker rotation when exposed to 20:80 and 50:50 CO_2/CH_4 gas mixtures between 1.10 and 4.36 bar.

Study by Sotelo (2015).[34] Method: Capillary Gas Cell - 20:80 CO_2:CH_4

Pressure (bar)	Space Group	Group 2 Linker Rotation (°)	Site Occupancy			Molecules per unit cell	CO_2 Uptake (mmol g^{-1})
			Site 1	Site 2	Site 3		
0.00	*Fddd*	7.7(1)	-	-	-	0.00	0.00
1.10		7.4(1)	0.06(1)	0.07(1)	-	3.20	0.69
1.99		7.1(1)	0.12(1)	0.10(1)	-	5.12	1.10
4.36		6.6(1)	0.15(1)	0.13(1)	-	6.56	1.41

Study by Sotelo (2015).[34] Method: Capillary Gas Cell - 50:50 CO_2:CH_4

Pressure (bar)	Space Group	Group 2 Linker Rotation (°)	Site Occupancy			Molecules per unit cell	CO_2 Uptake (mmol g^{-1})
			Site 1	Site 2	Site 3		
1.10	*Fddd*	7.0(1)	0.09(1)	0.10(1)	-	4.64	1.00
1.92		6.5(1)	0.13(1)	0.14(1)	-	6.56	1.41
2.92		6.1(1)	0.16(1)	0.15(1)	-	7.36	1.58
4.29	*C*2/*c*	1.4(2) (a) 8.5(2) (b)	0.36(2)	0.39(2)	0.24(2)	5.52	2.37

While the various diffraction experiments were proven successful in obtaining structural information in terms of subtle changes in the framework and identifying the guest molecule adsorption sites, the reasoning for the framework exhibiting the selective uptake behaviour and for why the *Fddd*⟶*C*2/*c* phase transition occurs only

under CO_2 adsorption was still not fully understood. Therefore, in order to provide an explanation for these unresolved issues, computational methods which could quantify the difference in energy between the two phases and study the interaction energies for both CO_2 and CH_4 inside the pores were required.

6.3.4 Solid-state DFT calculations

A series of DFT calculations on empty and guest occupied framework models of Sc_2BDC_3 were undertaken, after the in-situ gas capillary diffraction experiments reported in sections 6.3.1-6.3.3, to calculate the energy difference between the two phases of Sc_2BDC_3 and to determine guest-framework interaction energies in the two phases.[36] These recent calculations improved upon a previous set of DFT calculations on the same system,[1] by using a higher plane wave cut-off energy and higher k-point sampling, which were determined to be necessary for this system. However, due to these requirements, successful calculations on models of Sc_2BDC_3 with the inclusion of guest molecules were limited to the *Fddd* phase, specifically only with CO_2 adsorption in site 1 and, in a separate model, CH_4 adsorption in site 3.

These calculations firstly revealed that the energy difference between the two phases is very small, at less than 3 kJ mol^{-1}; *C*2/*c* phase was determined to be more stable, but upon the removal of the TS dispersion correction the *Fddd* phase was determined to be more stable, suggesting that the *C2/c* phase is more strongly influenced by weak dispersion interactions. Nevertheless, given the subtle changes in geometry to convert between the two phases, it is not surprising that no significant energy barrier is needed to be overcome to convert between the two phases of Sc_2BDC_3.

By comparing the energies of the experimental and optimised framework with the inclusion of the guest molecules, the strain energy of the experimentally-obtained framework could be determined. The framework, in the *Fddd* phase, was under

reasonable strain (*ca.* 10 kJ mol^{-1}) upon the inclusion of CO_2 molecules in the site 1 position; this could be expected to be even higher if occupation of both sites 1 and 2 were able to be modelled, given their close proximity inside the porous channels. In the case of CH_4 adsorption, the strain in the framework was very small (*ca.* 1 kJ mol^{-1}), but this value would also be expected to increase if occupation of all site 2 and 3 positions were modelled. The mean interaction energies associated with CO_2 and CH_4 adsorption were determined, with those for CO_2 (-43.0 kJ mol^{-1}) calculated to be slightly stronger than those for CH_4 (-39.2 kJ mol^{-1}), providing an indication that the selective uptake of CO_2 over CH_4 is driven by stronger interaction energies between the guest and the framework. However, without obtaining the interaction energies associated with CO_2 and CH_4 in all possible adsorption sites in both phases of the framework, justification of the experimental binding site hierarchy in terms of the site occupancies and the reasoning for the phase transition under CO_2 uptake but not under CH_4 uptake could not be provided. The DFT calculations did reveal however the interactions between the guest molecules and the framework are dispersion dominated; when the TS dispersion correction term was removed, the interactions for both guests weakened considerably (to -6.0 kJ mol^{-1} for CO_2 and +1.7 kJ mol^{-1} for CH_4).

The insights which could be obtained from this computational method were severely limited, given that occupation of all the adsorption sites was not possible and the adsorption sites that were modelled could be only be done so with 100 % occupancy, highlighting the incompatibility between this simulation method and system of interest. The use of only primitive unit cells, with full occupancy adsorption sites, does not accurately reflect the bulk framework system and the partial uptakes observed experimentally. Therefore, alternative simulation methods, in which partial occupancy can be freely explored, was required. Nevertheless, these DFT calculations provided benchmark binding energies which can be used in comparison to energy values calculated from better-suited simulation methods.

6.3.5 Aims of research

To overcome the limitations of the modelling approach in the DFT solid-state calculations, an alternative, but complementary, modelling approach in the form of stochastic classical-based grand canonical Monte Carlo (GCMC) simulations was proposed. This modelling technique has been implemented successfully in the recent past to model guest adsorption in MOFs with and without open metal coordination sites,[31, 37-42] and to analyse gas mixture separations.[43-46] These simulations would allow the study of larger supercells of the framework and quantify guest-framework and guest-guest interaction energies from the perspective of partial occupancy of the adsorption sites. Furthermore, using this method, the guest molecules are able to freely explore the accessible space within the porous material *via* a random walk to locate the lowest energy adsorption-site positions, without any symmetry constraints, rather than optimising around the experimentally-refined starting position as undertaken in the DFT calculations.

This chapter focuses on the results of the GCMC simulations undertaken for pure CO_2, pure CH_4, and CO_2/CH_4 mixture adsorption in a series of the framework structures of Sc_2BDC_3 obtained from the diffraction experiments undertaken with the capillary gas cell method at RT,[34] with the aim of providing clear explanation for the selective CO_2 uptake and phase transition behaviour under those experimental conditions.

6.4 Computational Methods

6.4.1 DFT solid-state calculations

The Mulliken atomic charges for the framework atoms necessary for the input files of the GCMC calculations (Table 6.5) were obtained from the output of DFT calculations carried out using the Cambridge Serial Total Energy Package (CASTEP v17.21) simulation package,[47] with the crystal structures obtained from the *in situ* diffraction experiments used as starting models.[35] The Perdew-Burke-Ernzerhof (PBE) exchange-correlation functional with the Tkachenko-Scheffler (TS) dispersion correction scheme was used,[48, 49] along with a maximum-separation k-point sampling grid of 0.05 $Å^{-1}$. The basis set was constructed from a linear combination of plane waves expressed by an energy cut-off of 800 eV, in conjunction with on-the-fly ultra-soft pseudopotentials, based on convergence to below 3 meV per atom. The initial models were optimised using the Broyden-Fletcher-Goldfarb-Shanno (BFGS) algorithm until the convergence criteria with respect to the energy change (0.005 meV/atom), maximum force (0.05 eV/Å), maximum stress (0.1 GPa) and maximum atomic displacement (0.0005 Å) were met.[50-53]

For simplicity, since the atomic charges varied only slightly between the different linker groups, all BDC linkers were treated equivalently and correspondingly charges on chemically equivalent atoms were averaged in such a way as to ensure charge neutrality across the whole framework.

Table 6.5: Mulliken partial atomic charges, derived from DFT calculations, used in the input for GCMC simulations on the specified structures of Sc_2BDC_3.

	Fddd		*C2/c*		
	All obtained at 298 K	**Obtained at 4.6 bar of CH_4 at 230 K**	**Obtained at 3 bar CO_2 at 298 K**	**Obtained at 10 bar of CO_2 at 298 K**	**Obtained at 4.29 bar 50:50 CO_2/CH_4 uptake at 298 K**
Sc	1.7900	1.7892	1.8000	1.7900	1.7892
O	−0.6000	−0.6008	−0.6025	−0.6004	−0.6008
C1	0.6100	0.6092	0.6162	0.6163	0.6125
C2	−0.0600	−0.0608	−0.0604	−0.0637	−0.0608
C3	−0.2400	−0.2408	−0.2395	−0.2404	−0.2425
H	0.2667	0.2692	0.2646	0.2663	0.2692

* C1 refers to the carboxylic group carbon, C2 refers to the carbon on the phenyl ring adjacent to the carboxylic group and C3 refers to the phenyl C-H carbon.

6.4.2 Grand canonical Monte Carlo (GCMC) simulations

GCMC simulations were carried out using the Multipurpose Simulation Code (MuSiC v3) on a selection of structures obtained from the in-situ diffraction experiments.[34, 54, 55] The framework structures were prepared for the simulations by removing any adsorbed guest molecules but the atomic positions of the framework were not altered, other than normalising C-H bond lengths to 1.089 Å. Supercells of the framework were constructed as close as possible to a cubic shape, by applying integer duplications of the unit cell along the *a*, *b* and *c* axis directions. Thus 4x2x1 and 4x1x3 supercells were used for the *Fddd* and *C2/c* phase structures respectively.

The framework atomic coordinates were kept rigid throughout the entire simulation on each structure. A total of 1×10^7, 5×10^6 and 1×10^7 iterations were used for the simulations concerning CO_2, CH_4 and CO_2/CH_4 adsorption respectively, with the first 50% of the iterations removed from analysis, ensuring that equilibration had been reached. All simulations were carried out at the temperature of the in-situ gas cell experiments,[34] and the fugacities for the gas mixture were determined by the Peng-Robinson equation of state.[56, 57] A cut-off radius of 15 Å was applied to all interactions.

The standard 12-6 Lennard-Jones potential was used to model the van der Waals interactions, with the relevant parameters for the framework atom taken from literature: the Dreiding force field for the linker group C, O and H atoms,[58] and the UFF force field for the Sc atoms (Table 6.6).[59] The guest molecule atoms were represented by the Trappe force field (Table 6.6).[60, 61] CO_2 was modelled by an all-atom model, whereas CH_4 was modelled using the united-atom approach as a spherical probe. The Lorentz-Berthelot mixing rules were used to calculate the mixed LJ parameters. Coulombic interactions were included for the simulations involving CO_2, using the Ewald summation method for guest-framework interactions and the Wolf summation method for guest-guest interactions.[53, 62, 63]

Table 6.6: Lennard-Jones parameters for the atoms in Sc_2BDC_3 framework and CO_2, and for the spherical probe used to model CH_4.

Atom Type	σ (Å)	ε / k_B (K)	Ref.
Sc	2.936	9.561	58
C	3.473	47.856	57
O	3.033	48.158	57
H	2.846	7.649	57
C in CO_2	2.800	28.129	59
O in CO_2	3.050	80.507	59
CH_4	3.730	148.00	60

In order to determine the simulated occupancy of each identified crystallographic adsorption position, a total of 20 snapshots (two groups of 10, using a different seed numbers for each group) of the guest positions were sampled from the GCMC output data, each separated by 50,000 simulation iterations thus ensuring guest position records were statistically unique. The centre-of-mass positions of the guests in each snapshot were then compared with the crystallographically-determined positions; simulated guest molecules that fell less than halfway between a crystallographic site and its nearest neighbouring site were marked as assigned. Simulated molecules that fell out-with this tolerance were marked as unassigned. Assignment rates in all cases exceeded 85%.

6.5 Results and Discussion

6.5.1 CO_2 adsorption in Sc_2BDC_3

Figure 6.5 shows the simulated adsorption isotherms between 0.01 bar and 800 bar for the five selected Sc_2BDC_3 structures. With the exception of the structure obtained experimentally at 10 bar of CO_2, all the adsorption isotherms overlap up to the simulation fugacity of around 5 bar, above which the simulated CO_2 uptake exceeds the highest CO_2 loading seen experimentally in the capillary gas cell studies.[34] This overlap highlights the gradual change in the framework structure observed experimentally; the non-overlapping isotherm for the 10 bar structure seems to suggest that there is a significant difference in the adsorption site environment in this framework which is more readily apparent under simulation since no unusually large change in the framework structure was observed experimentally between 3 bar and 10 bar.

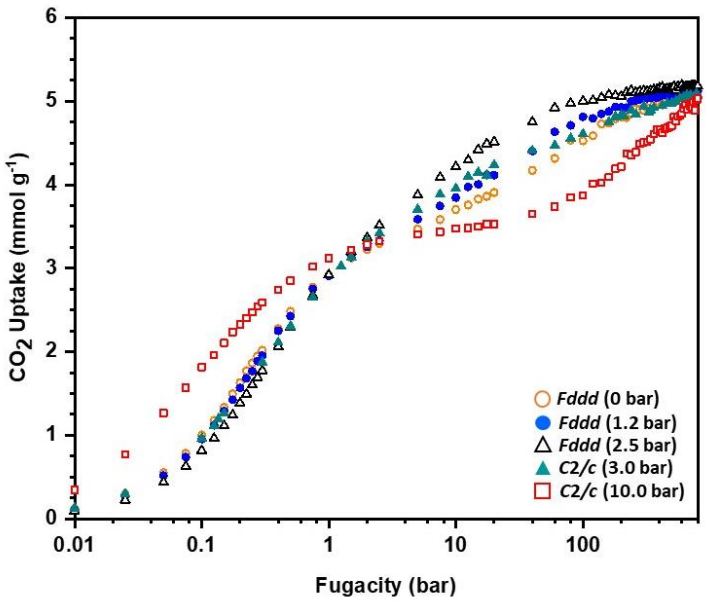

Figure 6.5: Simulated CO_2 adsorption isotherms for Sc_2BDC_3 using a range of experimentally derived framework structures from the variable gas pressure diffraction experiments, at the simulation temperature of 298 K.

Table 6.7 shows the simulated occupancy of each adsorption site in Sc_2BDC_3 at various fugacities or CO_2 uptakes, which can be used to compare with experimental values shown in Table 6.1 and explain the trends in the adsorption isotherms. The majority of guests could be assigned to an adsorption site; however, 100 % assignment was not always possible, due to the molecules occupying small pockets of space in the porous channels outside of the defined radius around each adsorption site, verifying that all accessible space in the porous channels was explored. In the *Fddd* phase at 1.2 bar and 2.5 bar, a strong binding hierarchy in favour of adsorption in site 2 is clearly apparent, with this site partially filling first, almost exclusively accounting for the simulated CO_2 uptake matching the uptake observed experimentally, with site 1 not filling simultaneously until higher fugacities. The simulations hence present an exaggerated preference for site 2 compared to that seen experimentally, in which occupancy is more balanced between the two sites.

Table 6.7: Simulated site occupancies at a range of CO_2 uptake levels in Sc_2BDC_3 for rigid framework models derived from in situ diffraction measurements.

Simulated CO_2 uptake/fugacity	Structure [a]	Simulated Occupancy			% Assigned [b]
		Site 1	Site 2	Site 3	
Matching Experimental Uptake	*Fddd* (1.2 bar)	0.00	0.17(3)	-	100
	Fddd (2.5 bar)	0.03(1)	0.25(6)	-	97
	*C*2/*c* (3.0 bar)	0.20(6)	0.37(3)	0.21(6)	100
	*C*2/*c* (10.0 bar)	0.85(2)	0.41(2)	0.09(6)	85
10 bar	*Fddd* (1.2 bar)	0.13(2)	0.49(1)	-	100
	Fddd (2.5 bar)	0.25(2)	0.47(1)	-	98
	*C*2/*c* (3.0 bar)	0.77(6)	0.51(1)	0.49(4)	99
	*C*2/*c* (10.0 bar)	0.84(2)	0.45(5)	0.08(4)	88
100 bar	*Fddd* (1.2 bar)	0.37(2)	0.53(1)	-	100
	Fddd (2.5 bar)	0.44(1)	0.49(1)	-	96
	*C*2/*c* (3.0 bar)	0.90(4)	0.59(2)	0.55(4)	95
	*C*2/*c* (10.0 bar)	0.86(2)	0.48(3)	0.32(10)	86
800 bar	*Fddd* (1.2 bar)	0.40(2)	0.59(1)	-	99
	Fddd (2.5 bar)	0.52(1)	0.49(1)	-	93
	*C*2/*c* (3.0 bar)	0.93(4)	0.68(2)	0.56(3)	93
	*C*2/*c* (10.0 bar)	0.87(1)	0.73(2)	0.70(5)	88

[a] Gas adsorption pressure at which the structures were determined shown in parenthesis.

[b] **%** Assigned denotes the percentage of CO_2 molecules inside the simulation box that could be assigned to a particular adsorption site.

In the 3.0 bar *C*2/c structure, the simulated occupancies at the experimental CO_2 uptake are within statistical agreement with those seen experimentally, with contribution to adsorption observed across all three adsorption sites, albeit with a slight preference for site 2. At higher fugacities, the occupancies of all three sites increase, with the greatest occupancy attributed to the site 1 position. The 10 bar *C*2/*c* structure displays much higher CO_2 uptake at lower fugacities, attributed to the considerably faster partial filling of site 1 and, to a lesser extent, site 2. The simulations hence exaggerate the site 1 > site 2 > site 3 binding site hierarchy seen experimentally. Between the simulation fugacities of 2.5 and 10.0 bar, the isotherm curve for the 10 bar *C*2/*c* structure plateaued with no change in the site occupancies observed in this fugacity range, prior to the occupancy of site 3 rapidly increasing up to that seen at maximum uptake. In the *C*2/*c* phase, simulated site 2 occupancy well-exceeded 50 % at 800 bar, hence verifying the experimental observation that the two disordered positions for site 2 can form two independent adsorption sites and be simultaneously occupied at higher loadings.[34, 35]

The highest simulated uptake of CO_2 in all five structures is very similar at 800 bar, at *ca.* 5 mmol g^{-1} (Figure 6.5), and falls short of the CO_2 uptake of above 6.2 mmol g^{-1} observed in the cryogenic loading high-pressure study.[35] As previously described, additional structural changes occur at much higher pressures, in terms of the group 1 linker and site 3 position becoming disordered and further group 2 rotation,[35] which are thus attributed for the framework to achieve the maximum possible CO_2 uptake. Therefore, it is unsurprising that this higher CO_2 loading was not achieved in the simulations on the fixed frameworks obtained experimentally at low CO_2 pressures.

Figure 6.6 shows the histograms for the CO_2-framework interaction energies obtained for each structure at their respective simulated uptakes which match that observed experimentally; these can be used to determine the change in CO_2-framework interaction energies across the two phases, and to identify different adsorption sites

on the basis of energy. It is apparent from the data that the CO_2-framework binding energies are *ca.* -40 kJmol^{-1}, in close agreement with the average binding energies derived from the DFT simulations, thus confirming that the force field parameters used in this study are modelling the CO_2 adsorbed Sc_2BDC_3 system well. The interaction energies stated here are a combined total of the individually calculated Coulombic and dispersion energy terms; these interactions are, on average, dispersive dominant, with this energy term accounting for 70-80% of the total energy.

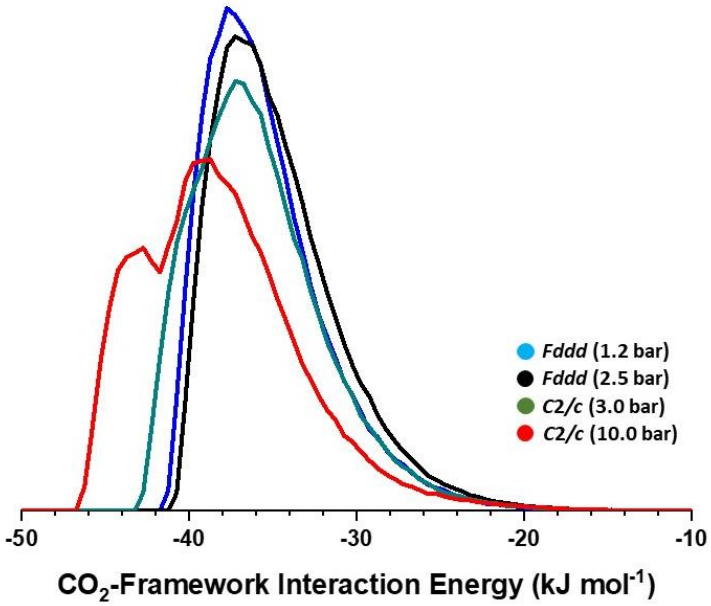

Figure 6.6: CO_2-framework interaction energy histograms for four Sc_2BDC_3 framework structures at their respective experimental CO_2 uptakes. Histogram bin size = 0.5 kJ mol^{-1}.

Only one peak was observed in the histograms for the *Fddd* structures, attributed to the CO_2 molecules mostly exploring the space exclusively around site 2. The histogram for the lower pressure *C*2/c structure only shows one peak, due to the similarity in energy between all adsorption site positions, justified by the similar site occupancies observed at this CO_2 loading. The histogram for the *C2/c* structure obtained at 10 bar contains two peaks, indicating a greater separation between the interaction energies associated with the site 1 and the other two adsorption sites, resulting in the much higher occupancy of site 1. From the overlap of the four

histograms, it is evident that the stronger CO_2-framework interaction energies are exhibited in the *C*2/*c* phase especially in the 10 bar structure, with a slightly narrowing of the interaction energies captured prior to the phase transition.

These trends are more apparent when the results of the simulations undertaken at the simulated fugacity of 800 bar, which allowed for weaker adsorption sites to be better represented, are analysed. The CO_2 centre-of-mass positions captured throughout the simulations revealed that all the experimental CO_2 positions were successfully explored. Although a wide spread of energies was observed in and around each adsorption site, the strongest-energy adsorption site positions could be assigned to site 2 in the *Fddd* phase and site 1 in the *C*2/*c* phase. (Figure 6.7).

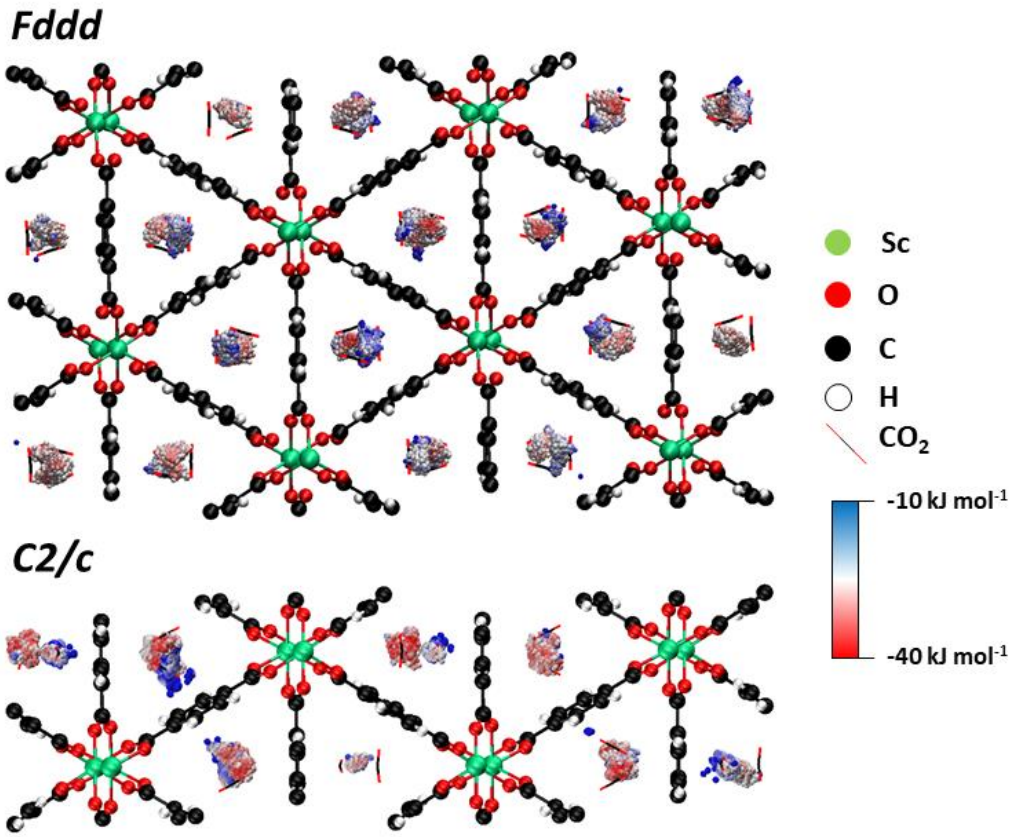

Figure 6.7: Simulated centre-of-mass positions of CO_2 (spheres)at the maximum simulated uptake in the Fddd (1.2 bar) and C2/c (10.0 bar) phases of Sc_2BDC_3, along with the experimental CO_2 positions (lines) for comparison, coloured according to the CO_2-framework interaction energy. Image created using VMD.[64]

The CO_2-framework energy histograms (Figure 6.8) at the simulated fugacity of 800 bar highlight the energetic shift associated with the site 1 position across the pressure series, strengthening from *ca.* -29 kJ mol^{-1} in the evacuated *Fddd* structure to *ca.* -44 kJ mol^{-1} in the 10 bar *C*2/*c* structure. Prior to the phase transition, the shift in the site 1 energy could be due to the increasing site 1···site 2 separation, observed experimentally to increase from 1.25 Å at 1.2 bar to 1.40 Å at 2.5 bar,[33] hence resulting in a less sterically-hindered, and thus more well-defined, site 1 position which allows the CO_2 molecule to bind more effectively to the wall of the porous channel formed by the group 1 linker. After the phase transition, the continued strengthening of the interaction energies associated with site 1 could be attributed to site 1 and site 2 being separated into different porous channels due to the reduction in symmetry, and thus are no longer competing with each other for occupancy. However, the site 2 adsorption site energy showed a minimal response to pressure, with the histogram site for this peak maintaining its position at *ca.* -38 kJ mol^{-1} throughout the pressure series. In any case, the trends observed in the CO_2-framework energy histograms explain the site occupancies, and thus the binding site hierarchies, observed both experimentally and under simulation (Tables 6.1 and 6.7).

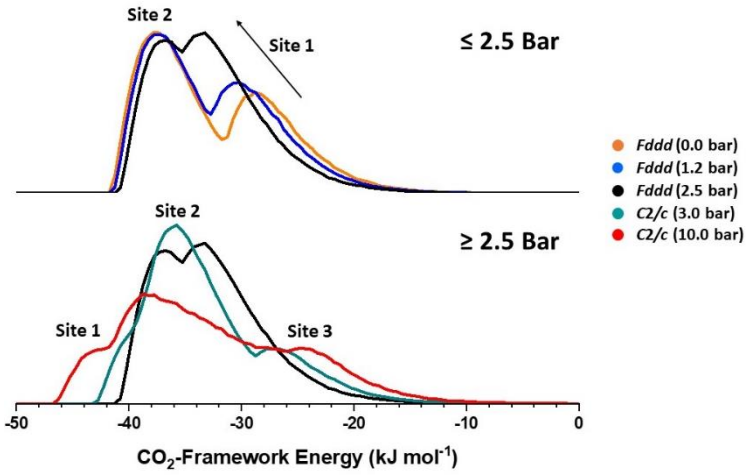

Figure 6.8: CO_2-framework interaction energy histograms obtained at simulated CO_2 fugacity of 800 bar for a selection of Sc_2BDC_3 rigid framework structures derived from the experimental study. The histogram for the Fddd (2.5 bar) structure is shown in both figures to act as a comparison with the trend that occurs before and after the completion of phase transition.

The trends observed in the CO_2-framework interaction energy histograms are summarised clearly by the mean interaction energies calculated for each structure across their respective simulated pressure series (Figure 6.9). At the experimental loadings of CO_2, the mean CO_2-framework interaction energy weakens prior to the phase transition; despite the clear energetic strengthening observed of the site 1 position, it is not sufficiently occupied at low fugacities to cancel out the slight weakening of the strongest interaction energies associated with site 2. After the phase transition, the mean interaction energies strengthen. However, the change in mean interaction energy between the structures obtained below 10 bar is relatively small (< 2 kJ mol^{-1}), which explains the considerable overlap observed in their simulated adsorption isotherms. As the CO_2 loading in all five structures surpasses the levels observed experimentally, the mean interaction energies weaken, a result of CO_2 being unreasonably forced into the framework and thus weaker adsorption sites become more populated. This results in the convergence of the mean interaction energies in both phases, indicating that there is no preference for either phase at these higher CO_2 loadings; the only difference between the two phases is that the *C*2/*c* phase structures exhibit a broader range of energies than those in the *Fddd* phase (Figure 6.8).

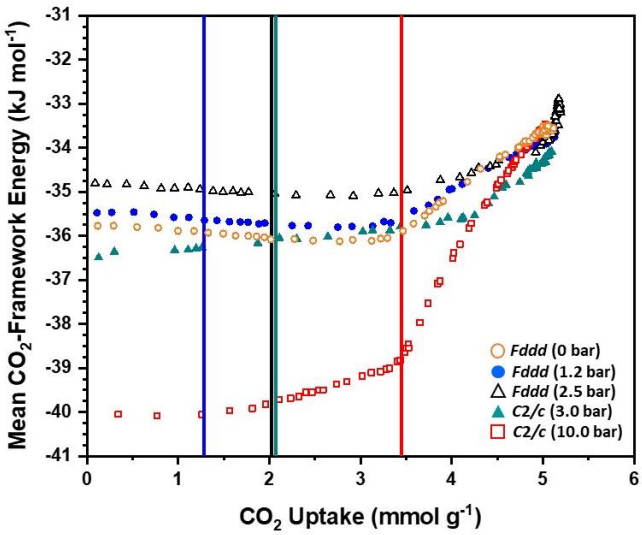

Figure 6.9: Mean CO_2-framework interaction energy obtained for Sc_2BDC_3 rigid framework structures at various CO_2 loadings. The vertical lines represent the experimental CO_2 loading for each structure.

An investigation into the mean $CO_2\cdots CO_2$ interaction energies (Figure 6.10) in the five examined Sc_2BDC_3 structures across the range of simulated CO_2 loadings showed that these interactions get stronger with increasing CO_2 uptake, due to the higher probability of shorter $CO_2(\delta+)\cdots(\delta-)CO_2$ contact distances as guest occupancy increases. However, the mean interaction energies (*ca.* -1 kJ mol^{-1}) were considerably weaker than the observed CO_2-framework interaction energies (*ca* -40 kJ mol^{-1}). This would seem to suggest that the $CO_2\cdots CO_2$ interactions do not provide a significant contribution to the total interaction energies. However, this result could be hiding a potentially considerable difference between the $CO_2\cdots CO_2$ interactions in either phase.

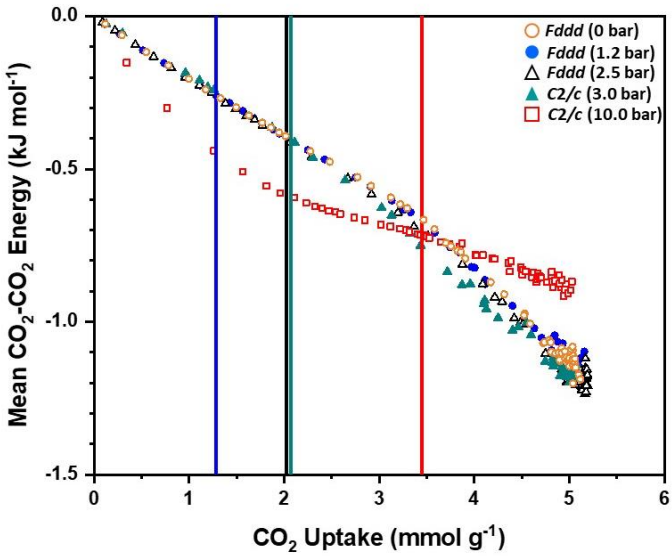

Figure 6.10: Mean CO_2-CO_2 interaction energy obtained for Sc_2BDC_3 rigid framework structures at various CO_2 loadings. The vertical lines represent the experimental CO_2 loading for each structure.

When considering the contact distances between the adsorbed CO_2 molecules according to their positions determined from the diffraction data, the *Fddd* phase exhibits much shorter O···O contact distances (*ca.* 1.3 Å between neighbouring site1···site2 and site2···site2 molecules respectively) than the *C*2/*c* phase (*ca.* 2-3 Å between neighbouring site1···site3 and site2···site2 molecules respectively). However, these distances are a consequence of the symmetries of the two phases and hence do

not reflect the contact distances that are achieved under partial occupancy. Analysis of the positions of CO_2 molecule during the simulations in the *Fddd* phase at experimental uptake showed that the intermolecular O···O contact distances exceeds 3 Å (Figure 6.11). These contact distances are considerably higher than those determined by examining the refined crystallographic positions, and hence this shows that simultaneous occupancy of neighbouring site 1···site 2 and site 2···site 2 positions is not obtainable. The shortest simulated CO_2-CO_2 O···O contact distances in the *C*2/*c* phase however were in the range of 2-3 Å (Figure 6.11), which does agree with the shortest site 2···site 2 (2.1 Å) and site 1···site 3 (2.9 Å) contact distances observed experimentally. This result was replicated when the CO_2···CO_2 C···C and C···O contact distances were considered, as shown in Figure 6.11.

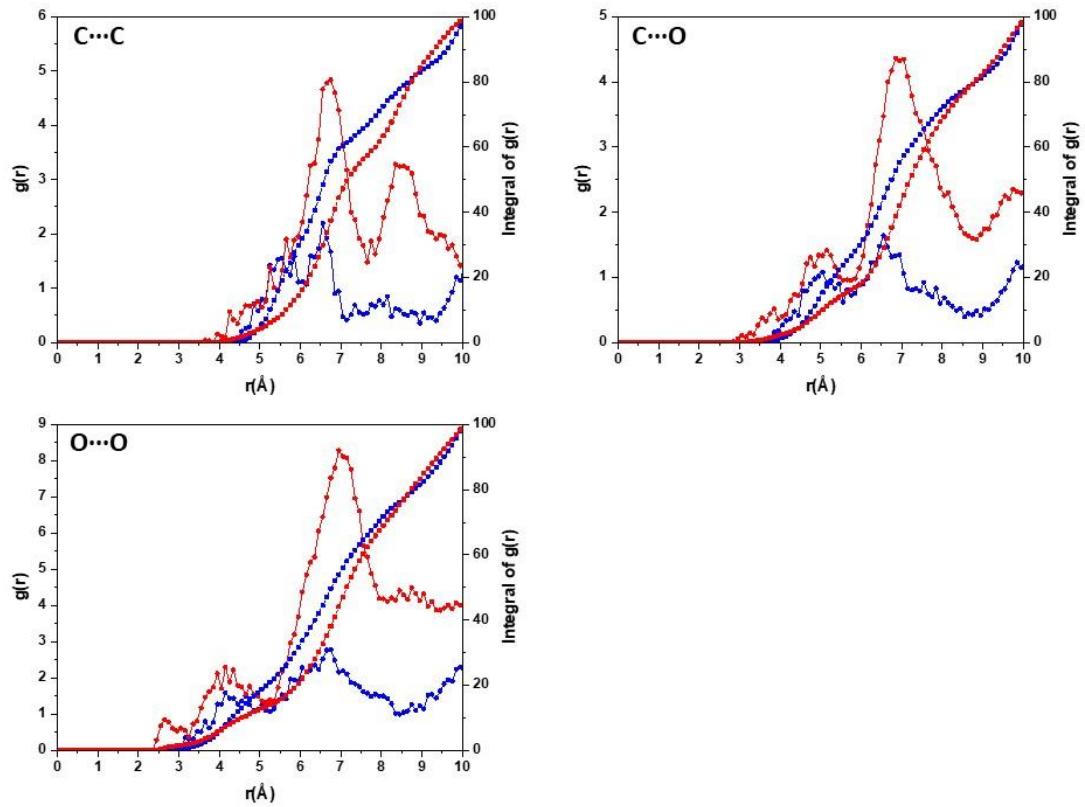

Figure 6.11: G(r) plots (left ordinate) and associated integrals (right ordinate) of the intermolecular C···C, C···O and O···O contact distances recorded during the simulations in the 1.2 bar Fddd (blue) and 10.0 bar C2/c (red) Sc_2BDC_3 frameworks modelled at their respective experimental CO_2 loading.

At the maximum simulated CO_2 uptake, the shortest $CO_2 \cdots CO_2$ contact distances in both phases are lower than those seen at experimental uptake, due to the greater propensity for neighbouring sites to be simultaneously occupied. The *C*2/*c* phase continues to exhibit shorter $CO_2 \cdots CO_2$ contact distances than the *Fddd* phase, but the difference is not as striking as in the snapshots from simulations modelling experimental values of CO_2 uptake (Figure 6.11). Analysing the CO_2-CO_2 interaction energy histograms, which were unobtainable at the time that these simulations were undertaken, would be required to fully understand the effect of the $CO_2 \cdots CO_2$ distances, as well as the specific motif and arrangements of the guest molecules inside the porous channels in the two phases of Sc_2BDC_3, and thus how much these interactions contribute to the thermodynamic driving force for the phase transition.

The array of GCMC simulations have clearly shown that the structural changes in the framework are associated with the formation of stronger CO_2-framework interactions, especially in the case of site 1, and potentially stronger attractive CO_2-CO_2 interaction energies. The changes in the framework structure and adsorption site energies are highly correlated, and thus it is difficult to determine if the phase transition occurs to allow CO_2 to access stronger adsorption sites or if it is the result of the framework reconfiguring around the higher CO_2 loadings and the accessibility to stronger adsorption site positions is serendipitous. In any case, the GCMC simulations have provided a far more detailed insight into the adsorption behaviour of CO_2 in Sc_2BDC_3 compared to that provided by the DFT calculations, as well as explaining the adsorption site binding hierarchies observed experimentally.

6.5.2 CH_4 adsorption in Sc_2BDC_3

A similar procedure was undertaken for modelling CH_4 adsorption in a range of Sc_2BDC_3 structures; the simulated adsorption isotherms and site occupancies are shown in Figure 6.12 and Table 6.8.

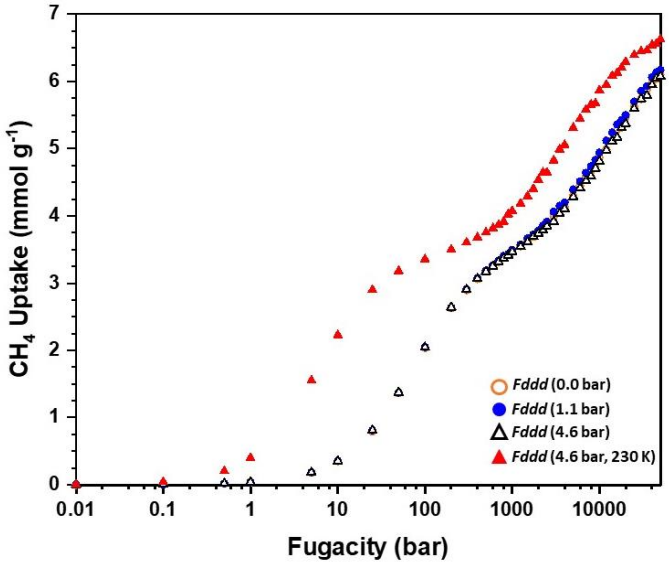

Figure 6.12: Simulated CH_4 adsorption isotherms for the range of Sc_2BDC_3 structures obtained experimentally under CH_4 uptake at the simulation temperature of 298 K unless otherwise stated. The curves for all structures, except that modelled at 230 K, are overlapping.

Table 6.8: Simulated CH_4 adsorption site occupancies at experimental and highest fugacity uptake in the Sc_2BDC_3 structure obtained experimentally at 4.6 bar and 230 K.

	Site 2 Occupancy	Site 3 Occupancy	% Assigned [a]
Experimental Uptake	0.00(0)	0.64(3)	100
30 kbar	0.44(2)	1.00(0)	100

[a] % Assigned denotes the percentage of CH_4 molecules inside the simulation box that could be assigned to a particular adsorption site.

The CH_4 adsorption greatly differs from that recorded for CO_2 in a couple of respects. Firstly, CH_4 uptake was not observed at low fugacities (below 10 bar) and there are two clear loading regimes, attributed to the complete filling of site 3 up to 500 bar and the filling of site 2 above 500 bar. The lack of framework structural changes at the various experimental CH_4 pressures resulted in the strong overlap of the three isotherms recorded at 298 K. Simulated CH_4 uptake of 6.41 mmol g^{-1} was calculated at 30 kbar in the simulation run at 230 K, which consistently produced higher CH_4 loadings due to the lower simulation temperature rather than as a result of significant framework structural changes. This uptake was attributed to 100 % occupancy of

site 1 and just under than 50 % occupancy of site 2, in good agreement with the maximum uptake hypothesised in the literature,[30] prior to the separation of neighbouring site 2 positions into independent adsorption sites seen at extremely high pressures.[35]

As expected from the distinctive filling of each adsorption site, only one peak was observed in the CH_4-framework interaction energy histograms (Figure 6.13) at low simulated fugacities, representing site 3, at *ca.* -19 kJ mol^{-1}. At higher simulated fugacities, a second peak became visible at *ca.* -9 kJ mol^{-1}, associated with adsorption at site 2. This was clarified by looking at the positions of the strongest and weakest CH_4-framework interaction energies observed throughout the simulation (Figure 6.14).

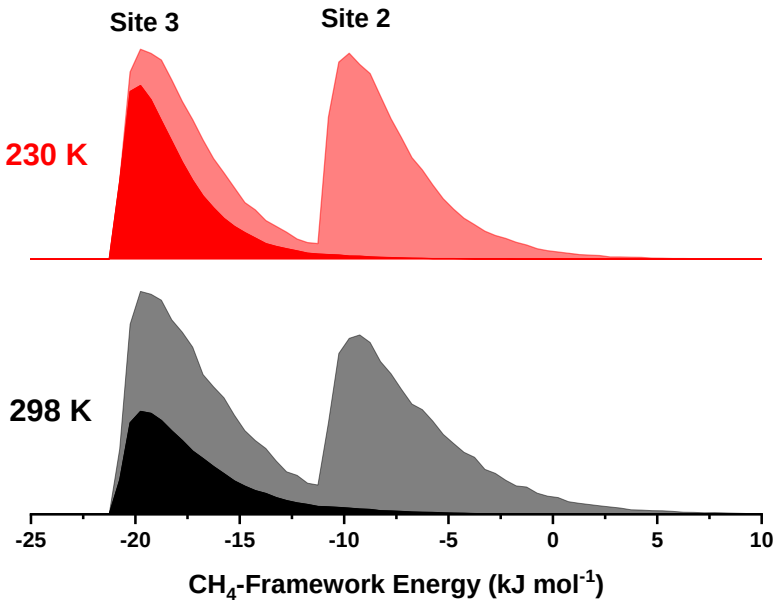

Figure 6.13: CH_4-framework interaction energy histograms for Sc_2BDC_3 structures obtained experimentally under 4.6 bar of CH_4 at 298 K and 230 K. Darker and lighter coloured areas represent energies obtained at low and high simulated levels of CH_4 uptake respectively.

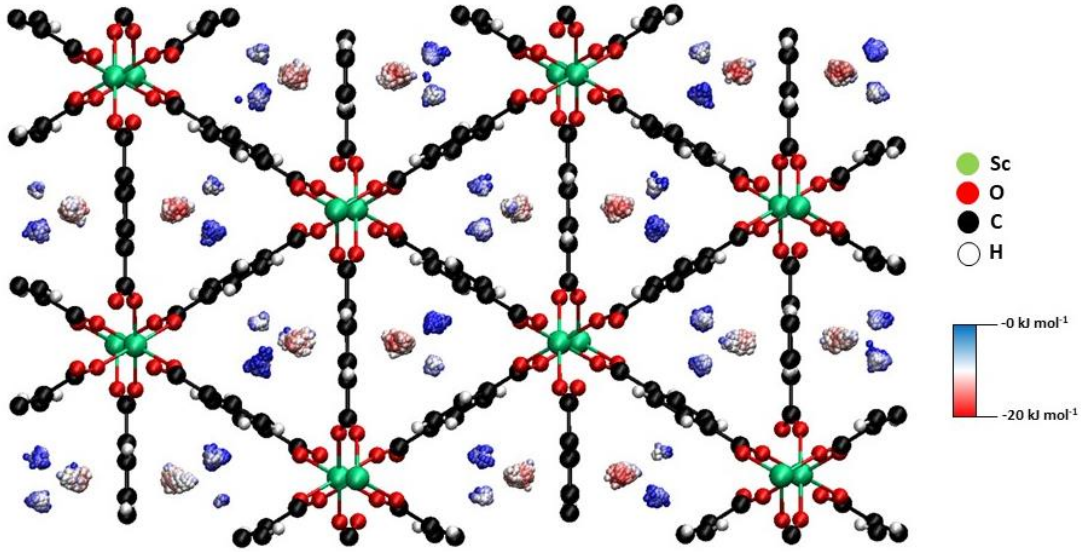

Figure 6.14: Simulated centre-of-mass positions of CH_4 (spheres) at the maximum simulated uptake in Sc_2BDC_3, coloured according to the CH_4-framework interaction energy. Image created using VMD.[64]

The DFT simulations predicted a stronger net binding energy for adsorbed CH_4 in Sc_2BDC_3 (*ca.* -34 $kJmol^{-1}$) than observed using the spherical probe model for CH_4 in the GCMC simulations. However, this disparity could be caused by the use of the dispersion correction in the DFT calculations resulting in an over-binding between CH_4 and the framework, as discussed in Section 6.3.4.

The results of the simulations modelling CH_4 adsorption in Sc_2BDC_3 were overall more straightforward to interpret compared to those in the CO_2 study. The CH_4 adsorption site energies were seen to be far more localised, which resulted in a much clearer binding site hierarchy with almost complete filling of site 3 prior to adsorption in the site 2 position, compared to the large overlap in the interaction energies associated with different adsorption sites and changing binding site hierarchy observed for CO_2. The considerably weaker CH_4-framework energies obtained from the GCMC simulations explain the lower CH_4 loadings seen experimentally, and thus have provided clarity over the apparent selectivity for CO_2 adsorption.

CH_4 uptake in the *C*2/*c* phase has not been evaluated up to this point, given the phase transition was not observed experimentally under CH_4 adsorption. Therefore, an additional set of calculations were undertaken to model the full range of CH_4 loadings in a *C*2/*c* phase structure (that was obtained under 10 bar of CO_2) to investigate the CH_4 adsorption behaviour in that phase. Figures 6.15 and 6.16 show the adsorption isotherms and CH_4-framework energy histograms respectively for CH_4 adsorption in the *C*2/*c* phase structure of Sc_2BDC_3 in comparison to the results already discussed for the *Fddd* phase structure obtained at 298 K and 4.6 bar of CH_4.

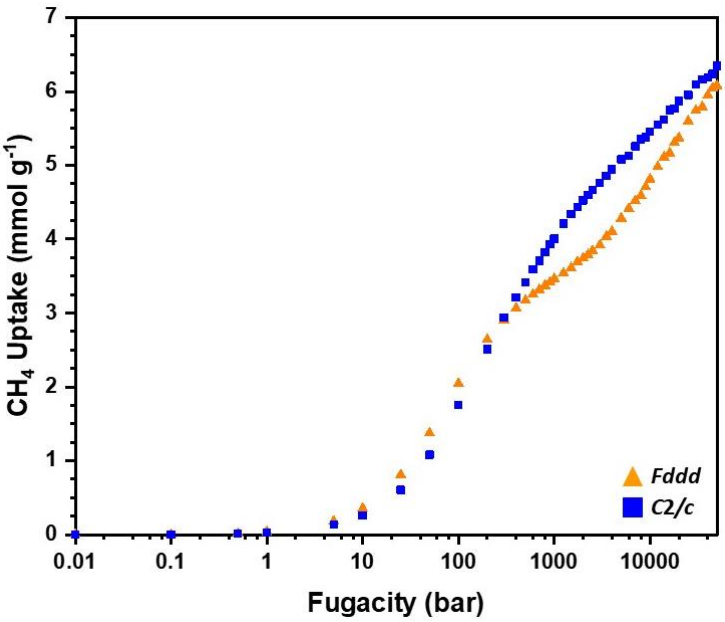

Figure 6.15: Adsorption isotherms of simulated CH_4 uptake in the Fddd (orange triangles) and C2/c (blue squares) phases of Sc_2BDC_3 framework structures, at a simulation temperature of 298 K.

Three distinctive phases in the simulated adsorption isotherms can be observed, which can be explained by the CH_4-framework interaction energies observed across the two phases. Firstly, up to 100 bar, the *Fddd* phase displayed slightly higher uptake; this is due to a larger proportion of the interaction energies associated with the primary adsorption site in the *Fddd* phase being stronger than those in the *C*2/*c* phase. Between 100 bar and 5000 bar, the simulated CH_4 loading in the *C*2/*c* phase overtook that of the *Fddd* phase; this is due to its weaker adsorption sites being represented by

interaction energies (between -15 and -10 kJ mol^{-1}) which are, in general, stronger than the energies recorded for adsorption at site 2 in the *Fddd* phase, and thus they are occupied faster. Above 5000 bar, while the *C*2/*c* phase continued to display higher uptake, the gap in loading between the two phases closed due to the filling of the site 2 position in the *Fddd* phase, with the two curves almost converging by the highest fugacity point.

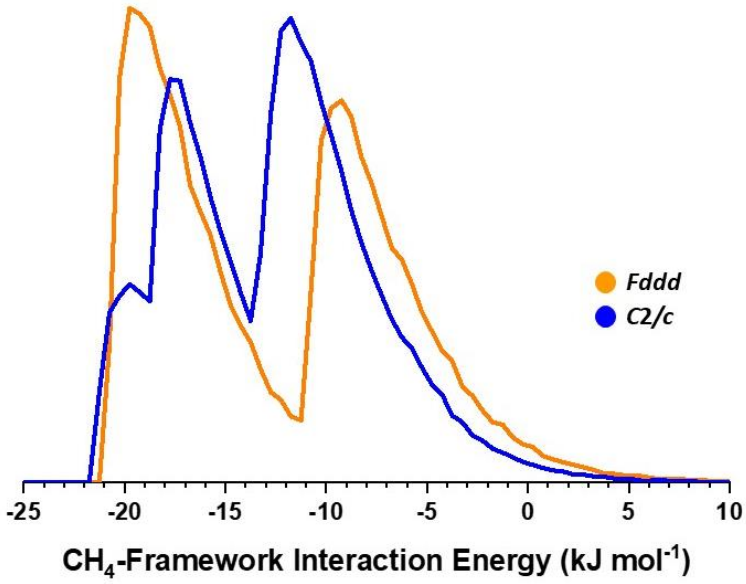

Figure 6.16: CH_4-framework interaction energy histograms at the maximum simulated CH_4 uptake in the two phases of Sc_2BDC_3.

Although the *C*2/*c* phase displayed higher uptake for a majority of the simulated adsorption isotherm, the *Fddd* phase displayed higher simulated uptake at the fugacities associated with the gas pressures used in the diffraction studies. Furthermore, there were no considerable differences in the mean interaction energy between the two phases. These results therefore clarify why the framework does not undergo the phase transition to the *C*2/*c* phase under pure CH_4 uptake; there is no energetic benefit in it doing so. Before moving onto the results of the simulations considering modelling adsorption of CO_2/CH_4 gas mixtures, there is one further result for discussion, which is that the CH_4 binding site hierarchy in the *C*2/*c* phase is not as

simplistic as in the *Fddd* phase, in that three peaks were observed in the CH_4-framework interaction energy histogram.

The recorded positions of the CH_4 guest molecules in the *C*2/*c* phase (Figure 6.17), revealed that the CH_4 guest molecules were clearly observed exploring the site 3 position in both porous channels; the CH_4 molecules thus seem to ignore the asymmetry of the porous channels. Additional complications arise from the fact that the site 3 positions either side of the group 1 linker appear to be energetically inequivalent. The site 3 position in the group 2b channel appears to be responsible for stronger guest-framework interactions, compared to the site 3 position in the group 2a channel. In the *C*2/*c* phase, occupation of adsorption site positions similar to that of site 2 are observed in the group 2b channel. However, in the channel surrounded by the group 2a linkers, it is difficult to determine if CH_4 occupation is occurring in two very close contact site 2 positions or the occupation is smeared out considerably across a position similar to the site 1 position seen for CO_2. This more complicated binding site hierarchy will need to be considered carefully in the modelling of adsorption of the gas mixture, since it may disrupt selectivity after the phase transition, given that the occupancy of site 3 either side of the group 1 linker by CH_4 could cause competition for adsorption with weakly-bound CO_2 molecules in sites 2 and 3, especially the latter since it is the weakest CO_2 adsorption site.

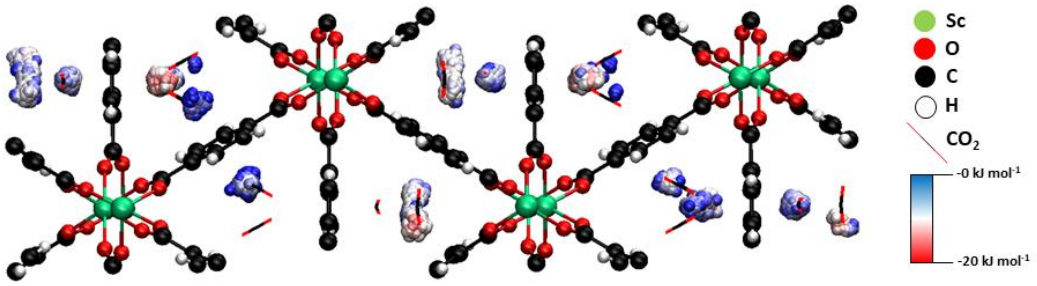

Figure 6.17: Simulated centre-of-mass positions of CH_4 at maximum simulated uptake in the 10.0 bar C2/c Sc_2BDC_3 structure from the pure CO_2 adsorption study, coloured according to the CH_4-framework interaction energy, along with the experimental CO_2 positions (lines) as reference points. Image created using VMD.[64]

6.5.3 50:50 CO_2/CH_4 mixture adsorption in Sc_2BDC_3

The X-ray diffraction experiments on Sc_2BDC_3 under the exposure of CO_2/CH_4 gas mixtures, as discussed in Section 6.3, revealed that the presence of CH_4 in the gas mixture causes a delay in the *Fddd*⟶*C*2/*c* phase transition, with respect to total gas mixture pressure; Sc_2BDC_3 remained in the *Fddd* phase until a partial pressure of CO_2 of *ca.* 2 bar.[34] Other than the delay in the phase transition, the system behaved in a similar manner to that observed under pure CO_2 adsorption, with the same adsorption sites in both phases as under pure CO_2, with seemingly no evidence of CH_4 adsorption.[34] Based upon the results obtained for both guests separately, specifically the much stronger guest-framework interaction energies calculated for CO_2 adsorption, the results obtained experimentally under the exposure of the gas mixtures are not surprising. However, to ascertain the true behaviour of the adsorption site occupancy and interaction energies under the uptake of the gas mixture, GCMC simulations were undertaken to model 50:50 CO_2/CH_4 adsorption in the related structures of Sc_2BDC_3.

The resulting adsorption isotherms, shown in Figure 6.18, reveal very similar adsorption behaviour compared to the pure gas adsorption models. The three isotherms for CO_2 loading overlap consistently at lower fugacities, due to the *C*2/*c* structure used here originating from a CO_2 partial pressure close to the phase transition pressure. Up to 100 bar, guest adsorption was almost exclusively observed for CO_2. Above 500 bar there appears to be an ordering of the different Sc_2BDC_3 structures in terms of CH_4 uptake, with considerably higher uptake observed in the *C*2/*c* phase, mirroring the results discussed in the previous section for pure CH_4 uptake. Above 500 bar, there was also a slight decrease in CO_2 uptake in the *C*2/*c* phase, and fluctuations in the uptake of both guests were observed between fugacity points, suggesting that exchange of CO_2 and CH_4 in certain adsorption sites was occurring.

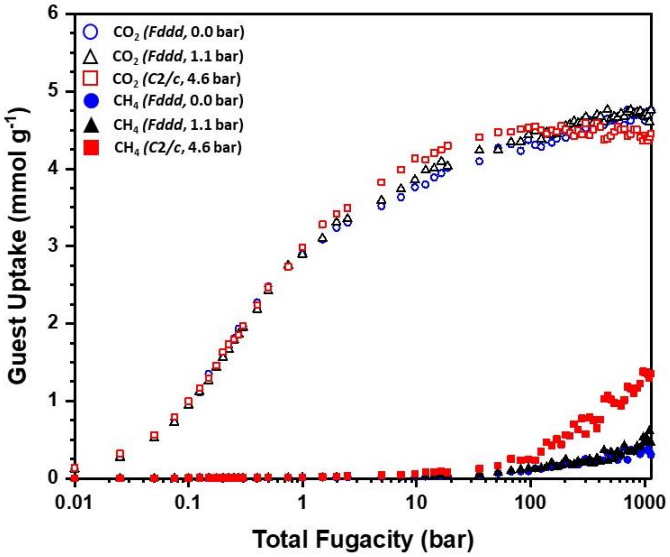

Figure 6.18: Simulated CO_2 and CH_4 adsorption isotherms from modelling of 50:50 CO_2:CH_4 gas mixture adsorption in various structures of Sc_2BDC_3 at a simulation temperature of 298 K.

An examination of the simulated site occupancies, by CO_2, in the *C*2/*c* phase between 100 bar and 1000 bar (Table 6.9) revealed a sharp decrease in the site 3 occupancy from 0.77(5) to 0.41(3). Some of this site occupancy decrease appeared to be offset by an increase in the occupancy of site 1, which is appropriate given the sites co-exist within the same porous channel, while the remainder could have caused by the desorption of CO_2 molecules from the framework, exchanging for CH_4 molecules. The loss of CO_2 molecules from the site 3 position cannot fully account for the higher CH_4 uptake in the *C*2/*c* phase; CH_4 adsorption was also observed in the site 2 position (Figure 6.19), seemingly in-between the sites already occupied by CO_2 since no decrease in the CO_2 occupancy of site 2 was observed between 100 and 1000 bar. Furthermore, the phenomenon observed under simulated pure CH_4 uptake, that the CH_4 guest molecules occupy site 3 positions both sides of the group 1 linker and thus ignore the asymmetric nature of the porous channels in the *C*2/*c* phase, was not observed under mixture uptake (Figure 6.19). It thus appears that the accessibility of the adsorption site positions for CH_4 is driven by the occupancy of the adsorption sites by CO_2, and there is not enough space in the group 2b porous channel to accommodate both CO_2 and CH_4 in site 2 positions and CH_4 in site 3.

Table 6.9: Simulated site occupancies of CO_2 in the crystallographic CO_2 adsorption site positions at a range of fugacity values in the 4.29 bar C2/c phase structure from the simulations modelling 50:50 CO_2/CH_4 adsorption.

Fugacity	Simulated Occupancy			Assigned %
	Site 1	Site 2	Site 3	
10 bar	0.50(5)	0.50(2)	0.61(5)	94
100 bar	0.52(4)	0.57(3)	0.77(5)	92
1000 bar	0.69(4)	0.59(3)	0.41(3)	91

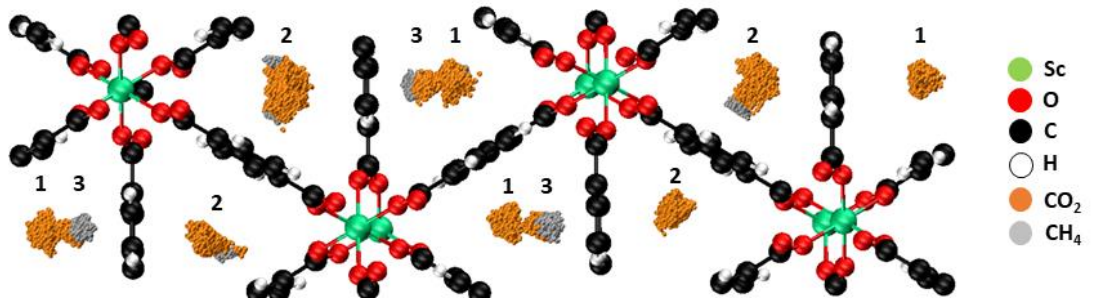

Figure 6.19: Simulated centre-of-mass positions of CO_2 and CH_4 at the maximum simulated uptake in the 4.29 bar C2/c Sc_2BDC_3 structure from the 50:50 CO_2/CH_4 gas mixture study. Image created using VMD.[64]

The CO_2-framework interaction energy histograms (Figure 6.20), obtained at the highest modelled fugacity, revealed very little difference to those seen in the pure CO_2 studies. Importantly, given that the *C*2/*c* phase was obtained at relatively low pressures, and thus the phase transition was only just complete, the majority of CO_2-framework interaction energies are represented by one large peak, thus explaining the even filling of each adsorption site observed from the simulated and experimental site occupancies.

The CH_4-framework energy histograms (Figure 6.20) also look similar to those seen in the pure CH_4 models, with the narrowing of the two main histogram peaks observed in the *C*2/*c* phase compared to those calculated for the *Fddd* phase. Therefore, while there is slight change in the adsorption site energies observed after the phase transition, it is evident that the CH_4 adsorption sites are far less responsive to the framework structural changes than the CO_2 adsorption sites, and there appears

to be minimal difference between the CH_4 adsorption site energies calculated in the 4.29 bar and 10.0 bar *C*2/*c* structures. Therefore, it is hypothesised that, with increasing pressure, the selectivity for CO_2 uptake over CH_4 would not be adversely affected. It should be noted that the results being discussed here are from the models at the highest simulation fugacity value, and thus the guest loading well-exceeds the experimental gas loadings. If only the strongest guest-framework interaction energies were considered, which is more the case at experimental loadings, the high selectivity for CO_2 uptake over CH_4 in both phases is more certain.

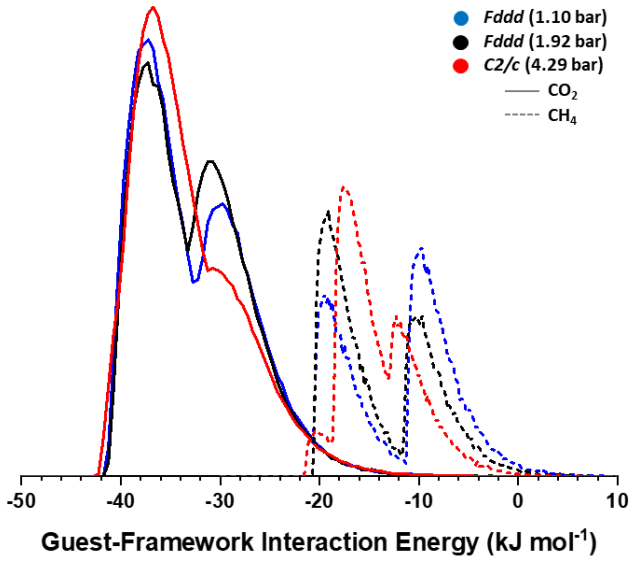

Figure 6.20: Guest-framework interaction energy histograms for CH_4 and CO_2 in Sc_2BDC_3 obtained at the highest fugacity value in the GCMC simulations of the 50:50 CO_2/CH_4 mixture study.

These results have shown that, below 10 bar at least, the models predict high selectivity for CO_2 under exposure to the CO_2/CH_4 gas mixture, which is unaffected by the phase transition, in good agreement with the diffraction studies that found no evidence of CH_4 uptake up to 4.29 bar. While the simulations have provided a strong basis to predict that selectivity for CO_2 would be maintained, diffraction studies under higher pressure CO_2/CH_4 gas mixtures would be required to confirm the suitability of this framework for sustained gas separation application.

6.6 Conclusions

This study has involved an extensive series of GCMC simulations on a range of experimentally-obtained framework structures to model CO_2, CH_4, and CO_2/CH_4 mixture adsorption in Sc_2BDC_3. The simulated results on the structures from across the entirety of the pressure series have been combined, providing an explanation for the phase transition and guest selectivity behaviour, which were unresolved from the diffraction experiments and previous solid-state calculations. The CO_2 adsorption sites were revealed to be strongly responsive to the changes in the framework structure *via* the rotation of the group 2 linkers, especially site 1 which shifted from the secondary binding site in the *Fddd* phase to the primary binding site in the *C*2/*c* phase. At partial uptake, the stronger CO_2-framework energies were identified in the *C*2/*c* phase, and thus showed that the phase transition is highly correlated with the changes in adsorption site environment, but at close to full occupancy the mean interaction energies in the two phases are indistinguishable. Therefore, the use of the classical-based simulations has been justified, since they were able to capture the behaviour at partial uptake, which cannot be achieved using DFT methods. Considerably-weaker CH_4-framework interaction energies were observed when CH_4 adsorption was modelled, thus explaining the experimental behaviour in terms of the much lower CH_4 loadings and the lack of evidence for CH_4 uptake when Sc_2BDC_3 was exposed to CO_2/CH_4 mixtures. The simulations also went beyond the experimental results to probe the behaviour of CH_4 adsorption in higher-pressure *C*2/*c* structures, to show that selectivity for CO_2 uptake would be maintained at higher pressures. This work has therefore provided another successful example of how GCMC simulations can be applied in a complementary approach with experimental methods. The results obtained from the unpublished experimental work outlined in the introduction combined with the GCMC simulations would serve as an important contribution to the understanding of gas adsorption behaviour in MOFs.

6.7 References

1. J. McHardy, MChemX Project Report, Edinburgh, 2015.
2. J. L. C. Rowsell and O. M. Yaghi, *Microporous Mesoporous Mater.*, 2004, **73**, 3-14.
3. S. L. Griffin and N. R. Champness, *Coord. Chem. Rev.*, 2020, **414**.
4. J. Lee, O. K. Farha, J. Roberts, K. A. Scheidt, S. T. Nguyen and J. T. Hupp, *Chem. Soc. Rev.*, 2009, **38**, 1450-1459.
5. Y. J. Cui, Y. F. Yue, G. D. Qian and B. L. Chen, *Chem. Rev.*, 2012, **112**, 1126-1162.
6. L. E. Kreno, K. Leong, O. K. Farha, M. Allendorf, R. P. Van Duyne and J. T. Hupp, *Chem. Rev.*, 2012, **112**, 1105-1125.
7. R. J. Young, M. T. Huxley, E. Pardo, N. R. Champness, C. J. Sumby and C. J. Doonan, *Chem. Sci.*, 2020, **11**, 4031-4050.
8. U. Mueller, M. Schubert, F. Teich, H. Puetter, K. Schierle-Arndt and J. Pastre, *J. Mater. Chem.*, 2006, **16**, 626-636.
9. L. J. Murray, M. Dinca and J. R. Long, *Chem. Soc. Rev.*, 2009, **38**, 1294-1314.
10. H. Furukawa, N. Ko, Y. B. Go, N. Aratani, S. B. Choi, E. Choi, A. O. Yazaydin, R. Q. Snurr, M. O'Keeffe, J. Kim and O. M. Yaghi, *Science*, 2010, **329**, 424-428.
11. J. R. Li, Y. G. Ma, M. C. McCarthy, J. Sculley, J. M. Yu, H. K. Jeong, P. B. Balbuena and H. C. Zhou, *Coord. Chem. Rev.*, 2011, **255**, 1791-1823.
12. J. R. Li, J. Sculley and H. C. Zhou, *Chem. Rev.*, 2012, **112**, 869-932.
13. Y. Y. Liu, Z. Y. U. Wang and H. C. Zhou, *Greenhouse Gas Sci. Technol.*, 2012, **2**, 239-259.
14. M. P. Suh, H. J. Park, T. K. Prasad and D. W. Lim, *Chem. Rev.*, 2012, **112**, 782-835.
15. H. Furukawa, K. E. Cordova, M. O'Keeffe and O. M. Yaghi, *Science*, 2013, **341**, 123044.
16. J. L. C. Rowsell, E. C. Spencer, J. Eckert, J. A. K. Howard and O. M. Yaghi, *Science*, 2005, **309**, 1350-1354.
17. H. Wu, W. Zhou and T. Yildirim, *J. Am. Chem. Soc*, 2007, **129**, 5314-5315.
18. H. Wu, W. Zhou and T. Yildirim, *J. Phys. Chem. C*, 2009, **113**, 3029-3035.
19. E. D. Bloch, L. J. Murray, W. L. Queen, S. Chavan, S. N. Maximoff, J. P. Bigi, R. Krishna, V. K. Peterson, F. Grandjean, G. J. Long, B. Smit, S. Bordiga, C. M. Brown and J. R. Long, *J. Am. Chem. Soc*, 2011, **133**, 14814-14822.
20. T. L. Easun, F. Moreau, Y. Yan, S. H. Yang and M. Schroder, *Chem. Soc. Rev.*, 2017, **46**, 239-274.
21. P. Z. Moghadam, A. Li, S. B. Wiggin, A. Tao, A. G. P. Maloney, P. A. Wood, S. C. Ward and D. Fairen-Jimenez, *Chem. Mater.*, 2017, **29**, 2618-2625.

22. E. J. Carrington, I. J. Vitorica-Yrezabal and L. Brammer, *Acta Crystallogr., Sect. B: Struct. Sci., Cryst. Eng. Mater.*, 2014, **70**, 404-422.

23. B. Pato-Doldan, M. H. Rosnes and P. D. C. Dietzel, *Chemsuschem*, 2017, **10**, 1710-1719.

24. L. Hamon, P. L. Llewellyn, T. Devic, A. Ghoufi, G. Clet, V. Guillerm, G. D. Pirngruber, G. Maurin, C. Serre, G. Driver, W. van Beek, E. Jolimaitre, A. Vimont, M. Daturi and G. Ferey, *J. Am. Chem. Soc*, 2009, **131**, 17490-17499.

25. M. I. Gonzalez, J. A. Mason, E. D. Bloch, S. J. Teat, K. J. Gagnon, G. Y. Morrison, W. L. Queen and J. R. Long, *Chem. Sci.*, 2017, **8**, 4387-4398.

26. T. R. Jensen, T. K. Nielsen, Y. Filinchuk, J. E. Jorgensen, Y. Cerenius, E. M. Gray and C. J. Webb, *J. Appl. Crystallogr*, 2010, **43**, 1456-1463.

27. D. S. Yufit and J. A. K. Howard, *J. Appl. Crystallogr*, 2005, **38**, 583-586.

28. J. Perles, M. Iglesias, M. A. Martin-Luengo, M. A. Monge, C. Ruiz-Valero and N. Snejko, *Chem. Mater.*, 2005, **17**, 5837-5842.

29. S. R. Miller, P. A. Wright, C. Serre, T. Loiseau, J. Marrot and G. Ferey, *Chem. Commun.*, 2005, **30**, 3850-3852.

30. S. R. Miller, P. A. Wright, T. Devic, C. Serre, G. Ferey, P. L. Llewellyn, R. Denoyel, L. Gaberova and Y. Filinchuk, *Langmuir*, 2009, **25**, 3618-3626.

31. A. J. Graham, A. M. Banu, T. Düren, A. Greenaway, S. C. McKellar, J. P. S. Mowat, K. Ward, P. A. Wright and S. A. Moggach, *J. Am. Chem. Soc*, 2014, **136**, 8606-8613.

32. J. P. S. Mowat, S. R. Miler, J. M. Griffin, V. R. Seymour, S. E. Ashbrook, S. P. Thompson, D. Fairen-Jimenez, A. M. Banu, T. Düren and P. A. Wright, *Inorg. Chem.*, 2011, **50**, 10844-10858.

33. K. Brendenburg, DIAMOND, Crystal Impact GbR, Bonn, Germany, 1999.

34. J. Sotelo, PhD thesis, University of Edinburgh, 2015.

35. J. Sotelo, C. H. Woodall, D. R. Allan, E. Gregoryanz, R. T. Howie, K. V. Kamenev, M. R. Probert, P. A. Wright and S. A. Moggach, *Angew. Chem., Int. Ed.*, 2015, **54**, 13332-13336.

36. C. A. Morrison, unpublished work.

37. T. Düren, L. Sarkisov, O. M. Yaghi and R. Q. Snurr, *Langmuir*, 2004, **20**, 2683-2689.

38. T. Düren, Y. S. Bae and R. Q. Snurr, *Chem. Soc. Rev.*, 2009, **38**, 1237-1247.

39. D. Fairen-Jimenez, S. A. Moggach, M. T. Wharmby, P. A. Wright, S. Parsons and T. Düren, *J. Am. Chem. Soc*, 2011, **133**, 8900-8902.

40. C. L. Hobday, C. H. Woodall, M. J. Lennox, M. Frost, K. Kamenev, T. Düren, C. A. Morrison and S. A. Moggach, *Nat. Commun.*, 2018, **9**, 1429.

41. D. F. Sava, M. A. Rodriguez, K. W. Chapman, P. J. Chupas, J. A. Greathouse, P. S. Crozier and T. M. Nenoff, *J. Am. Chem. Soc*, 2011, **133**, 12398-12401.

42. C. L. Hobday, T. D. Bennett, D. Fairen-Jimenez, A. J. Graham, C. A. Morrison, D. R. Allan, T. Düren and S. A. Moggach, *J. Am. Chem. Soc*, 2018, **140**, 382-387.
43. Q. Y. Yang and C. L. Zhong, *Chemphyschem*, 2006, **7**, 1417-1421.
44. Q. Y. Yang and C. L. Zhong, *J. Phys. Chem. B*, 2006, **110**, 17776-17783.
45. R. Babarao, Z. Q. Hu, J. W. Jiang, S. Chempath and S. I. Sandler, *Langmuir*, 2007, **23**, 659-666.
46. Y. S. Bae, K. L. Mulfort, H. Frost, P. Ryan, S. Punnathanam, L. J. Broadbelt, J. T. Hupp and R. Q. Snurr, *Langmuir*, 2008, **24**, 8592-8598.
47. P. J. Hasnip, K. Refson, M. I. J. Probert, J. R. Yates, S. J. Clark and C. J. Pickard, *Philos. Trans. R. Soc. A*, 2014, **372**.
48. J. P. Perdew, K. Burke and M. Ernzerhof, *Phys. Rev. Lett.*, 1996, **77**, 3865-3868.
49. A. Tkatchenko and M. Scheffler, *Phys. Rev. Lett.*, 2009, **102**, 073005.
50. C. G. Broyden, *J. Inst. Math. Appl.*, 1970, **6**, 76-90.
51. R. Fletcher, *Computer Journal*, 1970, **13**, 317-322.
52. D. Goldfarb, *Math Comput.*, 1970, **24**, 23-26.
53. D. F. Shanno, *Math. Comput.*, 1970, **24**, 647-656.
54. D. Frenkel and B. Smit, *Understanding Molecular Simulation*, Academic Press, San Diego, 2nd edn., 2002.
55. A. Gupta, S. Chempath, M. J. Sanborn, L. A. Clark and R. Q. Snurr, *Mol. Simul.*, 2003, **29**, 29-46.
56. D. Peng and D. B. Robinson, *Ind. Eng. Chem. Fundam.*, 1976, **15**, 59-64.
57. B. E. Poling, J. M.Prausnitz and J. P. O'Connell, *The properties of gases and liquids*, McGraw-Hill, London, 2007.
58. S. L. Mayo, B. D. Olafson and W. A. Goddard, *J. Phys. Chem*, 1990, **94**, 8897-8909.
59. A. K. Rappe, C. J. Casewit, K. S. Colwell, W. A. Goddard and W. M. Skiff, *J. Am. Chem. Soc*, 1992, **114**, 10024-10035.
60. J. J. Potoff and J. I. Siepmann, *Aiche Journal*, 2001, **47**, 1676-1682.
61. M. G. Martin and J. I. Siepmann, *J. Phys. Chem. B*, 1998, **102**, 2569-2577.
62. P. P. Ewald, *Ann. Phys-Berlin*, 1921, **369**, 253-287.
63. D. Wolf, P. Keblinski, S. R. Phillpot and J. Eggebrecht, *J. Chem. Phys.*, 1999, **110**, 8254-8282.
64. W. Humphrey, A. Dalke and K. Schulten, *J. Molec. Graphics*, 1996, **14**, 33-38.

Chapter 7

Conclusions and Future Work

The main achievements of the thesis, in terms of evaluating the structure-property relationships of pressure-responsive materials, can be summarised by considering the conclusions of each experimental chapter, alongside an outlook towards how the newly-found information can contribute to the respective material development and direct future work.

Chapter 3 concerned the high-pressure structural and band gap response of four Pt(II) compounds, previously-investigated or newly-synthesised for their piezoresistive capabilities. Firstly, the investigation clearly demonstrated that the striking difference between the piezoresistive responses of $Pt(bqd)_2$ and $MagNH_3$ was attributed to the differing extents of anisotropic compression and extent of delocalisation in the frontier bands. Focussing on the second point more closely, this investigation revealed that direct d-orbital overlap along the metal stacking direction in the HOCO, and thus the correct crystal packing to facilitate this, was not the sole prerequisite for a strong piezoresistive response; a delocalised LUCO, which contains metal···metal and/or interlayer ligand···ligand interactions of an overall bonding nature, is a vital factor that was previously under-discussed in the literature. The effect of ligand modification was also investigated. The small modification to form $MagNH_2Me$ might not have caused an initial disruption to the desired solid-state packing arrangement but was demonstrated to slow the band gap compression, due to a subtle difference in the interaction nature in the LUCO, and caused an unexpected structural phase transition at *ca.* 2 GPa. The larger modification used to form $Pt(bqd\text{-}butyl)_2$, while well-intentioned to improve thin film processability, resulted in complete disruption of the desirable crystal packing and thus the material exhibited a negligible piezoresistive response. This work not only consolidated a considerable amount of existing information that was sporadically featured in the literature, but also provided a host of new information to be used for future targeted material design. Specific guidance was provided from the calculations in terms of highlighting the construction of crystalline orbitals from molecular orbitals, although, as demonstrated in the comparison of $Pt(bqd)_2$ to $Pt(bqd\text{-}dibutyl)_2$, the nature of the

crystal packing also plays an important role, and the desired nature of the frontier orbitals to have sufficient delocalisation to ensure fast band-gap closure.

Chapter 4 followed on from the material application and techniques that featured in the previous chapter, but with a change in focus to open-shell Au(I) Mott insulators, and thus a different pressure-conductivity switch had to be considered. The investigation originally aimed to solely obtain higher-quality high-pressure structure solutions of the known $P2_1/c$ polymorph of Au(bpedt)$_2$, however the serendipitous discovery of a new polymorph ($P2_1$) caused the investigation to change course, allowing for a comparison between the structural and band gap response of the two polymorphs. Although similar intermolecular interactions were found in both polymorphs, the greater number of immediate neighbours at short distances around each molecule in the $P2_1/c$ polymorph facilitated a stronger piezoresistive response *via* greater sub-band delocalisation, and thus calculation results agreed with this known phenomenon in Mott insulator materials. This work was unfortunately somewhat hampered by poor crystal quality and the system size being too intensive to study under the same level of calculations as in Chapter 3. However, the results obtained here provide sufficient scope for future work on this material alone, with the need to obtain higher quality structural solutions and to investigate the cause of the polymorphism, the discovery of which acts as a note of caution to research groups investigating similar materials. Furthermore, the calculations revealed the important contribution in ligand···ligand interactions towards the closure of the Hubbard sub-band gap, given that the unpaired electron delocalised across the dithiolene component of the ligand. This fact provides strong guidance in designing Mott insulators which could form the conductive state at lower pressures by tuning the extent of short intermolecular ligand···ligand contact *via*, for example, the extent of steric bulk beyond the dithiolene component.

Chapter 5 focussed on the high-pressure structural response of TTTA, a small radical molecule known to exhibit magnetic bistability between a paramagnetic monoclinic

phase at higher temperature and a diamagnetic triclinic phase at lower temperatures. While previous studies revealed that the extent of paramagnetism decreases gradually upon application to pressure, the current work showed that this behaviour is not associated with any structural phase transition. It is instead likely caused by the decreasing intermolecular distance between the components accommodating the unpaired spin, thus facilitating stronger antiferromagnetic coupling at higher pressures. Moreover, this current work took advantage of the availability of the PIXEL method to quantify, in terms of energy, the hierarchy of intermolecular interactions in the crystal structure; this work revealed the three strongest interactions responsible for directing the construction of the majority of the crystal structure, providing an alternative, but complementary, view to the magnetic coupling hierarchy currently in the literature. Furthermore, the calculations revealed the energetic response of these interactions to compression of the unit cell; the strong response of the π-stacking interaction but continued stabilising of the crystal structure by the close contact inter-column interactions verify the source of the gradual suppression of paramagnetism without an associated structural phase transition as seen experimentally under the application of pressure. The results from this study, specifically the delicate combination of the primary magnetic interaction direction and relative strength of inter-column interactions, can aid the tuning of material design and crystal engineering according to the desired structural response to pressure and desired width of the magnetic hysteresis.

The final experimental chapter changes direction, firstly in its focus on gas adsorption in porous materials and secondly in its exclusive use of classical simulations to complement previously-unpublished crystallographic data. The in-depth simulations significantly bolstered the results of the diffraction experiments, by quantifying the interaction energies between the adsorbed guest molecules and the framework as well as evaluating the exploration of the porous channels by the guest molecules. The selective uptake for CO_2 over CH_4 was thus attributed to stronger interactions, and the structural phase transition in the framework seen experimentally under CO_2

uptake was rationalised by the access to stronger guest adsorption positions with the behaviour of the framework and adsorbed CO_2 being highly correlated. This study has highlighted the considerable effect on individual adsorption site positions that are associated with seemingly subtle framework changes, compared to some MOFs which undergo significant gate-opening/closing phase transitions. This work has also further highlighted the desirable gas selective capabilities of Sc_2BDC_3, and will expectantly encourage further in-depth investigations of gas mixture adsorption in candidate porous materials.

To summarise, this thesis has provided a considerable array of information on the structure-property relationships of pressure-responsive materials, in terms of consolidating and collating scattered literature understanding, clarifying some literature ambiguity and, most importantly, providing new insight and understanding behind the underlying source of the properties of these materials. Considerable focus has been placed upon the solid-state arrangement of these materials, highlighting its importance for the exhibition of the desired material properties. This thesis adds to the growing body of work that utilises the powerful combination of X-ray diffraction and computational techniques, especially in its applicability to a range of materials and property type, and has demonstrated the fundamental insights that are gained when experiment and theory are used in tandem. The computational methods have not been utilised to solely verify the experimental results, but allow for their greater interpretation, and thus gain further insight which act as guidance for next generation material design. This methodology can also be combined with other experimental techniques, such as high-pressure spectroscopy and conductivity measurements, depending on the material application of interest. Given the extent of valuable information that can be extracted about a system from the use of these methods, further work should involve more frequent utilisation of this methodology to ultimately provide more detailed criterion for devising new materials with pressure-responsive applications in mind.

Appendix

Publications and Conference Contributions

Crystallographic Data

Publications

"Pressure-induced non-innocence in bis(1,2-dionedioximato) Pt(II) complexes: an experimental and theoretical study of their insulator–metal transitions"
Benjamin, H.; Richardson, J. G.; Moggach, S. A.; Afanasjevs, S.; Warren, L.; Warren, M.; Allan, D. R.; Morrison, C. A.; Kamenev, K. V.; Robertson, N., *Phys. Chem. Chem. Phys.,* 2020, **22**, 6677.

"Probing the structural and electronic response of Magnus green salt compounds $[Pt(NH_2R)_4][PtCl_4]$ (R=H, CH_3) to pressure"
Richardson, J. G.; Benjamin, H.; Moggach, S. A.; Warren, L.; Warren, M.; Saunders, L. K; Allan, D. R.; Morrison, C. A.; Robertson, N. *Phys. Chem. Chem. Phys.,* 2020, **22**, 17668.

"Evaluating the crystalline orbital construction and resulting high-pressure structure-property responses of an extended-ligand platinum(II) bis(1,2-dioximato) complex"
Richardson, J. G.; Broadhurst, E.; Benjamin, H.; Moggach, S. A.; Morrison, C. A.; Robertson, N.
Manuscript in preparation for submission to *Dalton. Trans.* or *Mater. Chem. Front.*

"An unexpected polymorph: the structural and electronic band structure response to pressure of an Au-dithiolene Mott insulator"
Richardson, J. G.; Broadhurst, E.; Benjamin, H.; Mizuno, A.; Warren, L. R.; Warren, M; Allan, D. R.; Moggach, S. A.; Awaga, K.; Robertson, N.; Morrison, C. A.
Manuscript in preparation for submission to *Mater. Chem. Front.*

"Evaluating the high-pressure structural response and crystal lattice construction of magnetically-bistable organic radical TTTA"
Richardson, J. G.; Mizuno, A.; Awage, K.; Morrison, C. A.; Warren, M.; Allan, D. R.; Moggach, S. A.
Manuscript in preparation for *CrystEngComm*.

"Exploring phase change behaviour and selective CO_2 uptake at low pressure in Sc_2BDC_3 using in-situ gas cell crystallography and computational modelling"

Richardson, J. G.; Sotelo, J.; McHardy, J.; Warren, M.; Warren, A.; Allan, D. R.; Donval, G.; Mowat, J.; Düren, T.; Morrison, C. A.; Moggach, S. A.; Wright, P.

Manuscript in preparation for submission to *J. Am. Chem. Soc.*

Conference Contributions

Oral Presentations

"Investigating Guest Uptake in Sc_2BDC_3 Using XRD, DFT and GCMC Methods" ScotCHEM Computational Chemistry Symposium, St Andrews, UK, 15th June 2018

"Investigating Guest Uptake in Sc_2BDC_3 Using XRD, DFT and GCMC Methods" 31st European Crystallographic Meeting (Young Crystallographers Satellite Meeting), Oviedo, Spain, 22nd August 2018

"Investigating Guest Uptake in Sc_2BDC_3 Using XRD, DFT and GCMC Methods" 31st European Crystallographic Meeting, Oviedo, Spain, 25th August 2018

"Investigating Guest Uptake in Sc_2BDC_3 Using XRD, DFT and GCMC Methods" 6th International Conference on Metal-Organic Frameworks (Young Investigators' Meeting), Rotorua, New Zealand, 7th December 2018

"A High-Pressure X-ray Diffraction and Computational Investigation of Pt-containing Piezoresistive Candidate Materials" - Joseph Black Conference, Edinburgh, UK, 30th May 2019

Conference Contributions

Poster Presentations

"Investigating Gas Uptake in Sc_2BDC_3 Metal-Organic Framework Using GCMC Simulation Method" - ScotCHEM Computational Symposium, Glasgow, UK, 16th June 2017

"Investigating Guest Uptake in Sc_2BDC_3 Using XRD, ab initio DFT and GCMC Methods" - British Zeolite Association UK MOF Symposium, Southampton, UK, 9th-10th April 2018

"Investigating Guest Uptake in Sc_2BDC_3 Using XRD, ab initio DFT and GCMC Methods" - Joseph Black Conference, Edinburgh, UK, 31st May 2018

"Investigating Guest Uptake in Sc_2BDC_3 MOF using XRD, DFT and GCMC Methods" Asian Crystallographic Association Conference (AsCA 2018), Auckland, New Zealand, 2nd-5th December 2018

"Investigating Guest Uptake in Sc_2BDC_3 MOF using XRD, DFT and GCMC Methods" 6th International Conference on Metal-Organic Frameworks, Auckland, New Zealand, 9th-13th December 2018

"A High-Pressure X-ray Diffraction and Computational Investigation of Pt-containing Piezoresistive Candidate Materials" - Scottish Dalton Meeting, Edinburgh, UK, 10th June 2019

"A High-Pressure X-ray Diffraction and Computational Investigation of Pt-containing Piezoresistive Candidate Materials" - ScotCHEM Computational Chemistry Symposium, Edinburgh, UK, 26th June 2019

Crystallographic Data

The remaining pages of the appendix are dedicated to crystallographic data from all of the high-pressure series of diffraction experiments undertaken on the various compounds in Chapters 3-5, and are presented as follows:

- $Pt(bqd)_2$: Tables A1, A2
- $Pt(bqd\text{-}dibutyl)_2$: Tables A3, A4
- Magnus green salts: Tables A5, A6, A7, A8
- $Au(bpedt)_2$: Tables A9, A10
- TTTA: Table A11

The structure solutions for the ambient-pressure and high-pressure structures of $Pt(bqd)_2$ and both Magnus green salts have been published and submitted to the Cambridge Crystallographic Data Centre (reference numbers: 1971034-1971042 and 2009951-2009968 respectively), and can be obtained free of charge *via* https://www.ccdc.cam.ac.uk/structures/.

The structure solutions for the ambient-pressure and high-pressure structures of $Pt(bqd\text{-}dibutyl)_2$, polymorphs **1** and **2** of $Au(bpedt)_2$, and 1,3,5-triathia-2,4,6,-triazapentalenyl (TTTA) have yet to be submitted to the Cambridge Crystallographic Data Centre, and are awaiting finalisation prior to publication. As a result, the exact data presented in this appendix for those compounds are subject to change. However, the narrative presented in the relevant experimental chapters, concerning the results of the various high-pressure crystallographic studies and subsequent calculations, is not expected to be altered.

Table A1. Crystallographic data for each pressure point of the high-pressure series of experiments on $Pt(bqd)_2$.

	Ambient[a]	**0.11 GPa**	**0.16 GPa**	**0.29 GPa**	**0.58 GPa**	**1.03 GPa**	**1.47 GPa**	**1.98 GPa**	**2.38 GPa**
a (Å)	9.7525(3)	9.7489(10)	9.7361(8)	9.7115(8)	9.6689(7)	9.6376(8)	9.6249(11)	9.5883(19)	9.5805(9)
b (Å)	20.6661(6)	20.623(18)	20.626(13)	20.570(13)	20.509(11)	20.354(14)	20.271(19)	20.186(15)	20.129(16)
c (Å)	6.3580(2)	6.3270(9)	6.3029(7)	6.2627(7)	6.1816(5)	6.0986(6)	5.9805(10)	5.8532(9)	5.8077(9)
α (°)	90	90	90	90	90	90	90	90	90
β (°)	90	90	90	90	90	90	90	90	90
γ (°)	90	90	90	90	90	90	90	90	90
V (Å^3)	1281.4(1)	1272.1(2)	1265.7(2)	1251.1(2)	1225.8(1)	1196.31(1)	1166.8(2)	1132.9(2)	1120.0(2)
Space Group	*Ibam*	*Ibam*	*Ibam*	*Ibam*	*Ibam*	*Ibam*	*Ibam*	*Ibam*	*Ibam*
λ / Å	0.71073(Mo Kα)	0.4859	0.4859	0.4859	0.4859	0.4859	0.4859	0.4859	0.4859
Completeness	99.9%	43.6%	46.8%	47.9%	47.1%	49.0%	47.2%	48.0%	47.7%
Number of measured, independent and observed [I>2σ] reflections	6574, 728, 479	2309, 362, 260	1063, 195, 195	1043, 197, 196	1171, 189, 188	1224, 195, 194	1199, 184, 183	1149, 182, 181	1131, 180, 178
T min	1.971	2.855	2.861	1.585	1.592	1.598	1.601	1.607	1.609
T max	26.483	17.635	17.646	17.625	17.605	17.664	17.649	17.652	17.652
μ (mm^{-1})	10.973	11.054	11.109	11.239	11.471	11.754	12.051	12.412	12.554
Resolution / Å	0.80	0.80	0.80	0.80	0.80	0.80	0.80	0.80	0.80
Number of Parameters	71	71	71	71	69	71	69	69	69
Number of Restraints	10	88	122	122	121	122	114	114	114
R_{int}	0.051	0.071	0.066	0.059	0.047	0.074	0.065	0.056	0.057
wR (F^2)	0.0360	0.0976	0.0889	0.0696	0.0554	0.0850	0.1586	0.1779	0.1871
R[F^2>2σ(F^2)]	0.051	0.053	0.035	0.028	0.022	0.035	0.072	0.079	0.080

[a] First reported in the MChemX report of Edward Broadhurst (University of Edinburgh, 2018). Reported here for completeness of pressure series and for its importance for the solid-state calculations reported in this thesis.

Table A2. Selection of intramolecular and intermolecular structural components measured from the structure solutions for each pressure point of the high-pressure series of experiments on $Pt(bqd)_2$

Pressure (GPa)	Pt-N bond lengths (Å)	N-Pt-N angles (°)	N-Pt···Pt-N torsion angles (°)
Ambient[a]	1.988(6), 1.982(7)	100.4(4), 79.6(4)	93.2(3), 86.8(3)
0.11	1.983(17), 1.997(8)	99.9(5), 80.1(5)	93.5(4), 86.5(4)
0.16	1.980(20), 1.990(10)	98.2(7), 81.9(7)	92.7(6), 87.3(6)
0.29	1.982(17), 2.002(8)	99.0(6), 81.1(6)	92.5(7), 87.5(7)
0.58	1.999(14), 1.994(8)	100.7(5), 79.3(5)	93.9(4), 86.1(4)
1.03	2.062(18), 2.013(10)	100.8(6), 79.2(6)	93.2(5), 86.8(5)
1.47	2.100(30), 1.990(16)	101.6(8), 78.4(8)	94.2(7), 85.8(7)
1.98	2.110(30), 1.970(17)	101.2(8), 78.7(8)	94.4(7), 85.6(7)
2.38	2.100(30), 1.975(18)	101.3(9), 78.8(9)	94.1(7), 85.9(7)

[a] First reported in the MChemX report of Edward Broadhurst (University of Edinburgh, 2018). Reported here for completeness of pressure series and for its importance for the solid state calculations reported in this thesis.

Table A3. Crystallographic data for each pressure point of the in-house high-pressure series of experiments on Pt(bqd-dibutyl)$_2$. These structures were first reported in the MChemX final report of Edward Broadhurst (University of Edinburgh, 2018), but have been shown here to allow comparison to the other high-pressure series of experiments on Pt(bqd-dibutyl)$_2$ undertaken at the Diamond Light Source synchrotron I19 beamline (Table A4).

	Ambient	**0.14 GPa**	**0.76 GPa**	**1.43 GPa**
a (Å)	20.7074(11)	20.6020(17)	20.3289(19)	20.088(3)
b (Å)	4.9052(2)	4.8431(10)	4.7018(1)	4.6778(3)
c (Å)	28.1381(14)	27.9031(7)	27.4559(8)	27.3616(15)
α (°)	90	90	90	90
β (°)	90	90	90	90
γ (°)	90	90	90	90
V (Å^3)	2858.10(14)	2784.10(21)	2624.30()	2571.11()
Space Group	*Pna*2$_1$	*Pna*2$_1$	*Pna*2$_1$	*Pna*2$_1$
λ / Å	0.71073 (Mo Kα)	0.71073 (Mo Kα)	0.71073 (Mo Kα)	0.71073 (Mo Kα)
Completeness	96.8%	50.6%	44.7%	50.1%
Number of measured, independent and observed [I>2σ] reflections	30739, 6887, 5086	8690, 1963, 1308	7639, 1738, 1215	6446, 1486, 1029
T min	1.967	3.527	3.582	3.604
T max	28.512	23.293	23.257	22.042
*μ (*mm^{-1}*)*	4.948	5.080	5.389	5.500
Resolution / Å	0.74	0.90	0.90	0.95
Number of Parameters	335	150	149	150
Number of Restraints	337	161	161	161
R_{int}	0.031	0.041	0.046	0.078
wR (F^2)	0.0389	0.0957	0.1026	0.1159
R[F^2>2σ(F^2)]	0.0402	0.0702	0.0878	0.1052

Table A4. Crystallographic data for each pressure point of the high-pressure series of experiments on Pt(bqd-dibutyl)$_2$, collected at the Diamond Light Source synchrotron I19 beamline.

	0.11 GPa	**0.78 GPa**	**1.11 GPa**	**1.47 GPa**	**1.76 GPa**	**2.26 GPa**
a (Å)	20.403(19)	20.365(19)	20.00(2)	19.61(4)	19.64(4)	19.32(6)
b (Å)	4.7354(6)	4.7134(6)	4.7022(8)	4.6817(17)	4.6585(14)	4.6324(19)
c (Å)	27.814(3)	27.755(3)	27.772(3)	27.693(6)	27.495(7)	27.529(11)
α (°)	90	90	90	90	90	90
β (°)	90	90	90	92.81(6)	94.12(6)	94.48(9)
γ (°)	90	90	90	90	90	90
V (Å^3)	2687(3)	2664.2(3)	2611.3(3)	2539(50	2509(6)	2456(8)
Space Group	*Pna*2$_1$	*Pna*2$_1$	*Pna*2$_1$	*P*2$_1$	*P*2$_1$	*P*2$_1$
λ / Å	0.4859	0.4859	0.4859	0.4859	0.4859	0.4859
Completeness	47.6%	47.6%	47.2%	46.1%	45.9%	47.6%
Number of measured, independent and observed [I>2σ] reflections	6490, 1494, 1040	6484, 1497, 1124	6760, 1464, 1054	7352, 2702, 826	7266, 2681, 832	7087, 2703, 395
T min	1.6498	1.6528	1.6572	1.6674	1.6771	1.6774
T max	15.658	14.816	14.807	14.812	14.809	14.791
μ (mm^{-1})	5.263	5.308	5.416	5.571	5.637	5.754
Resolution / Å	0.95	0.95	0.95	0.95	0.95	0.95
Number of Parameters	157	335	335	313	313	-
Number of Restraints	171	377	377	455	435	-
R_{int}	0.095	0.096	0.085	0.135[a]	0.147[b]	0.242[c]
wR (F^2)	0.1244	0.1853	0.1764	0.2266	0.1844	-
R[F^2>2σ(F^2)]	0.1013	0.0729	0.0664	0.1846	0.1564	Structure Unsolved

[a] R_{merge} exceeded 45% beyond 1.15Å. [b] R_{merge} exceeded 45% beyond 1.18Å. [c] R_{merge} exceeded 45% beyond 1.69Å.

Table A5. Crystallographic data for each pressure point of the high-pressure series of experiments on $MagNH_3$.

	Ambient	**0.37 GPa**	**0.74 GPa**	**1.06 GPa**	**1.65 GPa**	**1.96 GPa**	**2.28 GPa**	**2.71 GPa**	**3.73 GPa**	**4.62 GPa**
a (Å)	8.97809(14)	8.9435(5)	8.8963(4)	8.8591(6)	8.7949(6)	8.7712(8)	8.7425(7)	8.7220(11)	8.6538(10)	8.6076(14)
b (Å)	8.97809(14)	8.9435(5)	8.8963(4)	8.8591(6)	8.7949(6)	8.7712(8)	8.7425(7)	8.7220(11)	8.6538(10)	8.6076(14)
c (Å)	6.4585(3)	6.4253(7)	6.3753(6)	6.3339(8)	6.2730(8)	6.2436(9)	6.2161(8)	6.1933(11)	6.1220(12)	6.0602(17)
α (°)	90	90	90	90	90	90	90	90	90	90
β (°)	90	90	90	90	90	90	90	90	90	90
γ (°)	90	90	90	90	90	90	90	90	90	90
V ($Å^3$)	520.59(3)	513.93(6)	504.57(4)	497.11(6)	485.22(6)	480.35(7)	475.10(6)	471.14(8)	458.47(9)	449.01(12)
Space Group	*P4/mnc*	*P4/mnc*	*P4/mnc*	*P4/mnc*	*P4/mnc*	*P4/mnc*	*P4/mnc*	*P4/mnc*	*P4/mnc*	*P4/mnc*
λ / Å	1.54178 (Cu Kα)	0.4859	0.4859	0.4859	0.4859	0.4859	0.4859	0.4859	0.4859	0.4859
Completeness	99.7%	82.9%	75.4%	81.0%	82.6%	83.2%	82.9%	82.8%	82.4%	83.1%
Number of measured, independent and observed [I>2σ] reflections	2295, 285, 244	1118, 207, 185	1037, 184, 144	1250, 200, 160	1410, 196, 147	1327, 196, 143	1341, 193, 145	1415, 193, 137	1130, 161, 115	1172, 163, 112
T min	6.975	2.669	4.128	4.148	2.239	2.245	2252	2.258	3.599	3.619
T max	72.916	16.534	16.566	16.555	16.579	16.567	16.599	16.579	15.621	15.658
μ (mm^{-1})	58.572	10.430	10.623	10.783	11.047	11.159	11.282	11.377	11.692	11.938
Resolution / Å	0.84	0.85	0.85	0.85	0.85	0.85	0.85	0.85	0.85	0.85
Number of Parameters	18	18	18	18	18	18	18	18	18	18
Number of Restraints	2	2	2	2	2	2	2	2	2	2
R_{int}	0.052	0.025	0.034	0.073	0.072	0.067	0.080	0.085	0103	0.115
wR (F^2)	0.0885	0.0968	0.2657	0.3035	0.2364	0.2159	0.2345	0.2080	0.2683	0.2746
R[F^2>2σ(F^2)]	0.056	0.039	0.111	0.125	0.101	0.089	0.095	0.087	0.110	0.086

Table A6. Crystallographic data for each pressure point of the high-pressure series of experiments on $MagNH_2Me$.

	Ambient	**0.16 GPa**	**0.25 GPa**	**0.58 GPa**	**0.90 GPa**	**1.23 GPa**	**1.61 GPa**	**1.92 GPa**	**2.33 GPa**
a (Å)	10.35151(12)	10.3266(8)	10.3078(8)	10.2482(7)	10.1964(7)	10.1452(13)	10.0908(14)	10.056(2)	14.160(9)
b (Å)	10.35151(12)	10.3266(8)	10.3078(8)	10.2482(7)	10.1964(7)	10.1452(13)	10.0908(14)	10.056(2)	14.179(3)
c (Å)	6.4977(2)	6.4805(10)	6.4712(10)	6.4309(9)	6.3876(9)	6.3581(11)	6.3306(17)	6.320(3)	6.274(1)
α (°)	90	90	90	90	90	90	90	90	90
β (°)	90	90	90	90	90	90	90	90	92.13(3)
γ (°)	90	90	90	90	90	90	90	90	90
V ($Å^3$)	696.25(3)	691.06(10)	687.57(11)	675.41(10)	664.10(9)	654.41(11)	644.60(18)	639.1(3)	1258.69
Space Group	*P4/mnc*	*P4/mnc*	*P4/mnc*	*P4/mnc*	*P4/mnc*	*P4/mnc*	*P4/mnc*	*P4/mnc*	*C2/c*
λ / Å	1.54178 (Cu Kα)	0.4859	0.4859	0.4859	0.4859	0.4859	0.4859	0.4859	0.4859
Completeness	96.7%	89.5%	93.1%	92.0%	97.2%	96.6%	98.4%	82.8%	58.0%
Number of measured, independent and observed [I>2σ] reflections	3522, 397, 268	1769, 306, 192	1889, 317, 204	1808, 306, 190	2051, 319, 197	2137, 314, 173	2159, 310, 184	2051, 296, 170	2746, 746, 260
T min	6.046	3.016	2.541	2.556	1.931	1.941	1.843	1.958	2.813
T max	75.793	16.778	16.809	16.794	16.803	16.799	15.808	16.810	26.371
μ (mm^{-1})	43.901	20.967	21.074	21.453	21.819	22.142	22.479	22.673	23.024
Resolution / Å	0.80	0.84	0.84	0.84	0.84	0.84	0.84	0.84	0.80
Number of Parameters	27	24	27	27	27	27	27	27	-
Number of Restraints	14	14	14	14	14	14	14	14	-
R_{int}	0.055	0.064	0.053	0.053	0.025	0.052	0.069	0.076	0.048
wR (F^2)	0.1176	0.1399	0.0975	0.1426	0.0883	0.1344	0.1238	0.1150	-
R[F^2>2σ(F^2)]	0.050	0.056	0.050	0.057	0.029	0.043	0.050	0.041	Structure Unsolved

Table A7. Selection of intramolecular and intermolecular structural components measured from the structure solutions for each pressure point of the high-pressure series of experiments on $MagNH_3$.

Pressure (GPa)	Pt–N bond length (Å)	Pt–Cl bond length (Å)	Cl–Pt···Pt–N torsion angle (°)
Ambient	2.068(10)	2.330(4)	-29.1(2)
0.37	2.058(8)	2.332(3)	-28.4(2)
0.74	2.064(12)	2.324(4)	-28.1(3)
1.06	2.069(13)	2.329(4)	-28.9(3)
1.65	2.061(14)	2.320(4)	-28.5(4)
1.96	2.079(18)	2.321(6)	-28.6(4)
2.28	2.066(18)	2.315(5)	-28.9(5)
2.71	2.069(17)	2.323(5)	-29.0(4)
3.73	2.074(18)	2.318(6)	-30.1(5)
4.62	2.050(30)	2.321(9)	-29.3(7)

Table A8. Selection of intramolecular and intermolecular structural components measured from the structure solutions for each pressure point of the high-pressure series of experiments on $MagNH_2Me$.

Pressure (GPa)	Pt–N bond length (Å)	Pt–Cl bond length (Å)	∠Pt–N–C angle (°)	Cl–Pt···Pt–N torsion angle (°)
Ambient	2.059(10)	2.320(3)	124.0(8)	31.3(2)
0.16	2.089(11)	2.329(3)	124.2(8)	32.5(3)
0.25	2.087(9)	2.325(3)	123.2(7)	32.3(2)
0.58	2.079(12)	2.326(4)	124.5(9)	33.5(3)
0.90	2.095(14)	2.321(4)	122.7(12)	32.6(3)
1.23	2.066(13)	2.309(5)	124.0(11)	33.4(3)
1.61	2.059(11)	2.303(5)	125.6(10)	33.8(3)
1.92	2.109(19)	2.316(6)	124.2(14)	33.4(4)

Table A9. Crystallographic data for each pressure point of the in-house high-pressure series of experiments on polymorph 1 ($P2_1/c$) of $Au(bpedt)_2$. These structures were first reported in the MChemX final report of Edward Broadhurst (University of Edinburgh, 2018), but have been shown here to allow comparison to the high-pressure series of experiments on polymorph 2 ($P2_1$) of $Au(bpedt)_2$ undertaken at the Diamond Light Source synchrotron I19 beamline (Table A10).

	Ambient	**0.33 GPa**	**0.94 GPa**	**1.36 GPa**	**1.76 GPa**	**2.11 GPa**
a (Å)	6.21586(8)	6.1182(5)	6.0443(4)	6.0151(6)	5.9664(10)	5.9252(19)
b (Å)	7.36044(10)	7.1487(5)	6.9977(4)	6.9706(6)	6.9198(10)	6.8731(19)
c (Å)	51.8984(6)	51.642(3)	51.504(2)	51.497(4)	51.523(6)	51.440(12)
α (°)	90	90	90	90	90	90
β (°)	92.5170(7)	92.411(6)	92.148(4)	92.076(6)	91.970(10)	92.04(2)
γ (°)	90	90	90	90	90	90
V ($Å^3$)	2372.14(5)	2256.7(3)	2176.9(1)	2157.78(15)	2125.9(5)	2093.5(5)
Space Group	$P2_1/c$	$P2_1/c$	$P2_1/c$	$P2_1/c$	$P2_1/c$	$P2_1/c$
λ / Å	0.71073 (Mo Kα)	0.71073 (Mo Kα)	0.71073 (Mo Kα)	0.71073 (Mo Kα)	0.71073 (Mo Kα)	0.71073 (Mo Kα)
Completeness	96.1%	50.8%	58.8%	58.6%	61.0%	72.2%
Number of measured, independent and observed [I>2σ] reflections	25995, 5656, 4080	7024, 1929, 984	6739, 1843, 1091	6722, 1846, 1008	6090, 1665, 778	2780, 721, 455
T min	1.571	3.716	3.314	3.530	3.175	3.188
T max	28.290	23.416	23.271	23.377	22.308	21.580
μ (mm^{-1})	6.570	6.906	7.159	7.223	7.333	7.442
Resolution / Å	0.75	0.89	0.90	0.90	0.94	1.20
Number of Parameters	298	298	298	298	298	138
Number of Restraints	282	360	360	360	360	168
R_{int}	0.030	0.041	0.036	0.052	0.063	0.094
wR (F^2)	0.0701	0.0530	0.0445	0.0279	0.0327	0.1354
R[F^2>2σ(F^2)]	0.0624	0.0425	0.0571	0.1009	0.1538	0.1199

Table A10. Crystallographic data for each pressure point of the high-pressure series of experiments on polymorph 2 ($P2_1$) of $Au(bpedt)_2$, collected at the Diamond Light Source synchrotron I19 beamline.

	0.11 GPa	**0.26 GPa**	**0.34 GPa**	**0.61 GPa**	**0.85 GPa**	**1.18 GPa**
a (Å)	11.67(3)	11.59(3)	11.65(3)	11.50(3)	11.31(4)	11.27(3)
b (Å)	7.4328(16)	7.3538(19)	7.2997(14)	7.2345(18)	7.2240(20)	7.1803(19)
c (Å)	14.529(8)	14.484(10)	14.472(7)	14.414(10)	14.475(14)	14.392(14)
α (°)	90	90	90	90	90	90
β (°)	113.00(16)	112.89(18)	113.37(14)	112.98(19)	112.7(3)	112.98(15)
γ (°)	90	90	90	90	90	90
V (Å^3)	1161(3)	1138(4)	1130(3)	1104(4)	1091(5)	1072(3)
Space Group	$P2_1$	$P2_1$	$P2_1$	$P2_1$	$P2_1$	$P2_1$
λ / Å	0.4859	0.4859	0.4859	0.4859	0.4859	0.4859
Completeness	0.414	0.413	0.410			
Number of measured, independent and observed [I>2σ] reflections	3139, 1123, 706	3122, 1136, 638	3086, 1111, 683	2891, 1063, 505	3045, 1071, 454	3125, 1058, 461
T min	1.8731	1.8921	1.9073	1.9184	1.9272	1.9322
T max	14.7671	14.8113	14.8131	14.7973	14.7321	14.7170
μ (mm^{-1})	6.716	6.850	6.897	7.059	7.144	7.270
Resolution / Å	0.95	0.95	0.95	0.95[a]	0.95[b]	0.95[c]
Number of Parameters	298	298	298	298	298	-
Number of Restraints	443	443	443	451	450	-
R_{int}	0.146	0.198	0.206	0.240	0.292	0.252
wR (F^2)	0.2692	0.3215	0.3180	0.3832	0.5367	-
R[F^2>2σ(F^2)]	0.1154	0.1468	0.1424	0.1813	0.2568	-

[a] R_{merge} exceeded 45% beyond 1.15Å. [b] R_{merge} exceeded 45% beyond 1.18Å. [c] R_{merge} exceeded 45% beyond 1.69Å.

Table A11. Crystallographic data for each pressure point of the high-pressure series of experiments on 1,3,5-triathia-2,4,6,-triazapentalenyl (TTTA).

	Ambient	**0.33 GPa**	**0.94 GPa**	**1.36 GPa**	**1.76 GPa**	**2.11 GPa**	**2.54 GPa**	**2.91 GPa**	**3.94 GPa**	**4.56 GPa**
a (Å)	9.4388(5)	9.430(8)	9.353(7)	9.332(7)	9.301(11)	9.287(12)	9.255(12)	9.204(9)	9.101(13)	9.081(17)
b (Å)	3.7100(2)	3.6047(3)	3.5177(3)	3.4658(2)	3.4244(3)	3.3977(4)	3.3745(4)	3.3539(3)	3.3020(4)	3.2672(60
c (Å)	15.0579(8)	14.937(2)	14.831(2)	14.742(2)	14.699(3)	14.643(3)	14.594(3)	14.565(2)	14.494(4)	14.419(4)
α (°)	90	90	90	90	90	90	90	90	90	90
β (°)	104.55(3)	104.49(4)	104.46(4)	104.34(3)	104.29(6)	104.28(6)	104.28(6)	104.33(5)	104.52(7)	104.71(9)
γ (°)	90	90	90	90	90	90	90	90	90	90
V (Å^3)	510.38(3)	491.59(7)	472.46(6)	461.93(6)	453.68(9)	447.79(9)	441.69(9)	435.64(7)	421.68(10)	413.81(13)
Space Group	$P2_1/c$	$P2_1/c$	$P2_1/c$	$P2_1/c$	$P2_1/c$	$P2_1/c$	$P2_1/c$	$P2_1/c$	$P2_1/c$	$P2_1/c$
λ / Å	0.71073 (Mo Kα)	0.4859	0.4859	0.4859	0.4859	0.4859	0.4859	0.4859	0.4859	0.4859
Completeness	99.5%	33.8%	34.6%	37.5%	37.6%	36.2%	36.3%	36.1%	40.2%	41.6%
Number of measured, independent and observed [I>2σ] reflections	4849, 1061, 1020	722, 229, 220	739, 232, 213	850, 248, 227	918, 245, 216	864, 232, 177	837, 231, 177	786, 224, 170	1080, 246, 207	1276, 247, 202
T min	2.796	3.7725	3.7998	3.8231	3.8350	3.8491	4.1286	3.8703	3.9715	3.9065
T max	26.518	15.5768	15.6441	15.6596	15.6588	15.6242	15.6429	15.5877	15.6609	15.6175
μ (mm^{-1})	1.315	1.365	1.420	1.453	1.479	1.499	1.519	1.541	1.592	1.622
Resolution / Å	0.80	0.90	0.90	0.90	0.90	0.90	0.90	0.90	0.90	0.90
Number of Parameters	73	73	73	33	35	33	33	33	73	73
Number of Restraints	21	104	104	50	50	71	50	50	104	104
R_{int}	0.011	0.021	0.027	0.019	0.038	0.067	0.045	0.037	0.047	0.039
wR (F^2)	0.0627	0.1153	0.0961	0.4180	0.4966	0.6342	0.6806	0.4036	0.2047	0.1944
R[F^2>2σ(F^2)]	0.0254	0.0589	0.0425	0.1686	0.2179	0.3667	0.3380	0.2062	0.0956	0.0840